NICOLAUS COPERNICUS UNIVERISTY IN TORUŃ
Faculty of Physics, Astronomy and Informatics
Scientific discipline: Physical Sciences

DOCTORAL THESIS

Development of Novel Semiconductor Scintillators

Author: Abdellah Bachiri
Supervisor: Prof. dr. hab. Winicjusz Drozdowski
Co-supervisor: Dr. Marcin E. Witkowski

Doctoral dissertation submitted to the Council of the Discipline of Physical Sciences in partial fulfillment of the requirements for the degree of Ph.D.

Toruń, 2024

I would like to extend my heartfelt gratitude to everyone who has played a role in the successful completion of this dissertation. In particular, I wish to acknowledge:

- My supervisors, Prof. Dr. hab. Winicjusz Drozdowski and Dr. Marcin Witkowski, whose invaluable support, wisdom, and academic mentorship have guided me throughout this journey.
- Dr. Zbigniew Gałązka, for his significant contribution to my scientific growth and our productive long-term collaboration, which has been both inspiring and enriching.
- Prof. Łukasz Świderski, for his warm hospitality and invaluable assistance during the measurements at the National Centre for Nuclear Research (NCBJ).
- The National Science Centre (NCN) and Deutsche Forschungsgemeinschaft (DFG), for their generous funding of the project "β-Ga_2O_3:Ce Semiconductor as a New Scintillator - Investigation of Spectroscopic and Scintillation Properties (GO SCINT)," project number 2016/23/G/ST5/04048 (NCN) / GA 2057/2-1 (DFG).
- My parents, for their unwavering dedication and sacrifices in raising me, my sisters Ahlam and Hanan, and my brother Abdessamed, whose love and support have been my foundation.
- Finally, to all those who have shaped me into the person I am today, even if I cannot name each one individually, your influence is deeply appreciated.

Thank you!

Abstract

This research focuses on the scintillation properties of three types of crystals: pure and doped gallium oxide (β-Ga_2O_3), Ga-based spinels ($MgGa_2O_4$ and $ZnGa_2O_4$), and mixed (Zn,Be)Se crystals with Be compositions from 2% to 20%.

The study includes pulse height spectra, scintillation time profiles, and radio- and thermoluminescence measurements. For β-Ga_2O_3, the pure crystals achieved the highest scintillation yield (~9000 ph/MeV) and the best energy resolution (10.6%) with free electron concentrations of 10^{16} cm^{-3}. Higher free carrier concentrations led to decreased light yield due to Auger quenching. $MgGa_2O_4$ and $ZnGa_2O_4$ crystals were also found to scintillate under gamma irradiation, with yields up to 2500 ph/MeV. Mixed (Zn,Be)Se crystals initially showed low scintillation efficiency, but zinc vapor annealing increased the yield to 7700 ph/MeV for Be concentration of 2%. A new method for analyzing scintillation decay curves was developed, involving recording both the sample and apparatus responses, which were deconvolved and fitted with multi-exponential decay functions. This revealed that the fastest mean decay times were observed for samples with lower scintillation yields. Thus, a balance is needed to achieve both fast and efficient scintillation in β-Ga_2O_3, $MgGa_2O_4$, $ZnGa_2O_4$ and (Zn,Be)Se crystals, which is to be found by adjusting selected parameters prior to the crystal growth. Radioluminescence spectra revealed typical bands for all the studied materials, with some negative thermal quenching. Thermoluminescence measurements detected glow peaks in crystals across all categories, which were analyzed quantitatively. Additionally, the temperature dependence of relative light yield was examined, showing significant variation with temperature. For instance, β-Ga_2O_3 exhibited only 40% of its light yield at room temperature as compared to liquid N_2.

Acknowledgements

This research has been financed from the funds of the Polish National Science Centre (NCN) and the German Research Foundation (DFG) in frames of a joint grant

(NCN: 2016/23/G/ST5/04048, DFG: GA 2057/2-1).

List of elements

Chapter 1

1 Introduction

A scintillator is defined as a material that emits light when it interacts with ionizing radiation, in a phenomenon known as scintillation. Scintillators are of great importance in a number of fields, including radiation detection, medical imaging and high-energy physics. There are numerous varieties of scintillators, including the more commonly encountered sodium iodide (NaI), lanthanum bromide ($LaBr_3$), cerium bromide (CeBr), and cesium iodide (CsI). Each of these materials possesses distinctive properties, rendering them appropriate for particular applications based on factors such as energy resolution, light output, decay time, and cost. Researchers and engineers meticulously select the most suitable scintillator to meet the specific requirements of their applications.

The journey of scintillating materials began in the early 1900s with the discovery of calcium tungstate ($CaWO_4$) and zinc sulfide doped with silver ions (ZnS:Ag) [1]. These were the primary scintillators known for approximately 40 years, representing the initial phase of their development. A significant turning point came in the 1930s and 1940s with the invention of the first photomultiplier tube [2]. This breakthrough ignited widespread interest in scintillating materials, leading to the discovery of numerous new compounds and marking the second phase of scintillator history. The 1960s brought another leap forward, as advancements in crystal growth techniques allowed for the creation of materials with much higher melting points. This period also saw the introduction of cerium ion doping, which significantly improved the speed and efficiency of d-f emission [3]. The discovery of cerium-doped lanthanum chloride ($LaCl_3$:Ce) in 2000 ushered in the third phase [4], characterized by more refined materials and enhanced performance. Today, we are in the fourth stage of scintillator development, marked by ongoing innovations and the exploration of new materials.

While diagrams published by Dorenbos have identified several key semiconductors, gallium oxide - the focus of this dissertation and a member of the scintillating semiconductors group - still remains underexplored. Gallium and its derivatives were first identified by de Boisbaudran in the late 1800s [5], but it was not until the 21st century that pure gallium oxide crystals began to attract significant scientific attention as a potential scintillating material. This increased interest is partly due to the relatively small number of known scintillating semiconductors, combined with the promising yet still largely untapped potential of gallium oxide. The material’s novelty as a scintillator suggests that significant advancements are still possible. Recent discussions have highlighted its potential applications in industries, including the development of Schottky diodes, photodetectors, and nuclear radiation detectors [6,7].

The first evidence of gallium oxide's scintillating properties came from Yanagida and his team in the early 2010s [8]. Although some of their reported scintillation efficiency values were later considered overestimated [9], their work generated substantial interest and set the stage for further research in this area.

This dissertation examines the scintillating and optical properties of two categories of samples. The first one includes pure β-Ga_2O_3 crystals, β-Ga_2O_3 crystals doped with silicon, and two Ga-based spinels, $MgGa_2O_4$ and $ZnGa_2O_4$. The second category comprises the investigation of luminescence properties of pure ZnSe and mixed (Zn,Be)Se with varying Be compositions ranging from 2% to 20%, extending the research to include their thermal properties. Most of the research was conducted at the Institute of Physics at Nicolaus Copernicus University in Toruń, encompassing scintillation, thermoluminescence, radioluminescence, and thermal property studies, as well as the crystal growth of pure ZnSe and (Zn,Be)Se. However, the growth of β-Ga_2O_3 and the Ga-based spinels was performed at the Leibniz Institute for Crystal Growth in Berlin. This collaborative Toruń-Berlin scientific effort was supported by funding from the National Science Centre (NCN) and the German Research Foundation (DFG) under the joint grant titled "β-Ga_2O_3:Ce Semiconductor as a New Scintillator-Investigation of Spectroscopic and Scintillation Properties (GO SCINT)” already mentioned in the acknowledgment.

References (chapter 1)

[1] P. Dorenbos, “The quest for high resolution γ-ray scintillators,” Optical Materials X, vol. 1, no. 1, p. 1, 2019.

[2] J. Rajchman and E. W. Pike, “Electrostatic Focusing in Secondary Emission Multipliers,” 1937.

[3] K. Takagi and T. Fukazawa, “Cerium-activated Gd_2SiO_5 single crystal scintillator,” Applied Physics Letters., vol. 43, no. 41, p. 42, 1982.

[4] E. V. D. van Loef, P. Dorenbos, C. W. E. van Eijk, K. Kramer, and H. U. Gudel, “Highenergy-resolution scintillator : Ce^{3+} activated $LaCl_3$,” Appl. Phys. Lett., vol. 10, no. 77, p. 1467, 2000.

[5] L. de Boisbaudran, “On the chemical and spectroscopic characters of a new metal (gallium),” Phil. Magazine, vol. 50, no. 332, p. 414, 1875.

[6] Z. Galazka, “β-Ga_2O_3 bulk crystal growth for wide-bandgap electronics and optoelectronics,” Semicond. Sci. Technol., no. 33, p. 1, 2018.

[7] S. I. Stepanov, V. I. Nikolaev, V. E. Bougrov, and A. E. Romanov, “Gallium oxide: Properties and applications - A review,” Rev. Adv. Mater. Sci., vol. 44, no. 1, p. 63, 2016.

[8] T. Yanagida, G. Okada, T. Kato, D. Nakauchi, and S. Yanagida, “Fast and high light yield scintillation in the Ga_2O_3 semiconductor material,” Appl. Phys. Express, vol. 9, no. 4, p. 1, 2016.

[9] W. Drozdowski, M. Makowski, M.E. Witkowski, A. Wojtowicz, Z. Galazka, K. Irmscher, R. Schewski, “β-Ga_2O_3:Ce as a fast scintillator: An unclear role of cerium,” Radiat. Meas., vol. 121, p. 49, 2019.

Chapter 2

2 Physical bases of the scintillation phenomenon

The scintillation phenomenon is a physical process where certain materials emit light when exposed to ionizing radiation. This occurs due to the interaction between the radiation and the material, leading to the excitation of electrons. As these electrons return to their ground state, they release energy in the form of light. Understanding the physical principles behind this process is crucial for the development of scintillators, which are widely used in radiation detection and medical imaging.

2.1 Interaction of ionizing radiation with matter

Unlike neutral particles such as neutrons and neutrinos, as well as short-wavelength electromagnetic radiation like X-rays and gamma rays, charged particles like electrons, positrons, protons, and helium nuclei have the ability to directly ionize matter. On the other hand, neutral particles and short-wavelength electromagnetic radiation do not possess this ionizing capability. When it comes to radiation, it can only be detected through its interaction with matter; technically speaking, it is never measured directly. There exist various types of interaction processes that occur between radiation and matter, which are common to charged particles, neutrons, neutrinos, X-rays, and other forms of radiation.

2.1.1 Definition of radiation

The term "radiation" was initially coined to describe the emissions of α-rays, β-rays, and γ-rays from natural radioactive isotopes. Over time, its definition has expanded to encompass not only elementary particles, nuclei, electrons, and photons, but also any objects moving at speeds comparable to or greater than those of rays emitted by radioactive isotopes. While particles do not travel in a straight line like rays, the term "rays" is still utilized because the particle paths have a discernible direction. When radiation interacts with matter, it can cause ionization of atoms and molecules, either directly or indirectly. Hence, the term "ionizing radiation" is employed to denote this ability.

Charged and uncharged particles can be used to categorize radiation. The charged particles are known as direct ionizing radiation, as they ionize atoms and molecules directly using their electric charge. X-rays, γ-rays, and neutrons belong to the non-charged particle category. Since they lack electric charge, they cannot ionize atoms using the electric force directly. However, when these particles interact with matter, they generate secondary charged particles. These particles are referred to as indirect ionizing radiation, as they ionize atoms and molecules through secondary charged particles.

Radiation can be generated by various sources depending on the type of radiation being produced. X-rays, for example, can be generated using specialized X-ray tubes, linear accelerators, or synchrotron radiation facilities. γ-rays, on the other hand, are typically produced through the decay of radioactive isotopes. Electrons can be generated using linear accelerators, betatrons, or microtrons, while β-rays are emitted by certain radioactive isotopes.

2.1.2 Solid state classification: insulators, semiconductors and conductors

Solid state materials can be classified into three groups based on their electrical properties: insulators, semiconductors and conductors (**Fig. 2.1**). Insulators are materials that lack free charge carriers under normal conditions and have an electrical conductivity below 10^{-8} S/cm. For example, diamond demonstrates a conductivity of approximately 10^{-16} S/cm. On the other hand, conducting materials possess an abundance of free electrons that enable electric conduction, resulting in high conductivities exceeding 10^{3} S/cm. Silver, for instance, exhibits a conductivity of approximately 10^{6} S/cm. Semiconductor materials occupy an intermediate position between insulators and conductors in terms of their electrical properties. They display conductivities ranging from 10^{-8} S/cm to 10^{3} S/cm. Silicon, a commonly used semiconductor, can exhibit conductivities within the range of 10^{-5} S/cm to 10^{3} S/cm.

The variation in electrical conduction properties among different elements and compounds can be explained by considering the energy levels of electrons in the valence and conduction bands. Electrons occupying lower energy bands, which are usually fully occupied, do not contribute to the conduction process.

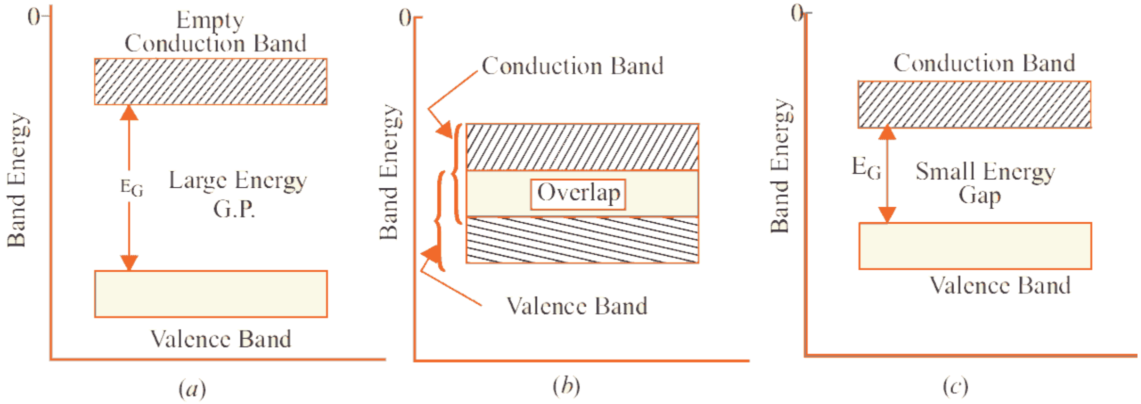

Fig. 2.1. Energy band diagram for an insulator (a), conductor (b), and a semiconductor (c).

a) Insulators

Insulators, in simple terms, refer to materials where valence electrons are tightly bound to their host atoms, requiring a significant electric field to overcome the attraction of the atomic nuclei. Insulators, under normal conditions, lack free charge carriers due to specific characteristics of their energy band structure. The valence band in insulators is fully occupied by electrons, while the conduction band remains empty, indicating a clear distinction between the two. This differentiation is the result of a substantial energy gap, typically measured in electronvolts (eV), that separates the valence and conduction bands. In such materials, electrons in the valence band have minimal probability of crossing the energy gap and transitioning to the conduction band without acquiring sufficient energy. This limited conductivity is depicted in **Fig. 2.2**.

As temperature increases, some electrons in insulators gain enough energy to cross the gap and enter the conduction band, which explains the observed negative temperature coefficient of resistance. It is worth mentioning that a significant portion of currently known scintillators, which are the subject of this doctoral dissertation focusing on scintillation properties, also belong to the group of insulators. Flagship examples of such insulating scintillators include yttrium aluminum garnet (YAG), lutetium aluminum garnet (LuAG), and gadolinium gallium garnet (GAGG) activated with rare earth ions [1]-[4].

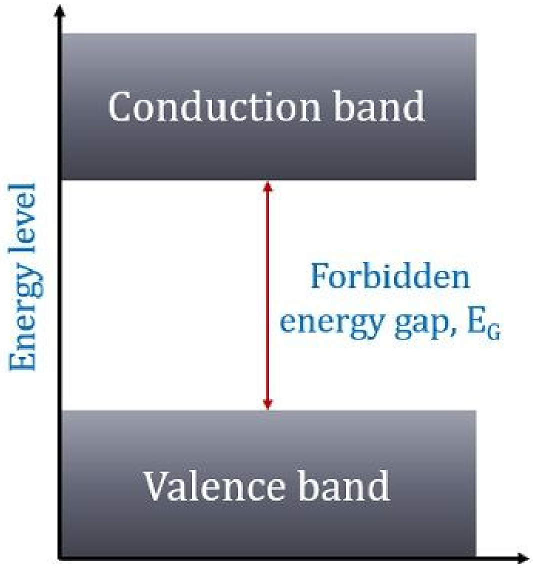

Fig. 2.2.Energy band level diagram of an insulator (Eg is large).

b) Semiconductors

Semiconductor materials exhibit electrical properties that fall between those of insulators and good conductors, with germanium and silicon being common examples. From an energy band perspective, semiconductors can be described as materials with an almost empty conduction band and an almost filled valence band, separated by a narrow energy gap, typically around 1 eV (**Fig. 2.3**). At a temperature of absolute zero (0 K), the conduction band contains no electrons, while the valence band is completely occupied. As temperature increases, the forbidden energy gap in semiconductors decreases, allowing electron transitions from the valence band to the conduction band. This temperature-dependent behavior leads to an increase in conductivity. Simultaneously, the movement of electrons creates positively charged holes in the valence band, resulting in a combined flow of electron and hole currents in opposite directions. This intricate interplay between electrons and holes characterizes the conductivity and behavior of semiconductors.

In this thesis, extensive research has been conducted on semiconductor scintillators, with a particular focus on gallium oxide (β-Ga_2O_3), as well as Ga-based spinels such as $MgGa_2O_4$ and $ZnGa_2O_4$ crystals [5-9]. These materials have emerged as promising candidates due to their relevance and ongoing scientific exploration. Furthermore, zinc oxide (ZnO) has also garnered attention as a noteworthy semiconductor scintillator, with continuous investigation despite its long-standing recognition [10], [11].

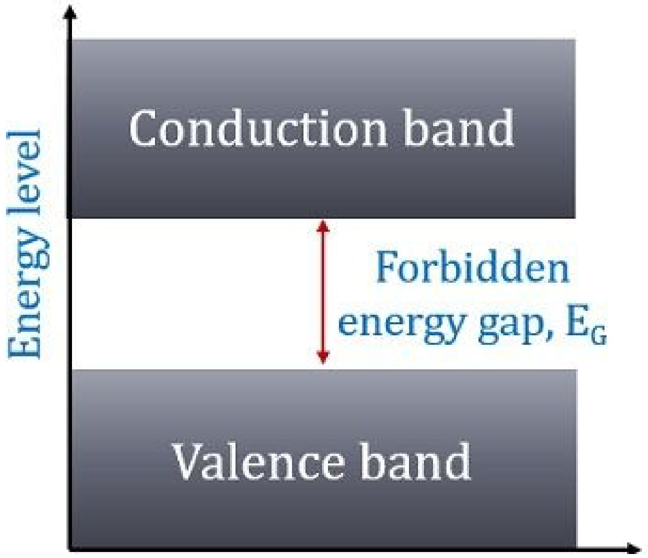

Fig. 2.3.Energy band level diagram of a semiconductor (Eg is small).

c) Conductors

Conducting materials, in simple terms, are characterized by having an abundance of free electrons available for electrical conduction. From an energy band perspective, conducting materials exhibit overlapping valence and conduction bands, as depicted in **Fig. 2.4**. Unlike insulators and semiconductors, there is no distinct separation between these two bands in conductors. This allows for a large number of conduction electrons to be readily available for conduction.

Conducting materials exhibit two additional characteristics in terms of their energy bands. Firstly, they lack a forbidden energy gap, which means there is no distinct energy barrier hindering the movement of electrons. This absence of an energy gap allows for unrestricted electron mobility, as electrons can freely move throughout the material. Additionally, in conducting materials, the total current flow is carried exclusively by electrons since there is no concept of holes, which play a significant role in semiconductors. The abundance of free electrons enables them to participate in conduction, making conducting materials efficient electrical conductors.

However, when it comes to scintillation and the generation of light flashes, it is important to note that this phenomenon occurs only in the presence of forbidden energy gaps. Scintillation relies on the excitation and de-excitation of electrons within these energy gaps. Consequently, it is not possible to have a conductive scintillator since conducting materials lack the necessary energy gaps for the production of scintillation. Scintillators typically require insulating or semiconducting materials where the presence of forbidden energy gaps allows for the formation and subsequent release of light energy upon excitation.

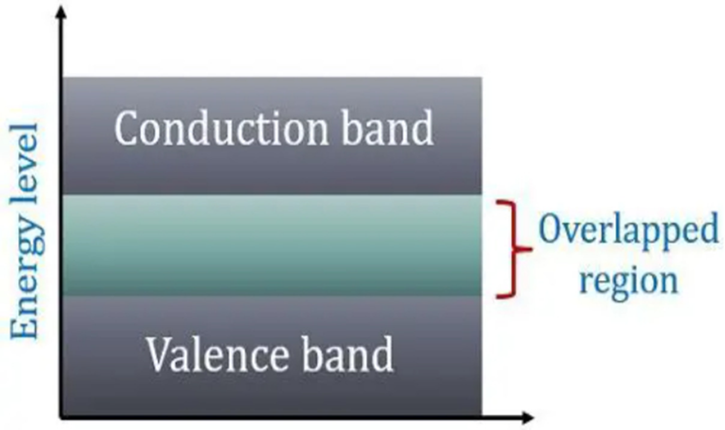

Fig. 2.4. Energy band level diagram of insulator

2.1.3 Types of interaction

Different types of interactions occur between energetically charged particles and matter, as well as between photons and matter. When energetic charged particles, such as electrons, move steadily, they experience electric interactions with the atoms in matter, resulting in the loss of energy. These electric interactions occur due to the charged particle's interactions with the electric fields of the atoms, leading to a transfer of energy. On the other hand, photons, being electrically neutral, undergo energy loss through a distinct mechanism due to their lack of electric charge. Photons can traverse a certain distance before interacting with an atom within a material. The likelihood of interaction per unit length, which relies on the properties of the medium and the energy of the photons, statistically determines the distance a photon can travel before an interaction takes place. Several processes can occur when photons interact with matter. In certain cases, photons may be absorbed by atoms, transferring their energy to the atoms in a process known as photoelectric absorption. Alternatively, photons may undergo scattering, resulting in a change in direction after interacting with atoms. Scattered photons can retain most of their energy or experience a partial loss, depending on the scattering mechanism involved. Thomson scattering and Rayleigh scattering are examples of photon interactions with matter that do not involve energy transfer. In Thomson scattering, photons interact with electrons in atoms, causing them to oscillate without significant energy transfer. Rayleigh scattering occurs when photons interact with atoms or molecules and scatter without a change in wavelength. Energy transfer can occur through various mechanisms when photons interact with matter. One such mechanism is Compton scattering, where photons transfer a portion of their energy to electrons during the scattering process. Another mechanism is pair creation, which occurs when a photon with sufficient energy transforms into an electron-positron pair in the presence of a strong electric field. Additionally, photons can undergo photonuclear reactions, where their energy is absorbed by atomic nuclei, resulting in nuclear excitation or the production of other particles. These interactions and the deposition of energy by photons in matter hold significant implications in various scientific and practical applications, including radiation therapy, imaging techniques, radiation detection, and nuclear physics research. The subsequent sections of this chapter will delve into further details regarding these processes.

i. Thomson scattering

A free electron interacts with an incident electromagnetic wave by oscillating in response to the electric field of the wave. When discussing low-energy phenomena, this kind of scattering is especially important. Without any energy being lost, the oscillating electron produces radiation at the same frequency as the incident wave. When the dispersed radiation collides with the electron, Thomson scattering mostly changes the angle at which the radiation is deflected. When the incident photon's energy becomes close to zero, Thomson scattering can be seen as a limiting case of Compton scattering from a quantum mechanical perspective.

ii. Compton scattering

The process of inelastic scattering of X-ray radiation by free electrons was first observed by Arthur H. Compton in 1922 [12], and the phenomenon was subsequently named after him as the Compton scattering. When a beam of photons interacts with weakly bound or free electrons in an absorbing material, some of the photons undergo partial scattering at an angle θ, resulting in the loss of their energy [13]. Compton scattering refers to the phenomenon where the energy of an X-ray or γ-ray photon decreases when it interacts with matter. This interaction leads to a change in the photon's energy, making it an inelastic scattering process. The significance of Compton scattering lies in its demonstration that light cannot be solely explained as a wave phenomenon. The classical theory of Thomson scattering, which describes an electromagnetic wave scattered by charged particles, fails to account for the observed low-intensity shifts in wavelength. To explain Compton scattering, light must be considered to behave as particles.

Compton's experiment confirmed that light exhibits characteristics of particle-like quanta, where the energy is proportional to the frequency. **Fig. 2.5** illustrates the scheme for Compton scattering. According to the quantum model, a photon with energy hν and momentum hν/c approaches a stationary free electron.

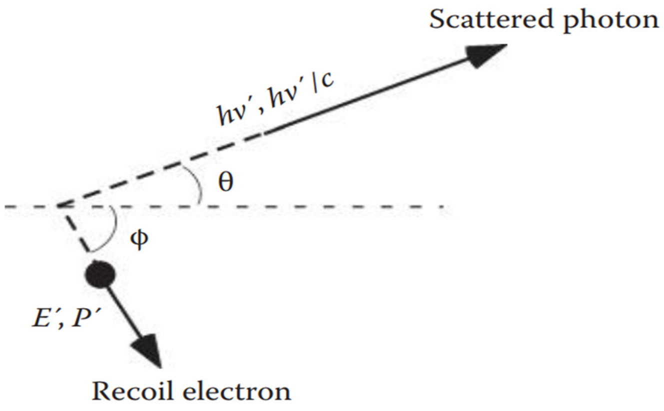

Fig. 2.5. A diagram illustrating the definition of angles after a collision.

After the collision, the photon is scattered at an angle θ with energy hν' and momentum hν'/c. Simultaneously, an electron is ejected at an angle ϕ with a total energy E' and momentum p'. The relativistic expressions for E' and p' are derived considering the rest mass m of the electron and its velocity $\beta = v/c$ is as follows:

$$\mathrm{E}' = \mathrm{mc}^2\sqrt{1-\beta^2} \ \ , \ \ \mathrm{p}' = \mathrm{m}\beta\mathrm{c}\sqrt{1-\beta^2} \tag{2.1}$$

The conservation laws of energy and momentum lead to the following equations:

$$\begin{gathered} \mathrm{h}\nu + \mathrm{mc}^2 = \mathrm{h}\nu' + \mathrm{E}' \\ \frac{\mathrm{h}\nu}{\mathrm{c}} = \frac{\mathrm{h}\nu'}{\mathrm{c}}\cos\theta + \mathrm{p}\cos\phi \\ \frac{\mathrm{h}\nu'}{\mathrm{c}}\sin\theta = \mathrm{p}\sin\phi \end{gathered} \tag{2.2}$$

By utilizing Equations (2.1) and (2.2), the energy of the scattered photon can be derived as follows:

$$\mathrm{h}\nu' = \frac{\mathrm{h}\nu}{1+\frac{\mathrm{h}\nu}{\mathrm{mc}^2}(1-\cos\theta)} \tag{2.3}$$

The kinetic energy of the recoiled electron, denoted as T, can be expressed as follows:

$$\mathrm{T} = \mathrm{h}\nu - \mathrm{h}\nu' = \mathrm{h}\nu\frac{1-\cos\theta}{1-\cos\theta+\frac{\mathrm{mc}^2}{\mathrm{h}\nu}} \tag{2.4}$$

When the scattering angle (θ) is equal to 180°, the electron possesses the maximum energy:

$$\mathrm{T}_{\mathrm{max}} = \frac{2\mathrm{h}\nu}{2+\frac{\mathrm{mc}^2}{\mathrm{h}\nu}} \tag{2.5}$$

In the field of γ-ray spectroscopy, $\mathrm{T}_{\mathrm{max}}$ is commonly referred to as the Compton edge. It is observed that $\mathrm{T}_{\mathrm{max}}$ approaches hν for hν >> mc^2. The relationship between θ and ϕ can be expressed by the following equation:

$$\mathrm{ctg}\frac{\theta}{2} = 1 + \frac{h\nu}{mc^2}\tan\phi \qquad (2.6)$$

As θ increases from 0° to 180°, ϕ decreases from 90° to 0°. This implies that the photon is scattered in all directions, while the recoil angle of the electron is limited to forward angles ($0° \leq \varphi \leq 90°$).

iii. Photoelectric effect

Alexander E. Becquerel's discovery of the photovoltaic effect in 1839 [14] laid the foundation for subsequent advancements in photovoltaics and photoconductivity [15]. Building upon this, in 1887 Heinrich Hertz made a groundbreaking contribution by elucidating the phenomenon of the photoelectric effect [16]. Hertz's work sparked vigorous debates among scientists, and his observation that a negatively charged zinc surface rapidly discharged when exposed to ultraviolet radiation was confirmed by numerous experimenters [17].

The photoelectric effect, a fascinating phenomenon, involves the emission of electrons from matter upon absorbing energy from electromagnetic radiation, such as X-rays or visible light (**Fig. 2.6**). These emitted electrons, known as photoelectrons, exhibit an intriguing behavior. Contrary to intuition, the energy of the emitted electrons is not determined by the intensity of the incident radiation but rather by its wavelength. Specifically, shorter wavelengths correspond to the emission of electrons with higher energy levels.

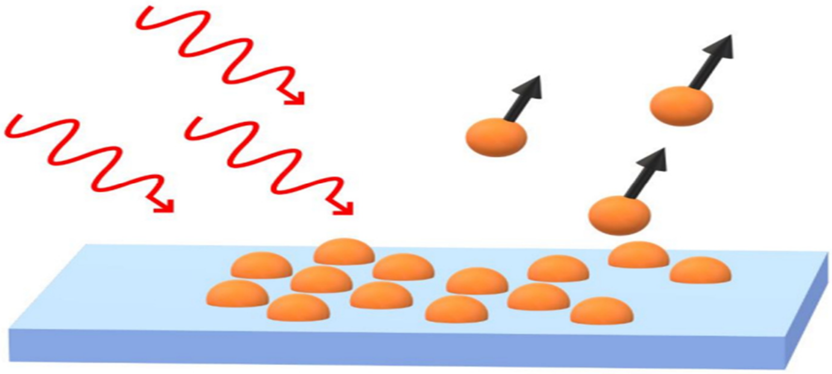

Fig. 2.6. Diagram illustrating electron emission from metal plates under the influence of energy from absorbed photons.

To explain these experimental findings, Einstein proposed that the incident radiation behaves as discrete packets of energy called photons, with each photon having an energy E = hν, where h represents Planck's constant and ν represents the frequency of the radiation. According to his hypothesis, a photoelectron is produced when an electron in the material fully absorbs a photon, causing the incident photon to disappear. The kinetic energy of a photoelectron, denoted as T, can be expressed as:

$$T = h\nu - B \qquad (2.7)$$

where B represents the binding energy of an electron in its orbit. This formula describes the relationship between the energy of the incident photon, the binding energy of the electron, and the resulting kinetic energy of the emitted photoelectron.

iv. Pair creation

In addition to the photoelectric effect and Compton scattering, there is another process by which photons can lose energy when interacting with matter. This process is called pair creation, it occurs when the energy of a photon is at least twice the rest mass of an electron ($h\nu \geq 2\ mc^2$), resulting in the conversion of the photon into an electron-positron pair near a nucleus (**Fig. 2.7**). In the case of pair creation in the field of atomic electrons, it is more likely to occur for photon energies greater than 4 mc^2, although the probability is generally low. This specific form of pair production is referred to as triplet pair creation because it involves the creation of an additional recoiled electron.

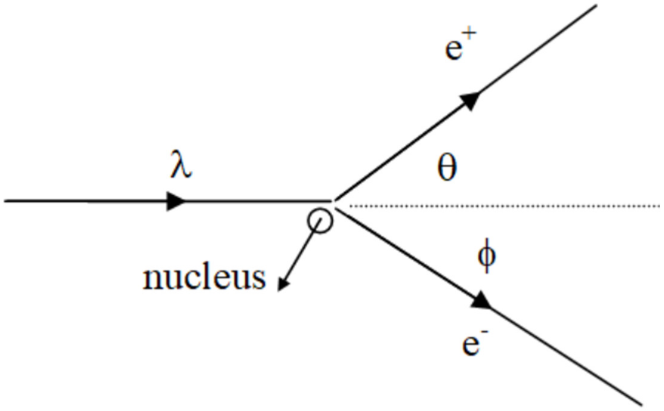

Fig. 2.7. Conversion of energy to mass in pair production.

In the process of photon-nucleus pair production, the recoiled energy of the heavy nucleus is considered negligible. The conversion of photon energy hν is mathematically represented by the equation:

$$h\nu = 2mc^2 + T_+ + T_- \tag{2.8}$$

where T_+ and T_- represent the kinetic energies of the positron and electron, respectively. With both spectra being almost identical, the energy distribution of the electron and positron continually varies between 0 and hν. The threshold energy for pair creation is 1.022 MeV. Conversely, the inverse process can occur where photons are produced through the annihilation of an electron-positron pair. The positron slows down and attracts an electron, forming a positronium, which resembles a hydrogen atom. Positronium exists for approximately 10^{-10} seconds before pair annihilation occurs. The annihilation process generates two photons with an energy of 511 keV each, which are emitted in opposite directions. The probability of in-flight annihilation is typically less than 10%.

v. Absorption

When gamma radiation, similar to other forms of electromagnetic radiation, traverses a material, it experiences exponential decay. Each gamma photon can be eliminated from the radiation beam through complete scattering or absorption. This phenomenon is governed by the widely recognized law of absorption, which establishes a relationship between the intensity I(x) of the beam and the thickness x of the absorber:

$$I(x) = I_0 \exp(-\alpha x) \tag{2.9}$$

Here, I_0 represents the intensity of the incident radiation beam, while α corresponds to the linear absorption coefficient.

Due to the fact that the photoelectric effect, Compton scattering, and pair creation occur independently of each other, it is necessary to determine the total linear attenuation coefficient, which is the sum of the individual components [18]. This coefficient depends on the three aforementioned phenomena, which can be expressed as the sum of coefficients associated with the photoelectric effect α_f, Compton scattering α_C, and pair creation α_p. Consequently, the overall absorption coefficient can be written as:

$$\alpha = \alpha_f + \alpha_C + \alpha_p \tag{2.10}$$

2.2 Scintillation as a three-step process

The phenomenon of scintillation, which involves the interaction of electromagnetic radiation with matter, can be divided into three main sub-processes: energy conversion, energy transfer, and luminescence (see **Fig. 2.8**). Depending on the energy of the incident radiation, the interaction (conversion) occurs through three mechanisms: the photoelectric effect, Compton scattering, and electron-positron pair creation. The photoelectric effect dominates for low energies (below 100 keV), while Compton scattering is the primary mechanism for medium energies (between 100 keV and 1 MeV). For energies above 1.02 MeV, the interaction is governed by electron-positron pair creation [19].

When radiation interacts with a scintillator material, it gives rise to the creation of primary electron-hole pairs, initiating a cascade effect that leads to the generation of secondary pairs. As the electronic excitations lose energy and drop below the ionization threshold, thermalization takes place. This stage, lasting less than a picosecond, results in the settling of all electrons at the bottom of the conduction band while the holes occupy the top of the valence band. Following thermalization, the free electron-hole pairs migrate through the material, transferring their energy to the luminescent centers. Energy transfer occurs rapidly, typically within the range of 10^{-12} to 10^{-8} seconds. Once the energy transfer is complete, the final phase of scintillation, known as luminescence, occurs. The duration of luminescence is dependent on the specific luminescent centers present in the material and can extend beyond 10-10 seconds.

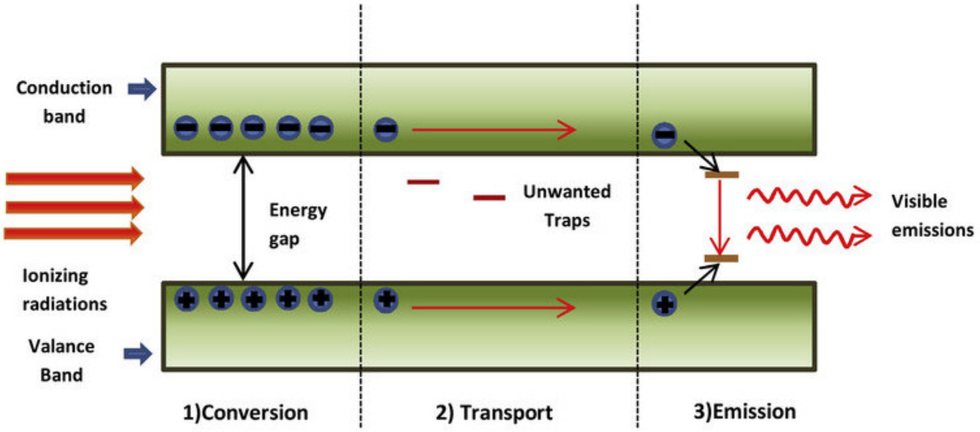

Fig. 2.8. Scintillation mechanism [20].

The energy of the emitted photon plays a crucial role in distinguishing between different radioisotopes. It is directly correlated to the energy of the incident radiation. By analyzing the relationship between the energy of emitted photons and the energy of the incoming radiation, it becomes possible to identify the radioactive source. In scintillator materials, the photoelectric effect is favored as it ensures the complete absorption of the incoming radiation. Conversely, the Compton effect generates lower-energy photons, introducing potential sources of error. To increase the likelihood of the photoelectric effect, materials with a high atomic number (Z) and a high photoelectric fraction are preferred. The photoelectric fraction represents the proportion of incoming photons that interact with the matter through the photoelectric effect. However, further details regarding the process of scintillation will be provided in the subsequent subsections.

2.2.1 Energy Conversion

In this phase the incident radiation is absorbed by the scintillator material, resulting in the formation of numerous electron-hole pairs within the crystalline lattice. This crucial stage of scintillation encompasses the previously discussed phenomena, namely the photoelectric effect, Compton scattering, and pair creation. The efficiency of the conversion process is directly influenced by the number of electron-hole pairs generated, making all other potential processes within the material secondary to scintillation. According to Robbins, considering minimal losses caused by phonons, the minimum energy required to create an electron-hole pair (E_{rad}) can be approximated as a multiple of the bandgap energy (E_g) [21]. The general formula for E_{rad} is expressed as:

$$E_{rad} \approx k\,E_g \tag{2.11}$$

Here, k represents a constant that takes into account the specific characteristics of the scintillator material and the efficiency of the conversion process. The value of k typically falls within the range of 2 to 3, indicating that the minimum energy required for electron-hole pair creation is roughly 2-3 times the bandgap energy.

The efficiency of the conversion process, denoted by the parameter β, can be determined using the formula:

$$\beta = n_{e\text{-}h} / n_0 \tag{2.12}$$

where:

$n_{e\text{-}h}$ is the number of created electron-hole pairs,

n_0 is the number of pairs that would be expected with no energy losses.

As can be easily understood, the values of parameter β are always less than unity. The higher the conversion efficiency, the better the scintillator. Each electron-hole pair possesses a certain kinetic energy, allowing it to move within the crystal and interact with the atoms of the material. If this energy is sufficient to generate another pair, the process occurs immediately and repeats until the remaining kinetic energy is insufficient for the creation of another pair.

2.2.2 Energy transfer

During the second stage of scintillation, thermalized electrons and holes are transported towards luminescence centers [22], as well as they transfer the energy to the atoms participating in the luminescence process. A multitude of electrons and holes, which were generated during the energy conversion process, traverse the scintillator material. This phase is of utmost importance in scintillation, as it is where a significant portion of efficiency loss occurs due to various factors such as trapping and non-radiative recombination. The observed phenomena can be ascribed to imperfections found within the scintillator crystal, which encompass impurities, ionic vacancies, and grain boundaries.

Trapping refers to the phenomenon where electrons or holes become temporarily localized in specific sites or defects within the material, hindering their movement towards the luminescence centers. This can lead to a decrease in the number of charge carriers available for energy transfer and subsequent light emission. Non-radiative recombination involves the loss of energy through processes other than the emission of photons, resulting in a reduction in the overall scintillation efficiency.The charge transport phase also plays a crucial role in the timing of the scintillation process. Delays in the transportation of charge carriers can introduce timing uncertainties and affect the accuracy of the detected signals. It is worth noting that the charge transport phase remains one of the least understood aspects of scintillation and heavily relies on the specific material involved, as well as its intrinsic charge conduction properties.

To mitigate efficiency loss and optimize the charge transport process, extensive research is being conducted to understand the underlying mechanisms and improve the quality of scintillator materials. This includes minimizing defects within the crystal lattice, developing materials with enhanced charge carrier mobility, and optimizing the structural and chemical composition of the scintillator.

2.2.3 Luminescence

Once the electrons and holes reach the luminescence centers, the third and final stage of scintillation takes place: luminescence. This stage is characterized by the radiative recombination of electrons and holes within the luminescent centers, resulting in the emission of photons. The luminescent centers can be intrinsic to the scintillator material or introduced through impurities or dopants. During the luminescence phase, the captured electrons and holes are guided along potential paths within the material by the luminescent centers. These centers act as localized energy states where the recombination of electron-hole pairs can occur. When an electron and a hole recombine, the excess energy is released in the form of a photon with a characteristic energy corresponding to the scintillator material's energy bandgap. The specific details of the luminescence phase depend on the type of material used for scintillation. Different materials have unique energy levels and luminescent properties, leading to variations in the emitted photon energies, intensity, and decay characteristics. For example, some scintillator materials exhibit prompt luminescence, where the emission of photons occurs almost immediately after electron-hole recombination. In contrast, others may exhibit delayed or long-lived luminescence, where photons are emitted over an extended period of time after the initial recombination event.

To enhance the understanding, let us consider an example: the luminescent characteristics of rare-earth (RE) ions are crucial in scintillator luminescence. The energy levels of these RE ions vary depending on their charge state, wherein higher charge states correspond to lower energy level positions. For instance, RE^{2+} ions might possess energy levels situated within the conduction band, whereas RE^{3+} ions may have energy levels within the valence band. In scintillator materials, a wide bandgap is preferred to accommodate the energy levels associated with RE ions. Luminescence in RE ions involves two types of transitions: intraconfigurational and interconfigurational transitions. In intraconfigurational transitions, electrons within the 4f orbitals undergo transitions between different 4f electron configurations, known as f-f transitions. These transitions are characterized by sharp lines in the spectra due to the weak interaction between 4f electrons and the crystal field. However, Laporte's rule prevents electric-dipole transitions between levels of the same parity. Despite this, f-f lines can still be present in the spectra of RE-activated crystals due to induced electric-dipole transitions, magnetic-dipole transitions, and electric-quadrupole transitions.

The luminescence of RE ions is associated with energetic levels within the 4f orbitals. For trivalent RE cations, the energetic levels range between 0 and 40000 cm^{-1}. A similar energy level scheme can be applied to divalent RE cations, with a "one element shift" in the ground state electron configurations compared to trivalent ions, except for ^{64}Gd and ^{71}Lu. The energy levels can be extended up to 70000 cm^{-1} for RE ions, particularly in d-f transitions. These transitions involve the interaction between 5d electrons and the crystal field, resulting in broad bands in the luminescence spectra. Electric-dipole transitions are allowed in d-f transitions due to the opposite parity of the initial and final state wave functions, according to selection rules: $|\Delta L| \leq 6$, $\Delta S = 0$, $|\Delta J| \leq 6$. The radiative lifetime of electric-dipole transitions is denoted as τ.

Understanding the energy levels and transitions of RE ions is crucial for optimizing the luminescence efficiency of scintillator materials. Researchers focus on enhancing the light output, decay times, and overall performance by manipulating factors such as the concentration and distribution of luminescent centers, crystal structure, and the presence of impurities or defects. By refining these factors, scintillators can exhibit improved sensitivity, signal-to-noise ratio, and timing characteristics, enabling their application in radiation detection, medical imaging, and scientific research.

As shown in **Fig. 2.9**, the so-called Dieke's diagram provides valuable insights into the luminescence behavior of RE ions. It visually represents the energy levels and transitions involved in rare-earth luminescence, helping researchers understand the electronic configurations and transition pathways of RE ions within the scintillator material. The Dieke's diagram is a useful tool for predicting and manipulating the luminescent properties of rare-earth activated scintillators, aiding in the design and optimization of scintillator materials for various applications.

2.3 Various mechanisms of energy transfer

Within the context of scintillators, there are several intricate mechanisms involved in the transfer of energy. These mechanisms are fundamental to the process of energy conversion and detection. Let us delve into the more detailed ways in which energy is transferred within scintillator materials:

2.3.1 Excitonic transfer

Exciton transfer is an important energy transfer mechanism observed in scintillators, particularly in materials where excitons are formed. Namely, when high-energy radiation interacts with the material, it can create excitons, which are bound electron-hole pairs. Excitons are formed when the incident radiation exceeds the material's bandgap energy, promoting an electron from the valence band to the conduction band. These excitons possess the ability to migrate through the crystal lattice of the scintillator material. Exciton migration is facilitated by the lattice structure of the material. As excitons migrate, they can encounter luminescent centers within the material, which can be impurities, defects, or specific doping elements. When an exciton reaches a luminescent center, the electron and hole can recombine, resulting in the emission of photons. The migration of excitons allows for the redistribution of energy within the scintillator material. Excitons can travel over significant distances, transferring energy and interacting with various luminescent centers. This process enhances the probability of recombination and the subsequent emission of photons.

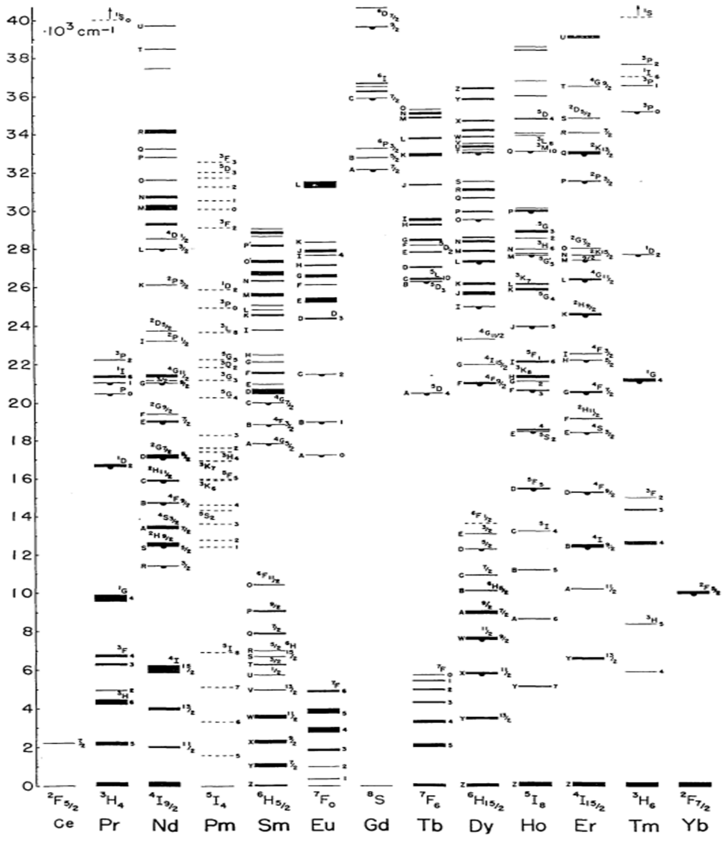

Fig. 2.9. Energy levels of the trivalent rare-earth ions (the Dieke's diagram) [23].

An example of exciton transfer can be observed in rare-earth activated scintillators, particularly in cerium-doped materials, e.g. $LaBr_3$:Ce [24]. In these scintillator materials, incident radiation generates excitons, which subsequently migrate through the crystal lattice. When an exciton encounters a luminescent center, the recombination of the electron and hole within the exciton occurs, resulting in the emission of photons. Understanding and optimizing exciton transfer is crucial for enhancing the performance and efficiency of scintillator materials. By controlling the migration of excitons and designing suitable luminescent centers, scientists and engineers can improve the energy conversion and light emission processes in scintillators, with applications ranging from radiation detection to medical imaging and particle physics research.

2.3.2 Consecutive capture of charge carriers

In scintillators, energy transfer can also occur through the consecutive capture of charge carriers. When incident radiation interacts with the scintillator material, it can create mobile charge carriers such as electrons or holes. These charge carriers can be captured by localized defects, impurities, or other trapping centers present within the material. The consecutive capture process involves the sequential trapping of charge carriers, leading to the redistribution of energy within the scintillator. This process can enhance the efficiency of energy conversion and subsequent light emission.

In rare-earth (RE) activated scintillators, such as $LuAlO_3$:Ce (LuAP:Ce), $Lu_3Al_5O_{12}$:Pr (LuAG:Pr), and BaF_2:Ce, energy transfer through consecutive capture of carriers has been observed [25], [26]. This process involves the interaction of the incident radiation with the RE ions and the subsequent capture of charge carriers, followed by the emission of photons.

In sequence no. 1, the process begins with the capture of a valence band hole (h_V) by the RE ion, resulting in the promotion of the RE ion from a charge state (RE^{m+}) to a charge state ($RE^{(m+1)+}$). Subsequently, a conduction band electron (e_C) is captured by the $RE^{(m+1)+}$ ion, forming an excited state denoted as $(RE^{m+})^*$. Finally, the excited state $(RE^{m+})^*$ undergoes a radiative transition, releasing a scintillation photon (hν), and returning the RE ion to its original state (RE^{m+}).

In sequence no. 2, the process involves first the capture of a conduction band electron (e_C) by the RE^{m+} ion, leading to the formation of a charge state ($RE^{(m-1)+}$). The $RE^{(m-1)+}$ ion then absorbs a valence band hole (h_V), creating an excited state denoted as $(RE^{m+})^*$. Similarly to sequence no. 1, the excited state $(RE^{m+})^*$ emits a photon (hν) and reverts to the RE^{m+} ion.

As an example, let us consider the Ce^{3+} ion. In sequence no. 1, the Ce^{3+} ion captures a valence band hole, becoming Ce^{4+}. Then, an electron is captured, forming the excited state $(Ce^{3+})^*$. The excited state subsequently emits a photon and returns to the Ce^{3+} ion ground state. In sequence no. 2, an electron is captured by the Ce^{3+} ion, producing Ce^{2+}. The Ce^{2+} ion captures a hole, forming the excited state $(Ce^{3+})^*$, which emits a photon and reverts to the Ce^{3+} ion ground state.

It is worth noting that in some cases, charge trapping and transfer can occur, resulting in a delayed energy transfer process. These consecutive capture mechanisms, involving the absorption and emission of photons and the capture of charge carriers, contribute to the overall energy conversion and light emission in RE activated scintillators. By understanding and optimizing these mechanisms, scientists and engineers can enhance the performance and efficiency of scintillator materials in radiation detection, medical imaging, and other applications.

2.3.3 Radiative Transfer

Radiative transfer is a fundamental mechanism in scintillators that involves the emission and absorption of photons to transfer energy. When excitons or other charge carriers are formed within the scintillator material, they can undergo radiative transitions between different energy states. These transitions involve the emission or absorption of photons, which serve as carriers of the transferred energy. The emitted photons can be detected and harnessed for various applications, including radiation detection and imaging.

In the context of rare-earth activated scintillators, such as those containing rare-earth ions like cerium (Ce), europium (Eu), or terbium (Tb), the radiative transfer process occurs through specific sequences of events:

Photon absorption: When incident radiation interacts with the scintillator material, it can be absorbed by the rare-earth ion, promoting it to an excited state. For example, in the case of Ce^{3+} ions, absorption of a photon can lead to the excitation of the Ce^{3+} ion to a higher energy level.

Energy transfer: The excited rare-earth ion can transfer the energy to the surrounding lattice or other charge carriers through non-radiative processes such as phonon interactions. This energy transfer mechanism allows the energy to be redistributed within the scintillator material.

Radiative emission: After the energy is transferred, the rare-earth ion in the excited state can undergo radiative decay. This process involves the emission of photons with specific wavelengths characteristic of the rare-earth ion. The emitted photons carry the transferred energy and can be detected by appropriate detectors, enabling the measurement and analysis of the incident radiation.

An example of radiative transfer can be observed in cerium-doped scintillators. When incident radiation interacts with the scintillator material containing Ce^{3+} ions, the absorption of photons by Ce^{3+} ions leads to their excitation. Subsequent energy transfer processes and radiative decay result in the emission of photons, which can be detected for radiation detection and imaging purposes. Optimizing radiative transfer in scintillators involves controlling the absorption and emission properties of the rare-earth ions, as well as the efficiency of energy transfer processes. By carefully selecting and engineering the scintillator material and rare-earth dopants, scientists and engineers can enhance the radiative transfer process, leading to improved sensitivity, efficiency, and performance of scintillator-based systems in various applications.

References (chapter 2)

[1] W. Drozdowski, K. Brylew, A.J. Wojtowicz, J. Kisielewski, M. Swirkowicz, T. Lukasiewicz, J.T.M. de Haas, P. Dorenbos, "33000 photons per MeV from mixed $(Lu_{0.75}Y_{0.25})_3Al_5O_{12}$:Pr scintillator crystals," Opt. Mater. Express, vol. 4, no. 6, p. 1207, 2014

[2] W. Drozdowski, M.E. Witkowski, K. Brylew, W. Lachmanski, M. Makowski, A.J. Wojtowicz, S. Turczynski, D.A. Pawlak, M. Malinowski, "A preliminary assessment of $Lu_2Y_2Al_2O_9$:Pr (LuYAM:Pr) as a potential scintillator," Radiat. Meas., vol. 93, p. 41, 2016

[3] W. Drozdowski et al., "A deeper insight into (Lu,Y)AG:Pr scintillator crystals," IOP Conference Series: Materials Science and Engineering, vol. 169, no. 1, p. 012010, 2017

[4] W. Drozdowski, M. E. Witkowski, P. Solarz, P. Głuchowski, M. Głowacki, and K. Brylew, "Scintillation properties of $Gd_3Al_2Ga_3O_{12}$:Ce (GAGG:Ce): a comparison between monocrystalline and nanoceramic samples," Opt. Mater., vol. 79, p. 227, 2018.

[5] T. Yanagida, G. Okada, T. Kato, D. Nakauchi, and S. Yanagida, "Fast and high light yield scintillation in the Ga_2O_3 semiconductor material," Appl. Phys. Express, vol. 9, no. 4, p. 042601, 2016

[6] M. Makowski, W. Drozdowski, M. E. Witkowski, A. J. Wojtowicz, K. Irmscher, R. Schewski, and Z. Galazka, "Tailoring the scintillation properties of β-Ga_2O_3 by doping with Ce and codoping with Si," Opt. Mater. Express, vol. 9, no. 9, p. 3738, 2019

[7] Z. Galazka, D. Klimm, K. Irmscher, R. Uecker, M. Pietsch, R. Bertram, M. Naumann, M. Albrecht, A. Kwasniewski, R. Schewski, and M. Bickermann, "$MgGa_2O_4$ as a new wide bandgap transparent semiconducting oxide: growth and properties of bulk single crystals," Phys. Status Solidi A, vol. 212, no. 7, p. 1455, 2015

[8] Z. Galazka, S. Ganschow, R. Schewski, K. Irmscher, D. Klimm, A. Kwasniewski, M. Pietsch, A. Fiedler, I. Schulze-Jonack, M. Albrecht, T. Schröder, and M. Bickermann, "Ultra-wide bandgap, conductive, high mobility, and high quality melt-grown bulk $ZnGa_2O_4$ single crystals," APL Mater., vol. 7, no. 2, p. 022512, 2019

[9] Z. Galazka, S. Ganschow, K. Irmscher, D. Klimm, M. Albrecht, R. Schewski, M. Pietsch, T. Schulz, A. Dittmar, A. Kwasniewski, R. Grueneberg, S. B. Anooz, A. Popp, U. Juda, I. M. Hanke, T. Schroeder, and M. Bickermann, "Bulk single crystals of β-Ga_2O_3 and Ga-based spinels as ultra-wide bandgap transparent semiconducting oxides," Prog. Cryst. Growth Charact. Mater., vol. 67, no. 1, p. 100511, 2021

[10] D. Luckey, "A fast inorganic scintillator," Nucl. Instruments Methods, vol. 62, no. 1, p. 119, 1968

[11] J. Ji et al., "ZnO Luminescence and scintillation studied via photoexcitation, X-ray excitation, and gamma-induced positron spectroscopy," Sci. Rep., vol. 6, pp. 1, 2016

[12] A. H. Compton, "A Quantum Theory of the Scattering of X-rays by Light Elements," Phys. Rev., vol. 21, no. 5, p. 483, 1923

[13] Y. Y. Peter and M. Cardona, "Fundamentals of Semiconductors Physics and Materials Properties", 4th ed. Springer, 2010

[14] V. Petrova-Koch, R. Hezel, and A. Goetzberger, "High-Efficient Low-Cost Photovoltaics," Springer, 2009

[15] W. Smith, “Effect of light on selenium during the passage of an electric current,” Nature, vol. 7, no. 173, p. 303, 1873

[16] H. Hertz, “Ueber einen Einfluss des ultravioletten Lichtes auf die electrische Entladung,” Ann. Phys., vol. 267, no. 8, p. 983, 1887

[17] H. A. Zinszer, “Note on photo-electric phenomena,” Proc. Ind. Acad. Sci., vol. 40, p. 291, 1931

[18] N. Tsoulfanidis, Measurement and Detection Radiation, 2nd ed. Taylor & Francis, 1995

[19] G. F. Knoll, Radiation Detection and Measurement, 3rd ed. John Wiley & Sons, Inc., 2000

[20] M. Nikl, “Scintillation detectors for X-rays,” Meas. Sci. Technol., vol. 17, p. R37, 2006

[21] D. J. Robbins, “On Predicting the Maximum Efficiency of Phosphor Systems Excited by Ionizing Radiation,” J. Electrochem. Soc., vol. 127, no. 12, p. 2694, 1980

[22] K. Lark-Horovitz and V. A. Johnson, “Solid State Physics: Electrical, Magnetic, and Optical Properties”, vol. 6. 1959

[23] G. H. Dieke and H. M. Crosswhite, “The Spectra of the Doubly and Triply Ionized Rare Earths,” Appl. Opt., vol. 2, p. 675, 1963

[24] G. Bizarri, P. Dorenbos, “Charge carrier and exciton dynamics in $LaBr_3:Ce^{3+}$ scintillators: Experiment and model,” Phys. Rev. B, vol. 75, p. 184302, 2007

[25] A.J. Wojtowicz, P. Szupryczynski, D. Wisniewski, J. Glodo, W. Drozdowski, “Electron Traps and Scintillation Mechanism in $LuAlO_3$:Ce,” J. Phys.: Condens. Mat., vol. 13, p. 9599, 2001

[26] A.J. Wojtowicz, P. Szupryczynski, J. Glodo, W. Drozdowski, D. Wisniewski, “Radioluminescence and Recombination Processes in BaF_2:Ce,” J. Phys.: Condens. Mat., vol. 12, p. 4097, 2000

Chapter 3

3 Present-day scintillator market

3.1 Different types of scintillators

As extensively elaborated upon in Chapter 2, scintillators release visible photons upon interaction with charged particles or photons. These scintillating materials often encompass transparent crystals, phosphors, plastics, or organic liquids, all of which demonstrate fluorescence when exposed to ionizing radiation. In order to qualify as effective scintillators, these materials need to fulfill specific criteria, including the maintenance of transparency to emitted light and the manifestation of a short decay time. To ensure precise detection, it is paramount to shield scintillators from ambient light, thereby preventing external photons from interfering with the ionization events triggered by incoming radiation. Typically, this protective measure involves the utilization of a thin, light-blocking material like aluminized mylar. It is imperative for this foil to possess minimal mass to prevent any substantial reduction in the intensity of the incoming radiation being measured. Scintillators can be categorized into various types, encompassing both organic and inorganic varieties, among others.

3.1.1 Organic scintillators

Organic scintillators cover a wide array of materials valued for their effectiveness in transforming radiation energy into visible light signals. These scintillating materials can be broadly categorized into three main groups: organic crystals, organic liquids, plastic scintillators, among others, each possessing distinct characteristics and versatile applications.

3.1.1.1 Organic crystals

Within the domain of organic scintillators, we encounter substances composed of aromatic hydrocarbon compounds featuring interconnected benzene ring structures. These organic scintillators typically manifest luminescence that undergoes decay within a few nanoseconds [1]. Certain organic scintillators exist naturally in a pure crystalline state, with notable examples including anthracene ($C_{14}H_{10}$, decay time of about 30 ns) [2], stilbene ($C_{14}H_{12}$, decay time of 4.5 ns) [2], and naphthalene ($C_{10}H_8$, decay time ranging within a few nanoseconds). Additionally, this category includes 9-Phenylcarbazole (PCz, $C_{18}H_{13}N$) and 9,10-Diphenylanthracene (DPA, $C_{26}H_{18}$). While these crystals exhibit remarkable durability, they present challenges, such as anisotropic responses that impact energy resolution in situations where the radiation source is not collimated. Furthermore, their limited ease of machining or growth into larger sizes makes them less commonly utilized. Anthracene, known for its high light output among organic scintillators, often serves as a benchmark, and the light outputs of other scintillators are occasionally expressed as a percentage of anthracene's luminescence [3].

Two noteworthy examples of organic crystals in this category include 9-Phenylcarbazole (PCz) and 9,10-Diphenylanthracene (DPA).

- **9-Phenylcarbazole (PCz, Fig. 3.1)**

Fig. 3.1. 9-Phenylcarbazole (PCz) organic scintillation crystal.

- Chemical Formula: $C_{18}H_{13}N$,

- Density: 1.24 g/cm^3,

- Emission wavelength: typically around 450 nm with a light yield of 20,000 ph/MeV,

- Operating temperature: should not exceed 50 °C,

- Care: while the crystals are relatively rugged, they should still be handled with care.

- **9,10-Diphenylanthracene (DPA, Fig. 3.2)**

- Chemical Formula: $C_{26}H_{18}$,

- Density: 1.22 g/cm^3,

- Emission wavelength: 468 nm with a light yield of 14,000 ph/MeV,

- Operating temperature: should not exceed 120 °C,

- Care: Crystals are very brittle and need to be handled with care.

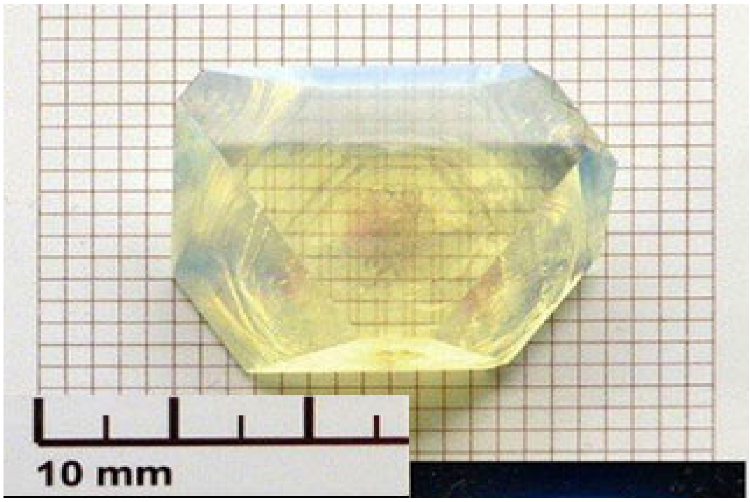

Fig. 3.2. 9,10-Diphenylanthracene (DPA) organic scintillation crystal.

3.1.1.2 Organic liquids

Organic liquids refer to liquid solutions that contain one or more organic scintillators dissolved within an organic solvent. These solutions typically integrate fluorescent substances like p-terphenyl ($C_{18}H_{14}$), PBD ($C_{20}H_{14}N_2O$), butyl PBD ($C_{24}H_{22}N_2O$), PPO ($C_{15}H_{11}NO$), and employ wavelength shifters such as POPOP ($C_{24}H_{16}N_2O$). Frequently utilized solvents in these solutions encompass toluene, xylene, benzene, phenylcyclohexane, triethylbenzene, and decalin. Liquid scintillators offer the flexibility to be easily modified by incorporating additional substances, such as wavelength shifters, to match the spectral sensitivity range of specific photomultiplier tubes (PMTs), or by introducing ^{10}B to enhance the neutron detection efficiency of the scintillation counter itself due to ^{10}B's high interaction cross section with thermal neutrons. In some instances, combinations of multiple solvents or the inclusion of various metals are employed for the purpose of particle identification [4,5]. It is of utmost importance to seal these solutions within an oxygen-free, hermetically sealed enclosure [6], because dissolved oxygen can act as a quenching agent, resulting in a reduction of light output.

3.1.1.3 Plastic scintillators

When we discuss “plastic scintillators,” we are typically referring to scintillating materials in which the primary fluorescent emitter, referred to as a fluor, is embedded within a solid polymer matrix (**Fig. 3.3**). This combination is typically achieved by dissolving the fluor before the bulk polymerization process. However, in some instances, the fluor may be directly bonded to the polymer, either through covalent bonds or coordination, as seen in the case of ^{6}Li plastic scintillators. Interestingly, polyethylene naphthalate has been identified as having inherent scintillation properties without requiring additives. This discovery, coupled with its improved performance and cost-effectiveness [7], suggests that it may replace existing plastic scintillators in the future.

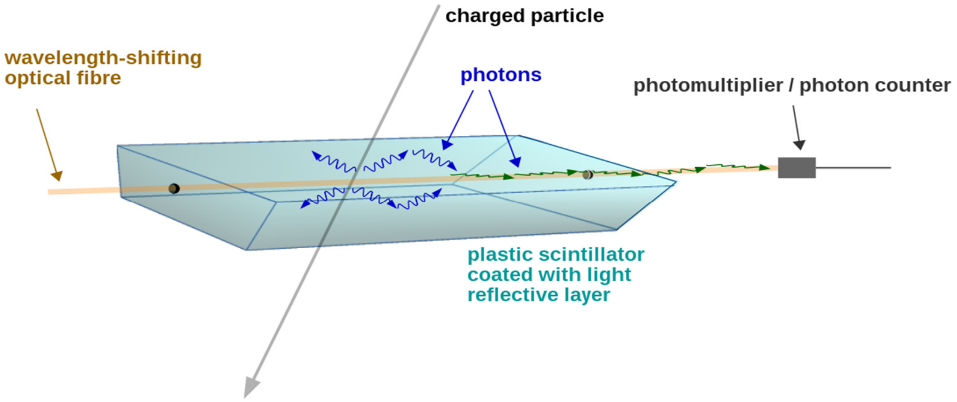

Fig. 3.3. Schematic depicting the operational mechanism of plastic scintillators.

Plastic scintillators present numerous benefits, such as a relatively high light output and a quick signal response, characterized by a decay time ranging from 2 to 4 nanoseconds. However, one of their notable strengths lies in their adaptability to be shaped into almost any desired form, often with a remarkable degree of robustness [8].

It is important to mention that plastic scintillators can experience light output saturation when exposed to high-energy densities, a phenomenon explained by the Birks' Law.

3.1.1.4 Base materials

The primary base materials employed in plastic scintillators are aromatic plastics, which are polymers featuring aromatic rings as pendant groups attached to the polymer's main chain. Among these, polyvinyltoluene (PVT) and polystyrene (PS) stand out as the most prevalent choices. While the base material does emit fluorescence upon exposure to ionizing radiation, its low yield and lack of transparency to its own emitted light necessitate the incorporation of fluorescent compounds in practical scintillator construction [8]. In addition to aromatic plastics, another commonly used base material is polymethylmethacrylate (PMMA). PMMA offers several advantages, including high transparency to ultraviolet and visible light, robust mechanical properties, and increased durability when compared to brittle materials. To compensate for PMMA's inherent lack of intrinsic fluorescence, an aromatic co-solvent, typically naphthalene, is often added. This modification enables a PMMA-based plastic scintillator to maintain transparency to its own radiation, ensuring consistent light collection [9]. Furthermore, there are several other frequently employed base materials, including polyvinyl xylene (PVX), polymethyl, 2,4-dimethyl, 2,4,5 trimethyl styrenes, polyvinyl diphenyl, polyvinyl naphthalene, polyvinyl tetrahydronaphthalene, and various copolymers.

3.1.1.5 Fluor compounds

Fluorescent compounds, alternatively referred to as luminophors, are substances that trap the scintillation produced by the base material and then re-emit it at extended wavelengths. This process effectively converts the base's ultraviolet radiation into visible light, making it easily detectable. To further enhance the attenuation length, a second fluor is often introduced, commonly referred to as a spectrum shifter or converter. This additional fluor typically results in the emission of blue or green light. Frequently used fluor compounds include polyphenyl hydrocarbons, as well as oxazole and oxadiazole aryls, such as n-terphenyl (PPP), 2,5-diphenyloxazole (PPO), 1,4-di-(5-phenyl-2-oxazolyl)-benzene (POPOP), 2-phenyl-5-(4-biphenylyl)-1,3,4-oxadiazole (PBD), and 2-(4’-tert-butylphenyl)-5-(4’’-biphenylyl)-1,3,4-oxadiazole (B-PBD) [10].

3.1.2 Inorganic scintillators

Inorganic scintillators encompass a wide array of materials known for their effectiveness in converting radiation energy into visible light signals. These materials can be categorized into specific groups, each distinguished by its unique properties and applications, setting them apart from their organic counterparts. The primary differentiation between organic and inorganic scintillators lies in their composition and performance characteristics. As previously discussed, organic scintillators consist of carbon-based compounds, often with aromatic rings, resulting in shorter decay times and lower light emission. They provide cost-effective solutions suitable for applications like medical imaging. In contrast, inorganic scintillators comprise non-carbon-based crystalline materials, offering longer decay times, higher light output, and increased durability. These attributes make them the preferred choice in fields such as high-energy physics and gamma-ray spectroscopy, primarily due to their outstanding energy resolution capabilities. This emphasis on their unique attributes is the focal point of my thesis.

3.1.2.1 Inorganic Crystals

In the realm of scintillators, inorganic crystals form a distinctive category characterized by their composition, involving crystals that undergo growth processes at elevated temperatures. These crystals primarily comprise alkali metal halides, often with a minor addition of activator impurities. A notable example within this category is NaI(Tl), which results from the incorporation of thallium into sodium iodide, leading to the emission of scintillating blue light. Expanding the spectrum of inorganic alkali halide crystals, one encounters CsI(Tl), CsI(Na), CsI (pure), CsF, KI(Tl), and LiI(Eu). Additionally, non-alkali crystals such as BGO, BaF_2, CaF_2(Eu), ZnS(Ag), $CaWO_4$, $CdWO_4$, YAG(Ce) ($Y_3Al_5O_{12}$(Ce)), GSO, and LSO significantly contribute to this field [11]. The landscape of inorganic scintillators continues to evolve, introducing innovative developments such as $LaCl_3$(Ce), which features lanthanum chloride doped with cerium, and cerium-doped lanthanum bromide, $LaBr_3$(Ce). While these materials exhibit a notable sensitivity to moisture (hygroscopicity), they are distinguished by exceptional attributes. For instance, $LaBr_3$(Ce) emits 63,000 photons/MeV of gamma energy, surpassing NaI(Tl)'s 38,000 photons/MeV output. Furthermore, it demonstrates rapid responsivity (16 ns for $LaBr_3$(Ce) compared to 230 ns for NaI(Tl) [2]), impeccable linearity, and consistent light emission across a wide temperature range. Moreover, $LaBr_3$(Ce) offers superior gamma ray attenuation capabilities, with a density of 5.08 g/cm^3, in contrast to NaI(Tl)'s 3.67 g/cm^3 [2]. LYSO ($Lu_{1.8}Y_{0.2}SiO_5$(Ce)), with a density similar to BGO (7.1 g/cm^3), retains non-hygroscopic properties and delivers enhanced light output relative to BGO (32,000 photons/MeV vs.

8,000 ph/MeV). Remarkably, it maintains a relatively rapid decay time of 41 ns, contrasting with BGO's 300 ns.

However, it is imperative to acknowledge that certain inorganic crystals, like NaI, possess hygroscopic traits and necessitate hermetic encasement to shield them from moisture. Conversely, CsI(Tl) and BaF_2, though slightly hygroscopic, typically operate without the requirement for such safeguarding measures. Among the hygroscopic category are CsF, NaI(Tl), $LaCl_3$(Ce), and $LaBr_3$(Ce), whereas BGO, CaF_2(Eu), LYSO, and YAG(Ce) remain immune to moisture intrusion. Inorganic crystals, owing to their capacity to be sectioned into diminutive dimensions and organized in arrays, furnish position sensitivity, a valuable feature extensively applied in fields like medical physics and security for the detection of X-rays and gamma rays. Scintillation in inorganic crystals exhibits distinct decay times, with exceptions like CsF (~5 ns), rapid BaF_2 (0.7 ns), and the aforementioned avant-garde materials.

We have worked on inorganic scintillators in this thesis, with a particular focus on gallium oxide (β-Ga_2O_3), known for its remarkable light output of up to 10,000 photons/MeV, and Ga-based spinel crystals such as $MgGa_2O_4$ and $ZnGa_2O_4$. These spinels currently exhibit scintillation yields of approximately 2,500 photons/MeV [12-16]. These materials have attracted significant attention due to their importance and ongoing scientific investigation. Furthermore, our investigation extends to ZnSe and (Zn,Be)Se (**Fig. 3.4**), and in the ensuing chapter, we will delve deep into their findings and properties.

Fig. 3.4. An inorganic crystal of (Zn,Be)Se grown using the vertical Bridgeman method.

3.1.2.2 Gaseous Scintillators

Gaseous scintillators consist of nitrogen and noble gases such as helium, argon, krypton, and xenon, with helium and xenon being the most frequently investigated. In these scintillators, the scintillation process occurs when individual atoms become excited and then rapidly de-excite (typically within ~1 ns) upon interaction with incoming particles. This rapid de-excitation contributes to a swift detector response. To enhance detection efficiency, it is often necessary to apply a wavelength shifter coating to the container walls. This is because these gases primarily emit ultraviolet light, while photomultiplier tubes (PMTs) are more sensitive to the visible blue-green spectrum. Gaseous detectors have found widespread application in nuclear physics for the detection of fission fragments and heavy charged particles [17].

3.1.2.3 Glasses

Glass scintillators most commonly employ cerium-activated lithium or boron silicates as their key components. These scintillators excel in detecting thermal (slow) neutrons, primarily owing to the substantial neutron cross-sections of lithium and boron. Among these, lithium is the favored choice due to its greater energy release upon neutron capture, resulting in higher light output. Glass scintillators also exhibit sensitivity to electrons and gamma rays, and discerning between particles can be accomplished through pulse height discrimination. They boast exceptional durability, capable of withstanding harsh environmental conditions. However, they have a response time of approximately 10 ns, and their light output is relatively modest, typically reaching around 30% of that produced by anthracene [3].

3.1.2.4 Solution-based perovskite scintillators

The scintillation characteristics of organic-inorganic methylammonium (MA) lead halide perovskites were initially documented by Shibuya et al. in 2002 [18], while the first gamma-ray pulse height spectrum was reported by van Eijk et al. in 2008 [19], specifically using $(C_6H_5(CH_2)_2NH_3)_2PbBr_4$. These materials, exemplified by compounds like $MAPbBr_3$ and $MAPbI_3$, emit light at distinct wavelengths associated with exciton emission near the band gap of the materials. However, this emission is significantly diminished at room temperature, with fewer than 1000 photons/MeV surviving. At lower temperatures, such as 10 K [30], intense emission is observed, with reported yields reaching up to 200,000 photons/MeV. This reduced emission at higher temperatures is attributed to the relatively small binding energy of the exciton, which decreases as the halide changes from chlorine to bromine to iodine.

Remarkably, by substituting the organic MA group with Cs^+, it becomes possible to produce entirely inorganic $CsPbX_3$ halide perovskites. The emission wavelength can be adjusted by varying the Cl, Br, or I content, and a similar tuning effect can be achieved through dilution with Rb. Recent advancements have revealed that both organic-inorganic and all-inorganic Pb-halide perovskites exhibit diverse scintillation properties. Two-dimensional perovskite single crystals, in particular, exhibit promising features, including a significantly larger Stokes shift of up to 200 nm compared to $CsPbBr_3$ quantum dot scintillators. This larger Stokes shift is crucial to prevent self-reabsorption.

3.1.2.5 Solution-based perovskite scintillators (OMHH)

A new material class known as 0D organic metal halide hybrids (OMHH), an extension of perovskite materials [21], has also gained attention. These materials exhibit strong exciton binding and high photoluminescent quantum efficiency due to their unique properties. They feature a large Stokes shift and are reabsorption-free, making them desirable for scintillation applications. Some OMHH materials have shown impressive light yields, such as $(C_{38}H_{34}P_2)MnBr_4$, which achieves a light yield of up to 80,000 photons/MeV despite its lower

Z number compared to traditional all-inorganic scintillators [22]. However, they are limited by their relatively long response time in the microseconds range, an area of ongoing research.

3.2 Important parameters and features of scintillators

As we delve into the realm of inorganic materials, which stand as the primary subjects of this thesis, with the aim of tailoring their scintillation properties, we find ourselves at the forefront of a continuous exploration. These materials hold significant importance across various applications, spanning from radiation detection to medical imaging. Within this context, we direct our attention to a set of critical parameters and characteristics. These elements assume a central role, influencing the efficacy and reliability of scintillators. They encompass scintillation yield, the duration of scintillation light emission, non-proportionality, temperature resilience, resistance to radiation, emission spectra, as well as mechanical and chemical stability. In the forthcoming sections, we will embark on a comprehensive exploration of each of these facets, commencing our journey with a detailed examination of scintillation yield.

3.2.1 Scintillation yield and energy resolution

Scintillation yield (Y) represents the number of scintillation photons (n_{ph}) emitted per unit energy (E_{rad}) of absorbed ionizing radiation. It serves as a crucial metric in scintillator materials research, quantifying the efficiency of a material's response to incoming radiation. Mathematically, it can be expressed as:

$$Y = \frac{n_{ph}}{E_{rad}} \tag{3.1}$$

Photoelectron yield Y_{phe} provides information on the number of photoelectrons (e^-) produced per unit energy of absorbed radiation (usually per MeV). It is often used to assess scintillation efficiency and can be expressed as:

$$Y_{phe} = \frac{n_{ph}}{E_{rad}} \tag{3.2}$$

A higher scintillation yield (Y or Y_{phe}) indicates that a scintillator is more effective at converting radiation energy into detectable light signals.

Energy resolution (R) provides an essential measure of a scintillator's precision in capturing radiation events. It is calculated as the Full Width at Half Maximum (FWHM) of the full energy peak in the pulse height spectrum (PHS) divided by the position of the full energy peak position (PP) in the PHS. In simpler terms, energy resolution gauges a scintillator's ability to distinguish between different energy levels of incoming radiation. Mathematically, it can be expressed as:

$$R = \frac{FWHM}{PP} \tag{3.3}$$

A smaller R value signifies superior energy resolution, enabling finer discrimination between radiation energies. Quantum efficiency (QE) is the probability that a scintillation event results in the emission of a photoelectron. It's typically expressed as a percentage and can be calculated as:

$$\mathrm{QE} = \frac{n_{phe}}{n_{scint}} \tag{3.4}$$

Gain (G) represents the signal amplification in photodetectors like photomultiplier tubes (PMTs). It quantifies the multiplication of photoelectrons for each incident photon. The total number of electrons produced (n_e) is given by:

$$n_e = G \cdot n_{phe} \tag{3.5}$$

In our laboratory at NCU, Toruń, researchers use advanced techniques to analyze PHS to understand the scintillation characteristics, energy resolution, quantum efficiency, and gain capabilities of various materials. This research contributes to the ongoing exploration of novel scintillator materials and enhances our understanding of radiation detection and measurement technologies. The forthcoming chapter will introduce additional mathematical formulations related to this research.

3.2.2 Scintillation time profile

The scintillation time profile does not have a single universal formula, as it can vary depending on the scintillator material and the nature of the ionizing radiation interaction. However, some scintillation profiles can be described using mathematical functions. Two commonly used functions are:

Exponential decay: Many scintillation processes exhibit exponential decay of light intensity over time. This decay can be described by the following formula:

$$I(t) = I_0 \cdot \exp\left(\frac{-t}{\tau}\right) \tag{3.6}$$

- I (t) is the intensity of emitted light at time t,

- I_0 is the initial intensity at t = 0,

- τ is the decay time constant, representing how quickly the scintillation light decays.

Gaussian profile: In some cases, the scintillation time profile may have a Gaussian-like shape:

$$I(t) = I_0 \cdot \exp\left(\frac{-(t-t_0)^2}{2\sigma^2}\right) \tag{3.7}$$

- I (t) is the intensity of emitted light at time t,

- I_0 is the maximum intensity at t = 0, the peak time,

- σ is the standard deviation, determining the width of the Gaussian curve.

The selection of the appropriate formula depends on the unique traits of the scintillator material and the type of radiation under investigation. Typically, researchers rely on experimental data and analysis to identify the suitable mathematical model for describing a specific scintillation time profile. In the following chapter, these formulas will be presented in detail. It is important to note that the actual scintillation time profile may deviate from these idealized functions due to various factors, including impurities in the scintillator, the presence of multiple scintillation processes, and the detection system response. Therefore, detailed experimental measurements and analysis are often necessary to accurately describe and understand the scintillation time profile for a particular scintillator material and application.

3.2.3 Non-proportionality

In the 1950s, researchers embarked on a quest to understand non-proportionality in scintillators, primarily focusing on inorganic scintillators like NaI:Tl and CsI:Tl, as well as organic materials such as anthracene and stilbene. They aimed to uncover how the number of scintillation photons produced depended on the type of incident particle, whether it was a 1 MeV electron or a 1 MeV alpha particle. Extensive studies involving a diverse range of particle types, including X-rays, gamma rays, electrons, protons, neutrons, alpha particles, and even fission fragments, were conducted during this era [23–31]. This investigative work continued until the late 1960s, yielding a prevailing consensus that the dependence on particle type and energy was closely linked to ionization density or dE/dx. In essence, particles of varying species and energies would produce equivalent scintillation light if they generated the same ionization density. This phenomenon was attributed to the saturation of luminescence centers, each capable of servicing only one electron-hole pair at a time. Consequently, if there were more electron-hole pairs in the ionization volume than available luminescent centers, the luminosity would decrease. In 1991, a significant breakthrough occurred with the discovery of LSO scintillator. LSO exhibited a remarkable combination of high density, high atomic number, short decay time, and substantial light output, surpassing the performance of the commonly used “heavy” scintillator of that era, BGO. What puzzled researchers was that despite LSO's 4–5 times higher light output compared to BGO, its energy resolution for 511 keV or 662 keV gammas remained nearly identical to that of BGO. This suggested that the energy resolution was not solely determined by counting statistics but influenced by another factor. In 1994, Valentine and Rooney proposed that this additional factor was non-proportionality [29, 32–34].

Since that pivotal moment, interest in the field of non-proportionality in scintillators has continued to grow steadily [35–40]. Non-proportionality in scintillators refers to a phenomenon where the amount of scintillation light produced is not directly proportional to the energy of the incident ionizing radiation. In an ideal scenario, the scintillation light yield should increase linearly with the energy of the incoming radiation, indicating that higher-energy radiation should yield more scintillation light. However, this linear relationship does not hold true for some scintillator materials, leading to deviations from linearity, particularly at higher energies. Several factors, including the scintillator material, impurities, and specific scintillation mechanisms, can influence this non-proportional response. It has significant implications for the accuracy of radiation detection and measurement using scintillation detectors. To ensure precise and reliable measurements, researchers and engineers working with scintillators must understand and characterize the non-proportional behavior of a particular scintillator material. Practical applications often involve applying corrections and calibration techniques to compensate for the effects of non-proportionality.

3.2.4 Thermal stability

In numerous real-world scenarios, scintillators are commonly utilized at room temperature. Nevertheless, while in operation, variations in temperature within the detector may occur due to factors like irradiation or shifts in environmental conditions. Ensuring a consistent operational environment, especially in the case of detectors employed in space missions, can prove to be quite demanding. These temperature fluctuations have the potential to cause changes in the scintillator light emission, consequently impacting the detector's resulting signal. As a result, guaranteeing the thermal stability of scintillation yield becomes a critical requirement for the effective performance of the detector.

In the case of directly exciting a luminescence center, known as photoluminescence, the temperature-dependent quantum efficiency (q), which represents the ratio of emitted photons to incident photons, is influenced by the thermal variations in the probability of nonradiative transitions (P_{nr}). This probability can be described as proportional to the Boltzmann factor $\exp\left(-\frac{E_q}{k_B T}\right)$, where E_q represents the quenching energy, and T is the temperature (in Kelvin). It is important to note that the probability of radiative transitions (P_r) remains unaffected by temperature. Therefore, the quantum efficiency of luminescence can be expressed as follows:

$$q(T) = \frac{P_r}{P_r + P_{nr}} = \frac{1}{1 + C\exp\left(-\frac{E_q}{k_B T}\right)} \tag{3.8}$$

In this equation, C represents a unitless quenching constant. At low temperatures (when $k_B T$ is much smaller than E_q), radiative decay takes precedence and the quantum efficiency q exhibits gradual changes with temperature. As temperature increases, nonradiative decay becomes increasingly significant, resulting in thermal quenching of luminescence over a relatively narrow temperature range. Typically, the parameters C and E_q are carefully selected to optimize Eq. (3.8) for the closest alignment with the experimental quenching curve. Thermal quenching leads to a reduction in both luminescence intensity and decay time, as denoted by:

$$\tau(T) = \tau_0 q(T)$$

Where τ_0 represents the decay time at temperature T = 0.

The significance of E_q can be grasped through the configuration coordinate diagram depicted in **Fig. 3.5**, which pertains to the luminescence center. This diagram plots the energy (E) against the configuration coordinate (Q), representing the average distance between the luminescence center and the neighboring ions. In **Fig. 3.5**, one can observe the potential energies associated with the ground and excited states of the center. In a simplified model akin to a harmonic oscillator, the ground and excited states can be represented by two parabolic curves within the configuration coordinate diagram.

In solid-state systems, the electronic states of luminescence centers, such as impurity ions or defects, are influenced by the positions of nearby ions. Consequently, the shape of the optical absorption and emission spectra of these centers is contingent upon the equilibrium positions and vibrations of these ions. The diagram in **Fig. 3.5** displays the vibration levels as horizontal lines, and the gap between these levels corresponds to ħω, where ω signifies the angular frequency of vibration. In some cases, for simplicity, ħω is considered as the energy of phonons in an ideal lattice, rather than the vibrations of the neighboring ions.

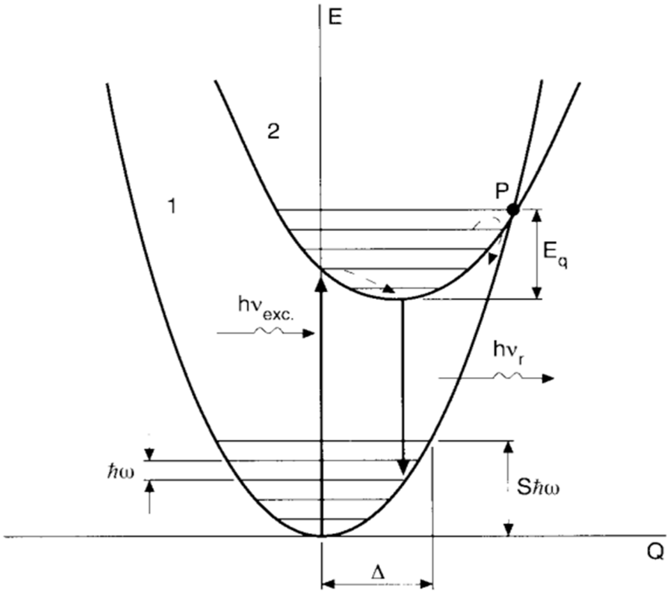

Fig. 3.5. Configuration coordinate diagram for a luminescence center (curve 1 - ground state, curve 2 - excited state) [41].

3.2.5 Emission spectra

3.2.5.1 Radioluminescence spectrum

This represents the distribution of wavelength (or frequency or energy) of scintillation light emitted when the medium is stimulated by ionizing radiation. Typically, it consists of several emission bands, each defined by its peak at λ_{sc} or ν_{sc}, and its width at half-maximum, $\Delta\lambda_{sc}$ or $\Delta\nu_{sc}$, at a specific temperature. Radioluminescence is alternatively referred to as cathodoluminescence, which harks back to its initial discovery at the cathode of an electron gun. In the forthcoming chapter, we will delve extensively into the radioluminescence spectra of the samples under study.

3.2.5.2 Photoluminescence spectrum

This is the wavelength (or frequency or energy) distribution of the scintillation light when the medium is excited by photons of energy below the ionization energy of the atoms. This information combined with the structure of the excitation spectrum, generally up to a few tens of eV, is very useful to determine the energy levels involved in the excitation and relaxation mechanisms. On the other hand, one has to be very careful not to draw too rapid conclusions about the properties of the scintillator on the basis of the photoluminescence spectrum only, which does not reflect at all the mechanisms of energy transfer and thermalization in the medium. This error is frequently made and leads to several misinterpretations. In the most dramatic case we can find materials with a good photoluminescent yield when excited in the UV range but with no light emitted under gamma-rays excitation. A typical example is given by the tungstate group which exhibits good scintillation properties in some host matrices ($CaWO_4$, $CdWO_4$, $PbWO_4$) and no scintillation at all in some other compounds ($BaWO_4$).

3.2.6 Radiation hardness

Radiation hardness, a critical aspect in the performance of scintillation crystals, emerges as a central concern due to the inevitable interaction between ionizing radiation and these materials. The intricate process of radiation damage not only involves the host material but also incorporates defects and impurities within the crystal. These inhomogeneities enhance the likelihood of radiation-induced point defects or color centers forming within the crystal structure. Consequently, incident radiation can induce alterations in both the optical and scintillation properties of the crystal, both during irradiation and after accumulating substantial doses. The impact of ionizing radiation on inorganic scintillators encompasses several key aspects:

- Induced Radioactivity: Heavy crystals exposed to high-energy hadrons such as protons, neutrons, and mesons can exhibit induced radioactivity. This radioactive behavior has implications for the operation of electromagnetic calorimeters.

- Formation of Color Center Absorption Bands: Ionizing radiation can trigger the creation of color center absorption bands within the crystal, resulting in the absorption of photons emitted by luminescence centers. This phenomenon is particularly concerning in large gamma detectors used in high-energy physics, as it leads to a reduction in optical transmission.

- Direct Effects on Luminescent Centers: Radiation can directly affect luminescent centers, leading to alterations in their emission characteristics, including efficiency, spectrum, and decay time. In some cases, luminescence centers may become inoperable (quenched) due to valence changes or compensatory ion diffusion. Additionally, the scintillator's light emission can degrade due to a reduction in energy transfer from electrons and/or holes to luminescence centers, caused by radiation-induced defects and traps. These defects can also impede the mobility of charge carriers.

- Creation of Shallow Traps: Radiation-induced shallow traps can elevate the level of afterglow, impacting the scintillator's performance.

Extensive research has indicated that the most significant effect of radiation damage typically revolves around the degradation in optical transmission. In many crystals, the observed decrease in scintillation light output can be attributed to a reduction in transmission rather than luminescence. Consequently, radiation hardness studies primarily involve the measurement of optical transmission in scintillators subjected to various radiation doses. This approach allows researchers to assess and mitigate the impact of radiation damage on the scintillator's performance, particularly its optical properties.

3.2.7 Considerations regarding costs

It is imperative to meticulously identify and examine the factors that contribute to the overall cost of crystals. In certain instances, the cost can be significantly influenced by the raw materials' level of purity. This becomes particularly relevant when dealing with crystals reliant on exceptionally rare elements like Lutetium. For applications necessitating substantial quantities of crystals, those reliant on such rare elements are often dismissed, despite some of them exhibiting rapid cross-luminescent properties (e.g., $BaLu_2F_8$) or exceptional scintillation efficiency (e.g. LSO:Ce). Cerium, being the most abundant of the rare-earth components, proves to be a more favorable choice. While the purification of Cerium in the presence of other rare-earth components can be challenging and costly, our preliminary investigations indicate that this is not a critical parameter.

The technique employed for crystal growth and the choice of crucible material stand out as pivotal factors. Crystals that can be cultivated, for example, using the relatively economical Bridgeman method within graphite crucibles offer evident advantages. Energy costs, determined by a combination of melting temperature and pulling rate, also exert significant influence. In this context, the high melting points of crystals like GSO or LSO (>1900 °C) and their susceptibility to cleavage, necessitating a low pulling rate (1–2 mm/h), may impose constraints on the minimum achievable price for such crystals.

Conversely, materials like PbF_2 (melting point: 822 °C) and $PbWO_4$ (melting point: 1123 °C) present lower costs owing to their low melting points and the abundance of their raw materials, akin to NaI(Tl). Crystal density, which directly impacts the overall volume of a calorimeter, as well as crystal dimensions and, consequently, furnace and crucible sizes, represent significant parameters affecting the total cost of a crystal-based detector. Lastly, excellent mechanical properties, such as those exhibited by $PbWO_4$, facilitate high production yields during mechanical processing, further contributing to cost reduction.

3.2.8 The mechanical and chemical stability

The mechanical and chemical stability of scintillator materials holds significant importance across various applications. In numerous industrial scenarios, scintillator crystals operate in harsh environments, necessitating qualities such as shock resistance, robust mechanical properties, and hardness. Crystals with hardness levels below 30 to 50 kg/mm^2 are typically classified as "soft." Such soft crystals require protective measures to shield their surfaces from contact with solids, primarily due to their elevated chemical reactivity. Furthermore, the presence of crystal cleavage can profoundly impact the scintillator's performance. Unfortunately, crystals like BaF_2 exhibit perfect cleavage and possess low hardness characteristics. Desirable scintillator materials demonstrate stability and chemical inertness under standard atmospheric conditions and irradiation. However, some scintillator materials exhibit hygroscopic properties, mandating protective encasing. This limitation both narrows the range of potential applications and elevates production costs.

For many applications, large-dimension scintillator crystals with specific shapes are in demand. Consequently, these crystals need to be precisely cut and machined. Perfect cleavage in a crystal poses challenges during mechanical processing and the shaping of scintillator modules. Additionally, scintillator surfaces may require either polishing for regular reflection or grinding for a diffuse reflection, necessitating distinct mechanical properties in the crystals. Anisotropic coefficients of thermal expansion and resultant thermal stresses create challenges when cooling large crystalline rods. For instance, the CeF_3 crystal exhibits substantial anisotropy in thermal expansion coefficients along its *a* and *c* axes, exceeding 20%. Therefore, the preferred qualities in scintillator crystals include the ability to grow large, clear crystals, cut and polish them into desired geometries, mechanical robustness and hardness, chemical inertness, low thermal expansion coefficient, absence of hygroscopic tendencies, lack of cleavage, and a high Young's modulus. Most of these characteristics are inherent material properties that are challenging to alter.

Recent advancements in extrusion methods have facilitated the production of polycrystalline blocks, often referred to as polyscins, exhibiting identical scintillation properties to single crystals. Polyscins offer increased stability against thermal loads and mechanical stresses. Polycrystalline scintillators based on alkali halides are available in various forms, including large rods, sheets, hemispheres, fibers, and more.

3.3 Applications of scintillators

Scintillation materials used in various applications, particularly for γ-ray detection, must meet a diverse set of specific material requirements. These requirements encompass a wide range of factors, including high light yield, excellent energy resolution, proportional scintillation response, low cost, high density, high effective atomic number, fast decay time, short rise time, absence of self-absorption, no afterglow, emission wavelength matching photodetector sensitivity, refractive index matching photodetector window material, absence of internal radioactivity, high temperature stability, excellent radiation hardness, high mechanical strength, and the ability to grow large crystals. Additionally, scintillation materials should ideally be non-hygroscopic to maintain their performance under varying environmental conditions. Meeting these criteria ensures the effectiveness and reliability of scintillators in their respective applications.

3.3.1 Medical diagnostics

Scintillation materials are used in several medical diagnostics and imaging techniques such as X-ray computed tomography, single-photon emission computed tomography (SPECT) and positron emission tomography (PET). In order to expose a patient to the lowest amount of radiation as possible, a high detection efficiency is crucial. This requires scintillation materials with a high light yield, a high density and high effective atomic number. A short rise time and fast scintillation decay time are essential for time-of-flight PET [42,43] measurements and for short acquisition times. For X-ray tomography, Gd_2O_2S:Pr,Ce,F and $(Y,Gd)_2O_3$:Eu,Pr ceramic scintillators are the most widely used. NaI:Tl and CsI:Tl are currently favored as scintillator in SPECT scanners. Due to its high density and reasonably fast decay time, BGO used to be the material of choice in PET scanners. However, Lu_2SiO_5:Ce offers an even faster decay time and much higher light yield and is therefore replacing $Bi_4Ge_3O_{12}$ in these scanners. Drawbacks of Lu_2SiO_5:Ce are the difficulties in growing large, good quality crystals and the high price of lutetium. $LaBr_3$:Ce has been considered to replace the current scintillators for SPECT and PET, however, high production costs and too low density are limiting its commercialization for these applications. A more detailed discussion of scintillator materials for medical diagnostics can be found in Ref. [44].

In the realm of Positron Emission Tomography (PET) techniques, scintillators play a pivotal role, serving as key components within detector rings composed of numerous scintillator pixels coupled with detectors. This intricate setup serves as the linchpin for the precise and sensitive detection of gamma rays emitted during PET scans (**Figs. 3.6** and **3.7**). Through the skillful conversion of gamma ray energy into detectable light signals, scintillators enable the creation of intricate three-dimensional images of biological tissues and processes. The examples of PET devices below underscore the significance of scintillators in this field:

The Advance PET scanner, engineered by General Electric, boasts an assembly of approximately 12,000 (BGO) crystals, each measuring 4 × 8 × 30 mm³. These scintillators excel in facilitating the precise detection and imaging of positron-emitting radionuclides within the human body as shown in **Fig. 3.6**.

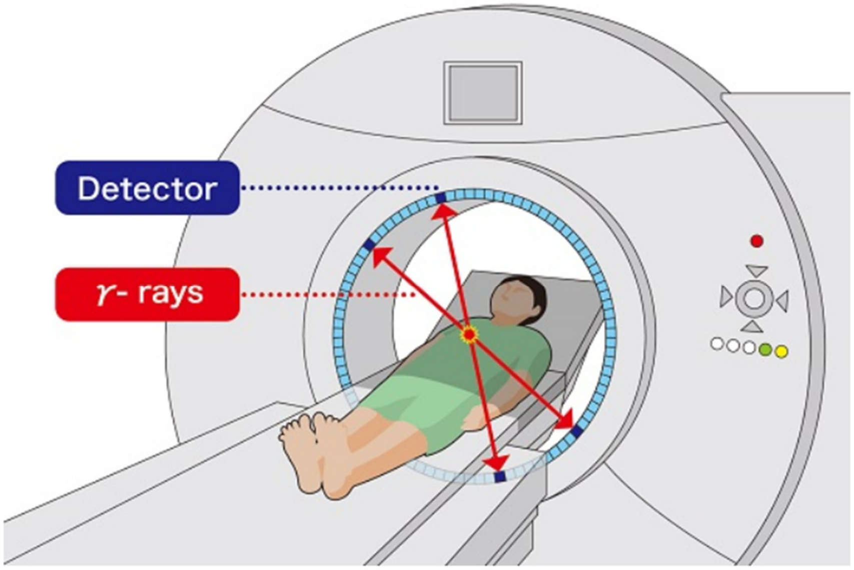

Fig. 3.6. Imaging of positron-emitting radionuclides within the human body [45].

Meanwhile, Philips' PET/CT Allegro/Gemini device harnesses the capabilities of nearly 18,000 GSO:Ce (Gadolinium Orthosilicate doped with Cerium) crystals, each characterized by dimensions of 4 × 6 × 20 mm³. These scintillators are instrumental in enabling precise fusion imaging by seamlessly integrating PET and CT (Computed Tomography) modalities, thus delivering invaluable insights for clinical diagnosis and treatment planning.

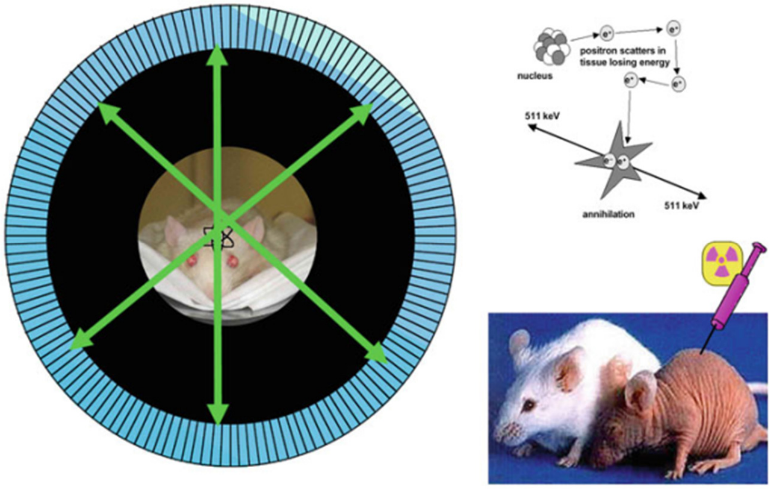

Fig. 3.7. Working principle of a PET scanner [44].

These applications of scintillators underscore their indispensable role in modern medical imaging, thereby contributing significantly to the advancement of our understanding and diagnosis of various medical conditions and diseases. Within the domain of PET technology, Time-of-Flight PET (ToF-PET) represents a groundbreaking approach. It involves the meticulous recording of the precise time at which each coincident photon is detected during an annihilation event. By calculating the time difference between these detections, ToF-PET significantly enhances the localization accuracy of the emission source, consequently elevating image quality while minimizing noise. Scintillator materials like $LaBr_3$:Ce and $CeBr_3$ exhibit immense potential in the context of ToF-PET tomographs.

Their rapid scintillation response and high timing precision align seamlessly with the stringent demands of ToF-PET applications. Furthermore, the advancement of scintillation timing techniques is a collaborative pursuit within the scientific community. Notably, initiatives such as FAST (Fast Advanced Scintillator Timing) operate as part of the COST (European Cooperation in Science and Technology) interdisciplinary network. FAST's primary objective is to pioneer photon instrumentation with an unparalleled timing precision, aiming for an astonishing accuracy level of less than 100 picoseconds (ps). This endeavor underscores the vital importance of precise timing in scintillation-based detectors, not only for ToF-PET but also for an extensive range of photon-based applications across diverse scientific fields.

3.3.2 High-energy physics

High-energy physics experiments, such as those conducted at particle accelerators like CERN, necessitate scintillation materials with a specific set of characteristics. These include high density to effectively stop and detect extremely high-energy (GeV - TeV) radiation, coupled with excellent radiation hardness. Notably, in the Large Electron-Positron Collider at CERN, nearly 12,000 $Bi_4Ge_3O_{12}$ crystals measuring 24 cm each were employed for the L3 detector. Similarly, for the CMS detector within the LHC, more than 75,000 $PbWO_4$ crystals, each with dimensions of 23 cm, were utilized. Both these scintillation materials offer high densities and boast a high effective atomic number, making them ideal candidates for high-energy physics experiments. The sheer quantities required for these detectors necessitate cost-effective production of scintillators on a large scale. Additionally, given the immense energy deposited in the scintillation material, even a relatively modest light yield, such as 300 ph/MeV for $PbWO_4$, is considered acceptable. Furthermore, a fast scintillation decay time is essential, ensuring it is at least faster than the collision rate within the particle accelerator.

These demanding requirements align with the need for dense, fast, and radiation-hard materials, all while keeping costs in check, especially due to the large volumes required. Notably, the scintillation yield, while significant, need not necessarily be exceptionally high. A tangible illustration of these requirements can be seen in the example of a calorimeter within the Compact Muon Solenoid (CMS) system at the Large Hadron Collider (LHC) in CERN, Geneva. This calorimeter relies on the use of over 60,000 $PbWO_4$ crystals, each shaped as truncated pyramids with specific dimensions (base 26 × 26 mm^2, front side 22 × 22 mm^2, height 230 mm). These crystals, characterized by their density, radiation hardness, and cost-effectiveness, exemplify their crucial role in addressing the rigorous demands of high-energy physics experiments, ensuring accurate and reliable data acquisition and analysis.

3.3.3 Astrophysics and space exploration

Scintillation materials are used in astrophysics experiments, for example to detect the characteristic X-rays emitted by newly formed stars or to study the radiation coming from supernova and other astrophysical events. γ-ray spectrometers containing scintillation materials are also put on-board spacecraft for planetary remote sensing. This provides valuable information regarding the planet's elemental surface composition. To accurately monitor and differentiate between the various emitted energies coming from the surface, a high energy resolution is necessary. Furthermore, the amount of radiation reaching the spacecraft is very low, which requires a high sensitivity. Essential for these low count-rate applications is to have an as low as possible background noise, which requires the scintillator to have sufficiently low internal radioactivity. Previously, only high-purity germanium detectors met the requirements to be used as γ-ray spectrometers for space applications.

Since 2000, $LaBr_3$:Ce scintillators provide excellent energy resolution, high sensitivity and room temperature operability that can compete with the semiconductor detectors. In the last decade, $LaBr_3$:Ce scintillator detectors were developed for the European Space Agency's BepiColombo mission to Mercury [46,47]. Unfortunately, $LaBr_3$:Ce contains a small amount of the naturally occurring radioactive ^{138}La isotope, which spoils its capability in low noise applications. Despite a slightly worse energy resolution, $CeBr_3$ emerged as a promising alternative to $LaBr_3$:Ce as it has an almost 30 times lower internal activity.

3.3.4 Security and environmental monitoring

Machines for luggage screening at airports and container scanning at naval ports contain scintillation materials. Most of the modern scanners operate in the same way as X-ray computed tomography scanners for medical diagnostics to image the contents inside a bag or container. A high light yield and fast decay time are the most important requirements for fast and accurate image acquisition. Also the protection from terrorism and monitoring of radiation from environmental disasters (like Chernobyl and Fukushima) requires accurate detection of dangerous neutron and/or gamma-emitting materials. In both cases, the amount of radiation is low which requires high light yield scintillators for a high sensitivity. A high energy resolution and good neutron/gamma discrimination are required for accurate isotope identification. Furthermore, low cost scintillation materials are needed for mass production of these radiation detectors. Scintillation materials that meet these requirements and are currently under development are Cs_2LiYC_{l6}:Ce, $Cs_2LiLaBr_6$:Ce and SrI_2:Eu.

Geophysical and well logging Gamma-ray detectors are used to remotely measure the natural radioactivity of the different soil layers of a drilled well or borehole. When the scintillator detector is lowered into a drilled well, it records the geophysical data as function of the well depth in a gamma-ray log. These gamma-ray logs are used in the search for oil and mineral sources but also to gather information on the age and formation of rock and soil layers. With temperatures over 200 ºC and shock and vibrations encountered during operation, the scintillation materials used for well logging should have a high temperature stability and should be mechanically rugged. Furthermore, these scintillation materials should also have a high density, high effective atomic number, fast decay and should be non-hygroscopic to avoid the need of special packaging. So far no scintillation material exists which meets all of these requirements. For most well logging applications NaI:Tl is used, however, $Bi_4Ge_3O_{12}$ and BaF_2 are in some cases favored.

3.4 Historical overview

The use of scintillation to detect radiation is over a century old. A history of the discovery of important inorganic scintillator materials - important in the sense that they either became commercially available and widely used or triggered further developments or new research directions - is shown in **Fig. 3.8**. The discovery of scintillator materials may be divided into three phases. The first phase included the earliest scintillators: $CaWO_4$ first used in the year following Röntgen's discovery of X-rays; uranyl salts used by Becquerel in 1896 to discover radioactivity; and ZnS used by Crookes to detect and count radioactivity and by Rutherford to study alpha particle scattering. This period of visual scintillation counting ended with the development of the photomultiplier tube.

The discovery of scintillation in naphthalene led in mid-century to a second phase triggered by Hofstadter's development of the thallium-activated NaI. In a burst of exploration during the following few years, the scintillation properties of most pure and activated alkali halide crystals were investigated [48]. Lithium-containing compounds used to detect neutrons and the first glass scintillators (activated with cerium) were also developed in the 1950s. A steady precession of new scintillator materials followed including the discovery of very fast (600 ps) core-to-valence luminescence in BaF_2.

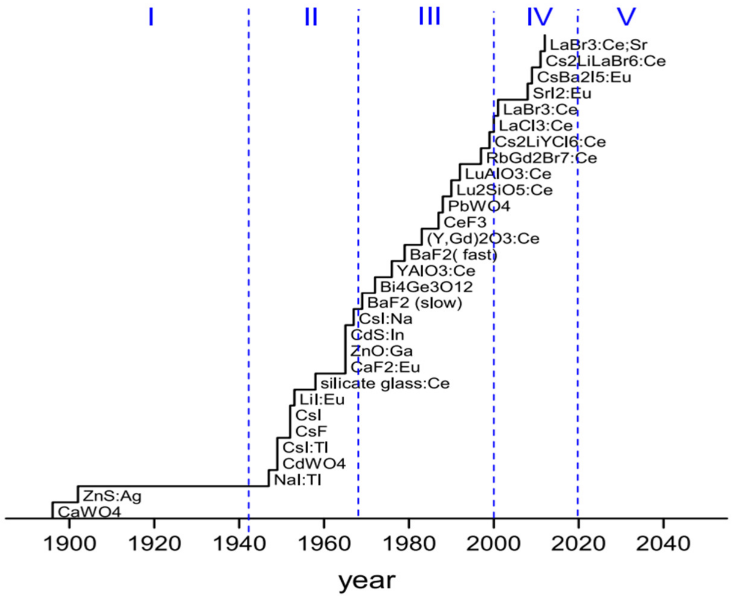

Fig. 3.8. History of scintillator discovery distinguishing phases I to IV and phase V for future discoveries [47].

A third phase - the past two decades - has witnessed a veritable renaissance in research and development of scintillator materials, prompted to a major degree by the need for scintillators for precision calorimetry in high-energy physics and for high-light-output scintillators for medical imaging, geophysical exploration, and numerous other scientific and industrial applications. A sense of the activity during the past decade can be gleaned from the proceedings of a series of conferences devoted to scintillator research and development, namely the Crystal 2000 - International Workshop on Heavy Scintillators for Scientific and Industrial Applications - Chamonix (1992) [49], the Materials Research Society Symposium on Scintillator and Phosphor Materials - San Francisco (1994) [50], followed by the bi-annual Inorganic Scintillators and Their Applications conferences (SCINT 95 - Delft [51], SCINT 97 - Shanghai [52], SCINT 99 - Moscow [53], and SCINT 01 - Chamonix [54]).

In addition to the materials noted in **Fig. 3.8**, other material developments included cerium-activated heavy-metal fluoride glasses, a dense chalcogenide Lu_2S_3:Ce, and $LiBaF_3$ and $Li_6Gd(BO_3)_3$:Ce for neutron detection. Recently lead-halide-based perovskite-type organic/inorganic hybrid compounds yielding excitonic luminescence of a semiconductor with decay time constants of ~100 ps have been reported [55].

Concurrent with the materials developments, the use of synchrotron radiation and laser spectroscopy has led to a greater understanding of the complexities inherent in exciton and defect formation and the numerous processes involved in scintillation. These physical processes are now generally well understood (although details of some specific materials may still be lacking) [41].

The various stages of the scintillation process [56,57] may be summarized beginning with the absorption of a high-energy photon or particle, thereby creating an inner shell hole and an energetic primary electron, followed by radiative decay (secondary X-rays), nonradiative decay (Auger processes - secondary electrons), and inelastic electron–electron scattering, all in the time domain of 10^{-15}-10^{-13} s. When the electron energies becomes less than the ionization threshold, hot electrons and holes thermalization by intraband transitions and electron–phonon relaxation together with exciton formation, self-trapping, and trapping on defects and impurities, all in 10^{-12}-10^{-11} s. The luminescent centers may be excited by hot electron impact excitation, by sequential electron-hole capture or sequential hole-electron capture, and by donor-acceptor energy transfer processes in times ranging from $<10^{-12}$ to $>10^{-8}$ s. The luminescent species in the scintillator may be intrinsic to the material and involve electron-hole recombination, free, self-trapped, and defect-trapped exciton luminescence, donor-acceptor pair transitions, core-to-valence band transitions, or charge transfer transitions within a molecular complex. Alternatively, the luminescent species may be extrinsic, such as luminescence associated with impurities or defects and additive dopant ions. In the role of activator, a dopant ion may be the luminescence species or may promote luminescence as in the case of impurity-bound exciton emission. Various types of inorganic scintillators and examples of representative materials are provided below:

Intrinsic Scintillators

- Excitonic: CsI, BaF_2

- Self-activated: $Bi_4Ge_3O_{12}$, CeF_3, $CdWO_4$, $LuTaO_4$

- Semiconductors: CuI, HgI_2, PbI_2

Extrinsic Scintillators

- Activated: $NaI:Tl^+$, $CsI:Na^+$, $CsI:Tl^+$, $CaF_2:Eu^{2+}$

- Cerium activated: $Lu_2SiO_5:Ce^{3+}$, $LaCl_3:Ce^{3+}$, $LaAlO_3:Ce^{3+}$, glass:Ce^{3+}

- Semiconductors: $CdS:Te^{2-}$, ZnO:Ga, CdS:In

Core-to-Valence Luminescence

- BaF_2, CsF, RbF, $KMgF_3$, $BaLu_2F_8$

3.5 Scintillators of the 21th century

The 21st century has ushered in remarkable developments in the field of scintillator materials, introducing a diverse array of inorganic options to cater to various applications. These materials encompass oxides, halides, and chalcogenides and are available in crystal, glass, and ceramic forms [58]. This progress prompts intriguing questions about the potential discovery of even more exceptional scintillators. If such materials exist, how do we identify them? What defines “better,” and to what extent can scintillators surpass their current capabilities? Is there more to uncover within the periodic table?

The definition of “better” varies depending on the application, and scintillation researchers must carefully consider various factors when pursuing enhanced scintillators tailored to specific uses. The requirements diverge considerably. Scintillation wavelength and light yield dictate the optimal choice of photodetector (e.g. photomultiplier tube, photodiode, or avalanche photodiode). While applications involving highly energetic particles may not prioritize light yield, scenarios with lower or fixed particle energy benefit from increased light yield, enhancing precision and spatial resolution. Energy resolution and proportionality are also influenced by light yield. For applications demanding swift signal rise and decay times, precise timing resolution, high counting rates, or time-of-flight operation, fast response characteristics are crucial. In fields like medical imaging, the absence of afterglow is imperative.

Stability encompasses several facets, including environmental and chemical durability, mechanical robustness, resistance to mechanical shock, and the material's performance under varying conditions such as temperature and time. Desirable characteristics include resistance to air, moisture, and light, as well as the absence of weak cleavage planes in crystals. In high radiation environments like those encountered in detectors for high luminosity colliders, radiation damage becomes a significant concern. Furthermore, attributes like high density and stopping power (indicated by a large effective atomic number) are vital for reducing the required amount of scintillator material. In neutron detection, a constituent ion with a substantial neutron absorption cross-section, such as ^{6}Li, ^{10}B, or ^{157}Gd, is essential.

Scintillator materials can take various forms, including bulk crystals, fibers, or sheets, and the ultimate cost depends on factors like raw material prices and the manufacturing process for shaping the material into the desired dimensions. While each of these factors holds importance in selecting superior materials for specific applications, there are intrinsic limits to the concept of “better” for many of the properties mentioned above. In this era, we have indeed witnessed the discovery of intriguing semiconductor scintillator materials, such as β-Ga_2O_3, and Ga-based spinel crystals such as $MgGa_2O_4$ and $ZnGa_2O_4$ as well as ZnSe, and (Zn,Be)Se [12-16], which have demonstrated promising performance characteristics for a range of applications. These materials represent examples of the ongoing exploration and innovation in the field, underscoring the potential for further advancements in semiconductor scintillator technology.

3.6 Semiconductor scintillators

In recent years, there has been a resurgence of interest in utilizing semiconductor materials as potential candidates for highly luminescent scintillators with fast response times. This renewed enthusiasm can be traced back to pioneering research by Lehmann in the 1960s [59], where he explored the use of donor impurities in direct semiconductors like ZnO and CdS. Notably, the substitution of gallium (Ga) atoms for zinc (Zn) in these materials led to a fascinating outcome - an overlapping degenerate donor band with the lower edge of the conduction band. This unique configuration facilitated the recombination of electrons from the donor band with ionization holes, resulting in the emission of a broad spectrum of near-band-edge light. A similar effect was observed in cadmium sulfide (CdS) doped with indium (In).

Semiconductor scintillators have garnered increasing attention in the scintillator market of today, which has been dominated by inorganic insulators. Among several potential candidates, semiconducting gallium oxide, with a density of 5.96 g/cm³ and a band gap of 4.85 eV, has recently emerged as a promising material for fast scintillation detection [60-71]. Subsequently, various dopants have been introduced into bulk β-Ga_2O_3 single crystals, with some of them investigated for their influence on scintillation properties. Among these dopants are Ce, Al, Mg, Pr, Sn, and Si. There was considerable hope regarding Ce doping, given that Ce^{3+} ions are known as versatile activators for various crystal hosts [72]. However, it should be noted that β-Ga_2O_3:Ce does not exhibit Ce^{3+} d-f luminescence, although there are distinct, albeit not well-understood, effects associated with the introduction of Ce into β-Ga_2O_3 [65].

In my thesis, we focused on critical scintillation parameters for both pure and Ce- and Si-doped β-Ga_2O_3 crystals grown through the Czochralski method. We also investigated Ga-based spinel crystals such as $MgGa_2O_4$ and $ZnGa_2O_4$, which currently demonstrate scintillation yields of approximately 2,500 photons/MeV [12-16]. These parameters include scintillation yield, energy resolution, and scintillation mean decay time. We analyzed these parameter values in relation to the conductivity of specific crystals, as indicated by their free electron concentration. Notably, β-Ga_2O_3 exhibited the highest yield, reaching up to 10,000 photons/MeV at 662 keV (as discussed in the following chapter).Furthermore, our investigation extended to ZnSe and (Zn,Be)Se, which are semiconducting materials characterized by a bandgap of approximately 2.7 eV (at room temperature) and a density of 5.27 g/cm³.

References (chapter 3)

[1] W. L. Reo, “Techniques for Nuclear and Particle Physics Experiments” (2nd ed.), Springer 1994, p. 159

[2] W. L. Reo, “Techniques for Nuclear and Particle Physics Experiments” (2nd ed.), Springer 1994, p. 161

[3] W. L. Reo, “Techniques for Nuclear and Particle Physics Experiments” (2nd ed.), Springer 1994, p. 167

[4] C. Buck, M. Yeh, “Metal-loaded organic scintillators for neutrino physics,” J. Phys. G: Nuclear and Particle Physics, vol. 43, no. 9, p. 093001, 2016

[5] S. Schoppmann, “Review of Novel Approaches to Organic Liquid Scintillators in Neutrino Physics,” Symmetry, vol. 15, no. 1, p. 11, 2023

[6] F. K. Glenn, “Radiation detection and measurement” (4th ed.), Wiley, ISBN 978-0470131480.

[7] H. Nakamura, Y. Shirakawa, S. Takahashi, H. Shimizu, “Evidence of deep-blue photon emission at high efficiency by common plastic,” EPL, vol. 95, no. 2, p. 22001, 2011

[8] S. W. Moser, W. F. Harder, C. R. Hurlbut, M. R. Kusner, “Principles and Practice of Plastic Scintillator Design”, Radiat. Phys. Chem., vol. 41, no. 1–2, p. 31, 1993

[9] V. N. Salimgareeva, S. V. Kolesov, “Plastic Scintillators Based on Polymethyl Methacrylate: A Review,” Instr. Exp. Techn., vol. 48, no. 3, p. 273, 2005

[10] J. Guo, J. Guo, T. Büch, Z. Y. Guo, Z. T. Guoyou, “Comparison of the performance of different converters for neutron radiography and tomography using fission neutrons”, Nuclear Instr. Meth. Phys. Res. A, vol. 605, no. 1–2, p. 69, 2009

[11] F. Maddalena, L. Tjahjana, A. Xie, Z. Arramel, W. Shuwen, C. P. Hong, W. Drozdowski, C. Dujardin, C. Dang, M. Birowosuto, “Inorganic, Organic, and Perovskite Halides with Nanotechnology for High–Light Yield X- and γ-ray Scintillators”, Cryst., vol. 9, no. 2, p. 88, 2019

[12] T. Yanagida, G. Okada, T. Kato, D. Nakauchi, and S. Yanagida, “Fast and high light yield scintillation in the Ga_2O_3 semiconductor material,” Appl. Phys. Express, vol. 9, no. 4, p. 042601, 2016

[13] M. Makowski, W. Drozdowski, M. E. Witkowski, A. J. Wojtowicz, K. Irmscher, R. Schewski, and Z. Galazka, “Tailoring the scintillation properties of β-Ga_2O_3 by doping with Ce and codoping with Si,” Opt. Mater. Express, vol. 9, no. 9, p. 3738, 2019

[14] Z. Galazka, D. Klimm, K. Irmscher, R. Uecker, M. Pietsch, R. Bertram, M. Naumann, M. Albrecht, A. Kwasniewski, R. Schewski, and M. Bickermann, “$MgGa_2O_4$ as a new wide bandgap transparent semiconducting oxide: growth and properties of bulk single crystals,” Phys. Status Solidi A, vol. 212, no. 7, p. 1455, 2015

[15] Z. Galazka, S. Ganschow, R. Schewski, K. Irmscher, D. Klimm, A. Kwasniewski, M. Pietsch, A. Fiedler, I. Schulze-Jonack, M. Albrecht, T. Schröder, and M. Bickermann, “Ultra-wide bandgap, conductive, high mobility, and high quality melt-grown bulk $ZnGa_2O_4$ single crystals,” APL Mater., vol. 7, no. 2, p. 022512, 2019

[16] Z. Galazka, S. Ganschow, K. Irmscher, D. Klimm, M. Albrecht, R. Schewski, M. Pietsch, T. Schulz, A. Dittmar, A. Kwasniewski, R. Grueneberg, S. B. Anooz, A. Popp, U. Juda, I. M. Hanke, T. Schroeder, and M. Bickermann, “Bulk single crystals of β-Ga_2O_3 and Ga-based spinels as ultra-wide bandgap transparent semiconducting oxides,” Prog. Cryst. Growth Charact. Mater., vol. 67, no. 1, p. 100511, 2021

[17] W. L. Reo, “Techniques for Nuclear and Particle Physics Experiments” (2nd ed.), Springer, p. 166 (1994)

[18] K. Shibuya, M. Koshimizu, Y. Takeoka, K. Asai, “Scintillation properties of $(C_6H_{13}NH_3)_2PbI_4$: Exciton luminescence of an organic/inorganic multiple quantum well structure compound,” Nuclear Instr. Meth. Phys. Res. A, vol. 194, no. 2, p. 207, 2002

[19] C. W.E. van Eijk, J. T.M. de Haas, P. A. Rodnyi, I. V. Khodyuk, K. Shibuya, F. Nishikido, K. Masanori, “Scintillation properties of $(C_6H_{13}NH_3)_2PbI_4$: Exciton luminescence of an organic/inorganic multiple quantum well structure compound,” IEEE Nuclear Science Symposium Conference Record N69 (3), p. 3525, 2008

[20] M.D. Birowosuto, D. Cortecchia, W. Drozdowski, K. Brylew, W. Lachmanski, A. Bruno, C. Soci, “X-ray Scintillation in Lead Halide Perovskite Crystals,” Scientific Reports, vol. 6, no. 1, p. 37254, 2016

[21] S. Sun, M. Lu, X. Gao, Z. Shi, X. Bai, W. W. Yu, Y. Zhang, “0D Perovskites: Unique Properties, Synthesis, and Their Applications,” Advanced Science, vol. 8, no. 24, p. 2102689, 2021

[22] X. L. Jin, L. Xinsong, H. Qingquan, W. Michael, M. Biwu, “Highly efficient eco-friendly X-ray scintillators based on an organic manganese halide,” Nature Communications, vol. 11, no. 1, p. 4329, 2020)

[23] C. D. Zerby, A. Meyer, R. B. Murray, “Intrinsic line broadening in NaI(Tl) gamma-ray spectrometers,” Nucl. Instr. Meth., vol. 12, p. 115, 1961

[24] R. B. Murray, A. Meyer, “Scintillation response of activated inorganic crystals to various charged particles,” Phys. Rev., vol. 122, p. 815, 1961

[25] W. C. Kaiser, S. I. Baker, A. J. MacKay, I. S. Sherman, “Response of NaI(Tl) to X-rays and low-energy gamma rays,” IEEE Trans. Nucl. Sci., vol. NS-9, p. 22, 1962

[26] A. J. L. Collinson, R. Hill, “The fluorescent response of NaI(Tl) and CsI(Tl) to X rays and δ,” Proc. Phys. Soc., vol. 81, p. 883, 1963

[27] R. Hill, A. J. L. Collinson, “The effect on the scintillation efficiency of NaI(Tl) of changes in the thallium concentration and strain,” Brit. J. Appl. Phys., vol. 17, p. 1377, 1966

[28] F. T. Porter, M. S. Freedman, J. F. Wagner, I. S. Sherman, “Response of NaI, anthracene and plastic scintillators to electrons and the problems of detecting low energy electrons with scintillation counters,” Nucl. Instr. Meth., vol. 39, p. 35, 1966

[29] B. D. Rooney, “Characterizing scintillator light yield nonproportionality using the compton coincidence technique,” Ph.D. dissertation, University of Cincinnati, OH 1996

[30] J. R. Prescott, G. H. Narayan, “Electron responses and intrinsic line-widths in NaI(Tl),” Nucl. Instr. Meth., vol. 39, p. 51, 1969

[31] G. C. Meggitt, “The effect of the crystal surface on the derived electron scintillation response of NaI(Tl),” Nucl. Instr. Meth., vol. 83, pp. 313, 1970

[32] J. D. Valentine, B. D. Rooney, “Design of a Compton spectrometer experiment for studying scintillator non-linearity and intrinsic energy resolution,” Nucl. Instr. Meth. Phys. Res. A, vol. 353, p. 37, 1994

[33] B. D. Rooney, J. D. Valentine, “Benchmarking the Compton coincidence technique for measuring electron response non-proportionality in inorganic scintillators,” IEEE Trans. Nucl. Sci., vol. 43, no. 6, p. 1271, 1996

[34] B. D. Rooney, J. D. Valentine, “Scintillator light yield nonproportionality: Calculating photon response using measured electron response,” IEEE Trans. Nucl. Sci., vol. 44, no. 3, p. 509, 1997

[35] P. Dorenbos, J. T. M. de Haas, C. W. E. van Eijk, “Non-proportionality in the scintillation response and the energy resolution obtainable with scintillation crystals,” IEEE Trans. Nucl. Sci., vol. 42, no. 11, p. 2190, 1995

[36] E. V. D. van Loef, W. Mengesha, J. D. Valentine, P. Dorenbos, C. W. E. van Eijk, “Nonproportionalityin the scintillation and energy resolution of a $LaCl_3$:10% Ce^{3+} scintillation crystal,” IEEE Trans. Nucl. Sci., vol. 50, no. 1, p. 155, 2003

[37] T. D. Taulbee, B. D. Rooney, W. Mengesha, J. D. Valentine, “The measured electron response nonproportionalities of CaF_2, BGO, and LSO,” IEEE Trans. Nucl. Sci., vol. 44, no. 5, p. 489, 1997

[38] W. Mengesha, T. D. Taulbee, B. D. Rooney, and J. D. Valentine, “Light yield nonproportionality of CsI(Tl), CsI(Na), and YAP,” IEEE Trans. Nucl. Sci., vol. 45, no. 5, p. 456, 1998

[39] M. Balcerzyk, M. Moszynski, M. Kapusta, D. Wolski, J. Pawelke, C. Melcher., “YSO, LSO, GSO and LGSO. A study of energy resolution and nonproportionality,” IEEE Trans. Nucl. Sci., vol. 47, no. 7, p. 1319, 2000

[40] M. Moszynski, J. Zalipska, M. Balcerzyk, M. Kapusta, W. Mengesha, J.D. Valentine, “Intrinsic energy resolution of NaI(Tl),” Nucl. Instr. Meth. Phys. Res. A, vol. 484, p. 259, 2002

[41] P.A. Rodnyi, "Physical Processes in Inorganic Scintillators", CRC Press, Boca Raton, FL, 1997

[42] S. Gundacker, F. Acerbi, E. Auffray, A. Ferri, A. Gola, M.V. Nemallapudi, G. Paternoster, C. Piemonte, P. Lecoq, “State of the Art Timing in TOF-PET Detectors with LuAG, GAGG and L(Y)SO Scintillators of Various Sizes Coupled to FBK-SiPMs,” J. Instrum., vol. 11, p. P08008, 2016

[43] P. Lecoq, “Pushing the Limits in Time-of-Flight PET Imaging,” IEEE Trans. Radiat. Plasma Med. Sci., vol. 1, p. 473, 2017

[44] P. Lecoq, “Development of New Scintillators for Medical Applications,” Nucl. Instr. Meth. A, vol. 809, p. 130, 2016

[45] https://www.m-chemical.co.jp/en/products/departments/mcc/ledmat/tech/1203829_7554.html (accessed on 3.11.2023)

[46] J. Benkhoff, J. van Casteren, H. Hayakawa, M. Fujimoto, H. Laakso, M. Novara, P. Ferri, H.R. Middleton, R. Ziethe, “BepiColombo - Comprehensive Exploration of Mercury: Mission Overview and Science Goals,” Planet. Space Sci., vol. 58, p. 2, 2010

[47] W. Drozdowski, P. Dorenbos, A.J.J. Bos, J.T.M. de Haas, S. Kraft, E. Maddox, A. Owens, F.G.A. Quarati, C. Dathy, V. Ouspenski, “Effect of Proton Dose, Crystal Size, and Cerium Concentration on Scintillation Yield and Energy Resolution of $LaBr_3$:Ce,” IEEE Trans. Nucl. Sci., vol. 54, p. 736, 2007

[48] M. J. Weber, “Inorganic scintillators: today and tomorrow,” J. Lumin., vol. 100, no. 1–4, p. 35, 2022

[49] F. DeNotoristefani, P. Lecoq, M. Schneegans (Eds.), “Heavy Scintillators for Scientific and Industrial Applications,” Editions Frontieres, Gif-sur-Yvette 1993

[50] M.J. Weber, P. Lecoq, R.C. Ruchti, C. Woody, W.M. Yen, R.Y. Zhu (Eds.), “Scintillator and Phosphor Materials,” Proceedings of Materials Research Society, vol. 348, Pittsburgh, PA 1994

[51] P. Dorenbos, C.W.E. van Eijk (Eds.), “Inorganic Scintillators and Their Applications, SCINT 95,” Delft University Press, Delft 1996

[52] Y. Zhiwen, L. Peijun, F. Xiqi, X. Zhilin (Eds.), “Inorganic Scintillators and Their Applications, SCINT 97,” CAS, Shanghai Branch Press, Shanghai 1997

[53] V. V. Mikhailin (Ed.), “Inorganic Scintillators and Their Applications, SCINT 99,” Moscow State University, Moscow 2000

[54] E. Auffray, R. Chipaux, P. Lecoq, C. Pedrini, M. Schneegans (Eds.), “Proc. Conf. on Inorganic Scintillators and Their Applications, SCINT 01,” Chamonix, in: Nucl. Instr. Meth. Phys. Res. A, vol. 486, 2002

[55] K. Shibuya, M. Koshimizu, Y. Takeoka, K. Asai, "Scintillation properties of $(C_6H_{13}NH_3)_2PbI_4$: Exciton luminescence of an organic/inorganic multiple quantum well structure compound induced by 2.0 MeV protons,",Nucl. Instr. Meth. Phys. Res. B, vol. 194, p. 207, 2002

[56] J. Becker, A.N. Belsky, D. Bouttet, et al., in: P. Dorenbos, C.W.E. van Eijk (Eds.), "Inorganic Scintillators and Their Applications, SCINT 95", Delft University Press, Delft, 1996, p. 118.

[57] A. N. Vasil’ev, in: V.V. Mikhailin (Ed.), “The Inorganic Scintillators and Their Applications,” Moscow 1999, p. 43.

[58] G.F. Knoll, “Radiation Detection and Measurement” (3rd ed.), Wiley, New York 2000

[59] W. Lehmann, “A simple method for making a fast inorganic scintillator screen for the detection of fission fragments,” Solid-State Electron., vol. 9, p. 1107, 1966

[60] T. Yanagida, G. Okada, T. Kato, D. Nakauchi, S. Yanagida, “Fast and high light yield scintillation in the Ga_2O_3 semiconductor material,” Applied Phys. Express, vol. 9, p. 042601, 2016

[61] D. Szalkai, Z. Galazka, K. Irmscher, P. Tutto, A. Klix, D. Gehre, “Tailoring the scintillation properties of β-Ga_2O_3 by doping with Ce and codoping with Si,” IEEE Trans. Nucl. Sci., vol. 64, p. 1574, 2017

[62] N. He, H. Tang, B. Liu, Z. Zhu, Q. Li, C. Guo, M. Gu, J. Xu, J. Liu, M. Xu, L. Chen, X. Ouyang, “Low temperature thermoluminescence of β-Ga_2O_3 scintillator,” Nucl. Instrum. Methods Phys. Res. A, vol. 888, p. 9, 2018

[63] Z. Galazka, “Semiconductor scintillator development: Pure and doped β-Ga_2O_3,” Semicond. Sci. Technol., vol. 33, p. 113001, 2018

[64] Y. Usui, D. Nakauchi, N. Kawano, G. Okada, N. Kawaguchi, T. Yanagida, “Scintillation and optical properties of Sn-doped Ga_2O_3 single crystals,” J. Phys. Chem. Solid., vol. 117, p. 36, 2018

[65] W. Drozdowski, M. Makowski, M.E. Witkowski, A.J. Wojtowicz, Z. Galazka, K. Irmscher, R. Schewski, “β-Ga_2O_3:Ce as a Fast Scintillator: an Unclear Role of Cerium,” Radiat. Meas., vol. 121, p. 49, 2019

[66] M. Makowski, W. Drozdowski, M.E. Witkowski, A.J. Wojtowicz, K. Irmscher, R. Schewski, Z. Galazka, “Tailoring the Scintillation Properties of β-Ga_2O_3 by Doping with Ce and Codoping with Si,” Opt. Mater. Express, vol. 9, no. 9, p. 3738, 2019

[67] Z. Galazka, R. Schewski, K. Irmscher, W. Drozdowski, M.E. Witkowski, M. Makowski, A.J. Wojtowicz, I.M. Hanke, M. Pietsch, T. Schulz, D. Klimm, S. Ganschow, A. Dittmar, A. Fiedler, T. Schroder, M. Bickermann, “Bulk β-Ga_2O_3 Single Crystals Doped with Ce, Ce+Si, Ce+Al, and Ce+Al+Si for Detection of Nuclear Radiation,” J. Alloys Compd., vol. 818, p. 152842, 2020

[68] Z. Galazka, K. Irmscher, R. Schewski, I.M. Hanke, M. Pietsch, S. Ganschow, D. Klimm, A. Dittmar, A. Fiedler, T. Schroeder, M. Bickermann, “On the bulk β-Ga_2O_3 single crystals grown by the Czochralski method,” J. Cryst. Growth, vol. 529, p. 125297, 2020

[69] A. Luchechko, V. Vasyltsiv, L. Kostyk, O. Tsvetkova, A.I. Popov, “Shallow and deep trap levels in X-ray irradiated β-Ga_2O_3:Mg,” Nucl. Instrum. Methods B, vol. 441, p. 12, 2019

[70] W. Li, Y. Peng, C. Wang, X. Zhao, Y. Zhi, H. Yan, L. Li, P. Li, H. Yang, Z. Wu, W. Tang, “Structural, optical and photoluminescence properties of Pr-doped β-Ga_2O_3 thin films,” J. Alloys Compd., vol. 697, p. 388, 2017

[71] Y. Usui, T. Oya, G. Okada, N. Kawaguchi, T. Yanagida, “Ce-doped Ga_2O_3 single crystalline semiconductor showing scintillation features,” Optik, vol. 143, p. 150, 2017

[72] M. Nikl, A. Yoshikawa, “Recent R&D Trends in Inorganic Single-Crystal Scintillator Materials for Radiation Detection,” Adv. Opt. Mater., vol. 3, p. 463, 2015

Chapter 4

4 Materials and experiment

4.1 Growth techniques and investigated crystals

This chapter presents a concise overview of the current state of art of the studied materials and diverse growth techniques employed for the fabrication of bulk single crystals of transparent semiconducting oxides (TSOs). The primary focus will be on three well-established crystal growth methods: Bridgman–Stockbarger (BS), Vertical Gradient Freeze (VGF), and Czochralski. These approaches are instrumental in cultivating high-quality scintillating materials. Notably, these techniques are implemented at the Leibniz-Institut für Kristallzüchtung (IKZ) in Berlin under the supervision of Dr. Zbigniew Galazka, with a close collaboration. Additionally, some crystals have been grown at Nicolaus Copernicus University in Toruń by the author of this thesis under the guidance of Prof. Karol Strzałkowski. These methods hold significant recognition for their pivotal role in advancing our research on scintillator development.

Before starting the crystal growth process using any of these methods, it is crucial to carefully choose a seed crystal that closely matches the desired ideal crystalline structure. This initial selection forms the basis for subsequent growth, ensuring the highest quality and precise structural integrity of the resulting scintillating materials, aligning with the objectives of our study.

4.1.1 Bridgman–Stockbarger (BS) and Vertical Gradient Freeze (VGF)

This method, originally introduced in 1925 by Percy W. Bridgman for growing low-melting-point metals [1], underwent subsequent modifications by Donald C. Stockbarger to facilitate the growth of LiF [2]. It is important to note that the contributions of others, such as Tammann, Obreimow, and Schubnikov, are also recognized by Lawson, Nielsen [3], and Buckley [4]. Often referred to as the Bridgman method, this technique involves a freezing growth process. The Bridgman method has been extensively employed not only for metals (e.g. Sb, Bi, Cd, Zn, Sn) and alloys, but also for the growth of III–V compounds (e.g. GaAs, GaP, InP) and II–VI compounds (e.g. CdTe, ZnSe, CdSe), as well as halides (e.g. CaF_2, MgF_2, BaF_2, NaI, CsI, $LaBr_3$, $LaCl_3$) and oxides (e.g. sapphire, $La_3Ga_5SiO_{14}$, $Bi_4Ge_3O_{12}$, $PbWO_4$, TeO_2). The Bridgman method can be configured either horizontally or vertically. Furthermore, it has been used to grow several transparent semiconducting oxide (TSO) single crystals using the

Bridgman/VGF method, including ZnSe and (Zn,Be)Se, ZnO [5–9], β-Ga_2O_3 [10, 11], $BaSnO_3$ [12], and Ga-based spinels [13, 14].

In the vertical configuration of the growth furnace for growing transparent semiconducting oxide (TSO) single crystals, depicted in **Fig. 4.1**, the setup comprises a metal crucible containing the initial material. It is supported by a translation mechanism and covered by a lid. The metal crucible is surrounded by thermal insulation and an inductive coil, which can potentially be replaced with resistive heating. The metal crucible has a conical bottom part, which serves as the nucleation center. Alternatively, a crystal seed can be placed at this conical part with a specific crystal orientation. The design of the growth furnace is tailored to follow a particular temperature profile along the crucible. This profile allows for the melting and crystallization of the initial material. To grow a crystal, the crucible is initially positioned at a high temperature T_f, causing the starting material to melt. However, if a seed is used, the seed portion is maintained at a lower temperature T_c, which is below T_f, preventing the seed from melting. Subsequently, the metal crucible along with the furnace is gradually moved downward out of the coil (or heating element, in general) to the lower-temperature segment of the temperature profile. This enables the crystallization of the molten material onto the crystal seed. The same general principle applies to the horizontal configuration, although its application for TSOs has not been demonstrated so far.

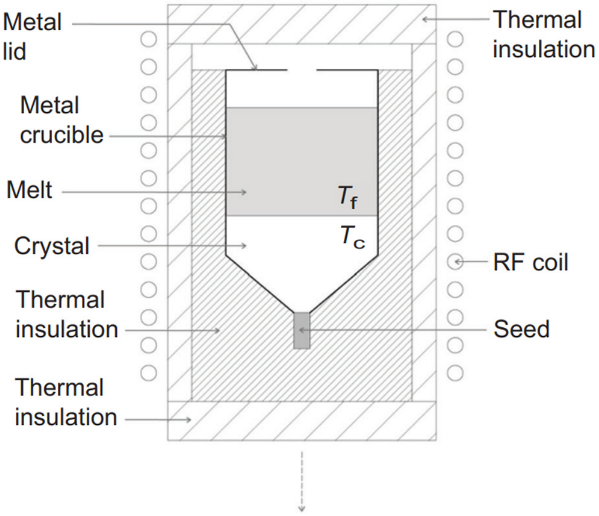

Fig. 4.1. Schematic view of the Bridgman/VGF/direct solidification method.

In an alternative technical approach, the crucible remains stationary, while the overall temperature gradually decreases, and crystallization occurs in response to temperature gradients. This modified technique is referred to as the vertical gradient freeze (VGF) method. Another variation of the VGF method, known as the direct solidification method, involves rapid solidification to minimize the decomposition of compounds, particularly when dealing with highly unstable multielement oxides with a high decomposition rate that cannot be effectively grown using other melt growth methods.

The most critical growth conditions include the shape of the crucible, the geometry of the furnace, temperature gradients (or temperature profile), crucible translation rate, and cooling rate. Transparent semiconducting oxide (TSO) materials suitable for methods like the Bridgman–Stockbarger Method include ZnO, β-Ga_2O_3, ZnSe, (Zn,Se)Be, $MgGa_2O_4$, and $ZnGa_2O_4$ [15-19].

Pros of these methods are as follows:

- Simplicity in operation,
- Short growth time,
- Production of large crystal sizes,
- Applicability to thermally unstable compounds,
- Yielding relatively good structural quality.

There are also some cons of these methods:

- The use of a metal crucible, which can introduce impurities,
- Occurrence of extended defects due to direct contact between the crystal and crucible wall,
- Often lack of a well-defined crystallographic orientation,
- Unsuitability for oxides with very high melting points (>2500°C) or those that undergo phase transitions below their melting points,
- The possibility of trace impurities from the crucibles affecting crystal quality.

4.1.2 Czochralski method

The Czochralski method is a highly significant and efficient technique for growing a wide range of bulk crystals, including classical semiconductors (e.g. Si, Ge), compound semiconductors (e.g. GaAs, GaP, InSb), oxides (e.g. sapphire, YVO_4, $Y_3Al_5O_{12}$, $Gd_3Ga_5O_{12}$, $YAlO_3$, $LiNbO_3$, $Bi_4Ge_3O_{12}$, Lu_2SiO_5, and more), and halides (e.g. NaCl, KCl, KBr, CaF_2, BaF_2, LaF_3, $LiCaAlF_6$) [20].

This method, named after Polish scientist Jan Czochralski, who invented it in 1916, is pivotal in the industrial production of large-volume single crystals with high crystal quality. Over the years it has undergone significant modifications and improvements by various researchers. These enhancements include the introduction of die and gas coolant by Gomperz (Germany, 1922), oriented crystal seeds by Grüneisen and Goens (Germany, 1923), seed necking by Hoyem and Tyndall (USA, 1929), and crystal rotation, shape, and diameter control by Walther (USA, 1937). These developments, combined with Jan Czochralski's original concept of pulling a crystal up from the melt, established key aspects of the method even before World War II. After the war, the Czochralski method was used to grow single crystals of elemental semiconductor Ge by Teal and Little (USA, 1950), with Dash's introduction of a neck procedure in 1958 leading to the production of high-quality, dislocation-free Si crystals. The method rapidly spread in the 1950s, enabling the growth of large-diameter (6-inch) Ge and Si single crystals, which became industrialized. Further advancements included the application of a magnetic field to control melt convection by Hoshikawa et al. (Japan, 1980), continuous melt feeding by Petrov and Zemskov (Russia, 1957), liquid encapsulation by Metz et al. (USA, 1962), and the use of electronic load cells for crystals and crucible weighing by various researchers (UK and USA, 1970s). These developments allowed for automatic diameter control during crystal growth. The Czochralski method was also adapted for growing oxide single crystals (e.g., $CaWO_4$) by Nassau and Van Uitert (USA) in 1960 [20].

The Czochralski method is now widely employed worldwide to grow various types of single crystals, including metals, elemental semiconductors, compound semiconductors, halides, and oxides. It can produce semiconductor and halide crystals as large as 450 mm in diameter and oxide crystals, such as sapphire and $Bi_4Ge_3O_{12}$, with diameters of up to 200 mm. The method is favored for its ability to produce large-diameter crystals, maintain high structural quality, and keep production costs per unit volume low. As a result, it is one of the most commonly used techniques in both research and industrial settings for growing a diverse range of single crystals. In the context of transparent semiconducting oxides (TSOs), the Czochralski method has been successfully applied to grow β-Ga_2O_3 and Ga-based spinel single crystals [21–25].

Fig. 4.2 provides a schematic representation of a growth furnace used in the Czochralski method for growing oxide single crystals, which is enclosed within a water-cooled growth chamber. The growth furnace consists of a metal crucible containing the initial material of the compound intended for growth. To ensure appropriate temperature gradients that minimize crystal cracking and the formation of defects like dislocations and twins, the crucible is enveloped by thermal insulation, typically made of alumina and/or zirconia. In the upper part of this insulation, a space is left for the growing crystal, and a metal afterheater can be placed to further reduce temperature gradients.

For high melting point oxides, the metal crucible and, if used, the metal afterheater are inductively heated by a radiofrequency coil powered by a radiofrequency generator under the control of a controller. In the space above the crucible, a crystal seed is provided in an axisymmetric manner and mounted within a seed holder, which is connected to translation and rotation mechanisms via a pulling rod. This setup enables the growing crystal to be pulled upward while rotating. The growth rate and rotation rate, ranging typically from 1 to 3 mm/h and 4 to 20 rpm, respectively, depend mainly on the thermophysical properties of the melt and the growing crystal.

Another crucial operating parameter is the atmosphere in which the growth occurs, which can range from reducing to neutral to oxidizing. However, for stabilizing transparent semiconducting oxides (TSOs), an oxidizing atmosphere is necessary. This presents additional challenges for the crucible material due to the high melting points of TSOs.

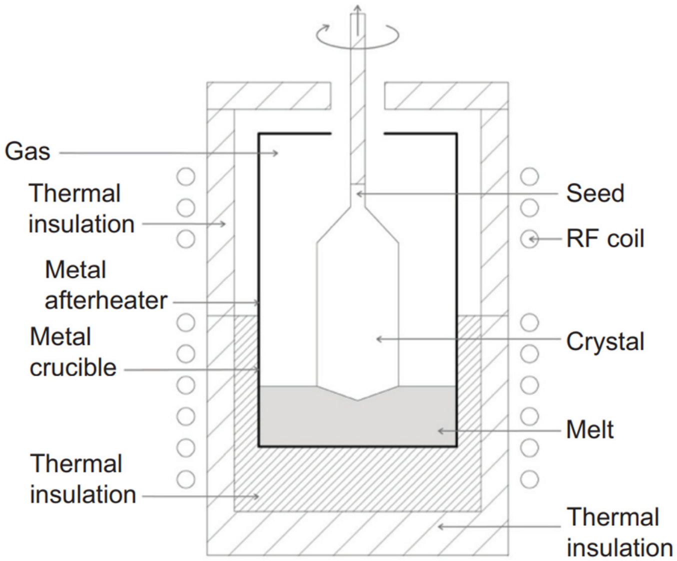

Fig. 4.2. Schematic diagram of a growth furnace illustrating the Czochralski method.

Key growth conditions for the Czochralski method include the design and materials of the furnace, the crucible material, temperature gradients, growth atmosphere, purity of the starting material, and the growth and rotation rates. Transparent semiconducting oxides such as β-Ga_2O_3, $MgGa_2O_4$, and $ZnGa_2O_4$ can be grown using this method [15-19]. Pros of these methods are the following:

- Ability to produce large crystal volumes,
- High crystal perfection, resulting in quality single crystals,
- Relatively short growth time,
- Suitability for high melting point oxides,
- Wide range of temperature gradients, growth rates, and rotation rates, offering flexibility in crystal growth parameters,
- Flexibility in furnace design.

Some cons of these methods should also be listed:

- Use of a metal crucible can introduce trace impurities,
- Not suitable for oxides with very high melting points (> 2500 °C) or those undergoing phase transitions below their melting points,
- Not ideal for highly thermally unstable oxides.

In summary, the Czochralski method is a versatile technique with several advantages, including the ability to produce large, high-quality single crystals. However, it has limitations, such as the use of metal crucibles and restrictions on certain oxide materials.

4.2 Investigated crystals

4.2.1 Gallium Oxide (β-Ga_2O_3)

β-Ga_2O_3, an oxide semiconductor characterized by an ultra-wide bandgap (UWBG) of approximately 4.85 eV, presents possibilities for the innovation of new devices, particularly in the realms of UV optoelectronics and high-power electronics. In the context of this thesis, β-Ga_2O_3, the primary focus, has been cultivated by the group led by Dr Z. Galazka at the Leibniz-Institut für Kristallzüchtung (IKZ) in Berlin [15-17]. The availability of bulk crystals boosted an intensive worldwide activity on Ga_2O_3 in different areas of crystal growth technology (bulk crystals and epitaxial layers), material science (exploration of materials' properties), and device engineering. Such parallel research activity brings, year by year, β-Ga_2O_3 to a higher level that offers industry new opportunities. A fast development of β-Ga_2O_3 as such, its properties, and device demonstrators have been credited in a large number of research papers and patent applications. Development of bulk crystal growth has been intensively followed by the development of hetero and homoepitaxial layers by all epitaxial techniques, particularly with the use of metal-organic chemical vapor deposition (MOCVD) or metal-organic vapor phase epitaxy (MOVPE).

Extensive characterization of both bulk crystals and layers by a diversity of techniques and support from theoreticians not only revealed properties of obtained materials but also indicated ways to control some of the properties and their limitations. Such cumulative knowledge and material availability enabled to demonstrate a diversity of devices for various applications. As the breakdown field of a material scales with the bandgap approximately parabolically, with its breakdown field of 8 MV/cm [26], β-Ga_2O_3 is a great candidate for high-power electronics, such as Schottky barrier diodes (SBDs), metal-oxide field-effect transistors (MOSFETs), and metal-semiconductor field-effect transistors (MESFETs).

Unique properties and a broad spectrum of possible applications place β-Ga_2O_3 in the frontline of UWBG materials as a complementary material to (Al,Ga)N, AlN, and SiC. This chapter discusses bulk β-Ga_2O_3 single crystals in terms of growth techniques, crystal size, etc., as the main candidate in frames of this thesis [15-17]. The main objective here is to show how to grow bulk β-Ga_2O_3 single crystals, which issues accompany crystal growth and which measures to apply to overcome the occurring issues, which methods enable to obtain large-size and high-quality crystals, and to reveal properties measured on bulk crystals obtained by different methods. In other words, this chapter shows the state of the art in the growth of bulk β-Ga_2O_3 single crystals that may facilitate an assessment of this compound for further study, development, and applications.

4.2.1.1 Polymorphism of Ga_2O_3

Ga_2O_3 has been the subject of thorough investigations, both experimental and theoretical, by various researchers, including Roy et al. [27], Zinkevich and Aldinger [28], Penner et al. [29], Playford et al. [30], Yoshioka et al. [31], Delgado and Areán [32], Fornari et al. [33], and Cora et al. [34]. These studies have unveiled several distinct polymorphs denoted as α, β, γ, δ, ε, and κ, each characterized by different crystallographic structures and formation conditions, as outlined in **Tab. 4.1**, which also includes their lattice parameters.

Notably, it has been proposed that the δ-phase may be a composite of the β- and ε-phases, as suggested by Playford et al. [30]. Furthermore, the ε-phase is believed to mimic the κ-phase, likely due to the presence of rotational grains forming on sapphire, as indicated by Cora et al. [34]. Theoretical investigations by Furthmüller and Bechstedt [35] focusing on the α, β, δ, and ε polymorphs of Ga_2O_3 have revealed that their electronic properties exhibit remarkable similarity. This similarity arises from the fact that polymorphism primarily results from distinct arrangements of Ga atoms, which are coordinated in tetrahedral and octahedral configurations, while the Ga–O bonding remains nearly unchanged across these polymorphs.

Tab. 4.1. Ga_2O_3 polymorphs

Polymorph	**System**	**Space group**	**Lattice parameters (Å)**	**Reference**
α	Hexagonal	$R\bar{3}c$	a = 4.9825 b = 13.433	[36]
β	Monoclinic	C2/m	a = 12. 214 b = 3.0371 c = 5.7981 β = 103.83	[37]
γ	Cubic	$Fd\bar{3}m$	a = 8.22	[38]
κ	Orthorhombic	$Pna2_1$	a = 5.0463 b = 8.7020 c = 9.2833	[34]
δ	Cubic	Ia3	a = 9.491	[31]
ε	Hexagonal	$P6_3mc$	a = 2.9036 a = 9.2554	[30]

Among the various polymorphs of Ga_2O_3, β-Ga_2O_3 stands out as the most thermodynamically stable modification at elevated temperatures, making it possible to grow it directly from the molten state. This particular polymorph, β-Ga_2O_3, boasts a melting point (MP) of approximately 1800°C. It is worth to note that the other polymorphs may emerge at lower temperatures but in metastable forms. The formation energy of these polymorphs follows the order: $\beta < \varepsilon < \alpha < \delta < \gamma$, as reported in [31].

4.2.1.2 Crystal Structure of β-Ga_2O_3

Gallium, a metal that falls within the third main group of the periodic system just after aluminum, exhibits both chemical and structural similarities with the latter and its compounds. The oxides of both metals, gallium and aluminum, display a diverse range of polytypes. Thermodynamically stable oxides for both metals possess distinct crystal structures, namely, trigonal α-Al_2O_3 (commonly known as corundum or sapphire) and monoclinic β-Ga_2O_3.

β-Ga_2O_3 crystallizes in the base-centered monoclinic system, belonging to the space group C2/m (Geller [39]), and is isomorphic to θ-Al_2O_3 [40]. The unit cell (**Fig. 4.3**) comprises 20 atoms, including crystallographically inequivalent Ga^{3+} and O^{2-} atoms. In this structure with lower symmetry, Ga atoms are coordinated tetrahedrally and octahedrally (designated as Ga(I) and Ga(II), respectively), while O atoms exhibit threefold and fourfold coordination (O(I)/O(II) and O(III), respectively). O(I) shares two bonds with Ga(II) and one bond with Ga(I); O(II) shares three bonds with Ga(II) and one bond with Ga(I). Meanwhile, O(III) shares two bonds with Ga(I) and one bond with Ga(II). Unlike the hexagonal dense oxygen packing in the α-phases of Ga_2O_3 and Al_2O_3, the oxygens in β-Ga_2O_3 and θ-Al_2O_3 conform to a distorted face-centered cubic packing of oxygen atoms. The lattice parameters for β-Ga_2O_3 are detailed in **Tab. 4.1.** Two easily cleavable planes are formed by O(III) atoms on the (100) plane and by O(I) atoms on the (001) plane.

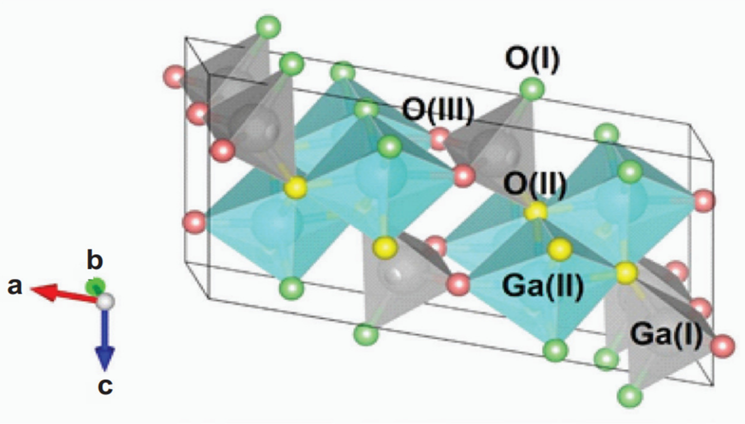

Fig. 4.3. The unit cell of β-Ga_2O_3. Gallium atoms Ga(I) and Ga(II) exhibit tetrahedral and octahedral coordination, respectively. Inequivalent oxygen atoms, O(I) and O(II), have threefold coordination, while O(III) has fourfold coordination [41].

4.2.1.3 Band Structure

The electronic band structure serves as a crucial foundation for understanding the intrinsic electronic and optical characteristics of a material. This knowledge is instrumental in designing devices with specific functionalities. The current computational capabilities and advanced laboratory tools have triggered a surge in the exploration of material physics, both through theoretical and experimental approaches. Computational studies offer insights into structural, electronic, and optical properties, including trapping effects, intrinsic defects, doping, conductivity type, energy gap, its nature, and optical transitions, as well as material limitations. Conversely, experimental results provide valuable feedback to validate mathematical models for electronic structure computation.

In the past decade, the electronic band structure of β-Ga_2O_3 has been extensively studied through first-principles calculations using methods like DFT (LDA, GGA) or hybrid-DFT. Researchers such as Yamaguchi et al. [42] (LDA-PW), He et al. [43] (hybrid-B3LYP), Furthmüller et al. [35, 44] (hybrid-HSE+G0W0), Varley et al. [45–47] (hybrid-HSE06), Peelaers et al. [48] (hybrid-HSE06), Zacherle et al. [49] (GGA-PBE, hybridHSE06), Navarro-Quezada et al. [50] (GGA-HSE03+G0W0), Cocchi et al. [51] (LDA-PW), Deák et al. [52] (hybrid-HSE06), Dong et al. [53] (GGA-PBE), Mock et al. [54] (GGA-GauPBE), Wei et al. [55] (hybrid-HSE06), and experimental measurements by Lovejoy et al. [56], Janowitz et al. [57], Mohamed et al. [58, 59], Zhang et al. [60], Michling and Schmeißer [61] have contributed to this exploration. The band structure of β-Ga_2O_3 is depicted in **Fig. 4.4**.

The top of the valence band (VB) primarily comprises O 2p states, resulting in a very flat VB. The minimal dispersion of the VB maximum (VBM) leads to an exceptionally high effective hole mass, consequently resulting in very low hole mobility, rendering practical p-type conductivity improbable. Moreover, theoretical findings by Kyrtsos et al. [62] (GGA-PBE, hybrid-HSE) indicate that mono- and divalent ions substituting Ga^{3+} in the crystal lattice introduce deep acceptor levels with ionization energies exceeding 1eV, making doping towards p-type conductivity unfeasible.

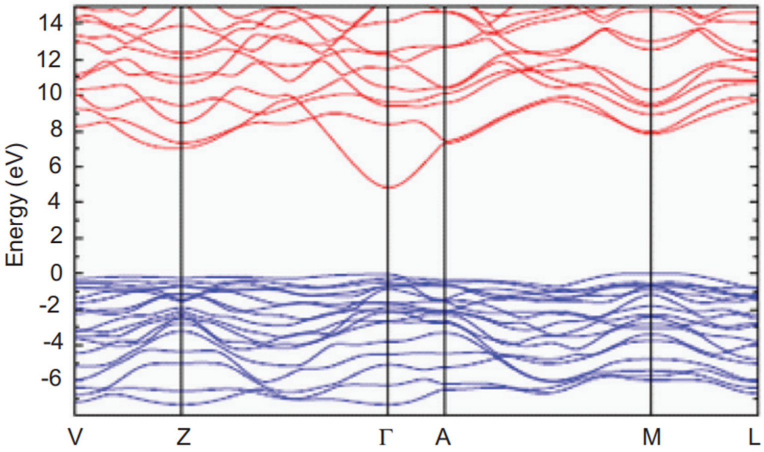

Fig. 4.4. Illustration of the band structure for β-Ga_2O_3, calculated using the primitive unit cell of the base-centered monoclinic β-Ga_2O_3 [45].

The local maxima in the valence band maximum (VBM) are observed at the G and M points of the Brillouin zone (BZ). Although the M point is only 30 meV away from the G point, β-Ga_2O_3 can be considered a direct semiconductor. This is due to momentum conservation, making the transition at G–G more probable than at M–G. In the conduction band (CB) bottom section, Ga-s and O-p states are hybridized, featuring a distinct local minimum at the G point and significant dispersion. This dispersion leads to a relatively low effective electron mass and high electron mobility.

4.2.1.4 Bulk Crystal Growth

The initial report on bulk β-Ga_2O_3 crystals dates back to 1957 when Kohn et al. [63] published findings on obtaining tiny crystals from the gas phase through the oxidation of molten elemental

Ga. Subsequently, in 1963, the first flux-grown crystals were achieved by Remeika [64], with ongoing contributions from other groups over the following three decades (Katz et al. [65], Garton et al. [66], Fischer et al. [67], Chani et al. [68]). The year 1964 saw the demonstration of the first melt-grown crystals by Chase [69], utilizing the Verneuil method, a practice continued intermittently for over a decade. Shortly thereafter, in 1967, the first reports on the chemical vapor transport (CVT) growth of β-Ga_2O_3 were introduced by Lorenz et al. [70]. This CVT method persisted in the subsequent two decades with contributions from various research groups, including Matsumoto et al. [71, 72], Gerlach and Oppermann [73], Juskowiak and Pajączkowska [74, 75], and Pajączkowska and Juskowiak [76, 77]. In 1983, Vasiltsiv et al. [78] mentioned the use of the Czochralski method for growing β-Ga_2O_3 crystals, although without providing specific details.

In 1996, Vasyltsiv et al. [78] reported the growth of β-Ga_2O_3 using the optical floating zone (OFZ) method, a technique subsequently adopted successfully by numerous groups (Ueda et al. [79], Tomm et al. [80], Villora et al. [81, 82], and Zhang et al. [83]). By the year 2000, Tomm et al. [84] provided some insights into the growth of β-Ga_2O_3 crystals by the Czochralski method, marking the beginning of its intensive development a decade later by Galazka et al. [24, 85–89]. In 2008, Aida et al. [90] presented the first detailed report on the edge-defined film-fed growth (EFG) method, with initial attempts mentioned by Shimamura et al. [91]. Kuramata et al. [92] then carried out an intensive development of the EFG method. The successful application of melt growth techniques, including the Czochralski and EFG methods, paved the way for other melt growth techniques. In 2015, Galazka et al. [87] demonstrated the vertical gradient freeze (VGF) and Bridgman methods, and in parallel in 2016, Hoshikawa et al. [93] showcased their application.

4.2.1.5 Czochralski

While the growth of bulk β-Ga_2O_3 crystals using the Czochralski method was previously mentioned or demonstrated by Vasyltsiv et al. [78] and Tomm et al. [85], a thorough and extensive development of this material was carried out by Galazka et al. [84-88, 94-97].

The Czochralski growth stations designed for growing bulk β-Ga_2O_3 single crystals encompass a stainless-steel chamber, a growth furnace inside the chamber, a puller equipped with translation and rotation mechanisms, a balance connected to a pulling rod extending into the growth furnace, an RF generator operating at 10–30 kHz to power an RF coil surrounding the growth furnace, and a control unit linked to the pulling and rotation mechanism, the balance, and the generator. The control unit employs a PID (proportional, integral, differential) controller to enable automatic diameter control of the growing crystal. The growth furnace comprises an iridium (Ir) crucible and an active Ir afterheater, ensuring low temperature gradients. Both are inductively heated by the RF coil, with thermal insulation composed of zirconia, alumina, and quartz surrounding the crucible and afterheater on all sides. The crucibles, made of high-purity iridium (3N), have diameters of either 40 or 100 mm for growing 20 mm and 2-inch-diameter crystals, respectively, defining a crystal-to-crucible ratio of about 0.5. Larger crucibles have an aspect ratio less than 1 (shallow crucibles). The growth rate typically ranges between 1 and 2 mm/h, with crystal rotation speeds of 8–15 and 4–8 rpm for 20 mm and 2-inch-diameter crystals, respectively. The length of the crystals reaches up to 70 and 100 mm for both diameters, with a crystallization ratio below 50%. For the 20 mm diameter β-Ga_2O_3 crystals, growth usually occurs at relatively low O_2 concentration, using the growth atmosphere (1–x)Ar + xCO_2 vol.% with x = 0.1–1.0, or (1−y)Ar + yO_2 vol.% with y = 0.02–0.05 under atmospheric pressure or an overpressure of 7 atm. In contrast, two-inch-diameter crystals are grown under much higher O_2 concentration supplied by the growth atmosphere (1−y)Ar + yO_2 vol.% with y = 0.08–0.35. Further details about the growth of bulk β-Ga_2O_3 single crystals using the Czochralski method are discussed in connection with thermodynamics, which plays a crucial role when growing this compound from the melt. The growth process involves a crystal seed dipped into the melt, and after equilibration, it is slowly pulled up while rotating. The seed diameter is enlarged to a predefined cylinder diameter, which, after reaching a predefined length, is separated from the melt and slowly cooled down to room temperature. In the Czochralski method, the growth proceeds from the exposed melt surface.

4.2.1.6 Pulling direction

The presence of two easily cleavable planes, {100} and {001}, in β-Ga_2O_3 poses a limitation on the pulling direction along the crystallographic axis (i.e., along the b-axis), which is parallel to both cleavage planes. In the Czochralski method, where a crystal is pulled upward, if any of the cleavage planes were substantially perpendicular to the pulling direction, the seed could potentially crack parallel to the cleavage plane under the crystal's weight and thermal stress induced in the seed due to existing temperature gradients. In such a scenario, the crystal could simply fall into the melt. This is particularly crucial during the growth of crystals with diameters exceeding 1 inch. For the same reasons, the edge-defined film-fed growth (EFG) method also utilizes the pulling direction along the b-axis. Additionally, numerical simulations of stress distribution in a real Czochralski growth furnace and growth conditions have revealed that the maximum stress values for the b-axis direction are twice as small as those for the a-axis direction (Miller et al. [98]). The situation differs in the case of the optical floating zone (OFZ) and Bridgman techniques, where a crystal is grown on top of the seed, eliminating the risk of the growing crystal disconnecting from the seed, the growth directions parallel to all main crystallographic directions were successfully demonstrated in these techniques.

Aside from the pulling directions, where the cleavage planes are inclined to the pulling direction, growth instabilities are induced by the growth kinetics. During growth along the b-axis direction, the surface of a cylindrical crystal is stabilized by the cleavage planes <100> and <001>, which have lower formation energy compared to the <010> plane. In other words, a deviation of the pulling direction from the b-axis will result in a crystal shape deviating from a straight cylinder. **Fig. 4.5** shows bulk β-Ga_2O_3 single crystals (side and top views) grown along the (**Fig. 4.5a**) and (**Fig. 4.5b**) crystallographic directions, respectively. The crystal grown along the b-axis direction forms a straight cylinder, kinetically stabilized by the cleavage planes <100> and <001>. Consequently, its cross section is not perfectly circular but slightly elliptical. However, the crystal pulled along the a-axis direction tends to grow along the b-axis direction. As the growth progresses, the crystal gradually approaches the crucible wall, the hottest part of the growth furnace. At a certain point, the crystal cannot continue its journey toward the crucible wall and returns toward the center of the crucible. The cross section of such a crystal is more elliptic and asymmetric. In conclusion, the most preferable growth direction for bulk β-Ga_2O_3 crystals using the Czochralski method is that which is parallel to the crystallographic b-axis direction.

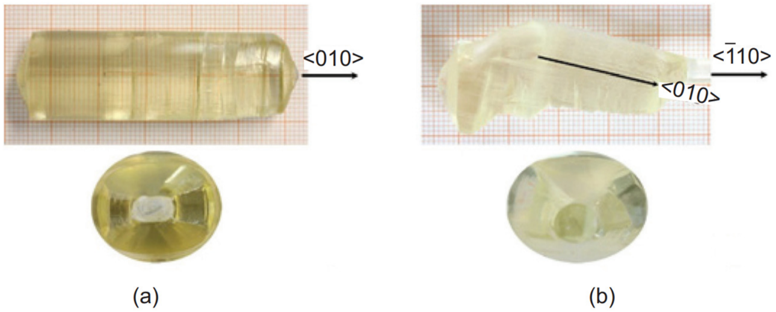

Fig. 4.5. Side and top views of bulk β-Ga_2O_3 single crystals grown using the Czochralski method along the (a) and (b) crystallographic directions [41].

4.2.2 Ga-Based Spinels: $ZnGa_2O_4$, $MgGa_2O_4$

Galazka has successfully grown various Ga-based spinel compounds at the Leibniz-Institut für Kristallzüchtung in Berlin [18, 19]. Only $ZnGa_2O_4$, whether in the form of thin films [99] or ceramics [100], has been demonstrated as a transparent semiconducting oxide. Recently, Galazka et al. [101, 95] showcased the semiconducting capabilities of $MgGa_2O_4$ and mixed (Zn,Mg)Ga_2O_4 single crystals. The cubic structure of Ga-based spinels is advantageous, providing more isotropic properties, facilitating easy wafer fabrication, and serving as versatile substrates for both homoepitaxy and heteroepitaxy. Additionally, these spinels possess ultra-wide bandgaps, exceeding 4.5 eV, making them suitable for UV electronics and optoelectronics. Significantly, as demonstrated by Galazka et al. [95, 101, 102], the growth of truly bulk single crystals of Ga-based spinels directly from the melt enables the production of crystals and wafers of suitable size for diverse applications. Indeed, a variety of devices have been successfully demonstrated using $ZnGa_2O_4$ ceramics, films, and nanostructures. These include MOSFETs [103], photodetectors [104], electroluminescent devices (phosphors) [105–114], photocatalytic devices [115, 116], and gas sensors [117]. Demonstrations of $MgGa_2O_4$-based devices encompass phosphors [118] and laser host materials [119]. On the other hand, $CoGa_2O_4$ has exhibited magnetic properties [120–122].

Among the discussed Ga-based spinel single crystals, $CoGa_2O_4$ crystals do not exhibit semiconducting behavior; however, they display surface p-type conductivity after hydrogen annealing at elevated temperatures. In addition to their semiconducting properties, Ga-based spinels have proven to be excellent substrates for magnetic films of $NiFe_2O_4$ and are suitable for other Fe-based magnetic films. The small lattice mismatch between $NiFe_2O_4$ thin films and

$MgGa_2O_4$ and $CoGa_2O_4$ spinel substrates has allowed the elimination of anti-phase boundaries in $NiFe_2O_4$ and the exploration of its magnetic properties [123, 124]. $ZnGa_2O_4$ shows an almost ideal lattice match with $NiFe_2O_4$ [102]. Moreover, $Zn_{1-x}Mg_xGa_2O_4$ offers the ability to tune the lattice parameter between 8.281 and 8.334 Å. This presents another crucial application for bulk single crystals of Ga-based spinels.

The availability of bulk single crystals and the exploration of their optical and electrical properties may not only contribute to a better understanding of the underlying physics but also lead to an expansion of the area of applications by leveraging the specific properties characteristic of each material.

4.2.2.1 Crystal Structure

Compounds $MeGa_2O_4$ (Me = Zn, Mg, Zn+Mg, Co) crystallize in the spinel structure, represented as AB_2X_4, where X denotes the anion, typically oxygen, although other spinel-type compounds with X = F, S, Se can also be found. The anions form a cubic dense packing. The cations A and B are distributed over half of the octahedral and one-eighth of the tetrahedral sites (**Fig. 4.6**), resulting in the space group Fd3m for the structure. A and B can be identical, and some mixed-valence oxides, such as Fe(II,III)3O4 and Co(II,III)3O4, crystallize as spinels [125, 126].

At very high temperatures, the distribution of cations over the tetrahedral and octahedral sites is nearly random, leading to a high degree of disorder and a significant configuration entropy of 15.8 J/(mol·K) [127, 128] in comparison to the fully ordered state. This randomness contributes to the stability of many spinels as they exhibit high melting points. At lower temperatures, the thermodynamically preferred state involves the ordering of different A and B cations over the octahedral and tetrahedral sites.

O'Neill and Navrotski [127] provide an overview of the structural features of spinels, classifying $ZnGa_2O_4$ as mainly a normal spinel. The lattice parameters for $ZnGa_2O_4$ measured by Phani et al. [129] for ceramics and Galazka et al. [102] for bulk single crystals are 8.3313 and 8.3336 Å, respectively. In contrast, $MgGa_2O_4$ is mainly an inverse spinel with a lattice parameter of 8.281 Å, as reported for bulk single crystals by Schwarz et al. [128]. It is important to note that the lattice constant depends not only on the chemical composition, but also on the cation distribution over the tetrahedral and octahedral sites, and hence on the inversion degree. $ZnGa_2O_4$ forms a complete series of a solid solution with the spinel-type Zn_2SnO_4 [130]. Finally, the lattice parameter of $CoGa_2O_4$ is reported as 8.3229 Å according to the work of Brik et al. [131].

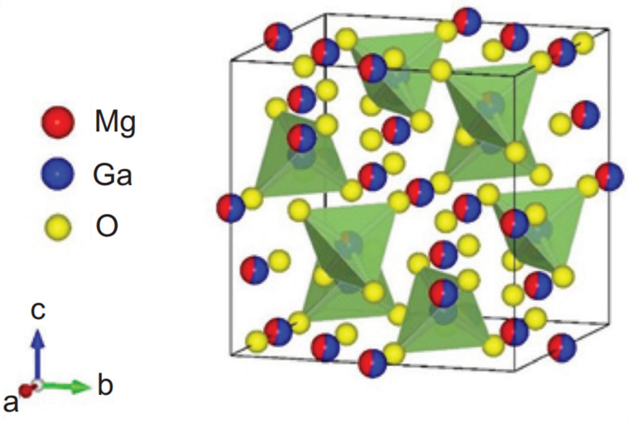

Fig. 4.6. The spinel structure, predominantly inverse, of MgGa$_2$O$_4$. The tetrahedral sites are occupied by 84% Ga (remaining Mg), while the octahedral sites are occupied by 55% Ga (remaining Mg) [128].

4.2.2.2 Band Structure and Native Point Defects

Like other Transparent Conductive Oxides (TSOs), Ga-based spinels have undergone both theoretical and experimental scrutiny to understand their electronic structure and properties, albeit not as extensively. The insights gained from these studies play a crucial role in designing and producing devices with anticipated properties and functionalities. The crystal structure and physical properties of Ga-based spinels offer a platform for fundamental investigations in this material class and provide a basis for conceptualizing new devices. The electronic structure, being a fundamental characteristic, serves as a cornerstone for subsequent endeavors in material synthesis, property exploration, and device development.

4.2.2.3 Band Structure

Theoretical investigations into the band structure of ZnGa$_2$O$_4$ have been conducted by various researchers, including Sampath et al. [132], Pisani et al. [133], López et al. [134], Brik [135], Dixit et al. [136], Zerarga et al. [137], and Xia et al. [138]. **Fig. 4.7** provides an example of the calculated band structure of ZnGa$_2$O$_4$. The valence band maximum (VBM) is predominantly composed of O atoms (O 2p orbitals), while the conduction band minimum (CBM) originates from Ga and O atoms, particularly Ga 4s and O 2p orbitals forming a dispersed sp-class band. The CBM is located at the G-point of the Brillouin zone (BZ), and the VBM is positioned in the K–G region, indicating the semiconductor's indirect nature, consistent with other theoretical calculations [134, 135, 137]. The calculated indirect and direct bandgaps are 4.36 eV and approximately 4.5 eV, respectively [138]. Other theoretical values of the indirect (K–G)/direct (G–G) bandgaps include -/4.57–4.71 eV [136], 2.78/4.24 eV [134], and 2.69/2.74 eV [137]. However, owing to a small energetic difference of about 120 meV between the uppermost valence bands, ZnGa$_2$O$_4$ can be considered a pseudo-direct gap material.

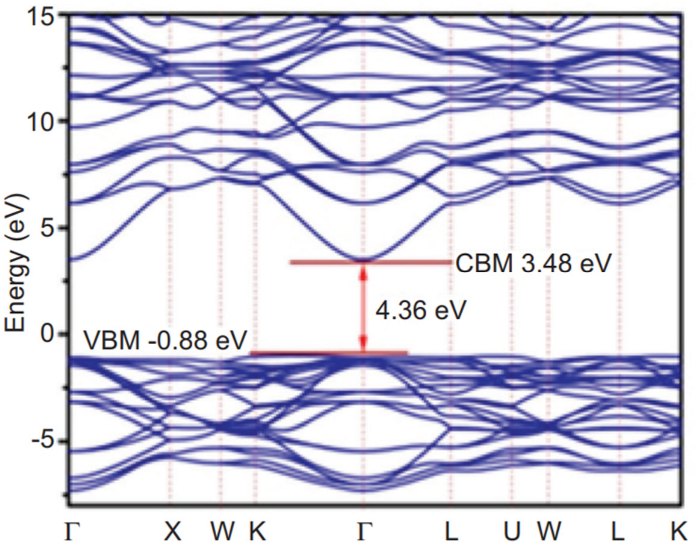

Fig. 4.7. The calculated band structure of $ZnGa_2O_4$, determined through first principles using the GGA+U functional. The indirect gap from K to G is measured at 4.39 eV, while the direct gap at G to G is approximately 4.5 eV [138].

The band structure of $MgGa_2O_4$ was recently elucidated by Varley [139] and Thielert et al. [140], as illustrated in **Fig. 4.7**. Both theoretical (DFT, HSE06) and experimental (angle-resolved photoemission spectroscopy, ARPES) band structures reveal an exceedingly flat VBM with minimal dispersion, approximately 0.6 eV [140]. The CBM is situated at the G-point of the Brillouin Zone (BZ), and the presence of a local maximum of the VBM at the G-point (**Fig. 4.7**) suggests a direct nature of the bandgap. Indeed, calculated values for the bandgap are approximately 5.013 and 5.014 eV for the indirect and direct bandgaps, respectively [139], aligning well with the experimental bandgap of about 4.9 eV [101]. Similar to $ZnGa_2O_4$, the VBM of $MgGa_2O_4$ comprises O 2p states, while the CBM comprises Ga 4s and O 2p states.

The band structure of mixed $(Zn,Mg)Ga_2O_4$ has not been documented in the literature, but it is anticipated to resemble the individual compounds $ZnGa_2O_4$ and $MgGa_2O_4$, featuring an extremely flat VBM and CBM at the G-point of the BZ. The projected bandgap, likely of a direct or pseudo-direct nature, is anticipated to fall between 4.6 and 4.9 eV.

4.2.2.4 Bulk Crystal Growth

The first bulk single crystals of $ZnGa_2O_4$, acquired from flux, were documented in 1967 by Chase and Osmer [141]. Subsequent growth from flux was undertaken by Boom et al. [142], van der Straten et al. [143], and Yan et al. [144, 145]. In 1995, Jia et al. [146] mentioned the growth of fiber $ZnGa_2O_4$ crystals from the melt using laser-heated pedestal growth (LHPD). Then, in 2018, Galazka et al. [102] reported the pioneering achievement of truly bulk $ZnGa_2O_4$ single crystals, obtained through the vertical gradient freeze (VGF) and Czochralski methods.

Bulk $MgGa_2O_4$ single crystals made their debut in 1962, grown from flux by Giess [147], followed by the Czochralski method in 1972 by Scott et al. [148]. The optical floating zone

(OFZ) method contributed to the growth of $MgGa_2O_4$ single crystals in 2010, as reported by Suzuki et al. [149]. In 2014, Galazka et al. [102] made a groundbreaking discovery regarding the semiconducting properties of $MgGa_2O_4$ and successfully produced bulk single crystals from the melt using the Czochralski, Bridgman, and Kyropoulos-like methods. The mixed $(Zn,Mg)Ga_2O_4$ crystals joined the roster in 2018, grown by the VGF method by Galazka and Hanke [95]. For $CoGa_2O_4$, the saga began in 1985 when Kramer et al. [150] published the first reports on bulk $CoGa_2O_4$ single crystals obtained directly from the melt via the OFZ and Czochralski methods. The Czochralski and Kyropoulos-like methods were enlisted for the growth of bulk $CoGa_2O_4$ single crystals by Galazka [151] in 2014. In 1986, Leccabue et al. [152] achieved bulk $CoGa_2O_4$ crystals from the gas phase using the CVT method. In 2006, Nakatsuka et al. [153] reported the successful growth of $CoGa_2O_4$ single crystals using the flux method.

4.2.2.5 Vertical gradient freeze (VGF) / vertical Bridgman (VB)

The Vertical Gradient Freeze (VGF) or Vertical Bridgman (VB) techniques, as employed by Galazka et al. [95, 101, 102], played a pivotal role in growing bulk $ZnGa_2O_4$, $MgGa_2O_4$, and mixed $(Zn,Mg)Ga_2O_4$ single crystals. The process involved using Ir crucibles with diameters of either 40 or 60 mm and cylinder lengths of 40 or 60 mm, featuring flat or conical bottoms. To control temperature gradients and minimize thermal decomposition, the crucibles were fitted with Ir lids, incorporating a small central opening (1–3 mm). Thermal insulation surrounded the crucibles, leaving a window for temperature monitoring via a pyrometer. The inductive heating of the crucibles was facilitated by an RF coil surrounding the thermal insulation, powered by an RF generator operating at 10 or 30 kHz.

Tailored to the thermal stability of each compound (refer to **Fig. 4.8**), different growth atmospheres were utilized: N_2 for $MgGa_2O_4$, Ar + 8–40 vol.% O_2 for $ZnGa_2O_4$, and Ar + 10 vol.% O_2 for $(Zn,Mg)Ga_2O_4$. The crystals were typically grown under atmospheric pressure, although $ZnGa_2O_4$ crystals underwent growth under overpressure conditions of 2 and 10 bars to further mitigate the evaporation of Zn(g).

The composition of the starting materials played a crucial role in the growth process. For $MgGa_2O_4$, an excess of Ga was incorporated as $MgGa_{2+x}O4$ (where x=0–0.02) to compensate for the high vapor pressure of Ga relative to Mg. $ZnGa_2O_4$ was tailored with an excess of Zn as $Zn_{1+y}Ga_2O_4$ (where y=0–0.04) and mixed $(Zn,Mg)Ga_2O_4$ was adjusted to $(Zn_{1+z}Mg_z)Ga_2O_4$ (with z=0.1,0.25,0.5) to counteract the vapor pressure discrepancy between Zn and Ga.

The VGF or VB method, characterized by short growth times and low temperature gradients within the crucible, resulted in minimal losses of volatile species. Starting materials were prepared by firing MgO, ZnO, and Ga_2O_3 powders individually in air to eliminate moisture and other volatile impurities. These powders were mixed at appropriate molar ratios, cold pressed, and subsequently fired in air to enhance compactness (referred to as the sintering step).

For doping purposes aimed at inducing or enhancing electrical conductivity, suitable dopant oxides were added to the starting materials. For instance, Si^{4+} was used to dope $MgGa_2O_4$ and $(Zn,Mg)Ga_2O_4$, added in the form of SiO_2 at a concentration of 0.2–0.25 mol.%. $ZnGa_2O_4$ was doped with Si^{4+} and Zr^{4+} by incorporating SiO_2 and ZrO_2 at concentrations of 0.25 mol.% each.

The growth process involved homogenizing the molten starting material within the crucible, followed by controlled cooling. After growth, crystallized material was core-drilled from the crucible, resulting in crystalline bulks of $ZnGa_2O_4$, $MgGa_2O_4$, and $(Zn,Mg)Ga_2O_4$. The bulk materials comprised several single crystal grains with volumes of 1–5 cm^3, allowing the fabrication of wafers up to 10 × 10 mm^2.

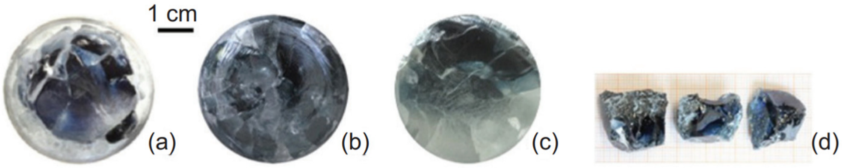

Fig. 4.8. The crystallized states of $ZnGa_2O_4$ (a), $MgGa_2O_4$ (b), and $Zn_{0.5}Mg_{0.5}Ga_2O_4$ (c) within Ir crucibles (40 mm diameter) achieved through the VGF/VB method; single crystal grains of $ZnGa_2O_4$ (d) [101].

4.2.2.6 Czochralski and Kyropoulos-like methods

Scott et al. [148] and Galazka et al. [100] employed the Czochralski method to grow bulk single crystals of $MgGa_2O_4$, $ZnGa_2O_4$, and $CoGa_2O_4$. In each case, high-melting-point inductively heated Ir crucibles were used, surrounded by thermal insulation made of zirconia and alumina. The crucible had a free space above it for the growing crystal. Among these crystals, $MgGa_2O_4$, known for its thermal stability and NIR transparency at room temperature, allowed efficient heat dissipation during crystal growth, ensuring stability and reasonable crystal size.

For $MgGa_2O_4$, Scott et al. [148] utilized a growth furnace with a 38 mm diameter Ir crucible, a 66 mm diameter zirconia crucible lined with zirconia felts, and filled with zirconia powder. The crucible was inductively heated by an RF coil. The growth atmosphere consisted of 1 vol.% O_2 + 99 vol.% N_2. Growth and rotation rates were 12.5–25 mm/h and 20–45 rpm, respectively, resulting in stoichiometric, clear crystals of about 12.5 mm diameter and 19–38 mm length.

Galazka et al. [100, 154] employed a 40 mm diameter Ir crucible heated by an RF coil powered by a 10 or 30 kHz RF generator for growing bulk $MgGa_2O_4$ single crystals. The thermal insulation included zirconia granules, zirconia felts, and low-density alumina. An inductively heated Ir afterheater above the crucible reduced temperature gradients in the pulling zone. The starting composition was typically stoichiometric or with a slight excess of Ga_2O_3. Various growth atmospheres were used, such as CO_2, 20% CO_2 + 80% N_2, and 2–32 vol.% O_2 + Ar. Growth and rotation rates were 1–2 mm/h and 5–10 rpm, respectively, resulting in colorless, clear, and transparent crystals with a diameter and length of about 20 and 20–40 mm, respectively. However, a tendency for foot and spiral formation was observed, especially at low crystallization ratios. The crystals remained electrically insulating and transparent in the NIR spectrum at room temperature, but transparency decreased at high temperatures, accompanied by potential foot/spiral formation, especially when melt viscosity was relatively high.

Fig. 4.9. a) Bulk $MgGa_2O_4$ single crystals obtained through the Czochralski method [153]; b) crystals obtained using the Kyropoulos-like method [100].

While the Czochralski method yielded crystals with a reasonable volume of 6–12 cm^3, the Kyropoulos-like method, a variant of Czochralski, allowed for even larger crystal volumes (**Fig. 4.9**). In this method, the pulling rate was significantly smaller (below 0.5 mm/h), with no crystal rotation and slow crucible cooling at a rate of 2–3 K/h until the entire melt crystallized on the crystal seed. The growth atmosphere consisted of either CO_2 or Ar, producing blue and dark-blue crystals, respectively, whether doped or undoped with Si (0.2 mol.%). The blue coloration resulted from absorption in the red part of the visible spectrum, extending from absorption in the NIR region caused by free carrier absorption, indicating semiconducting behavior. Crystals grown using this technique reached a size of 35 diameter and 20 mm length, with a volume of about 19 cm^3.

Galazka et al. [95,101] also tested the Czochralski method to grow bulk $ZnGa_2O_4$ and $(Zn,Mg)Ga_2O_4$ single crystals. Due to strong incongruent evaporation leading to a rapid composition shift, only short crystals (up to 10 mm) could be obtained. These crystals also exhibited a tendency for foot and spiral formation immediately after seeding due to the unstable melt flow at the surface caused by intense evaporation.

Kramer et al. [149] employed the Czochralski method to grow bulk $CoGa_2O_4$ single crystals from the melt. An inductively heated Ir crucible containing a $CoO–Ga_2O_3$ composition at a molar ratio of 1:1 was used. The growth furnace, surrounded by zirconia thermal insulation, included a zirconia disk with a central opening for the growing crystal and an upper zirconia tube defining a space for the pulled crystal. Growth occurred at either atmospheric pressure or an overpressure of 3.4 bar, with growth and rotation rates of 1–6 mm/h and 20–50 rpm. Atmospheric pressure growth faced challenges such as high evaporation rates and unstable growth due to a concave interface toward the melt, leading to lateral growth and disconnection from the melt (melt-back). Overpressure at 3.4 bar, combined with slower growth and rotation rates, as well as a water-cooled seed holder, minimized evaporation and improved heat transfer, resulting in more stable growth with a flat or slightly convex profile.

4.2.3 ZnSe and (Zn,Be)Se mixed crystals

As per the findings reported by Niiyama and Watanabe [155], II-VI semiconductors hold great promise for various applications, making them a subject of significant research interest. Some notable applications include their potential use in visible radiation sources, as well as in the development of green laser diodes. Additionally, II-VI crystals have shown their versatility in fields such as spintronics [156], solar cells [157], ionizing radiation detection [158], infrared detectors [159], and as substrates [160] for various electronic and optoelectronic devices. In this thesis, we conducted an in-depth investigation into two types of crystals: pure zinc selenide (ZnSe) and mixed (Zn,Be)Se crystals. Zinc selenide is recognized as a semiconducting material with a bandgap of approximately 2.7 eV at room temperature and a density of 5.27 g/cm³. It is important to note that II-VI crystals, in general, are known for their weak ionic-type bonding, which can impact their overall properties.

To address this bonding issue and enhance the crystal structure's stability, we explored the incorporation of beryllium (Be) into the ZnSe host material. This addition results in a transformation of the bonding nature from primarily ionic to more covalent. As a result, the lattice constant is reduced, leading to an increase in the fundamental energy gap. This enhancement in energy gap is highly beneficial for various optoelectronic applications.

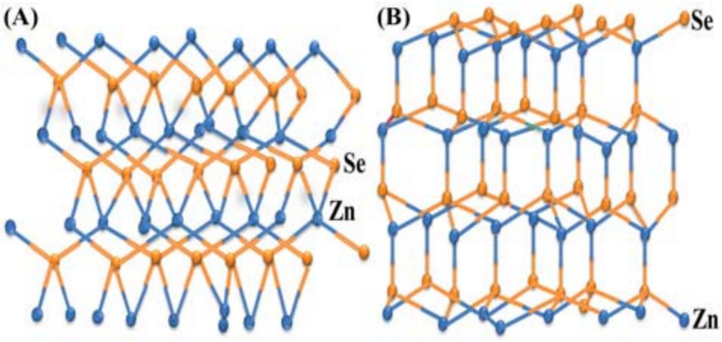

Fig. 4.10. Models of ZnSe crystal structures, featuring (A) the cubic (Zinc blende) and (B) hexagonal (wurtzite) forms [164, 167].

However, the introduction of beryllium also comes with a potential downside. It tends to introduce lattice disorder within the crystal structure. To mitigate this issue and maintain crystal quality, post-growth annealing in a zinc vapor environment is utilized, a method that has proven to be effective. This annealing process aids in reducing the undesirable lattice defects introduced by beryllium incorporation. Furthermore, our research revealed that it is feasible to grow epitaxial thin layers with exceptional quality [161]. Epitaxial growth is a crucial aspect of many semiconductor applications, particularly in the development of advanced electronic devices.

4.2.3.1 Crystal Structure

ZnSe, classified as a binary octet semiconductor, can adopt either a hexagonal (wurtzite) or cubic (zinc blende) crystal structure, as illustrated in **Fig. 4.10**. The material properties may vary based on the physical state (e.g. film or bulk), while the specific structure of ZnSe is primarily influenced by the chosen synthesis method [163, 164].

Distinguishing characteristics between the wurtzite and zinc blende structures involve either the relative handedness of the fourth interatomic bond or differences in dihedral conformation, resulting in distinct lattice parameters [164]. In the zinc blende structure, selenide atoms arrange in a cubic symmetry, with zinc atoms occupying half of the tetrahedral holes. On the other hand, in the wurtzite structure, despite its hexagonal crystal symmetry, the atom connectivity resembles the cubic structure, specifically tetrahedral [163, 164].

For the zinc blende structure, lattice parameters are a = b = c = 5.68 Å, with the space group F4-3m. In contrast, the wurtzite structure has lattice parameters a = b = 3.996 Å and c = 6.55 Å, with the space group P63mc. The cubic phase of ZnSe is more thermodynamically stable at room temperature, transitioning to the wurtzite structure upon annealing at higher temperatures [165, 166]. Coexistence of both structures (wurtzite-blende) has also been reported, attributed to the relatively low.

4.2.3.2 Growth

At the Institute of Physics, Nicolaus Copernicus University in Torun, single crystals of zinc beryllium selenide (Zn, Be)Se are grown using the high-pressure, high-temperature vertical Bridgman method (**Fig. 4.11**). This process utilizes high-purity ZnSe (6N) and Be (99.98%) powders as starting materials. For this thesis, we have two series of crystals: the first series includes pure ZnSe crystals and (Zn, Be)Se crystals with 10% Be ($Zn_{0.90}Be_{0.1}Se$). The second series consists of four types of crystals successfully produced by the author under the scientific guidance of Prof. Karol Strzałkowski: (Zn, Be)Se with 2% Be ($Zn_{0.98}Be_{0.02}Se$), (Zn, Be)Se with approximately 5% Be ($Zn_{0.95}Be_{0.05}Se$), (Zn, Be)Se with 10% Be ($Zn_{0.90}Be_{0.1}Se$), and (Zn, Be)Se with 20% Be ($Zn_{0.80}Be_{0.2}Se$),. The growth procedure involved placing the graphite crucible containing the powders into the hot zone of the growth chamber, which was evacuated and filled with argon up to 100 atm. The temperature was meticulously controlled to approximately 1850 K, with stabilization achieved within 0.1 K.

Following a few hours of powder melting, the crucible was gradually pulled out at a rate of 2.4 mm/h, resulting in crystal rods measuring 5-6 cm in length and 1 cm in diameter. Samples of about 1.5 mm thickness were then cut from the rods using a wire saw and prepared accordingly. Some cut plates underwent polishing, while others were subjected to annealing in a closed quartz ampoule with a zinc atmosphere for 24 hours at 1350 K. X-ray diffraction analysis, applying Vegard's law, verified the composition of the ternary compounds (Zn,Be)Se, with the confirmation of the presence of the zinc blende phase in the grown ternary alloy. Additional details about the growth process can be found in reference [168].

Fig. 4.11. Picture of the vertical Bridgeman equipment employed at Nicolaus Copernicus University in Toruń.

4.3 Measurement techniques

At the Institute of Physics, Nicolaus Copernicus University in Toruń, the measurements have been carried out using experimental setups of the Scintillator and Phosphor Materials Spectroscopy Group led by Prof. Winicjusz Drozdowski. Besides, an alternative technique has been applied at the National Centre for Nuclear Research in Świerk-Otwock close to Warsaw.

4.3.1 Pulse height spectra

The gamma spectroscopy measurement system can be categorized into two distinct subsystems, both featuring the common components of the Tukan multichannel 8K analyzer [169] and the ^{137}Cs gamma radiation source. **Fig. 4.12** displays an actual photograph of the system specifically designed for conducting pulse height spectra (PHS) measurements.

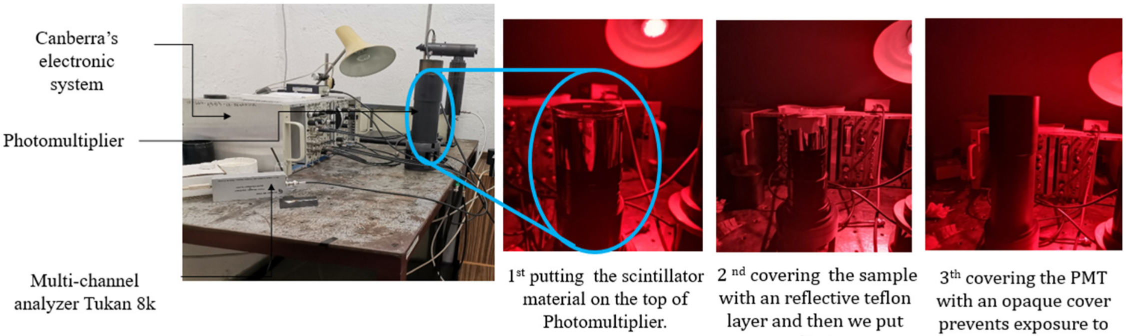

1st putting the scintillator material on the top of Photomultiplier.

2 nd covering the sample with an reflective teflon layer and then we put radiation ^{137}Cs source on it.

3th covering the PMT with an opaque cover prevents exposure to external light.

Fig. 4.12. Representation of the system for pulse height spectra measurements.

The measurement system consists of various components, each serving a specific function:

- A Hamamatsu R878 photomultiplier (PMT) detects photons emitted by the tested crystal;
- A preamplifier (Preamp) performs initial signal amplification and inversion from the photomultiplier anode;
- An amplifier (Amp) provides final signal amplification and gating, allowing for the adjustment of integration time (shaping time); the choice of integration time (0.5 to 12 µs) facilitates the registration of spectra with decay components of desired durations;
- A Tukan 8K multichannel analyzer processes incoming signals into computer-friendly data, and accompanying measurement software is installed on the computer;
- A computer equipped with software records and processes the results.

With this configured measurement system, pulse height spectra of solid materials can be recorded. After absorbing incident ionizing radiation, the excited sample tends to release accumulated excess energy, commonly in the form of light emission (luminescence). The recorded signal produces a pulse height spectrum, illustrated in **Fig. 4.13**. For a comprehensive representation of the pulse height spectrum, the measurement result for the (Zn,Be)Se crystal is provided, as not all characteristic peaks are present in the samples studied in this doctoral thesis, including the backscattering peak.

To fully understand pulse height spectrum measurements, analyzing the spectrum itself is essential. Starting from the left, a peak indicates the emission of radiation by the excited sample. Further along, a distinct backscatter peak appears. There is also a full energy peak observed, which typically occurs around channel 1500, representing the complete energy of the incoming radiation. Additionally, the Compton edge can be seen, marking the maximum energy transferred to the electrons during scattering. This phenomenon occurs when some gamma quanta reflect off the surrounding material, return to the sample, and induce excitation. The signals from these events are recorded in the pulse height spectrum, including the backscatter peak and the features related to Compton scattering.

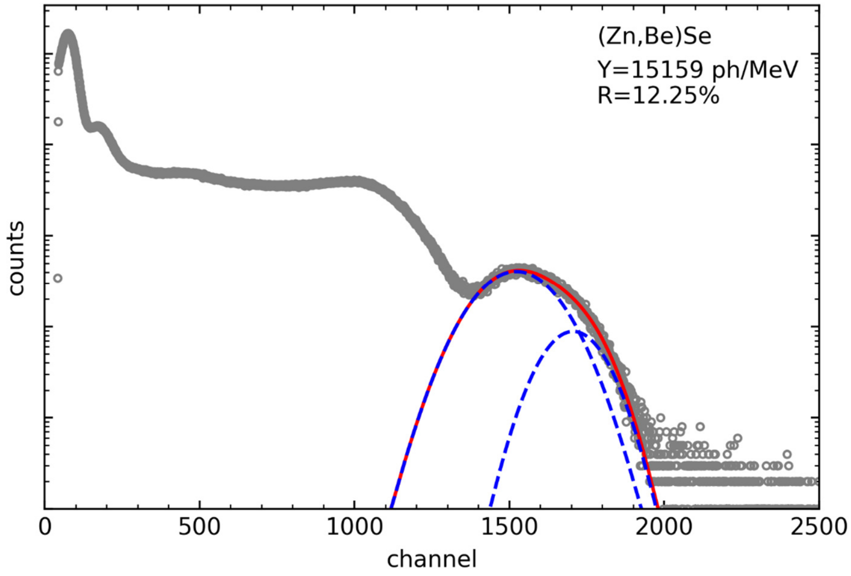

Fig. 4.13. A pulse height spectrum of the (Zn,Be)Se crystal measured at Nicolaus Copernicus University.

The last and arguably most significant peak from the scintillator's perspective is the full energy peak (FEP). This peak corresponds to the emission of photons with energy equal to the excitation energy, which is 662 keV for excitations using the ^{137}Cs isotope (utilized by the author of the thesis). Analyzing the full energy peak yields valuable information about the tested sample.

The key parameters characterizing each scintillator include energy resolution (R) and scintillation light yield (LY). These crucial metrics can be determined by appropriately adjusting the parameters of a shape function, such as a Gaussian function, to accurately replicate the recorded peak (fitting in Fig. 4.4). The pivotal parameters for estimation are the peak position and its full width at half maximum (FWHM). These quantities play a vital role in assessing the scintillation light yield and energy resolution [170], directly influencing the suitability of the studied crystal for scintillation applications.

$$\mathrm{Y_{phe}} = \frac{\mathrm{PP \cdot G_{SPP}}}{\mathrm{SPP \cdot G_{PP} \cdot E_{exc}}} \tag{4.1}$$

$$\mathrm{LY} = \mathrm{Y_{phe}} \cdot \frac{1-\mathrm{R_{eff}}}{0.98 \cdot \mathrm{Q_{eff}}} \tag{4.2}$$

$$\mathrm{R} = \frac{\mathrm{FWHM}}{\mathrm{PP}} \cdot 100 \tag{4.3}$$

In these equations:

- $\mathrm{Y_{phe}}$ and LY represent scintillation light yield in photoelectrons and photons per 1 MeV, respectively,
- PP is the position of the full energy peak maximum,
- SPP is the position of the peak for single photoelectron measurements,

- G_{PP} and G_{SPP} are the respective instrumental gains used in scintillation light yield and single photoelectron measurements,
- E_{exc} is the energy of the gamma radiation used for the measurement expressed in MeV,
- R_{eff} and Q_{eff} are the effective reflection coefficient on the photomultiplier photocathode and the photomultiplier's effective quantum efficiency, respectively,
- In the case of the energy resolution formula, FWHM is the full width at half maximum of the full energy peak.

The scintillation light yield Y_{phe} provides insights into the number of photons emitted from the tested sample due to the absorption of a 1 MeV ionizing radiation quantum. This value is intricately tied to the measurement system used. To ensure accurate comparisons across different detectors, knowledge of the quantum efficiency curve of the photomultiplier employed is crucial. This allows the conversion of the determined scintillation light yield value to the number of photons emitted by the crystal (photons per megaelectronvolt).

Conversely, energy resolution (expressed as a percentage) is a parameter indicating the tested crystal's ability to differentiate close excitation energies. As indicated by formula 4.3, achieving small values of energy resolution is contingent on narrow full energy peaks (small FWHM values) situated in as distant channels as possible (**Fig. 4.13**).

4.3.2 Temperature dependence of the light yield

A parallel trend to what has been observed for radioluminescence spectra in Toruń has been anticipated for scintillation yield. The opportunity to delve into this phenomenon arose with the implementation of a new experimental configuration, initiated by the Radiation Detectors and Plasma Diagnostics Division at the National Centre for Nuclear Research (NCBJ) in Świerk by Prof. Łukasz Świderski. For recording pulse height at various temperatures ranging from 80 K (using LN_2) to 320 K, a custom-designed cryostat was constructed (**Fig. 4.14**). The scintillation light was collected using a Hamamatsu S13360-6050PE silicon photomultiplier (SiPM) with an area of 6 x 6 mm² and a pixel size of 50 x 50 µm². The sample, with all surfaces covered in Teflon tape except the one facing the SiPM, was mounted on a copper frame inside the cryostat.

Initially, the experimental setup was verified at room temperature using analog electronics for signal processing. As the SiPM's response slows down substantially at low temperatures compared to room temperature, the SiPM was placed on a separate copper frame connected to the outer housing to maintain its temperature close to RT. The distance between the sample surface and the SiPM was approximately 1.5 mm at room temperature. Two voltage regulators were attached to the copper holder to serve as heaters for temperature control. A Keysight B2901A power supply was used for breakdown voltage measurements and MPPC biasing. The signal from the photodetector was preamplified using CR-113 and shaped with an Ortec 672 spectroscopy amplifier before being analyzed by the TUKAN-8K-USB MCA.

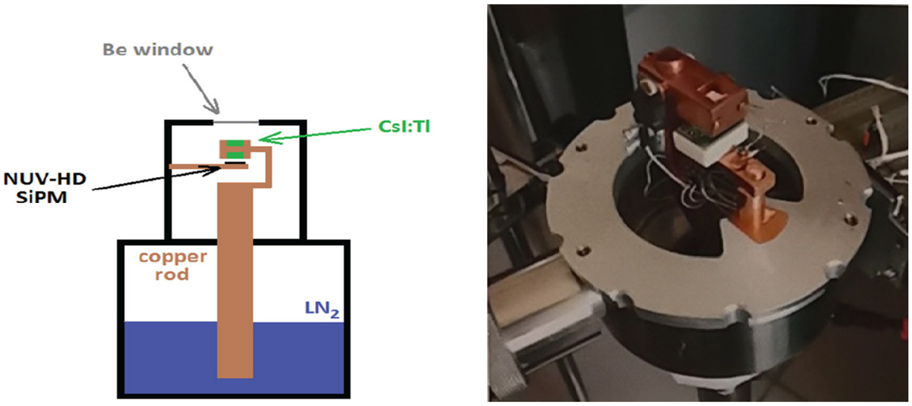

Fig. 4.14. A schematic representation and a photograph of the experimental setup utilized at NCBJ.

4.3.3 Scintillation time profiles

An alternative system utilized in gamma spectroscopy is specifically designed for the measurement of scintillation time profiles (STP). This system is somewhat similar to the PHS setup, but features a distinct cable arrangement and utilizes two photomultiplier tubes (PMTs) instead of one. The notion of capturing STP spectra through the delayed-coincidence method with the assistance of this measurement system was originally introduced by Bollinger and Thomas in 1961 [171].

The measurement system comprises the following components, each accompanied by a brief explanation:

- Two photomultipliers (PMT 1: Hamamatsu R1104 and PMT 2: Hamamatsu R928), employed to register signals identified as START (PMT 1) and STOP (PMT 2);
- Two discriminators (Discr. 1 and Discr. 2) tasked with distinguishing the start and stop signals; to accurately measure the time profile of scintillation in the tested sample, it is crucial to set appropriate discrimination thresholds for both signals; incorrect settings may lead to distorted recorded spectra, marked by the appearance of an additional peak referred to as an "afterpulse" [172]; maintaining a START to STOP signal intensity ratio of approximately 100:1 is essential;
- Time-to-Amplitude Converter (TAC), which, upon the arrival of the START signal, triggers a linearly increasing voltage generator as a function of time; upon the arrival of the STOP signal, the TAC measures this voltage using a multichannel analyzer;
- Delay line, facilitating the acquisition of the necessary delay between the START and STOP signals in the TAC; in the utilized measurement system at the IF UMK, a 30-meter delay line was implemented, resulting in a delay of approximately 472 ns.

The system also integrates a Tukan 8K multichannel analyzer and a computer employed for the conversion, registration, and analysis of scintillation time profile spectra.

With this configuration, it becomes feasible to measure scintillation time profile spectra characterized by multi-exponential decays. Properly adjusting discrimination thresholds for the START and STOP signals, while maintaining their ratio at around 100:1, is crucial to preventing scenarios where another START signal is recorded before the arrival of the STOP signal during the rising voltage on the TAC. Such misalignment could distort the recorded spectrum. **Fig. 4.15** illustrates an example of a correctly recorded scintillation time profile spectrum for the β-Ga_2O_3 crystal.

A comprehensive analysis of the collected data offers valuable insights into the scintillation time profile of the tested sample. One set of parameters, obtainable through fitting a function - comprising several exponential decays - to the measurement data, includes individual time constants denoted as τ_i, for each exponential decay function. Utilizing the relationship that the area under an exponential curve approximates the product of the amplitude (A_i) and the corresponding exponential of the time constant (τ_i) [173], it becomes straightforward to determine the percentage contribution of each component in the overall decay, as we will see the following chapter.

$$\int_0^{\infty} A_i \exp\left(-x/\tau_i\right) dx = -A_i\tau_i \exp\left(-x/\tau_i\right)\Big|_0^{\infty} = A_i\tau_i \tag{4.4}$$

Knowing the contributions of individual components in the total decay allows for an assessment of whether a particular component significantly influences the recorded STP spectrum. Components with contributions less than 1% can be considered insignificant, as even if their corresponding τ_i values are relatively short, their contribution to the overall recorded spectrum is negligible.

The final parameter obtainable through the analysis of STP spectra, simplifying the comparison of multi-exponential decays [174], is the mean decay time (τ_m), defined as:

$$\tau_m = \frac{\sum_{i=1}^{N} A_i\tau_i^2}{\sum_{i=1}^{N} A_i\tau_i} = C_i\tau_i \tag{4.5}$$

Here, C_i represents the contribution of the i-th component. The mean decay time, as defined, indicates the time after which the radiation emitted by the excited crystal will lose approximately 1/e ≈ 0.37 of its initial intensity.

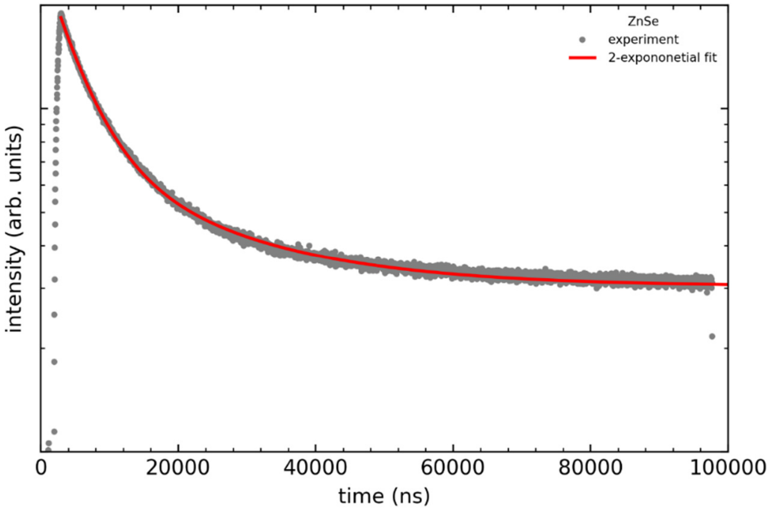

Fig. 4.15. An example of a scintillation time profile for ZnSe measured at Nicolaus Copernicus University.

4.3.4 Radio- and thermoluminescence research setup

In both of the previously mentioned experiments (PHS and STP), the luminescence signal from the tested sample directly reaches the photomultiplier's photocathode, leading to the collection of quantitative rather than qualitative information about the recorded signal. To gain qualitative insights, luminescence measurements are conducted concerning the wavelength of emitted radiation, employing various non-ionizing forms of excitation. One technique suitable for this purpose is the measurement of radioluminescence spectra (RL), which entails luminescence observed when the tested crystal is excited by X-ray radiation.

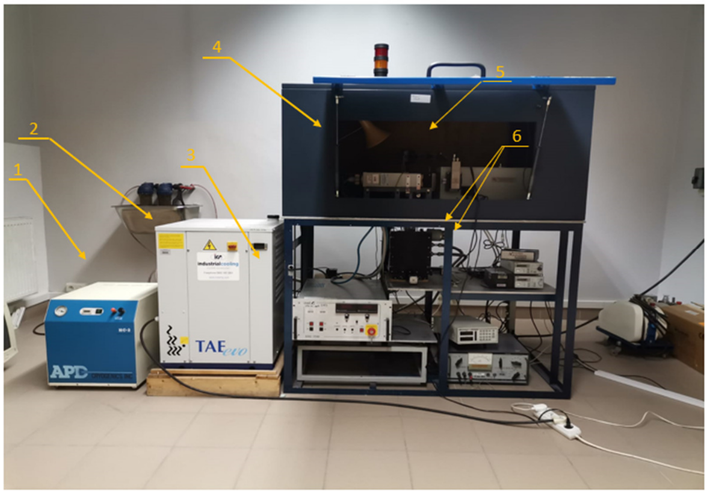

1-Helium coller
2-Water supply
3-X-ray lamp power supply system
4-X-ray lamp
5-Monochromator
6-Power supplies

Fig. 4.16. Configuration of conducting measurements of radio- and thermoluminescence spectra.

Radioluminescence setup is illustrated in **Fig. 4.16**, featuring the following components:

- High voltage generator (Inel XRG3500 - HV generator) utilized to generate the voltage necessary for the proper operation of the X-ray tube; standard voltage and current values employed during measurements are indicated on the diagram (45 kV and 10 mA);
- X-ray tube with a copper anode (X-ray tube) employed for the generation of X-ray radiation;
- Temperature control system in the cryostat (cryostat chamber with He cooling) utilizing a closed-cycle helium cooler (APD Cryogenics Inc.); RL measurements can be conducted in the temperature range from 10 to 350 K; temperature control within the cryostat is achieved using a specialized controller (LakeShore 330);
- Double-convex lens with a focal length of 25 mm used to focus the radiation emitted by the sample directly on the input slit of the monochromator;
- Acton SpectraPro 500i monochromator (ARC SP500i) facilitating the measurement of luminescence as a function of the wavelength of incident radiation; this is made possible by the use of diffraction gratings with a density of 1200 grooves per millimeter: a holographic ultraviolet (HUV) grating with an optimal working range of 190-400 nm and a 500 nm blazed grating with an optimal working range of 400-800 nm;
- Photomultiplier (PMT - Hamamatsu R928) employed for detecting the incident radiation;
- Microprocessor-based data acquisition system for the photomultiplier (Acton Spectra Hub);
- Computer with suitable software used for recording and processing the recorded radioluminescence spectra.

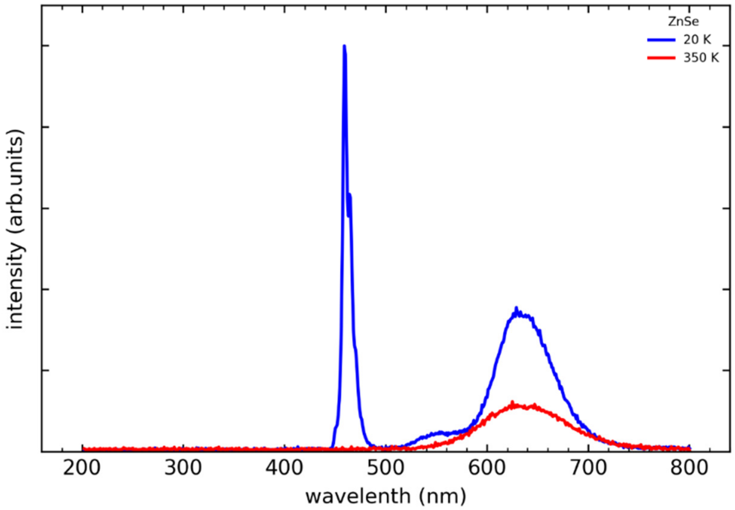

Fig. 4.17. Exemplary radioluminescence spectra of ZnSe measured at Nicolaus Copernicus University.

Radioluminescence measurements enable the observation of radiative and non-radiative transitions in the studied material, facilitating a more precise characterization of electronic levels within the forbidden energy band. An example of radioluminescence spectra of ZnSe are presented in **Fig. 4.17**. The measurement setup depicted in **Fig. 5.16** not only facilitates radioluminescence (RL) spectrum measurements, but can be employed for thermoluminescence (TL) measurements as well. In contrast to RL spectra, where luminescence spectra are measured as a function of the wavelength of emitted radiation at each given temperature, TL measurements follow a step-by-step procedure:

1. Heating the crystal to 350 K - this process empties charge traps that could distort the TL spectrum.
2. Cooling the crystal to 10 K.
3. Measuring background for 2 minutes.
4. Exposing the sample to X-ray radiation for 10 minutes; the monochromator slits are adjusted to ensure that the signal from stationary radioluminescence does not saturate the detector.
5. Measuring afterglow for 48 minutes: After turning off the X-ray lamp, the sample relaxes, and the recorded signal on the photomultiplier aligns with the background level measured before exposure. The observed decay of the crystal's luminescence occurs in a multi-exponential manner, known as afterglow. If the sample were heated immediately after exposure, the recorded thermoluminescence peaks would be on the decaying exponential slope, complicating or even preventing accurate fitting to obtain comprehensive information about charge traps in the studied crystal.
6. Heating the sample to a maximum temperature of 350 K with a heating rate of 9 K/min.

An example of a thermoluminescence measurement result for (Zn,Be)Se is presented in **Fig. 5.18**.

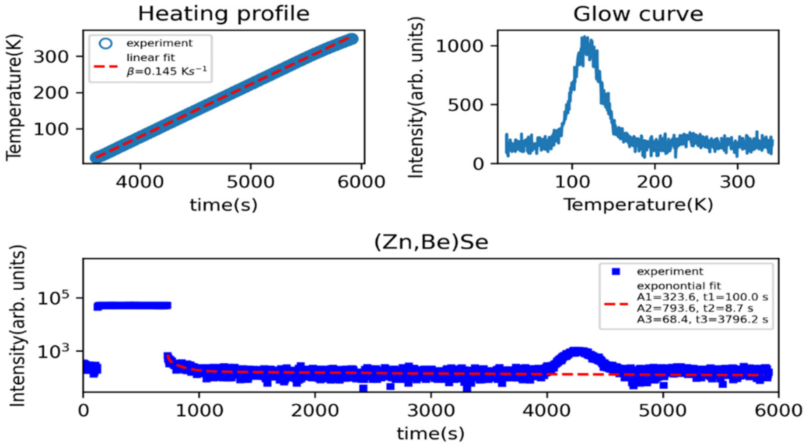

Fig. 4.18. An example of a thermoluminescence measurement for (Zn,Be)Se performed at Nicolaus Copernicus University.

4.3.5 Absorbance and transmittance spectroscopy technique

Spectrophotometry involves quantifying the light absorption of a chemical substance by measuring light intensity as it passes through a sample solution. Its fundamental principle lies in the fact that every compound absorbs or transmits light within specific wavelength ranges. This technique is not only capable of determining the concentration of known substances, but also finds extensive utility in quantitative analysis across diverse domains including chemistry, physics, biochemistry, material and chemical engineering, as well as clinical applications.

Every chemical compound interacts with light (electromagnetic radiation) in a specific manner across a range of wavelengths, either by absorbing, transmitting, or reflecting it. Spectrophotometry serves as a method for quantifying the extent to which a chemical substance absorbs or transmits light. Widely employed across various fields including chemistry, physics, biology, biochemistry, material and chemical engineering, clinical applications, industrial sectors, and more, spectrophotometry finds utility in any domain involving chemical substances or materials. For instance, in biochemistry, it aids in discerning enzyme-catalyzed reactions, while in clinical settings, it facilitates the examination of blood or tissues for diagnostic purposes. Additionally, spectrophotometry encompasses several variations such as atomic absorption spectrophotometry and atomic emission spectrophotometry.

A spectrophotometer is a device utilized to gauge the quantity of photons, or the intensity of light, absorbed once it traverses a sample solution. Through this instrument, the concentration of a known chemical substance can be ascertained by assessing the intensity of the detected light. This apparatus can be categorized into two distinct types based on the wavelength range of the light source:

- UV-visible spectrophotometer: uses light over the ultraviolet range (185-400 nm) and visible range (400-700 nm) of the electromagnetic radiation spectrum;
- IR spectrophotometer: uses light over the infrared range (700-1500 nm) of the electromagnetic radiation spectrum.

In visible spectrophotometry, the absorption or transmission of a substance can be deduced from its observed color. For example, a solution sample that absorbs light across the entire visible spectrum (i.e., transmitting none of the visible wavelengths) theoretically appears black. Conversely, if the sample transmits all visible wavelengths (i.e. absorbs none), it appears white. When a solution absorbs red light (~700 nm), it manifests as green because green is the complementary color of red. Visible spectrophotometers typically employ prisms to isolate specific ranges of wavelengths, effectively filtering out other wavelengths, allowing a particular beam of light to pass through the solution sample.

4.3.5.1 Devices and mechanism

Fig. 5.19 depicts the fundamental setup of spectrophotometers, which includes components such as a light source, a collimator, a monochromator, a wavelength selector, a sample cuvette, a photoelectric detector, and a digital display or meter. A detailed explanation of the mechanism is provided below. **Fig. 5.21** presents an example of a spectrophotometer (model: Spectronic 20D).

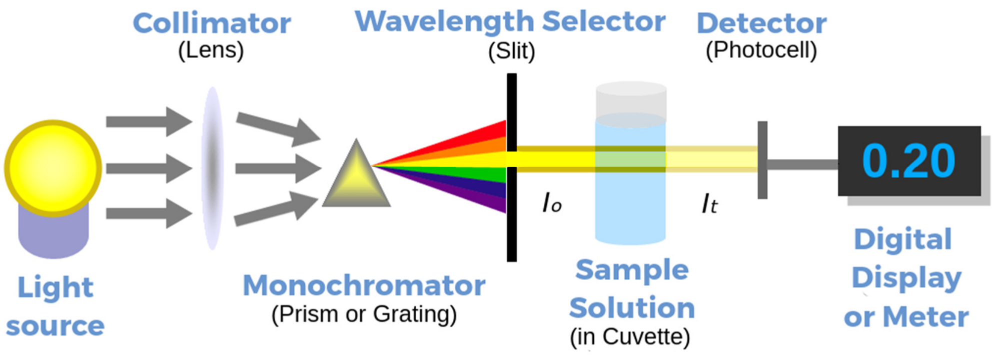

Fig. 4.19. A fundamental configuration of spectrophotometers.

In broad terms, a spectrophotometer comprises two main devices: a spectrometer and a photometer. The spectrometer is responsible for generating, often dispersing, and measuring light, while the photometer serves as a photoelectric detector that quantifies the intensity of light.

- Spectrometer: It produces a desired range of wavelengths of light. First, a collimator (lens) transmits a straight beam of light (photons) that passes through a monochromator (prism) to split it into several component wavelengths (spectrum). Then a wavelength selector (slit) transmits only the desired wavelengths, as shown in **Fig. 4.19**.
- Photometer: After the desired range of wavelength of light passes through the solution of a sample in a cuvette, the photometer detects the amount of photons that are absorbed and then sends a signal to a galvanometer or a digital display, as illustrated in **Fig. 4.19**.

Referring back to **Fig. 4.19** (and **Fig. 4.20**), the quantity of photons passing through the cuvette and reaching the detector relies on the length of the cuvette and the concentration of the sample. Once the light intensity post-cuvette passage is determined, it can be correlated with transmittance (Tt). Transmittance represents the fraction of light that successfully traverses the sample and can be calculated using the equation:

$$\mathrm{Tt} = \frac{\mathrm{I_t}}{\mathrm{I_0}} \tag{4.6}$$

where I_t is the light intensity after the beam of light passes through the cuvette/sample, and I_0 is the light intensity before the beam of light passes through the cuvette. Transmittance is interconnected with absorption through the expression:

$$\mathrm{A} = -\log(\mathrm{Tt}) = -\log\left(\frac{\mathrm{I_t}}{\mathrm{I_0}}\right) \tag{4.7}$$

where absorbance (A) represents the quantity of photons absorbed. Given the absorbance value obtained from the previous equation, the unknown concentration of the sample can be determined using the Beer-Lambert Law. **Fig. 4.20** illustrates the transmittance of light through a sample, with the length l utilized in the Beer-Lambert Law described below.

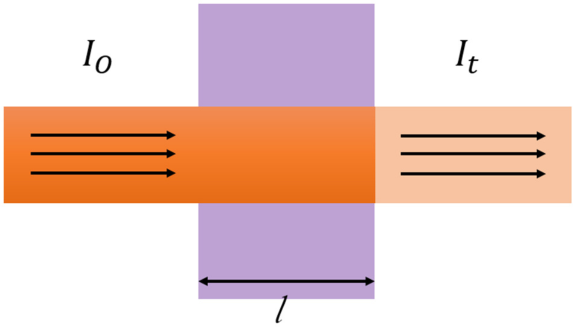

Fig. 4.20. A schematic representation of the transmittance diagram.

- **Beer Law**

The Beer-Lambert Law (also known as the Beer's Law) states that there is a linear relationship between the absorbance and the concentration of a sample. For this reason, the Beer's Law can only be applied when there is a linear relationship. It is written as:

$$A = \epsilon l c \tag{4.8}$$

where A is the measure of absorbance (no units), ϵ is the molar extinction coefficient or molar absorptivity (or absorption coefficient), l is the path length, and c is the concentration.

The molar extinction coefficient, denoted as ϵ, is a constant that varies for each molecule. As absorbance is unitless, the units for ϵ must offset the units of length and concentration. Therefore, ϵ is expressed in units of $L \cdot mol^{-1} \cdot cm^{-1}$. The path length, denoted as l, is typically measured in centimeters. In standard spectrometers, a cuvette with a width of 1 cm is commonly used, so l is assumed to be 1 cm. With absorption, ϵ, and path length known, the concentration (c) of the sample can be calculated.

In case of the studies reported in this dissertation, the crystals underwent thorough analysis using a UV-Vis spectrophotometer (model 200 PLUS, manufactured by SPECORD-Analytik Jena AG), enabling precise measurement of absorbance across a wide spectral range from 300 to 800 nm. Renowned for its accuracy and sensitivity in detecting subtle changes in light absorption, this instrument provided valuable insights into the optical properties and energy transitions within the investigated crystals. **Fig. 4.21** displays the absorbance spectrum of (Zn,Be)Se containing 10% Be across the wavelength range of 200 to 1100 nm, along with the experimental setup employed.

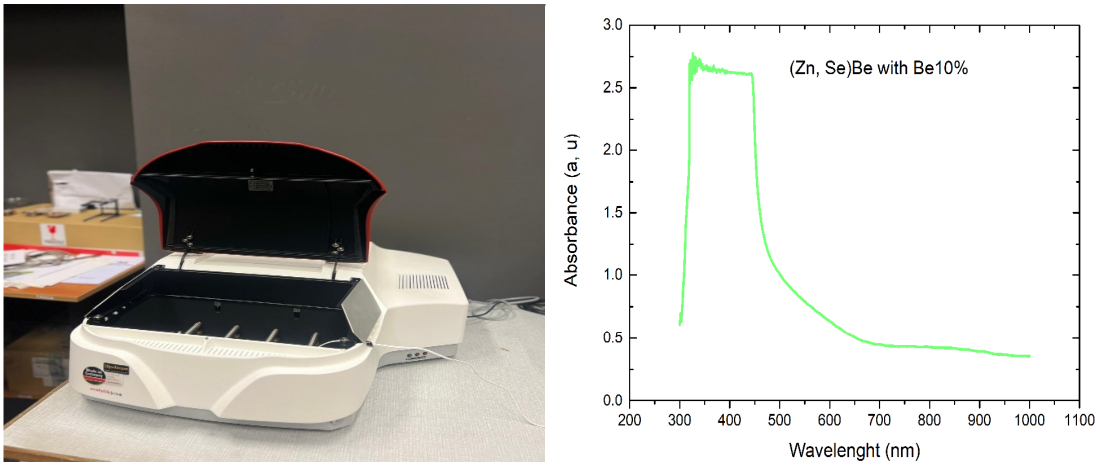

Fig. 4.21. The setup of spectroscopy absorption, featuring a plot depicting the absorption of (Zn, Be)Se with a 10% concentration of Be.

4.3.6 Photopyroelectric technique PPE

The photopyroelectric technique (PPE), employed in both back (BPPE) and front (FPPE) configurations, was utilized for thermal examination of the samples [175]. This technique, known for its simplicity, sensitivity, and non-destructive nature [176], enables the determination of thermal diffusivity and effusivity in the back and front configurations, respectively. Subsequently, thermal conductivity can be easily calculated. The study presented and discussed the impact of composition on the thermal properties of specific crystals. Additionally, the composition-dependent thermal resistivity of semiconducting alloys was analyzed using the Adachi model.

4.3.6.1 Experimental setup

For thermal investigations, the photopyroelectric calorimetry method was employed using various experimental configurations. The experimental setup comprised a 0.5 mm pyroelectric detector made of $LiTaO_3$ coated with thin layers of Cr and Au on both surfaces, an electronically modulated 300 mW power blue diode laser (Omicron, $\lambda = 405$ nm), and a two-phase lock-in amplifier SR850. The faces of the pyroelectric sensors were coated with opaque electrodes to absorb the incident light. Modulation of the incident radiation was achieved using the reference signal provided by the lock-in's internal oscillator. An optically opaque sample was placed on the sensor (refer to **Fig. 4.22**). The sample was directly excited by the laser in the back detection configuration, with the sensor detecting the heat generated as it propagated through the plate. In this setup, the back configuration facilitated the determination of the specimen's thermal diffusivity, while in the front configuration, the sensor was directly exposed to laser radiation, and the specimen dissipated the heat. In this case, the measurement delivered the value of thermal effusivity. A small amount of ethylene glycol was a coupling liquid for excellent thermal contact between the pyro and the sample. The excitation light was modulation in the frequency range of 1 to 15 Hz and 5 to 45 Hz for the back and front modes, respectively. A normalizing procedure using an empty sensor was used for both BPPE and FPPE configurations [177]. The investigated samples' thermal characterization was computer-controlled and performed at ambient temperature.

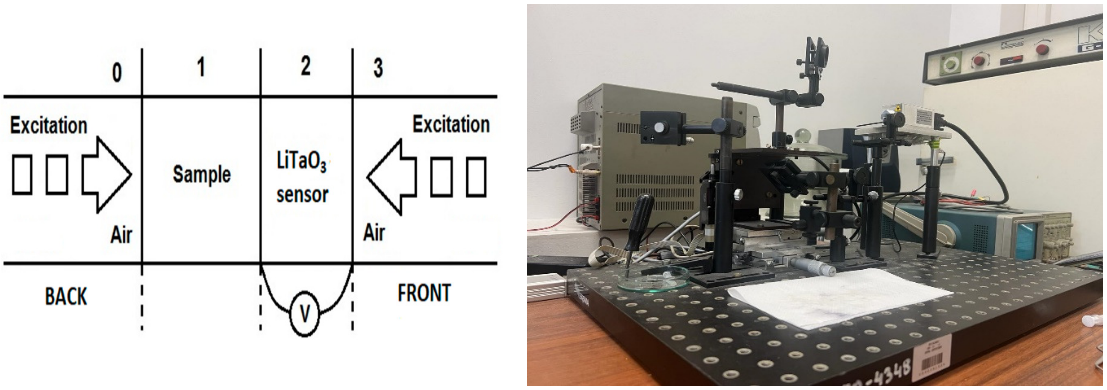

Fig. 4.22. Back and front PPE detection configuration.

The typical photoluminescence setup employed in the study included two lasers: a He-Cd laser emitting at 325 nm with a power of 30 mW, or a 405 nm diode laser (Omicron) capable of delivering up to 300 mW output power. Other components comprised a spectrometer (MicroHR Horiba Jobin Yvon), a helium cryostat (Advanced Research Systems), and a temperature controller (LakeShore 331). Additionally, a filter wheel thermoelectrically cooled CCD camera (Synapse Horiba Jobin Yvon) with a resolution of 1024 × 256 pixels, and diffraction gratings (1200 or 2400 lines/mm) were integrated into the spectrometer. All measurements were performed within a temperature range spanning from 9 K to room temperature. The spectral resolution of the described setup for a single step was 0.14 nm.

4.3.6.2 Basic Theory of PPE

The photothermal techniques relied on inducing a temperature field in the specimen through the absorption of electromagnetic radiation, with this process contingent upon the sample's optical and thermal properties. The photopyroelectric method, utilizing the phase-lag technique, was capable of determining the thermal diffusivity [177,178]. The normalized phase Q_n is described as a function of modulation frequency (f) under the assumption of one-dimensional heat transport through the sample and ideal thermal contact between the specimen and the pyro:

$$\Theta_n = \Theta_0 - L_s \left(\frac{\pi f}{\alpha_s}\right)^2 \qquad (4.9)$$

where Ls are the thermal diffusivity and the thickness of the sample. The thermal diffusivity of the specimen can be determined from the slope a of the phase-frequency graph using the following formula [177,178]:

$$\alpha_s = \frac{L_s^2 \pi}{a^2} \qquad (4.10)$$

The thermal effusivity of the specimen can be measured in the FPPE configuration. In this case, the definition of the expression for the normalized phase is [177,178]:

$$\Theta_n = \arctan \frac{(1+R_{sp})e^{-a_p L_p} \sin(a_p L_p)}{1-(1+R_{sp})e^{-a_p L_p} \cos(a_p L_p)} \tag{4.11}$$

Here, e represents the thermal effusivity, where s denotes the sample and p signifies the sensor. and $b_{sp} = e_s/e_p$, $R_{sp} = (b_{sp} - 1)/(b_{sp} + 1)$ is the thermal wave reflection coefficient at the sample/pyro contact, L_p is the thickness of the sensor, a_p is the reciprocal of the thermal diffusion length μ_p where $a_p = 1/\mu_p$, $\mu_p = (2\alpha_p/\omega)^{1/2}$, and w is the angular modulation frequency.

All thermal parameters were interrelated. The following formula can be taken to determine the thermal conductivity k of the specimen [177]:

$$k = e\alpha^{1/2} \tag{4.12}$$

References (chapter 4)

[1] P. W. Bridgman, “Certain Physical Properties of Single Crystals of Tungsten, Antimony, Bismuth, Tellurium, Cadmium, Zinc, and Tin”, Proceedings of the American Academy of Arts and Sciences, vol. 60, no. 6, p. 305, 1925

[2] D. C. Stockbarger, “ The Production of Large Single Crystals of Lithium Fluoride”, Review of scientific instruments, vol. 7, p. 133, 1936

[3] W. D. Lawson, S. Nielsen, “Preparation of Single Crystals”, Butterworths Scientific Publications, vol. 73, p. 480, 1961

[4] H. E. Buckley, “Crystal Growth”, John Wiley & Sons Inc., vol. 77, p. 73, 1951

[5] D. Schulz, S. Ganschow, D. Klimm, K. Struve, “Growth of Oxide Compounds under Dynamic Atmosphere Composition”, Journal of Crystals Growth, vol. 310, p. 1832, 2008

[6] D. Klimm, S. Ganschow, D. Schulz, R. Fornari, “Reactive Atmospheres for Oxide Crystal Growth”, Journal of Crystal Growth, vol. 310, p. 3009, 2008

[7] D. Schulz, S. Ganschow, D. Klimm, “Application of predominance diagrams in melt growth of oxides”, Materials Research Society Symposium, vol. 43, p. 1201, 2010

[8] K. Jacobs, D. Schulz, D. Klimm, S. Ganschow, “ Melt growth of ZnO bulk crystals in Ir crucibles”, Solid State Sciences, vol. 12, p. 307, 2010

[9] R. Fornari, S. Ganschow, D. Klimm, M. Neubert, D. Schulz, “Growth of Oxide Compounds under Dynamic Atmosphere Composition”, Journal of Crystal Growth, vol. 311, p. 534, 2009

[10] Z. Galazka, R. Uecker, D. Klimm, M. Bickermann, “Method for growing beta phase of gallium oxide (β-Ga_2O_3) single crystals from the melt contained within a metal crucible”, WO/2016/110385, 2015

[11] K. Hoshikawa, E. Ohba, T. Kobayashi, J. Yanagisawa, C. Miyagawa, Y. Nakamura, “ Growth of β-Ga_2O_3 single crystals using vertical Bridgman method in ambient air”, Journal of Crystal Growth, vol. 447, p. 36, 2016

[12] Z. Galazka, R. Uecker, K. Irmscher, D. Klimm, R. Bertram, A. Kwasniewski, M. Naumann, R. Schewski, M. Pietsch, U. Juda, A. Fiedler, M. Albrecht, S. Ganschow, T. Markurt, C. Guguschev, M. Bickermann, “Melt growth and properties of bulk $BaSnO_3$ single crystals”, Journal of Physics: Condensed Matter, vol. 29, p. 075701, 2017

[13] Z. Galazka, D. Klimm, K. Irmscher, R. Uecker, M. Pietsch, R. Bertram, M. Naumann, M. Albrecht, A. Kwasniewski, R. Schewski, M. Bickermann, “Scaling-Up of Bulk β-Ga_2O_3 Single Crystals by the Czochralski Method”, ECS Journal of Solid State Science and Technology, vol. 212, p.1455, 2014

[14] Z. Galazka, S. Ganschow, R. Schewski, K. Irmscher, D. Klimm, A. Kwasniewski, M. Pietsch, A. Fiedler, I. Schulze-Jonack, M. Albrecht, T. Schröder, M. Bickermann, “Two inch diameter, highly conducting bulk β-Ga_2O_3 single crystals grown by the Czochralski method”, Applied Physics Letters, vol. 7, p. 152101, 2022

[15] T. Yanagida, G. Okada, T. Kato, D. Nakauchi, and S. Yanagida, “Fast and high light yield scintillation in the Ga_2O_3 semiconductor material”, Applied Physics Express, vol. 9, p. 042601, 2016

[16] M. Makowski, W. Drozdowski, M. E. Witkowski, A. J. Wojtowicz, K. Irmscher, R. Schewski, and Z. Galazka, "Tailoring the scintillation properties of β-Ga_2O_3 by doping with Ce and codoping with Si", Optical Material Express, vol. 9, p. 3738, 2019

[17] Z. Galazka, S. Ganschow, K. Irmscher, D. Klimm, M. Albrecht, R. Schewski, M. Pietsch, T. Schulz, A. Dittmar, A. Kwasniewski, R. Grueneberg, S. B. Anooz, A. Popp, U. Juda, I. M. Hanke, T. Schroeder, and M. Bickermann, "Bulk single crystals of β-Ga_2O_3 and Ga-based spinels as ultrawide bandgap transparent semiconducting oxides", Progress in Crystal Growth and Characterization of Materials, vol. 67, p. 100511, 2021

[18] Z. Galazka, D. Klimm, K. Irmscher, R. Uecker, M. Pietsch, R. Bertram, M. Naumann, M. Albrecht, A. Kwasniewski, R. Schewski, and M. Bickermann, "$MgGa_2O_4$ as a new wide bandgap transparent semiconducting oxide: growth and properties of bulk single crystals", Physica Status Solidi A, vol. 212, p. 1455, 2015

[19] Z. Galazka, S. Ganschow, R. Schewski, K. Irmscher, D. Klimm, A. Kwasniewski, M. Pietsch, A. Fiedler, I. Schulze-Jonack, M. Albrecht, T. Schröder, and M. Bickermann, "Ultra-wide bandgap, conductive, high mobility, and high quality melt-grown bulk $ZnGa_2O_4$ single crystals", Applied Materials, vol. 7, no. 2, p. 022512, 2019

[20] K. Nassau, L. G. Van Uitert, "Preparation of Large Calcium-Tungstate Crystals Containing Paramagnetic Ions for Maser Applications", Journal of Applied Physics, vol. 31, p. 1508, 1960

[21] Y. Tomm, P. Reiche, D. Klimm, T. Fukuda, "Czochralski grown Ga_2O_3 crystals", Journal of Crystal Growth, vol. 220, p. 510, 2000

[22] Z. Galazka, R. Uecker, K. Irmscher, M. Albrecht, D. Klimm, M. Pietsch, M. Brützam, R. Bertram, S. Ganschow, R. Fornari, "Scaling-Up of Bulk β-Ga_2O_3 Single Crystals by the Czochralski Method", ECS Journal of Solid State Science and Technology, vol. 45, p. 1229, 2010

[23] Z. Galazka, K. Irmscher, R. Uecker, R. Bertram, M. Pietsch, A. Kwasniewski, M. Naumann, T. Schulz, R. Schewski, D. Klimm, M. Bickermann, "On the bulk β-Ga_2O_3 single crystals grown by the Czochralski method", Journal Crystal Growth, vol. 404, p.184, 2014

[24] Z. Galazka, R. Uecker, D. Klimm, K. Irmscher, M. Naumann, M. Pietsch, A. Kwasniewski, R. Bertram, S. Ganschow, M. Bickermann, "Scaling-Up of Bulk β-Ga_2O_3 Single Crystals by the Czochralski Method", ECS Journal of Solid State Science and Technology, vol. 6, p. Q3007, 2017

[25] Z. Galazka, S. Ganschow, A. Fiedler, R. Bertram, D. Klimm, K. Irmscher, R. Schewski, M. Pietsch, M. Albrecht, M. Bickermann, "Two inch diameter, highly conducting β-Ga_2O_3 single crystals grown by the Czochralski method", Journal of Crystal Growth, vol. 486, p. 82, 2018

[26] M. Higashiwaki, K. Sasaki, A. Kuramata, T. Masui, S. Yamakoshi, "Gallium oxide (Ga_2O_3) metal-semiconductor field-effect transistors on single-crystal β-Ga_2O_3 (010) substrates", Applied Physics Letters, vol. 100, p. 013504, 2012

[27] R. Roy, V. G. Hill, E. F. Osborn, "Polymorphism of Ga_2O_3 and the System Ga_2O_3—H_2O", Journal of the American Chemical Society, vol. 74, p. 719, 1952

[28] M. Zinkevich, F. Aldinger, "Thermodynamic Assessment of the Gallium-Oxygen System", Journal of the American Ceramic Society, vol. 87, p. 683, 2004

[29] S. Penner, C. Zhuo, R. Thalinger, M. Grünbacher, C. Hejny, S. Vanicek, M. Noisternig, " Transparent Semiconducting Oxides: Bulk Crystal Growth and Fundamental Properties", Monatshefte für Chemie, vol. 147, p. 289, 2016

[30] H. Y. Playford, A. C. Hannon, E. R. Barney, R. I. Walton, "Structures of uncharacterised polymorphs of gallium oxide from total neutron diffraction", Chemistry: A European Journal, vol. 19, p. 2803, 2013

[31] S. Yoshioka, H. Hayashi, A. Kuwabara, F. Oba, K. Matsunaga, I. Tanaka, "Structures and energetics of Ga_2O_3 polymorphs", Journal of Physics: Condensed. Matter, vol. 19, p. 346211, 2007

[32] M. R. Delgado, C. O. Areán, "Synthesis and Characterization of Spinel-Type Gallia-Alumina Solid Solutions", Materials Science, Chemistry Zeitschrift für anorganische und allgemeine Chemie, vol. 631, p. 2115, 2005

[33] R. Fornari, M. Pavesi, V. Montedoro, D. Klimm, F. Mezzadri, I. Cora, B. Pécz, F. Boschi, A. Parisini, A. Baraldi, C. Ferrari, E. Gombia, M. Bosi, "Thermal stability of ε-Ga_2O_3 polymorph", Acta Materialia., vol.140 p. 411. 2017

[34] I. Cora, F. Mezzadri, F. Boschi, M. Bosi, M. Čaplovičová, G. Calestani, I. Dódony, B. Pécza, R. Fornari, "The real structure of ε-Ga_2O_3 and its relation to κ-phase", Journal of Royal Society of Chemistry, vol. 19, p. 1509, 2017

[35] J. Furthmüller, F. Bechstedt, "Quasiparticle bands and spectra of Ga_2O_3 polymorphs", Physical Review B, vol. 93, p. 115204, 2016

[36] M. Marezio, J. P. Remeika, "Bond Lengths in the α-Ga_2O_3 Structure and the High-Pressure Phase of $Ga_{2-x}Fe_xO_3$", Journal of Chemical Physics, vol. 46, p. 1862, 1967

[37] J. Åhman, G. Svensson, J. Albertsson, "A Reinvestigation of β-Gallium Oxide", Acta Crystallographica C, vol. 52, p. 1336, 1996

[38] K. Pohl, "Hydrothermale Bildung von γ-Ga_2O_3", Naturwissenschaften, vol. 55, p. 82, 1968

[39] S. Geller, "Crystal Structure of β-Ga_2O_3", Journal of Chemical Physics, vol. 33, p. 676, 1966

[40] Z. Łodziana, K. Parliński, "Dynamical stability of the α and θ phases of alumina", Physical Review B, vol. 67, p. 174106, 2003

[41] Z. Galazka, "Transparent Semiconducting Oxides: Bulk Crystal Growth and Fundamental Properties" , Jenny Stanford Publishing, p. 750, 2020

[42] K. Yamaguchi, "First principles study on electronic structure of β-Ga_2O_3", Solid State Communications, vol. 131, p. 739, 2004

[43] H. He, R. Orlando, M. A. Blanco, R. Pandey, E. Amzallag, I. Baraille, M. Rérat, "First-principles study of the structural, electronic, and optical properties of Ga_2O_3 in its monoclinic and hexagonal phases", Physical Review B, vol. 74, p. 195123, 2006

[44] J. Furthmüller, F. Bechstedt, "Quasiparticle bands and spectra of Ga_2O_3 polymorphs", Physical Review B, vol. 93, p. 115204, 2016

[45] J. B. Varley, J. R. Weber, A. Janotti, C. G. Van de Walle, "Oxygen vacancies and donor impurities in β-Ga_2O_3", Applied Physics Letters, vol. 97, p. 142106, 2010

[46] J. B. Varley, H. Peelaers, A. Janotti, C. G. Van de Walle, “Hydrogenated cation vacancies in semiconducting oxides”, Journal of Physics: Condensed Matter, vol. 23, p. 334212, 2011

[47] J. B Varley, A. Schleife, “Bethe–Salpeter calculation of optical-absorption spectra of $In_2 O_3$ and Ga_2O_3,” Semiconductor Science and Technology, vol. 30, p. 024010, 2015

[48] H. Peelaers, C. G. Van de Walle, “Brillouin zone and band structure of β-Ga_2O_3”, Physica Status Solidi (b), vol. 252, p. 828, 2015

[49] T. Zacherle, P. C. Schmidt, M. Martin, “Ab initio calculations on the defect structure of β-Ga_2O_3”, Physical Review B, vol. 87, p. 235206, 2013

[50] A. Navarro-Quezada, S. Alamé, N. Esser, J. Furthmüller, F. Bechstedt, Z. Galazka, D. Skuridina, P. Vogt, “Near valence-band electronic properties of semiconducting β-Ga_2O_3 (100) single crystals”, Physical Review B, vol. 92, p. 195306, 2015

[51] C. Cocchi, H. Zschiesche, D. Nabok, A. Mogilatenko, M Albrecht, Z. Galazka, H. Kirmse, C. Draxl, C T. Koch, “Atomic signatures of local environment from core-level spectroscopy in β-Ga_2O_3”, Physical Review B, vol. 94, p. 075147, 2016

[52] P. Deák, Q. D. Ho, F. Seemann, B. Aradi, M. Lorke, T. Frauenheim, “Choosing the correct hybrid for defect calculations: A case study on intrinsic carrier trapping in β-Ga_2O_3”, Physical Review B, vol. 95, p. 075208, 2017

[53] L. Dong, R. Jia, C. Li, B. Xin, Y. Zhang, “Effects of oxygen vacancies on the structural and optical properties of β-Ga_2O_3”, Journal of Alloys and Compounds, vol. 712, p. 379, 2017

[54] A. Mock, R. Korlacki, C. Briley, V. Darakchieva, B. Monemar, Y. Kumagai, K. Goto, M. Higashiwaki, M. Schubert, “Band-to-band transitions, selection rules, effective mass, and excitonic contributions in monoclinic β-Ga_2O_3”, Physical Review B, vol. 96, p. 245205, 2017

[55] Y. Wei, X. Li, J. Yang, C. Liu, J. Zhao, Y. Liu, S. Dong, “Interaction between hydrogen and gallium vacancies in β-Ga_2O_3”, Scientific Reports, vol. 8, p. 10142, 2018

[56] T. C. Lovejoy, E. N. Yitamben, N. Shamir, J. Morales, E. G. Villora, K. Shimamura, S. Zheng, F. S. Ohuchi, M. A. Olmstead, “Surface morphology and electronic structure of bulk single crystal β-Ga_2O_3(100)”, Applied Physics Letters, vol. 94, p. 081906, 2009

[57] C. Janowitz, V. Scherer, M. Mohamed, A. Krapf, H. Dwelk, R. Manzke, Z. Galazka, R. Uecker, K. Irmscher, R. Fornari, M. Michling, D. Schmeißer, J. R. Weber, J. B. Varley, C. G Van de Walle, “Experimental electronic structure of In_2O_3 and Ga_2O_3”, New Journal of Physics, vol. 13, p. 085014, 2011

[58] M. Mohamed, C. Janowitz, I. Unger, R. Manzke, Z. Galazka, R. Uecker, R. Fornari, J. R. Weber, J. B. Varley, C. G. Van de Walle, “The electronic structure of β-Ga_2O_3”, Applied Physics Letters, vol. 97, p. 211903, 2010

[59] M. Mohamed, I. Unger, C. Janowitz, R. Manzke, Z. Galazka, R. Uecker, R. Fornari, “The surface band structure of β-Ga_2O_3”, Journal of Physics: Conference Series, vol. 286, p. 012027, 2011

[60] G.-L. Li, F. Zhang, Y.-T. Cui, H. Oji, J.-Y. Son, Q. Guo, “ Electronic structure of β-Ga_2O_3 single crystals investigated by hard X-ray photoelectron spectroscopy,” Applied Physics Letters, vol. 107, p. 022109, 2015

[61] M. Michling, D. Schmeißer, “Resonant Photoemission at the O1s threshold to characterize β-Ga_2O_3 single crystals”, IOP Conference Series: Materials Science and Engineering., vol. 34, p. 012002, 2012

[62] A. Kyrtsos, M. Matsubara, E. Bellotti, “On the feasibility of p-type Ga_2O_3”, Applied Physics Letters, vol. 112, p. 032108, 2018

[63] J. A. Kohn, G. Katz, J. D. Broder, “Characterization of β-Ga_2O_3 and its Alumina Isomorph, θ-Al2O3”, American Mineralogist, vol. 42, p. 398–407, 1957

[64] J. P. Remeika, “Rowth Of Single Crystals Of Corundum And Gallium Oxide”, US 3075831, 1963

[65] G. Katz, R. Roy, “Flux Growth and Characterization of β-Ga_2O_3 Single Crystals”, Journal of the American Ceramic Society, vol. 49, p. 168, 1966

[66] G. Garton, S. H. Smith, B. M. Wanklyn,” Crystal growth from the flux systems PbO V_2O_5 and Bi_2O_3 V_2O_5,” Journal of Crystal Growth, vol. 13–14, p. 588, 1972

[67] K. Fischer, D. Linzen, E. Sinn, H. Stieff, F. Voigt, “Cryoscopic Investigation of Lead Oxide Mixtures with Garnet Forming Oxides, Garnets, and Related Oxide Compounds”, Kristall und Technik, vol. 14, p. 1521, 1979

[68] V. I. Chani, K. Inoue, K. Shimamura, K. Sugiyama, T. Fukuda, “Synthesis and search for equilibrium compositions of borates with the huntite structure”, Journal of Crystal Growth, vol.132, p. 335, 1993

[69] A. B. Chase, “Growth of β-Ga_2O_3 by the Verneuil Technique”, Journal of the American Ceramic Society, vol. 47, p. 470, 1964

[70] M. R. Lorenz, J. F. Woods, R. J. Gambino,” Some electrical properties of the semiconductor β-Ga_2O_3,” Journal of Physics and Chemistry of Solids, vol. 28, p. 403, 1967

[71] T. Matsumoto, M. Aoki, A. Kinoshita, T. Aono, “Absorption and Reflection of Vapor Grown Single Crystal Platelets of β-Ga_2O_3”, Japanese Journal of Applied Physics., vol. 13, p. 737, 1974

[72] T. Matsumoto, M. Aoki, A. Kinoshita, T. Aono, “Absorption and Reflection of Vapor Grown Single Crystal Platelets of β-Ga_2O_3”, Japanese Journal of Applied Physics, vol. 13, p. 1578, 1974

[73] Von U. Gerlach, H. Oppermann, “Zum chemischen Transport von Fe_2O_3 mit Tellurtetrachlorid”, Zeitschrift für anorganische und allgemeine Chemie, vol. 432, p. 17, 1977

[74] H. Juskowiak, A. Pajączkowska, “Chemical transport of β-Ga_2O_3 using chlorine as a transporting agent”, Journal Material Science, vol. 21, p. 3430, 1986

[75] H. Juskowiak, A. Pajączkowska, “Chemical vapour transport of β-Ga_2O_3 using a two-component, S$^+$Cl mixture as the transporting agent,” Materials Research Bulletin, vol. 23, p. 1071, 1988

[76] A. Pajączkowska, H. Juskowiak, “On the chemical transport of gallium oxide in the Ga_2O_3/H-Cl system”, Journal of Material Science, vol. 21, p. 3435–3439, 1986

[77] A. Pajączkowska, H. Juskowiak, “On the chemical transport of gallium oxide in the Ga_2O_3/H-Cl system”, Journal of Crystal Growth, vol. 79, p. 421, 1986

[78] V. I. Vasyltsiv, Y. I. Rym, Y. Zakharko, “Optical absorption and photoconductivity at the band edge of β-$Ga_{2-x}In_xO_3$”, Physica Status Solidi (b), vol. 195, p. 653, 1996

[79] N. Ueda, H. Hosono, R. Waseda, H. Kawazoe, “Anisotropy of electrical and optical properties in β-Ga_2O_3 single crystals,” Applied Physics Letters., vol. 71, p. 933, 1997

[80] Y. Tomm, J. M. Ko, A. Yoshikawa, T. Fukuda, “Floating zone growth of β-Ga_2O_3: a new window material for optoelectronic device applications”, Solar Energy Materials and Solar Cells, vol. 66, p. 369, 2001

[81] E. G. Villora, K. Shimamura, Y. Yoshikawa, K. Aoki, N. Ichinose,” Large-size β-Ga_2O_3 single crystals and wafers,” Journal of Crystal Growth, vol. 270, p. 420, 2004

[82] E. G. Víllora, K. Shimamura, Y. Yoshikawa, T. Ujiie, K. Aoki, “Excitation and photoluminescence of pure and Si-doped β-Ga_2O_3 single crystals”, Applied Physics Letters, vol. 92, p. 202120, 2008

[83] J. Zhang, B. Li, C. Xia, G. Pei, Q. Deng, Z. Yang, W. Xu, H. Shi, F. Wu, Y. Wu, J. Xu, “ Growth and spectral characterization of β-Ga_2O_3 single crystals”, Journal of Physics and Chemistry of Solids, vol. 67, p. 2448, 2006

[84] Y. Tomm, P. Reiche, D. Klimm, T. Fukuda,” Czochralski grown Ga_2O_3 crystals,” Journal of Crystal Growth, vol. 220, p. 510, 2000

[85] Z. Galazka, R. Uecker, K. Irmscher, M. Albrecht, D. Klimm, M. Pietsch, M. Brutzam, R. Bertram, S. Ganschow, R. Fornari,” Czochralski growth and characterization of β-Ga_2O_3 single crystals,” Crystal. Research and Technology, vol. 45, p. 1229, 2010

[86] Z. Galazka, K. Irmscher, R. Uecker, R. Bertram, M. Pietsch, A. Kwasniewski, M. Naumann, T. Schulz, R. Schewski, D. Klimm, M. Bickermann, “On the bulk β-Ga_2O_3 single crystals grown by the Czochralski method”, Journal Crystal Growth, vol. 404, p. 184, 2014

[87] Z. Galazka, R. Uecker, D. Klimm, M. Bickermann, “Melt growth and properties of bulk $BaSnO_3$ single crystals”, PCT / EP2015 / 079938 (WO/2016/110385) (2015)

[88] Z. Galazka, S. Ganschow, A. Fiedler, R. Bertram, D. Klimm, K. Irmscher, R. Schewski, M. Pietsch, M. Albrecht, M. Bickermann, “Doping of Czochralski-grown bulk β-Ga_2O_3 single crystals with Cr, Ce and Al”, Journal of Crystal Growth, vol. 486, p. 82, 2018

[89] Z. Galazka, S. Ganschow, A. Fiedler, R. Bertram, D. Klimm, K. Irmscher, R. Schewski, M. Pietsch, M. Albrecht, M. Bickermann, “Doping of Czochralski-grown bulk β-Ga_2O_3 single crystals with Cr, Ce and Alx”, Journal of Crystal Growth., vol. 486, p.82, 2018

[90] H. Aida, K. Nishiguchi, H. Takeda, N. Aota, K. Sunakawa, Y. Yaguchi, “Growth of β-Ga_2O_3 Single Crystals by the Edge-Defined, Film Fed Growth Method”, Japanese Journal of Applied Physics, vol. 47, p. 8506, 2008

[91] K. Shimamura, E. G. Villora, K. Matsumura, K. Aoki, M. Nakamura, S. Takekawa, N. Ichinose, and K. Kitamura, “Rf-plasma-assisted molecular-beam epitaxy of β-Ga_2O_3”, Nihon Kessho Seicho Gakkaishi, vol. 33, p. 147, 2006

[92] A. Kuramata, K. Koshi, S. Watanabe, Y. Yamaoka, T. Masui, S. Yamakoshi, “High-quality β-Ga_2O_3 single crystals grown by edge-defined film-fed growth”, Japanese Journal of Applied Physics, vol. 55, p. 1202A2, 2016

[93] K. Hoshikawa, E. Ohba, T. Kobayashi, J. Yanagisawa, C. Miyagawa, Y. Nakamura, “Growth of β-Ga_2O_3 single crystals using vertical Bridgman method in ambient air”, Journal of Crystal Growth, vol. 447, p. 36, 2016

[94] Z. Galazka," β-Ga_2O_3 for wide-bandgap electronics and optoelectronics, "Semiconductor Science and Technology, vol. 33, p. 113001, 2018

[95] Z. Galazka, I. M. Hanke; Leibniz-Institut für Kristallzüchtung, Berlin, Germany (2018–2019), unpublished data

[96] Z. Galazka, K. Irmscher, R. Schewski, I. M. Hanke, M. Pietsch, S. Ganschow, D. Klimm, A. Dittmar, A. Fiedler, T. Schroeder, M. Bickermann, "Czochralski-grown bulk β-Ga_2O_3 single crystals doped with mono-, di-, tri-, and tetravalent ions", Journal of Crystal Growth, vol. 529, p. 125297, 2020

[97] Z. Galazka, R. Schewski, K. Irmscher, W. Drozdowski, M. E. Witkowski, M. Makowski, A. J. Wojtowicz, I. M. Hanke, M. Pietsch, T. Schulz, D. Klimm, S. Ganschow, A. Dittmar, A. Fiedler, T. Schroeder, M. Bickermann, "Bulk β-Ga_2O_3 single crystals doped with Ce, Ce+Si, Ce+Al, and Ce+Al+Si for detection of nuclear radiation", Journal of Alloys and Compounds, vol. 818, p. 152842, 2020

[98] W. Miller, K. Böttcher, Z. Galazka, J. Schreuer, "Numerical Modelling of the Czochralski Growth of β-Ga_2O_3", Crystals, vol. 7, p. 26, 2017

[99] R.-H. Horng, C.-Y. Huang, S.-L. Ou, T.-K. Juang, P.-L. Liu, "Epitaxial Growth of $ZnGa_2O_4$: A New, Deep Ultraviolet Semiconductor Candidate", Crystal Growth and Design, vol. 17, p. 6071, 2017

[100] T. Omata, N. Ueda, K. Ueda, H. Kawazoe, "New ultraviolet-transport electroconductive oxide, $ZnGa_2O_4$ spinel", Applied Physics Letters, vol. 64, p. 1077, 1994

[101] Z. Galazka, D. Klimm, K. Irmscher, R. Uecker, M. Pietsch, R. Bertram, M. Naumann, M. Albrecht, A. Kwasniewski, R. Schewski, M. Bickermann, "$MgGa_2O_4$ as a new wide bandgap transparent semiconducting oxide: growth and properties of bulk single crystals", Physica Status Solidi (a), vol. 212, p. 1455, 2015

[102] Z. Galazka, S. Ganschow, R. Schewski, K. Irmscher, D. Klimm, A. Kwasniewski, M. Pietsch, A. Fiedler, I. Schulze-Jonack, M. Albrecht, T. Schröder, M. Bickermann, "Ultra-wide bandgap, conductive, high mobility, and high quality melt-grown bulk $ZnGa_2O_4$ single crystals", Journal of Applied Materials, vol. 7, p. 022512, 2019

[103] L.-C. Cheng, C.-Y. Huang, R.-H. Horng, "Thickness Effect on Operational Modes of $ZnGa_2O_4$ MOSFETs", Journal of the Electron Devices Society, vol. 6, p. 432, 2018

[104] Z. Lou, L. Li, G. Shen, "High-performance rigid and flexible ultraviolet photodetectors with single-crystalline $ZnGa_2O_4$ nanowires", Nano Research, vol. 8, p. 2162, 2015

[105] T. Minami, T. Maeno, Y. Kuroi, S. Takata, "High-Luminance Green-Emitting Thin-Film Electroluminescent Devices Using $ZnGa_2O_4$:Mn Phosphor", Japanese Journal of Applied Physics, vol. 34, p. L684, 1995

[106] T. Minami, Y. Kuroi, T. Miyata, H. Yamada, S. Takata, "$ZnGa_2O_4$ as host material for multicolor-emitting phosphor layer of electroluminescent devices", Journal of Luminesence, vol. 72-74, p. 997, 1997

[107] G. Anoop, K. M. Krishna, M. K. Jayaraj, "Characteristics of A.C Electroluminescence in $ZnGa_2O_4$:Mn^{2+} Thin film Devices", Journal of The Electrochemical Society, vol. 158, p. J269, 2011

[108] H. I. Kang, J. S. Kim, M. Lee, J. H. Bahng, J. C. Choi, H. L. Park, G. C. Kim, T. W. Kim, Y. H. Hwang, S. I. Mho, S. H. Eom, Y. S. Yu, H. J. Song, W. T. Kim, "Tunable color emission of $ZnGa_2O_4:Si^{4+}$ phosphors with enhanced brightness due to donor formation", Solid State Communications, vol. 122, p. 633, 2002

[109] J. S. Kim, H. L. Park, G. C. Kim, T. W. Kim, Y. H. Hwang, H. K. Kim, S. I. Mho, S. D. Han," Color variation of $ZnGa_2O_4$ phosphor by reduction-oxidation processes, "Solid State Communications., vol. 126, p. 515, 2003

[110] Y. S. Jeong, J. S. Kim, H. L. Park, "First applicability of $ZnGa_2O_4$: Ge^{4+}, Li^{+}, Mn^{2+} phosphor for a plasma display panel", Solid State Communications., vol. 139, p. 157, 2006

[111] S. Itoh, H. Toki, Y. Sato, K. Morimoto, T. Kishino, "The $ZnGa_2O_4$ Phosphor for Low-Voltage Blue Cathodoluminescence", Journal of The Electrochemical Society, vol. 138, 1509, 1991

[112] M. Flynn, A. H. Kitai, "$ZnGa_2O_4$: Mn phosphors for Thin-Film Electroluminescent Displays Exhibiting Improved Brightness", Journal of The Electrochemical Society, vol. 148, p. H149, 2001

[113] S.-H. Yang, T.-J. Hsueh, S.-J. Chang, "Cathodoluminescence of a White $ZnGa_2O_4$/ZnO Phosphor Screen", Journal of The Electrochemical Society, vol. 152, p. H191, 2005

[114] A. Bessière, S. Jacquart, K. Priolkar, A. Lecointre, B. Viana, D. Gourier, "$ZnGa_2O_4:Cr^{3+}$: a new red long-lasting phosphor with high brightness", Optical Express, vol. 19, p. 10131, 2011

[115]. X. Xu, A. K. Azad, J. T. S. Irvine, "Photocatalytic H2 generation from spinels $ZnFe_2O_4$, $ZnFeGaO_4$ and $ZnGa_2O_4$", Catalysis Today Focus Issue: Solar Fuels, vol. 199, p. 22, 2013

[116] X. Li, X. Zhang, X. Zheng, Y. Shao, M. He, P. Wang, X. Fu, D. Li, "A facile preparation of $ZnGa_2O_4$ photonic crystals with enhanced light absorption and photocatalytic activity", Journal of Materials Chemistry A, vol. 2, p. 15796, 2014

[117] C. Chen, G. Li, Y. Liu, "Perovskite Photovoltaics for Dim-Light Applications", Powder Technology, vol. 281, p. 7, 2015

[118] B. Yasoda, R. P. S, Chakradhar, J. L. Rao, N. O. Gopal, C. N. Xu, "Electron paramagnetic resonance and luminescent properties of $Mn^{2+}:MgGa_2O_4$ phosphor", Journal of Applied Physics, vol. 98, p. 053910, 2005

[119] T. Suzuki, M. Hughes, Y. Ohishi, "Cathodoluminescence of a White $ZnGa_2O_4$/ZnO Phosphor Screen", Journal of Luminesence, vol. 130, p. 121, 2010

[120] D. Fiorani, S. Viticoli, "Magnetic properties of $CoGa_2O_4$", Solid State Communications, vol. 25, p. 155, 1978

[121] M. Ogata, H. Kozaka, N. Uryu, "Magnetic Interactions in Spinel Compound $CoGa_2O_4$", Physica Status Solidi (b), vol. 127, p. K33, 1985

[122] J. L. Soubeyroux, D. Fiorani, E. Agostinelli, "Spin-glass behaviour in cobalt oxyspinel $CoGa_2O_4$", Journal of Magnetism and Magnetic Materials, vol. 54–57, p. 83, 1986

[123]. A. V. Singh, B. Khodadadi, J. B. Mohammadi, S. Keshavarz, T. Mewes, D. S. Negi, R. Datta, Z. Galazka, R. Uecker, A. Gupta, "Bulk Single Crystal-Like Structural and Magnetic Characteristics of Epitaxial Spinel Ferrite Thin Films with Elimination of Antiphase Boundaries", Advanced Materials, vol. 29, p. 1701222, 2017

[124]. J. Shan, A. V. Singh, L. Liang, L. J. Cornelissen, Z. Galazka, A. Gupta, B. J. van Wees, T. Kuschel, "Enhanced magnon spin transport in $NiFe_2O_4$ thin films on a lattice-matched substrate", Applied Physics Letters, vol.113, p. 162403, 2018

[125] H. J. van Hook, M. L. Keith, "The system Fe_3O_4—Mn_3O_4," American. Mineralogist, vol. 43, p. 69, 1958

[126] K. Mocala, A. Navrotsky, D. M. Sherman, "High-Temperature Heat Capacity of Co_3O_4 Spinel: Thermally Induced Spin Unpairing Transition", Physics and Chemistry of Minerals, vol. 19, p. 88, 1992

[127] H. S. C. O'Neill, A. Navrotsky, "Simple spinels; crystallographic parameters, cation radii, lattice energies, and cation distribution", American Mineralogy, vol. 68, p. 181, 1983

[128] L. Schwarz, Z. Galazka, T. M. Gesing, D. Klimm, "On the influence of inversion on thermal properties of magnesium gallium spinel", Crystal Research and Technology, vol.50, p. 961, 2015

[129] A. R. Phani, S. Santucci, S. Di Nardo, L. Lozzi, M. Passacantando, P. Picozzi, C. Cantalini, "Preparation and characterization of bulk $ZnGa_2O_4$", Journal of Material Science., vol. 33, p. 3969, 1998

[130] G. Palmer, K. Poeppelmeier, "Phase relations, transparency and conductivity in Ga_2O_3–SnO_2–ZnO", Solid State Sciences, vol. 4, p. 317, 2002

[131] M. G. Brik, A. Suchocki, A. Kamińska, "Lattice parameters and stability of the spinel compounds in relation to the ionic radii and electronegativities of constituting chemical elements", Inorganic Chemistry, vol. 53, p. 5088, 2014

[132] S. K. Sampath, D. G. Kanhere, R. Pandey, "Electronic structure of spinel oxides: zinc aluminate and zinc gallate", Journal of Physics: Condensed Matter, vol. 11, p. 3635, 1999

[133] L. Pisani, T. Maitra, R. Valentí, "Effects of Fe substitution on the electronic, transport, and magnetic properties of $ZnGa_2O_4$: A systematic ab initio study", Physical Review B, vol. 73, p. 205204, 2006

[134] S. López, A. H. Romero, P. Rodríguez-Hernández, A. Muñoz, "First-principles study of the high-pressure phase transition in $ZnAl_2O_4$ and $ZnGa_2O_4$: From cubic spinel to orthorhombic post-spinel structures", Physical Review B, vol. 79, p. 214103, 2009

[135] M. G. Brik," First-principles calculations of electronic, optical and elastic properties of $ZnAl_2S_4$ and $ZnGa_2O_4$," Journal of Physics and Chemistry of Solids, vol. 71, p. 1435, 2010

[136] H. Dixit, N. Tandon, S. Cottenier, R. Saniz, D. Lamoen, B. Partoens, V. Van Speybroeck, M. Waroquier, "Electronic structure and band gap of zinc spinel oxides beyond LDA: $ZnAl_2O_4$, $ZnGa_2O_4$ and $ZnIn_2O_4$", New Journal of Physics, vol. 13, p. 063002, 2011

[137]. F. Zerarga, A. Bouhemadou, R. Khenata, S. Bin-Omran, "Structural, electronic and optical properties of spinel oxides $ZnAl_2O_4$, $ZnGa_2O_4$ and $ZnIn_2O_4$", Solid State Sciences, vol. 13, p. 1638, 2011

[138] Y. Xia, T. Wang, X. Zhao, X. Jiao, D. Chen, "Theoretical and Experimental Investigations on Effects of Native Point Defects and Nitrogen Doping on the Optical Band Structure of Spinel $ZnGa_2O_4$", Journal of Physical Chemistry C, vol. 122, p. 5509, 2018

[139] J. B. Varley; Lawrence Livermore National Laboratory, CA, USA (2017), unpublished data

[140] B. Thielert, C. Janowitz, Z. Galazka, M. Mulazzi, “Theoretical and experimental investigation of the electronic properties of the wide band-gap transparent semiconductor $MgGa_2O_4$”, Physical Review B, vol. 97, p. 235309, 2018

[141]. A. B. Chase, J. A. Osmer, “Localized Cooling in Flux Crystal Growth”, Journal of the American Ceramics Society, vol. 50, p. 325, 1967

[142] H. van den Boom, J. C. M. Henning, J. P. M. Damen, “Electron spin resonance on chromium doped $ZnGa_2O_4$”, Solid State Communications, vol. 8, p. 717, 1970

[143] P. J. M. van der Straten, R. Metselaar, H. D. Jonker, “Flux growth of $ZnGa_2O_4$ single crystals”, Journal of Crystal Growth, vol. 43, p. 270, 1978

[144] Z. Yan, H. Takei, “Flux growth of single crystals of spinel $ZnGa_2O_4$ and $CdGa_2O_4$”, Journal of Crystal Growth, vol. 171, p. 131, 1997

[145] Z. Yan, H. Takei, H. Kawazoe, “Electrical Conductivity in Transparent $ZnGa_2O_4$: Reduction and Surface-Layer Structure Transformation”, Journal of the American Ceramics Society, vol. 81, p. 180, 1998

[146] W. Jia, H. Liu, S. Huang, X. Wu, L. Lu, W. M. Yen, “Photoluminescence of Mn^{2+} Doped $ZnGa_2O_4$ Single-Crystal Fibers”, Journal of The Electrochemical Society, vol. 142, p. 1637, 1995

[147] E. A. Giess, “Growth of Single-Crystal $MgGa_2O_4$ Spinel from Molten PbO-PbF_2 Solutions”, Journal of Applied Physics, vol. 33, p. 2143, 1962

[148] B. A. Scott, K. H. Nichols, R. M. Potemski, J. M. Woodall, “Magnesium gallate spinel: a substrate for the direct liquid-phase epitaxial growth of (Ga,Al)As”, Applied Physics Letters, vol. 21, p. 121, 1972

[149] T. Suzuki, M. Hughes, Y. Ohishi, “Optical properties of Ni-doped $MgGa_2O_4$ single crystals grown by floating zone method”, Journal of Luminescence, vol. 130, p. 121, 2010

[150] W. E. Kramer, A. M. Stewart, R. H. Hopkins, “The growth of $CoGa_2O_4$ single crystals as substrates for the epitaxial growth of ferrites”, Journal of Crystal Growth, vol. 73, p. 329, 1985

[151] Z. Galazka, Leibniz-Institut für Kristallzüchtung, Berlin, Germany (2014), unpublished data

[152] F. Leccabue, C. Pelosi, E. Agostinelli, V. Fares, D. Fiorani, E. Paparazzo, “Crystal growth, thermodynamical and structural study of $CoGa_2O_4$ and $ZnCr_2O_4$ single crystals”, Journal of Crystal Growth, vol. 79, p. 410, 1986

[153] A. Nakatsuka, Y. Ikeda, N. Nakayama, T. Mizota, “Inversion parameter of the $CoGa_2O_4$ spinel determined from single-crystal X-ray data”, Acta Crystallographica Section E-structure Reports Online E, vol. 62, p. i109, 2006

[154] Z. Galazka, I. M. Hanke; Leibniz-Institute für Kristallzüchtung, Berlin, Germany (2017), unpublished data

[155] Y. Niiyama, M. Watanabe, “BeMgZnSe-based ultraviolet lasers”, Semiconductor Science and Technology, vol. 20, p. 1187, 2005

[156] P. Wojnar, E. Janik, L. T. Baczewski, S. Kret, E. Dynowska, T. Wojciechowski, J. Suffczyski, J. Papierska, P. Kossacki, G. Karczewski, J. Kossut, T. Wojtowicz, “Giant spin splitting in optically active ZnMnTe/ZnMgTe core/shell nanowires”, Nano Letters, vol. 12, p. 3404, 2012

[157] K. M. Yu, M. A. Mayer, D. T. Speaks, H. He, R. Zhao, L. Hsu, S. S. Mao, E. E. Haller, W. Walukiewicz, “Ideal transparent conductors for full spectrum photovoltaics”, Journal of Applied Physics, vol. 111, p. 123505, 2012

[158] E. Kamieniecki, “Effect of charge trapping on effective carrier lifetime in compound semiconductors: High resistivity CdZnTe”, Journal of Applied Physics, vol. 116, p. 193702, 2014

[159] Y. Lin, Q. Qin, X. Wang, J. Chen, L. Li, J. Jiang, Y. He, X. Wang, P. Zhao, S. Yuan, “Effect of annealing on the structure of composite passivation films prepared by magnetron sputtering deposition on the surface of hgcdte”, Crystals, vol. 12, p. 983, 2022

[160] S. Sen, C. S. Liang, D. R. Rhiger, J. E. Stannard, H. F. Arlinghaus, “Reduction of CdZnTe substrate defects and relation to epitaxial HgCdTe quality”, Journal of Electronic Materials, vol. 25, p. 1188, 1996

[161] S. Guo, Y. Luo, W. Lin, O. Maksimov, M. Tamargo, I. Kuskovsky, C. Tian, G. Neumark, “High crystalline quality znbese grown by molecular beam epitaxy with bezn co-irradiation”, Journal of Crystal Growth, vol. 208, p. 205, 2000

[162] Ashraf MA, Hussain I, Rasheed R, Iqbal M, Riaz M, Arif MS, “Advances in microbe-assisted reclamation of heavy metal contaminated soils over the last decade: a review,” Journal of Environmental Management, vol. 198, p. 132, 2017

[163] A. Hassanien, K. Aly, A. Akl, “Study of optical properties of thermally evaporated ZnSe thin films annealed at different pulsed laser powers”, Journal of Alloys and Compounds, vol. 685, p. 733, 2016

[164] Q. Zhang, H. Li, Y. Ma, T. Zhai, “ZnSe nanostructures: Synthesis, properties and applications”, Progress in Materials Science, vol. 83, p. 472, 2016

[165] K. Yadav, N. Jaggi, “Effect of Ag doping on structural and optical properties of ZnSe nanophosphors”, Materials Science in Semiconductor Processing, vol. 30, p. 376, 2015

[166] E. Yildirim, H. M. Gubur, S. Alpdoğan, M. Arı, E. Harputlu, K. Ocakoğlu, “The effect of annealing of ZnSe nanocrystal thin films in air atmosphere”, Indian Journal of Physics, vol. 90, p. 793, 2015

[167] A. Ayeshamariam, M. Kashif, S. Raja, S. Jagadeswari, D. Saravanakkumar, N. Alhaji, A. Uduman, Mohideen, M. Bououdina, M. Jayachandran, “Optical Characterisation of ZnSe Thin Films by Using Electro Deposition Technique”, Materials Science, Physics (on-line), 2014 (http://api.semanticscholar.org/CorpusID:18366441)

[168] F. Firszt, S. Łęgowski, H. Męczyńska, J. Szatkowski, W. Paszkowicz, K. Godwod, “Growth and characterisation of $Zn_{1-x}Be_xSe$ mixed crystals”, Journal of Crystal Growth, vol. 184-185, p. 1335, 1998

[169] Z. Guzik, S. Borsuk, K. Traczyk, and M. Płomiński, “Tukan - An 8K pulse height analyzer and multi-channel scaler with a PCI or a USB interface”, IEEE Trans. Nucl. Sci., vol. 53, p. 231, 2006

[170] J. T. M. De Haas, P. Dorenbos, and C. W. E. Van Eijk, “Measuring the absolute light yield of scintillators”, Nuclear Instruments and Methods Phys. Res. A, vol. 537, p. 97, 2005

[171] L. M. Bollinger and G. E. Thomas, “Measurement of the time dependence of scintillation intensity by a delayed-coincidence method”, Review of Scientific Instruments, vol. 32, p. 1044, 1961

[172] G. A. Morton, H. M. Smith, and R. Wasserman, “Afterpulses in photomultipliers”, IEEE Transactions on Nuclear Science., vol. NS-14, p. 443, 1967

[173] W. Krysicki and L. Włodarski, “Analiza Matematyczna w Zadaniach I”, Wydawnictwo Naukowe PWN, 1999

[174] M. Makowski, W. Drozdowski, M.E. Witkowski, A.J. Wojtowicz, K. Irmscher, R. Schewski, Z. Galazka, “Tailoring the scintillation properties of β-Ga_2O_3 by doping with Ce and codoping with Si”, Optical Material Express, vol. 9, p. 3738, 2019

[175] L. Cuibus, D. Dadarlat, M. Streza, F.V. Dulf, Z. Diaconeasa, C. Socaciu, “Rapid, non-destructive determination of butter adulteration by means of photopyroelectric (PPE) calorimetry”, Journal of Thermal Analysis and Calorimetry., vol. 127, p. 1193, 2017

[176] J. Zakrzewski, K. Strzałkowski, M. Boumhamdi, A. Marasek, A. Abouais, D.M. Kamiński, “Photothermal Determination of the Surface Treatment of $Cd_{1-x}Be_xTe$ Mixed Crystals” , Applied Science., vol. 13, p.2113. 2023

[177]. K. Strzałkowski, “Effect of lattice disorder on the thermal conductivity of ZnBeSe, ZnMgSe and ZnBeMgSe crystals”, Materials Chemistry and Physics., vol. 163, p.453, 2015

[178]. D. Dadarlat, “Photopyroelectric calorimetry of liquids; recent development and applications” , Laser Physics., vol. 54, p.1330, 2009

Chapter 5

5 Results of conducted research with discussion

5.1 Investigation of β-Ga_2O_3 pure and doped with silicon

In this part of the thesis pulse height spectra, scintillation time profiles, radio- and thermoluminescence spectra of gallium oxide crystals β-Ga_2O_3, both in their pure form and doped with silicon (β-Ga_2O_3:Si), are presented and analyzed. Multiple samples, each signifying a unique crystal, are delineated below. Despite a diverse array of samples tested, variations predominantly arose in efficiency, signaling discrepancies in sample surface quality. Consequently, only samples showcasing the highest efficiency were chosen for presentation. Crucial details are listed in **Tab. 5.1**.

Tab. 5.1. List of samples from pure crystals β-Ga_2O_3.

Sample ID	Host	Activator	n_e (cm^{-3})	Size (mm^3)
I1	β-Ga_2O_3	none	$2.5 \cdot 10^{16}$	$5 \times 5 \times 0.52$
I2			$2.5 \cdot 10^{16}$	$5 \times 5 \times 0.41$
I3			$2.5 \cdot 10^{16}$	$5 \times 5 \times 0.49$
I4			$2.5 \cdot 10^{16}$	$5 \times 5 \times 0.75$
I5			$2.5 \cdot 10^{16}$	$5 \times 5 \times 2.72$
I6			$4.66 \cdot 10^{16}$	$5 \times 5 \times 0.49$
I7			$8.90 \cdot 10^{16}$	$5 \times 5 \times 0.59$
I8			$5.86 \cdot 10^{17}$	$5 \times 5 \times 0.47$

5.1.1 Pulse height spectra of β-Ga_2O_3 and β-Ga_2O_3:Si

For all measurements detailed within this subsection, the excitation source employed was the ^{137}Cs isotope, emitting γ radiation with an energy of 662 keV. The pulse shaping time was consistently set at 2 μs for all measurements and a gain of 0.3x10 was chosen. The pulse height spectra from the initial series of crystals are illustrated in **Figs. 5.1-5.4**. Notably, sample I1, which exhibits the most optimal pulse height spectrum structure, has been designated as the reference sample, and consequently, its spectrum is showcased in each figure pertaining to this particular series of crystals.

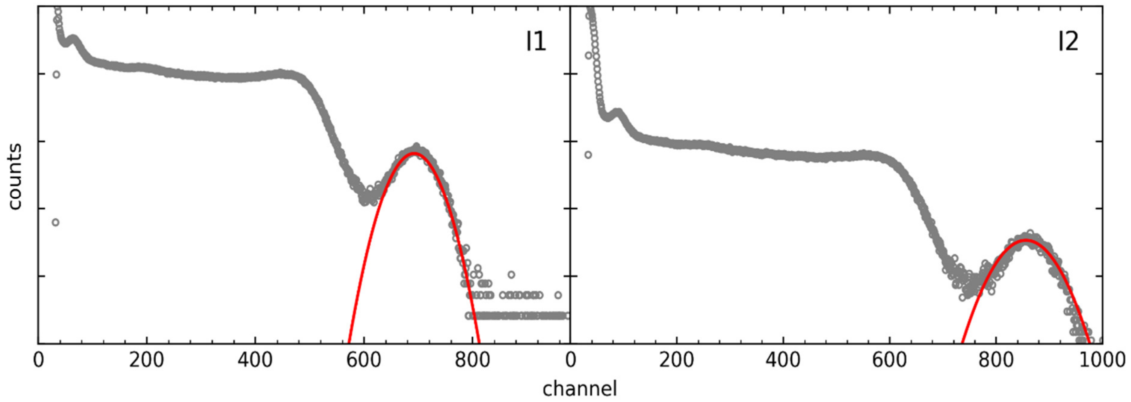

Fig. 5.1. Pulse height spectra of samples I1 and I2 excited by the ^{137}Cs source (662 keV).

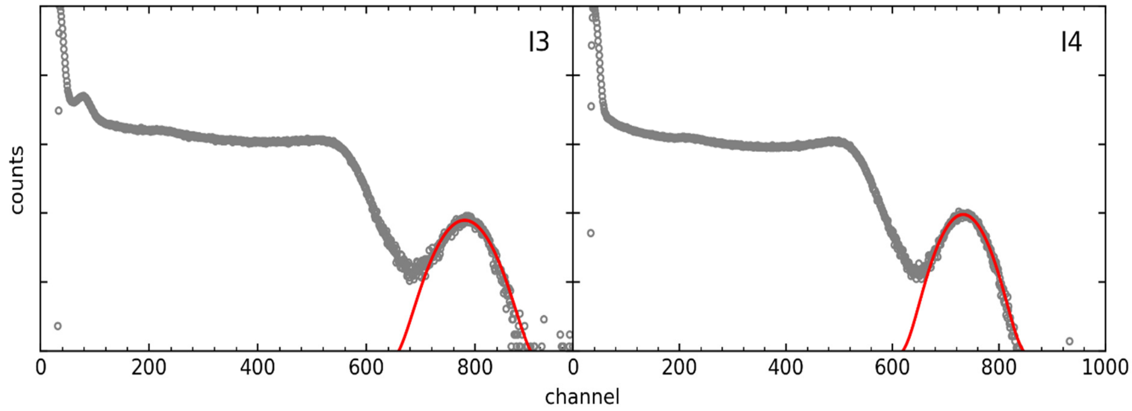

Fig. 5.2. Pulse height spectra of samples I3 and I4 excited by the ^{137}Cs source (662 keV).

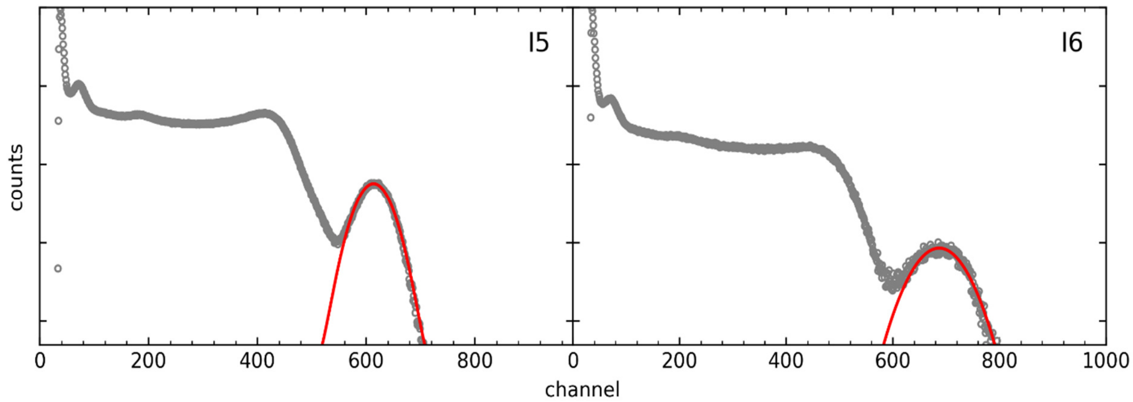

Fig. 5.3. Pulse height spectra of samples I5 and I6 excited by the ^{137}Cs source (662 keV).

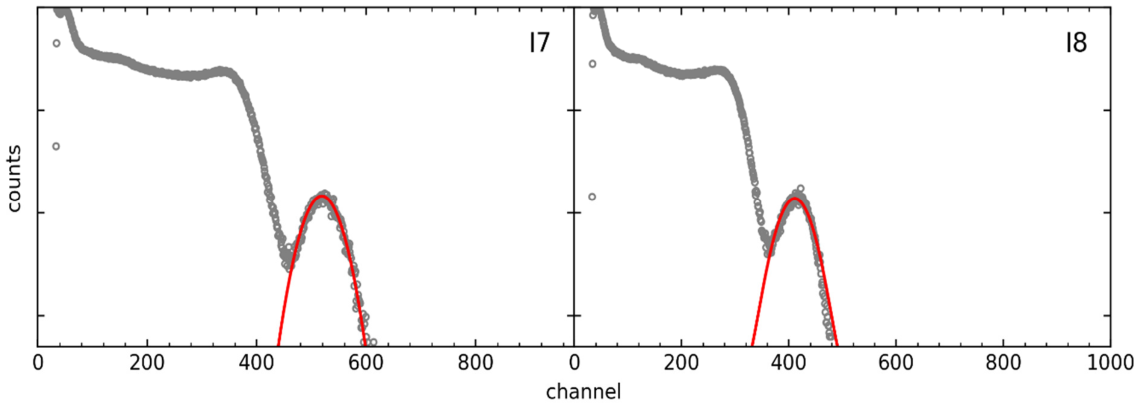

Fig. 5.4. Pulse height spectra of samples I7 and I8 excited by the ^{137}Cs source (662 keV)

Tab. 5.2. Scintillation characteristics of samples from pure crystals β-Ga_2O_3.

Sample ID	n_e (cm^{-3})	LY (ph/MeV)	R (%)
I1	$2.5 \cdot 10^{16}$	9090	10.6
I2	$2.5 \cdot 10^{16}$	8920	12.3
I3	$2.5 \cdot 10^{16}$	8420	11.3
I4	$2.5 \cdot 10^{16}$	7500	10.6
I5	$2.5 \cdot 10^{16}$	6490	11.3
I6	$4.66 \cdot 10^{16}$	7650	15.0
I7	$8.90 \cdot 10^{16}$	5880	13.9
I8	$1.90 \cdot 10^{17}$	4740	16.5

Worth to be reminded here that, as described in chapter **4**, for each sample the LY was calculated with the current position of the single-photoelectron peak taken into account (checked before and after the pulse height measurement). This is why the values of LY do not correspond directly to full energy peak positions.

Upon careful examination of the data presented in **Tab. 5.2**, we uncover valuable insights into the relationship between free electron concentration and scintillation effects:

- Samples marked as Ij (j = 7,8), which have higher levels of conductivity due to more free electrons, show lower scintillation yields compared to samples with a more balanced concentration of free carriers. This suggests that having too many free electrons can hinder the efficiency of scintillation.
- The highest light yield (LY) values are found when the concentration of free carriers is around 10^{16} cm^{-3}. This sweet spot indicates an optimal balance for efficient scintillation.
- A noteworthy achievement is seen with a scintillation yield of 9,090 photons per MeV. This milestone, achieved with β-Ga_2O_3 crystals grown using the Czochralski method, aligns with one of the objectives pursued in the PhD project, which aimed for 10,000 photons per MeV. The actual result of 9,090 photons per MeV is relatively close to that target.

In the upcoming **Tab. 5.3**, we shift our focus to doped crystals of β-Ga_2O_3, which involve gallium oxide doped with silicon (Si), thereby introducing an alternative dimension to our exploration of scintillation phenomena.

Tab. 5.3. List of samples from Si-doped crystals of β-Ga_2O_3.

Sample ID	Host	Activator	n_e (cm^{-3})	Size (mm^3)
D1	β-Ga_2O_3	Si	$2.80 \cdot 10^{18}$	5·5·0.55
D2			$4.27 \cdot 10^{18}$	5·5·0.64
D3			$4.27 \cdot 10^{18}$	5·5·0.70
D4			$8.87 \cdot 10^{17}$	5·5·0.53
D5			$8.87 \cdot 10^{17}$	5·5·0.53
D6			$5.49 \cdot 10^{17}$	5·5·0.51
D7			$5.49 \cdot 10^{17}$	5·5·0.59

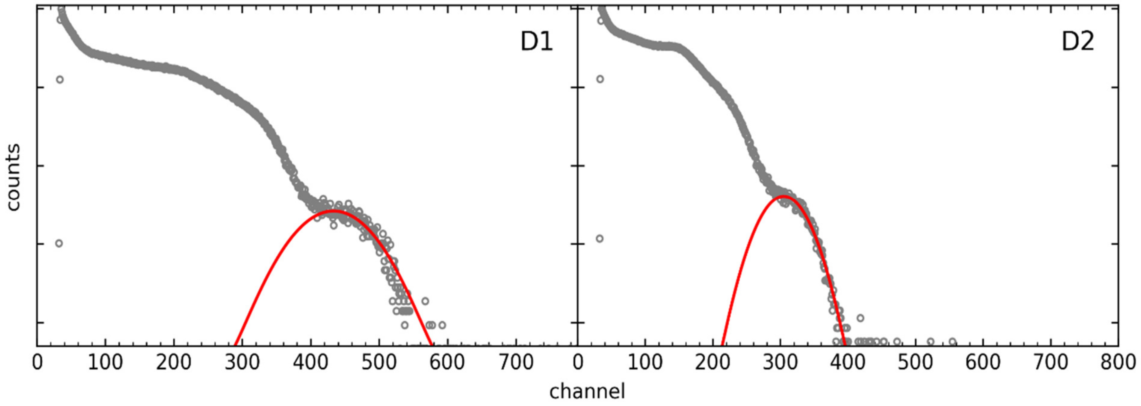

Fig. 5.5. Pulse height spectra for samples D1 and D2 excited by the ^{137}Cs source (662 keV).

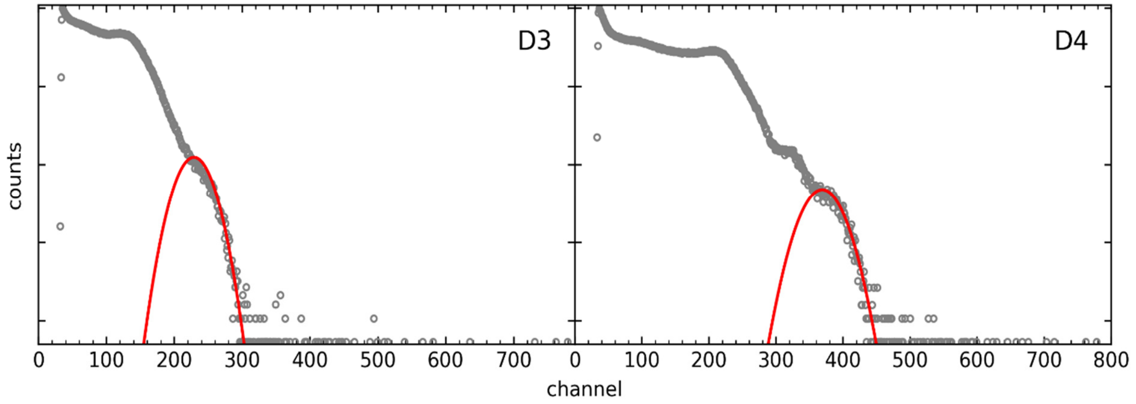

Fig. 5.6. Pulse height spectra for samples D3 and D4 excited by the ^{137}Cs source (662 keV).

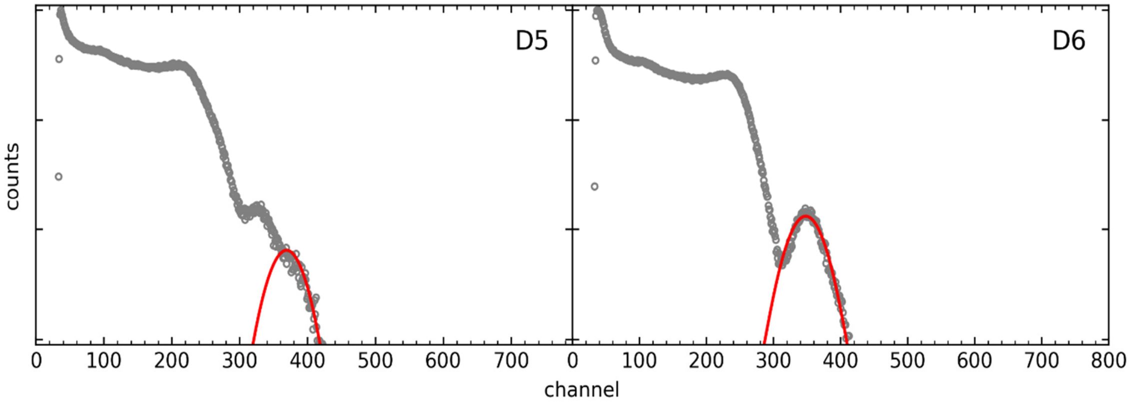

Fig. 5.7. Pulse height spectra for samples D5 and D6 excited by the ^{137}Cs source (662 keV).

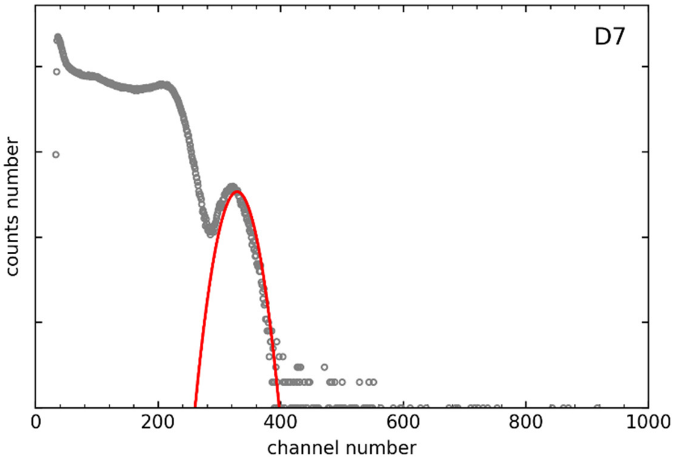

Fig. 5.8. Pulse height spectra for sample D7 excited by the ^{137}Cs source (662 keV).

Tab. 5.4. Scintillation characteristics of samples from codoped crystals β-Ga_2O_3:Si.

Sample ID	**n_e (cm^{-3})**	**LY (ph/MeV)**	**R (%)**
D1	$2.80 \cdot 10^{18}$	2840	26.6
D2	$4.27 \cdot 10^{18}$	1990	23.5
D3	$4.27 \cdot 10^{18}$	1490	22.9
D4	$8.87 \cdot 10^{17}$	4420	16.9
D5	$8.87 \cdot 10^{17}$	4500	15.8
D6	$5.49 \cdot 10^{17}$	4170	17.5
D7	$5.49 \cdot 10^{17}$	3870	14.4

Analyzing the data for semiconductor crystals provided in **Tab. 5.2** and **5.4**, it can be concluded that doping gallium oxide crystals with silicon significantly decreases scintillation efficiency. This is most likely due to the fact that β-Ga_2O_3:Si crystals are characterized by a higher concentration of free carriers compared to pure crystals of gallium oxide.

Based on the data collected in this section of the work, one can examine the relationship between scintillation efficiency and the concentration of free carriers. This relationship has been illustrated in **Fig. 5.9**. It is clear that the highest value of LY was obtained for samples with free carrier concentrations in the range of 10^{16}-10^{17} cm^{-3}. The decrease in scintillation efficiency with increasing concentration of free carriers (n_e) can be explained by the fact that the probability of the Auger effect occurrence (parasitic relative to scintillation) is proportional to the third power of n_e [1].

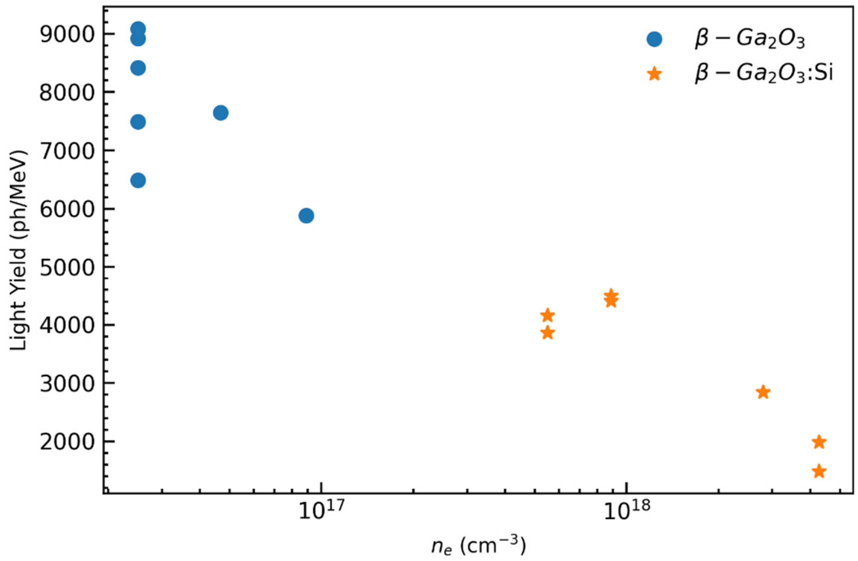

Fig. 5.9. Scintillation efficiency as a function of free carrier concentration.

Comparing samples based on their concentrations of free carriers, it is apparent that the silicon dopant has a rather negative impact on the efficiency of the scintillation process. Therefore, it appears that the ionizing radiation does not stimulate any luminescence of silicon ions, and only the intrinsic emission of β-Ga_2O_3 contributes to the yield. The absence of internal luminescence in silicon ions implies that these ions do not contribute significantly to the scintillation process, likely due to their electronic configuration or energy levels. Overall, these findings underscore the importance of material purity in optimizing scintillation performance. Understanding the impact of dopants like silicon on scintillation efficiency is crucial for various applications, such as radiation detection and medical imaging. It highlights the need for careful selection of materials and doping strategies to achieve desired performance characteristics in scintillators devices.

5.1.2 Scintillation time profiles of β-Ga_2O_3 and β-Ga_2O_3:Si

Scintillation time profiles are pivotal in scintillation spectroscopy as they offer insights into the temporal behavior of emitted light following excitation. Essentially, they illustrate how the intensity of emitted light changes over time after exposure to radiation. Typically, scintillation time profiles are analyzed using a sum of exponential decays, providing a convenient method for fitting recorded data. However, this approach has limitations, particularly the oversight of the instrumental response of the detection system, also known as background noise.

To overcome this limitation, alternative methods for analyzing scintillation time profiles have been proposed, taking into account the instrumental response of the measurement system, which can introduce disturbances in the recorded spectrum. Similar to Gundacker's method, it assumes that the measurement result is a convolution of the scintillation time profile of the tested crystal and the instrumental response of the system. To solely analyze the time profile of the scintillation sample, both signals must be separated. This necessitates the measurement of the instrumental response of the system. A program was developed using the Python programming language to facilitate these calculations. Once a clean signal from the tested crystal is obtained, the analysis proceeds by fitting using a sum of exponential decays. This methodology lays the groundwork for all subsequent analyses of scintillation time profiles for the sample, as it will be employed throughout the remainder of this study.

Based on observations from the figure depicting free electron concentration, it is evident that the free electron concentration significantly impacts the scintillation parameters. Therefore, for our subsequent investigation, we have deliberately selected samples with varying free electron concentrations. These samples, denoted as I1, I6, I7, and I8 for the pure gallium oxide, demonstrate distinct free electron concentrations. In the case of doped samples, we already have varying free electron concentrations. Nonetheless, we will present different outputs of scintillation time profiles, essentially showcasing the best results obtained from these samples.

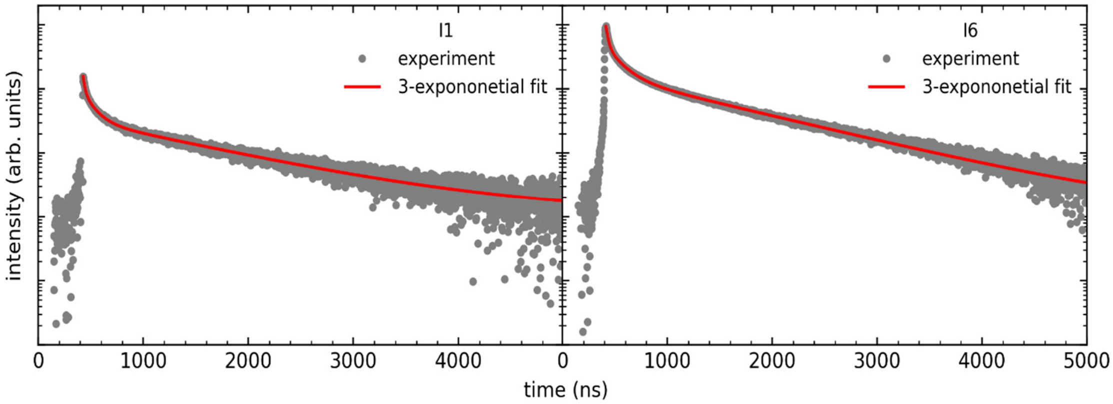

Fig. 5.10. Scintillation time profiles of samples I1 and I6 of pure gallium oxide excited by the ^{137}Cs source (662 keV).

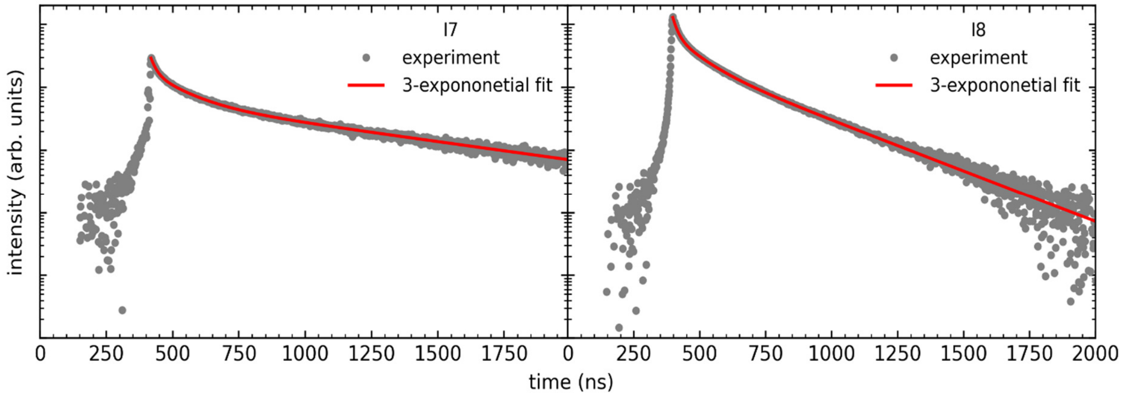

Fig. 5.11. Scintillation time profiles of samples I7 and I8 of pure gallium oxide excited by the ^{137}Cs source (662 keV).

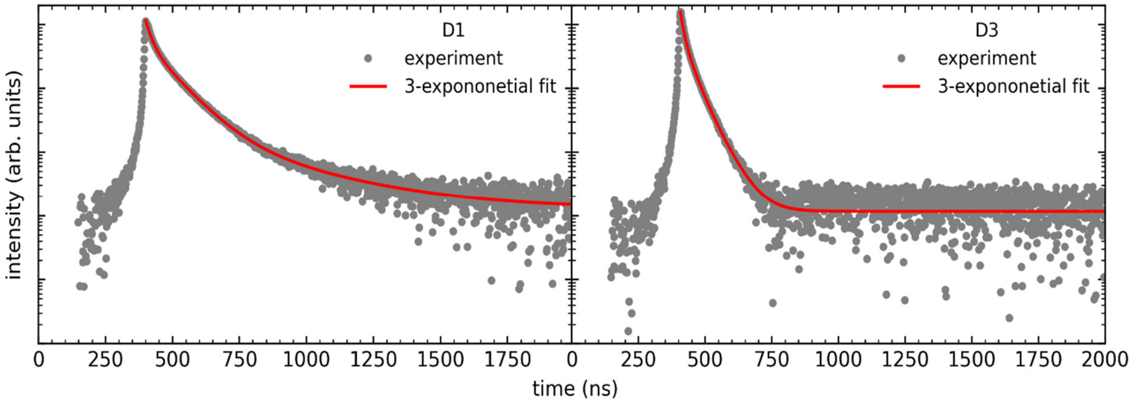

Fig. 5.12. Scintillation time profiles of samples D1 and D3 of Si-doped gallium oxide excited by the ^{137}Cs source (662 keV).

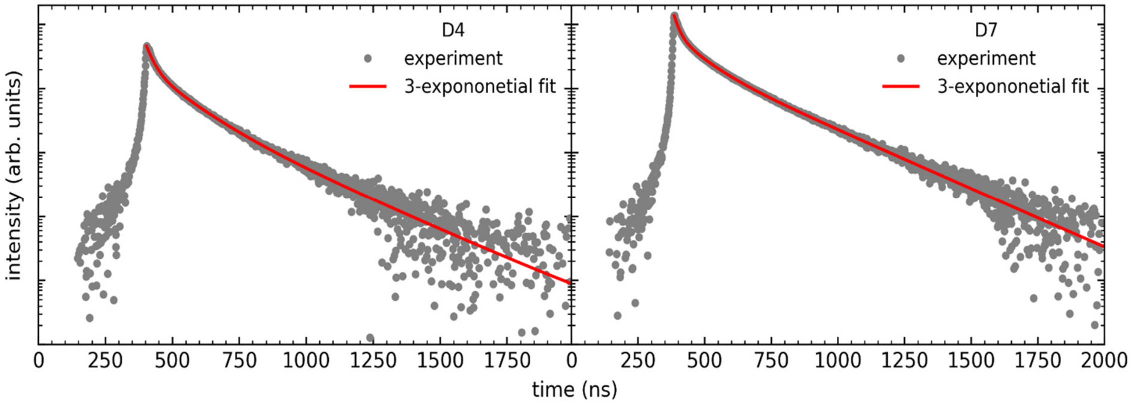

Fig. 5.13. Scintillation time profiles of samples D4 and D7 of Si-doped gallium oxide excited by the ^{137}Cs source (662 keV).

Tab. 5.5 contains the values of the scintillation decay constants and their contributions for all of the samples studied. To make comparisons more manageable, we extend the number of parameters with a so-called scintillation mean decay time τ_{mean}. We calculate this value in accordance with Eq. (2) by Zatryb and Klak [2], arriving at:

$$\tau_{mean} = \frac{\sum_{i=1}^{3} A_i \tau_i^2}{\sum_{i=1}^{3} A_i \tau_i} \tag{5.1}$$

where A_i and τ_i are amplitudes and decay time constants of each decay component, respectively.

Tab. 5.5. Comparison of fitting parameters of the STP spectrum for the selected β-Ga_2O_3 crystals pure and doped with Si.

ID	Sample	n_e (cm^{-3})	τ_i (ns)	τ_m (ns)
I1	β-Ga_2O_3	$2.5 \cdot 10^{16}$	17 (3%) 107 (15%) 1183 (82%)	989
I6	β-Ga_2O_3	$4.66 \cdot 10^{16}$	22 (5%) 145 (20%) 1098 (75%)	857
I7	β-Ga_2O_3	$8.90 \cdot 10^{16}$	19.2 (4%) 115 (22%) 734 (74%)	569
I8	β-Ga_2O_3	$1.90 \cdot 10^{17}$	16.8 (9%) 84 (27%) 268 (64%)	195
D1	β-Ga_2O_3:Si	$2.80 \cdot 10^{18}$	20.3 (21%) 90 (66%) 324 (13%)	106
D3	β-Ga_2O_3:Si	$4.27 \cdot 10^{18}$	10.2 (21%) 28 (38%) 54 (41%)	35
D4	β-Ga_2O_3:Si	$8.87 \cdot 10^{17}$	26 (18%) 111 (43%) 238 (39%)	145
D7	β-Ga_2O_3:Si	$5.49 \cdot 10^{17}$	18.3 (10%) 82 (28%) 235 (62%)	170

As depicted in the figures provided (**Fig. 5.10** to **Fig. 5.13)**, the triple-exponential decay pattern provided a good fit to the data. For pure crystals, this pattern revealed a relationship between free electron concentration and mean decay time, as indicated in the accompanying **Tab. 5.5.** With an increase in free electron concentration, the decay time decreased, leading to faster scintillation, exemplified by sample I8 with a shorter mean decay time (195 ns). Similarly, semiconductor samples doped with Si ions also exhibited a triple-exponential decay pattern, showing successful fitting. Moreover, highly conductive samples demonstrated a significantly faster decay of scintillation compared to pure crystals. This difference is evident in the average decay time of scintillation between pure crystals and those doped with Si, consistent with the findings from PHS measurements. These observations imply that doping directly affects the decay rate of the scintillation process by modifying the concentration of free carriers in the crystal.

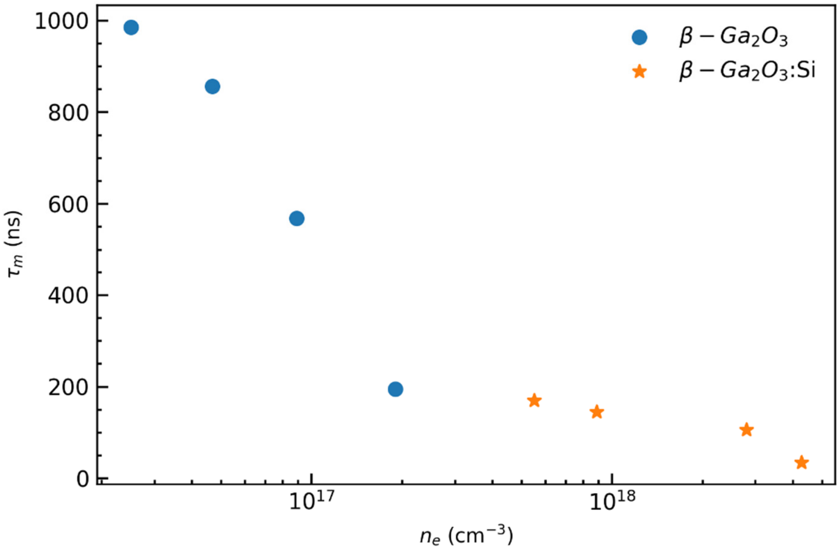

Fig. 5.14. Scintillation time profile as a function of free carrier concentration.

Upon analyzing **Figs 5.9** and **5.14**, it becomes apparent that in the context of gallium oxide crystals, achieving a specific concentration of free carriers around 10^{17} cm^{-3} is crucial. This concentration range enables the maintenance of relatively high scintillation yields and ensures shorter mean decay times, essential factors for efficient scintillation processes. However, when considering doping with Si ions, which is elaborated upon in this section of the study, there are additional considerations. While Si doping results in shorter decay times, it also significantly influences the scintillation decay rate and efficiency. The introduction of Si ions alters the crystal's properties, affecting its response to ionizing radiation and thereby impacting its scintillation characteristics. Moreover, doping the starting material during crystal growth introduces complexities. This process can increase the likelihood of introducing various impurities into the crystal structure, which may further influence its scintillation properties. Therefore, understanding the effects of doping and carefully controlling the crystal growth process are essential for optimizing scintillation performance in gallium oxide crystals.

5.1.3 Radioluminescence of β-Ga_2O_3 and β-Ga_2O_3:Si

In this section the results of radioluminescence spectra measurements for both doped and undoped crystals of gallium oxide are presented. For each sample, two figures were generated. The first figure displays RL spectra acquired at specific representative temperatures: 10, 100, 200, and 350 K (left part of the figure), alongside the dependencies of RL yield (divided into two components) on temperature (right part of the figure). The second figure illustrates all radioluminescence spectra plotted as a function of temperature, presented in the form of a spectral map.

It can easily be noticed that the shape of the excitonic emission band does not change from sample to sample. The differences can only be noticed in thermal dependencies. Therefore, utilizing the Shibata's model [3], adjustments were made for thermal luminescence quenching (Eq 5.2). The Shibata's model is depicted in **Fig. 5.15,** where A and G denote the initial and final states, respectively, between which the luminescence process takes place. Electrons thermally excited from the B_i states elevate the occupancy of state A, leading to the emergence of extra peaks on the TQ plots. This phenomenon is termed negative thermal luminescence quenching (NTQ). Between state A and states E_j, non-radiative processes occur, resulting in luminescence quenching as the crystal temperature rises.

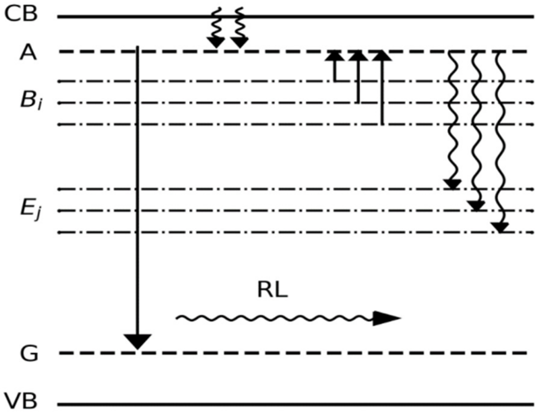

Fig. 5.15. Illustrative diagram of the band structure model proposed by Shibata.

The change in occupancy of state A over time can be described by the formula:

$$\frac{\partial A(t,T)}{\partial t} = A^{(0)} + A^{(1)} + A^{(2)} + A^{(3)} \tag{5.2}$$

where $A^{(0)}$, $A^{(1)}$, $A^{(2)}$, $A^{(3)}$, respectively, are contributions originating from:

- relaxation of electrons to state A from all higher states (CB → A),

- radiative transitions (A → G),

- temperature-dependent non-radiative transitions (A → E_j),

- thermal excitations of electrons from lower states (B_i → A).

For k possible radiative transitions in the material, the coefficient $A^{(1)}$ can be expressed by the formula:

$$A^{(1)} = -\sum_k \frac{A(t,T)}{\tau_k} \tag{5.3}$$

where τ_k is the lifetime of the k-th emission. For j possible non-radiative transitions, the coefficient $A^{(2)}$ can be expressed by the formula:

$$A^{(2)} = -\sum_j \frac{A(t,T)}{\gamma_i} \tag{5.4}$$

where

$$\frac{1}{\gamma_j} = \Gamma_j \exp\left(-\frac{E_j^D}{k_B}\right) \tag{5.5}$$

where γ_i is the lifetime of the j-th non-radiative emission, E_j^D is the activation energy of the j-th transition, and Γ_j is the proportionality coefficient, and k_B is the Boltzmann constant (expressed in eV/K). For i possible thermal excitations of electrons from lower energy states, the factor $A^{(3)}$ can be expressed by the formula:

$$A^{(3)} = -\sum_i \lambda_i B_i \tag{5.6}$$

where

$$\lambda_i = \Lambda_i \exp\left(-\frac{E_i^N}{k_B T}\right) \tag{5.7}$$

where λ_i and Λ_i are the proportionality coefficients, and E_i^N is the energy difference between state A and states B_i.

Based on the above formulas, the luminescence intensity as a function of temperature can be expressed by the formula:

$$A(T) = A(0)\frac{1+\sum_i D_i \cdot \exp\left(-E_i^N/k_B T\right)}{1+\sum_J C_J \cdot \exp\left(-E_j^D/k_B T\right)} \tag{5.8}$$

where:

$$A(0) = \frac{A^{(0)}}{\sum_k \tau_k},\ D_i = \frac{\lambda_i B_i}{A^{(0)}},\ C_i = \frac{\Gamma_j}{\sum_k \tau_k}$$

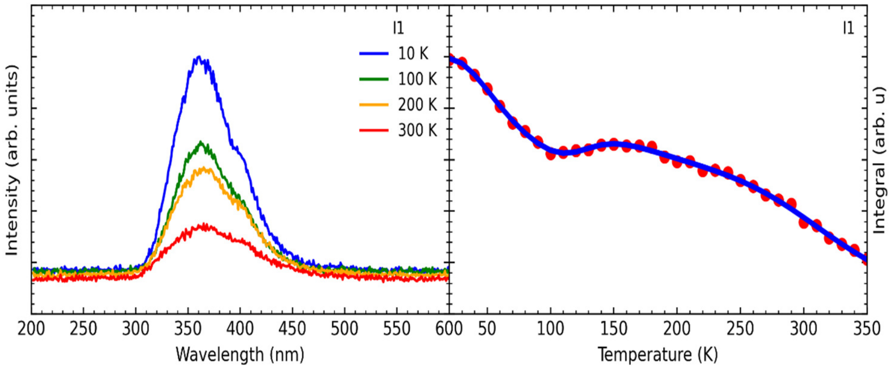

Fig. 5.16. Radioluminescence spectra for four specific temperatures (left side) and the NTQ chart with its fitting (right side) for β-Ga_2O_3 sample I1.

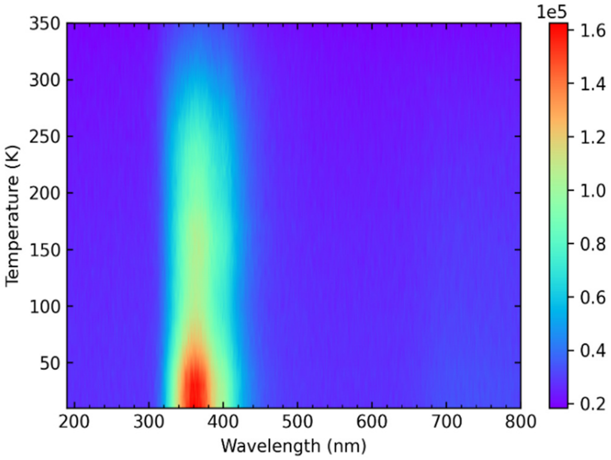

Fig. 5.17. Spectral map for β-Ga_2O_3 sample I1.

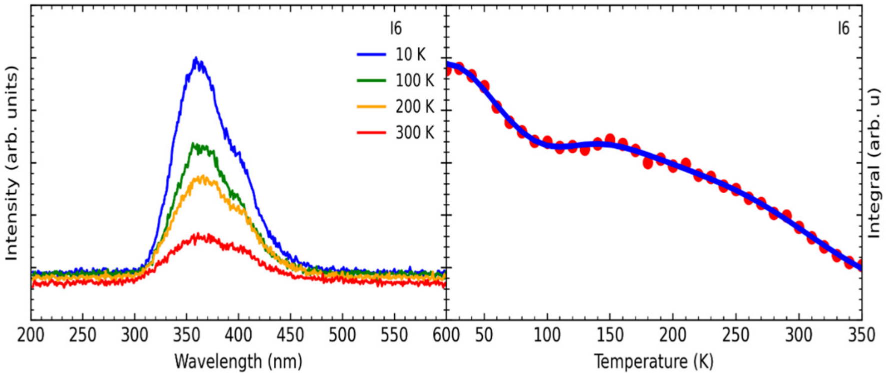

Fig. 5.18. Radioluminescence spectra for four specific temperatures (left side) and the NTQ chart with its fitting (right side) for β-Ga_2O_3 sample I6.

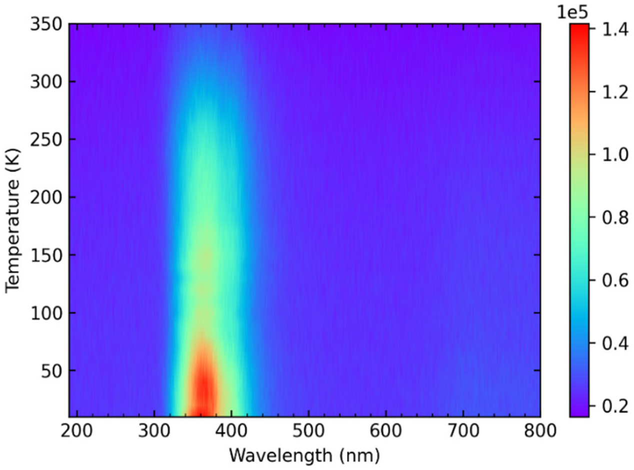

Fig. 5.19. Spectral map for β-Ga_2O_3 sample I6.

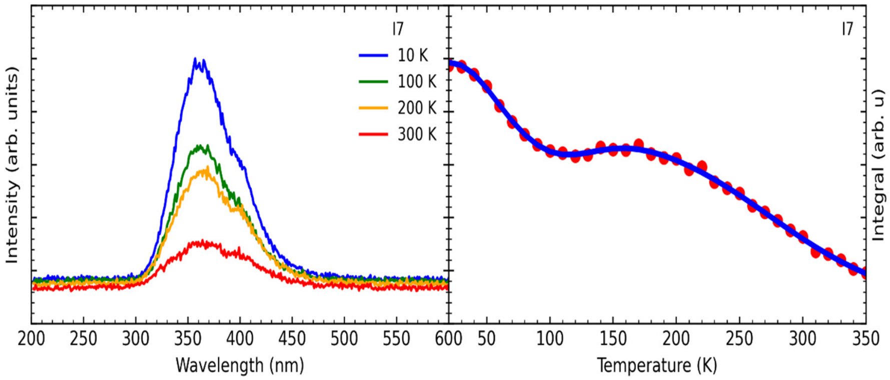

Fig. 5.20. Radioluminescence spectra for four specific temperatures (left side) and the NTQ chart with its fitting (right side) for β-Ga_2O_3 sample I7.

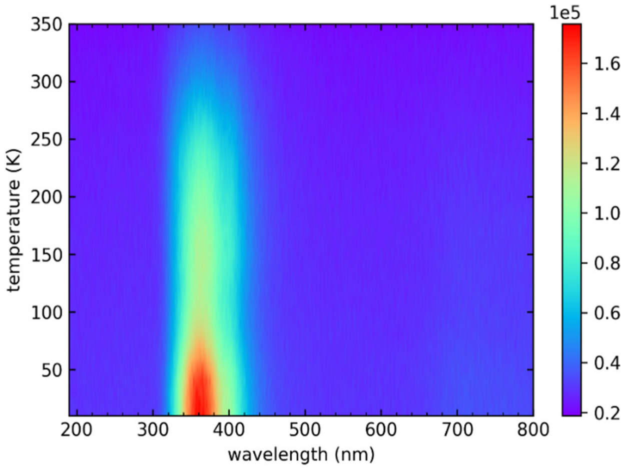

Fig. 5.21. Spectral map for β-Ga_2O_3 sample I7.

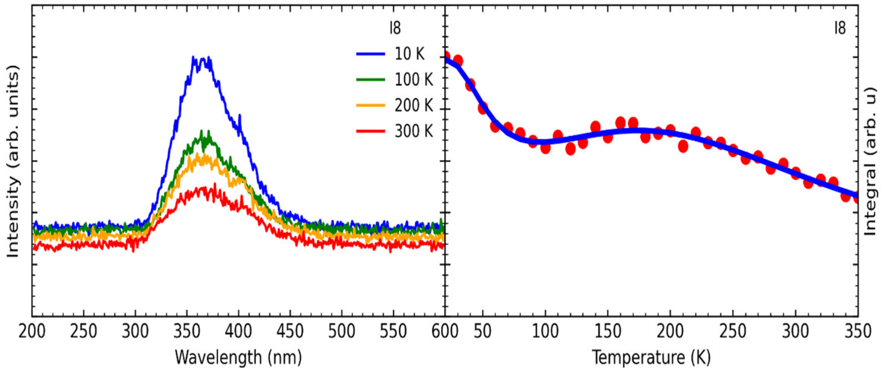

Fig. 5.22. Radioluminescence spectra for four specific temperatures (left side) and the NTQ chart with its fitting (right side) for β-Ga_2O_3 sample I8.

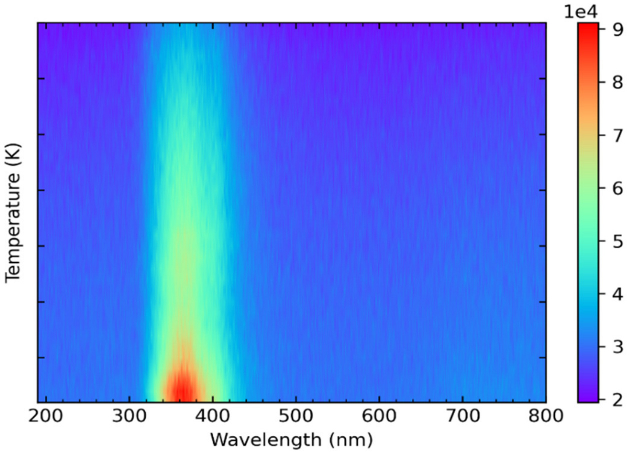

Fig. 5.23. Spectral map for β-Ga_2O_3 sample I8.

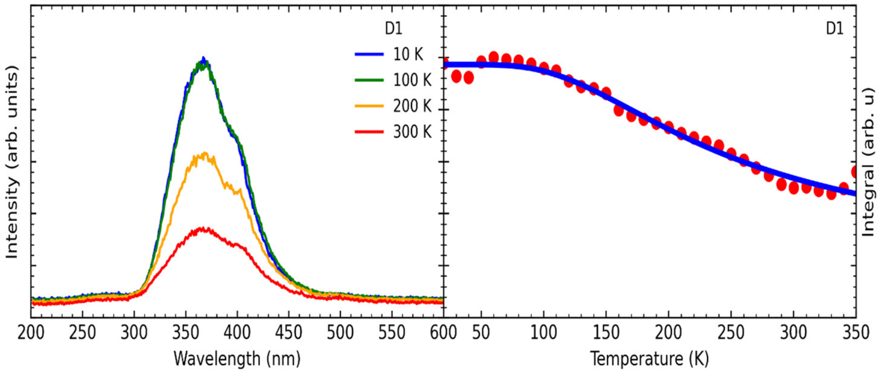

Fig. 5.24. Radioluminescence spectra for four specific temperatures (left side) and the NTQ chart with its fitting (right side) for β-Ga_2O_3:Si sample D1.

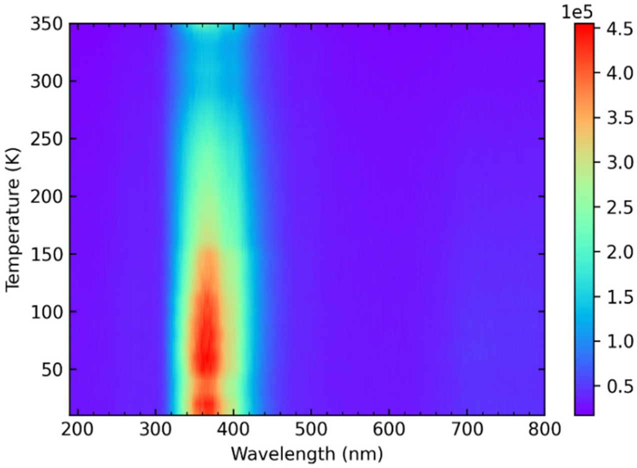

Fig. 5.25. Spectral map for β-Ga_2O_3:Si sample D1.

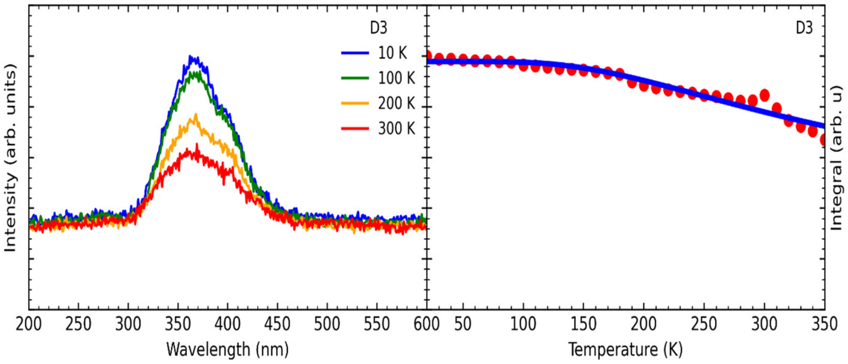

Fig. 5.26. Radioluminescence spectra for four specific temperatures (left side) and the NTQ chart with its fitting (right side) for β-Ga_2O_3:Si sample D3.

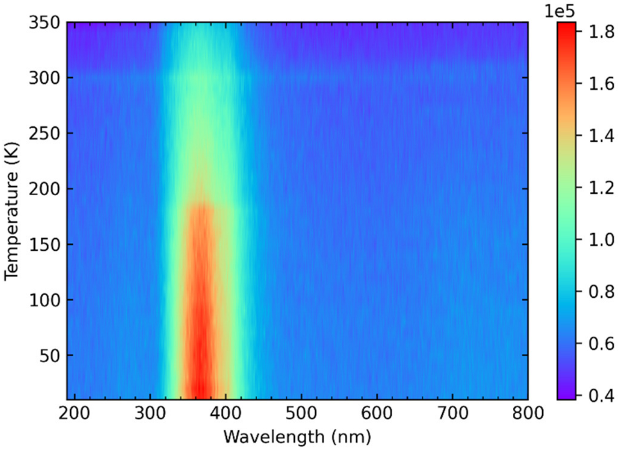

Fig. 5.27. Spectral map for β-Ga_2O_3:Si sample D3.

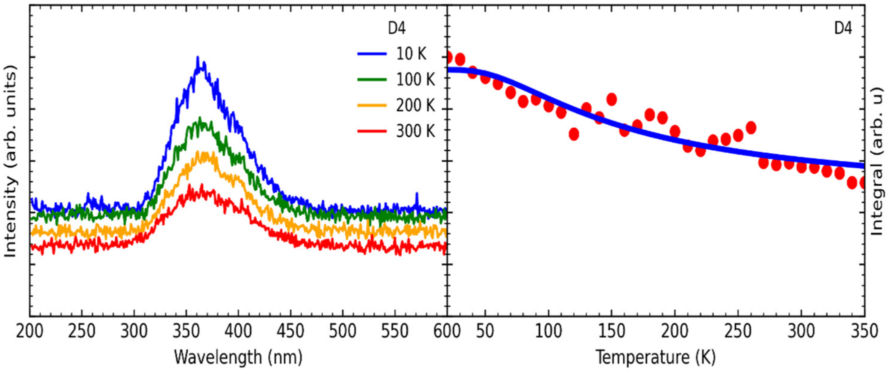

Fig. 5.28. Radioluminescence spectra for four specific temperatures (left side) and the NTQ chart with its fitting (right side) for β-Ga_2O_3:Si sample D4.

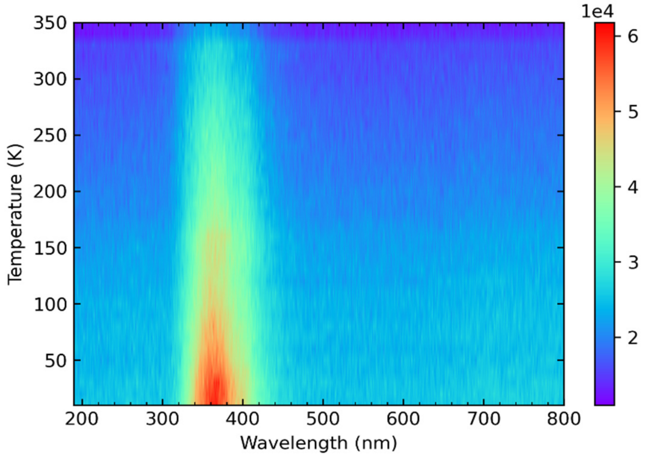

Fig. 5.29. Spectral map for β-Ga_2O_3:Si sample D4.

Tab. 5.6. Fitting parameters of the NTQ curves for samples from the first series of crystals.

ID	**Sample**	**n_e (cm^3)**	**A(0)**	**D1**	**E_1^N (meV)**	**C1**	**E_1^D (meV)**	**C2**	**E_2^D (meV)**	**C3**	**E_3^D (meV)**
I1	β-Ga_2O_3	$2.5 \cdot 10^{16}$	$1.07 \cdot 10^7$	$7.75 \cdot 10^3$	103	2.48	12	$2.2 \cdot 10^4$	113	$5.93 \cdot 10^7$	343
I6	β-Ga_2O_3	$4.66 \cdot 10^{16}$	$8.9 \cdot 10^6$	$7.88 \cdot 10^2$	70	2.77	14	$1.36 \cdot 10^3$	84	$2.93 \cdot 10^6$	307
I7	β-Ga_2O_3	$8.90 \cdot 10^{16}$	$1.12 \cdot 10^7$	$1.98 \cdot 10^2$	67	3.26	15	$7.46 \cdot 10^2$	85	2.55·105	248
I8	β-Ga_2O_3	$1.90 \cdot 10^{17}$	$5.56 \cdot 10^6$	7.61	26	6.29	13	$1.19 \cdot 10^2$	97	-	-
D1	β-Ga_2O_3:Si	$2.80 \cdot 10^{18}$	$5.21 \cdot 10^7$	-	-	4.58	47	-	-	-	-
D3	β-Ga_2O_3:Si	$4.27 \cdot 10^{18}$	$4.65 \cdot 10^7$	-	-	4.42	58	-	-	-	-
D4	β-Ga_2O_3:Si	$8.87 \cdot 10^{17}$	$3.12 \cdot 10^6$	-	-	1.20	19	-	-	-	-

Based on the data provided in tables **Tab. 5.6**, the band structure scheme proposed by Shibata was modified to be suitable for β-Ga_2O_3 crystals (Figure 5.64).

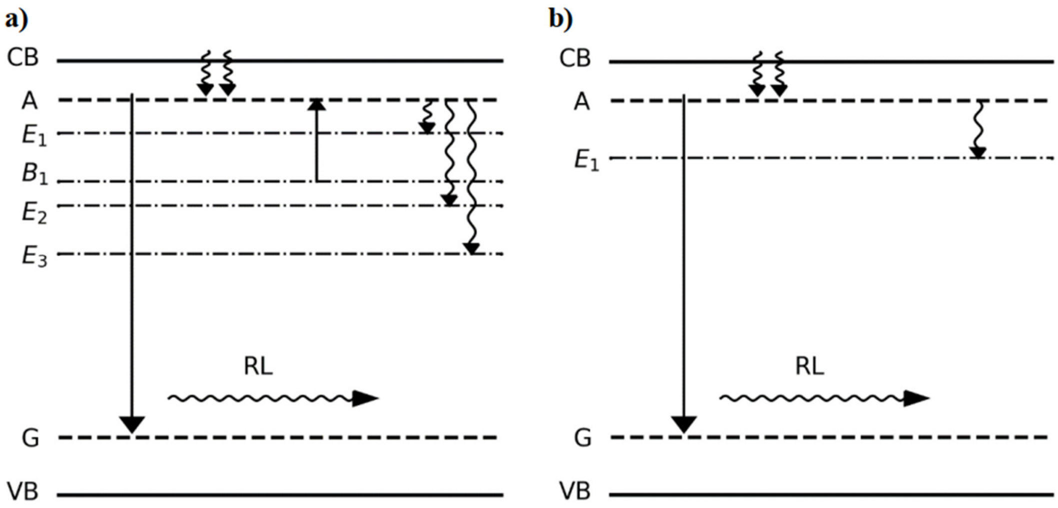

Fig. 5.30. Band structure scheme of gallium oxide crystals without silicon doping (a) and with silicon doping (b).

It is worth noting that depending on the sample, the B_1 and E_2 levels change their positions, swapping places. Additionally, based on the data provided in **Tab .5.6**, it can be observed that with an increase in the concentration of free carriers in the crystal, the distance between the B_1 and A levels decreases, resulting in a decrease in the activation energy of the respective transition.

In addition to the quantitative analysis presented, it is also important to consider the thermal dependence of RL qualitatively. For each of the crystals studied, it was observed that the RL efficiency (measured by the area under the RL spectrum) at room temperature is significantly lower than at the temperature of liquid helium or nitrogen. This difference is more pronounced for pure samples and those containing silicon, and smaller but still visible for samples with silicon. This implies that measuring scintillation efficiency based on pulse height spectra, if conducted at low temperatures, would likely yield high results on the order of tens of thousands of ph/MeV. This indicates a significant potential in β-Ga_2O_3, which could be utilized in the future if a way to reduce thermal damping is found.

5.1.4 Thermoluminescence of β-Ga_2O_3 and β-Ga_2O_3:Si

The last of the techniques used for the characterization of scintillators is thermoluminescence. It is one form of luminescence that involves the emission of electromagnetic radiation after a time period not shorter than 10 seconds as a result of energy absorption by the particles of the substance under investigation. To be more precise, thermoluminescence pertains to non-stationary luminescence that appears along with the increase in temperature of the substance previously excited by ionizing radiation, thermally releasing charge carriers from traps occurs, followed by their recombination with ionized luminescent centers.

To fully understand the process of thermoluminescence, knowledge of band theory of dielectrics is required. The simplest situation is an ideal dielectric, which contains only a filled valence band, a wide energy gap, and an empty conduction band. However, all materials contain certain irregularities (defects) in the structure of the crystal lattice, presented in the form of electron or hole traps. For simplicity, we will limit our interest to electron traps and also consider the presence of spontaneous or intentionally introduced luminescent centers (as impurities) into the material.

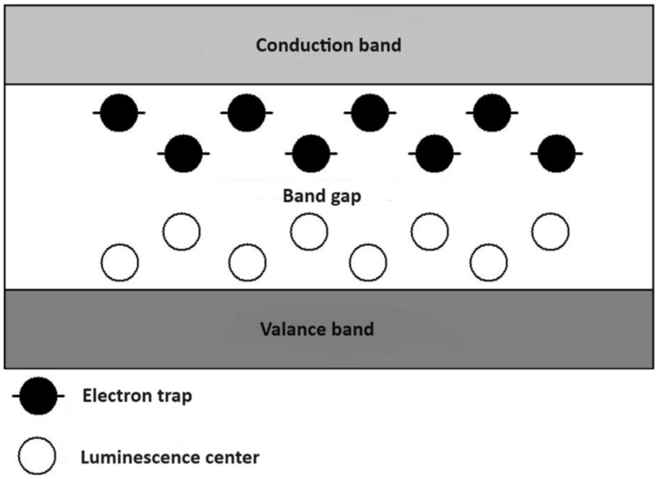

Fig. 5.31. Diagram of a dielectric including electron traps and luminescent centers.

The process of thermoluminescence essentially consists of two stages: ionizing radiation absorption and thermal excitation. In the first stage, electrons are excited by ionizing radiation and move to the conduction band, where they diffuse until they recombine with a hole in the valence band or are captured by an electron trap. An electron captured by an electron trap becomes bound to the energy of that trap and may contribute to the thermoluminescence process. Trapped electrons can be released from the trap by supplying them with energy optically or thermally. Traps can have various depths, with the shallowest traps being able to be emptied much faster than the deeper ones (however not only the depth plays a role). The last element of the first stage of the process is the recombination of spatially and energetically diffusing holes formed due to the excitation of electrons in the upper layer of the valence band with electrons occupying defects in the crystal lattice. The processes occurring in the dielectric are depicted in the diagram below (**Fig. 5.32**). An electron excited from the valence band to the conduction band due to ionizing radiation (1) undergoes diffusion (2) and can then be trapped by a trap (3), recombine with a luminescent center, emitting a quantum of radiation in the process (6), or recombine with a hole in the valence band (7). Electron diffusion may not occur in the conduction band but may occur in the valence band (4), resulting in recombination with an electron located at the luminescent center (5).

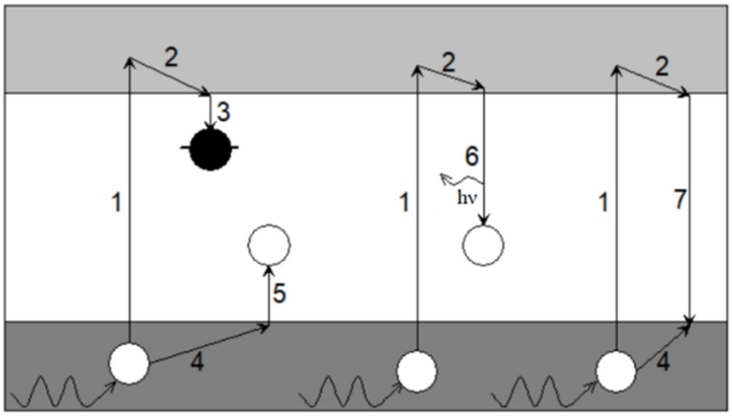

Fig. 5.32. Diagram of processes occurring in a dielectric.

The second stage, called thermal excitation, is a phenomenon that involves the recombination of previously trapped electrons with luminescence centers. This recombination occurs when energy exceeding the trap depth is supplied, allowing the electron to transition to the conduction band. This energy is called the activation energy. Subsequently, the electron diffuses near the luminescence center, where it recombines, releasing the excess energy provided to it in the form of radiation quanta.

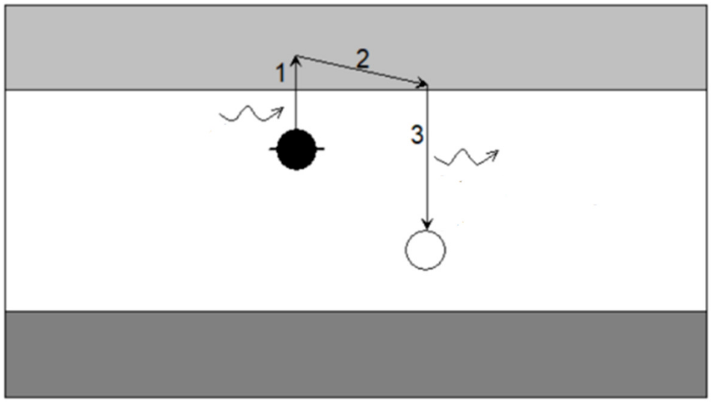

Fig. 5.33. Thermal excitation schematic (1 - heat, 3 - quantum of radiation).

The description of the phenomenon of thermoluminescence contains a considerable amount of mathematics, and one of the fundamental relationships is the classical Arrhenius equation, which determines the probability p of releasing an electron from the trap and the lifetime τ of this trap as follows:

$$p = \frac{1}{\tau} = s \cdot \exp\left(-\frac{E}{k_B T}\right) \tag{5.9}$$

where s is the so-called "attempt-to-escape frequency", E is the trap depth (expressed in eV), k_B is the Boltzmann constant (expressed in eV/K), and T is the temperature (expressed in K). The attempt-to-escape frequency is expressed in inverse seconds (s^{-1}), and its typical values range from 10^7 to 10^{15} s^{-1}. By choosing $s = 10^{14}$ s^{-1} we stay within this typical range, ensuring that our model is physically realistic and aligns with observed behavior in similar materials. Another important quantity is the number of trapped electrons released per unit time at a specific temperature, given by the relationship:

$$\frac{\mathrm{dn}}{\mathrm{dt}} = -\mathrm{n}^{\mathrm{b}}\mathrm{s} \cdot \exp\left(-\frac{\mathrm{E}}{\mathrm{k_B T(t)}}\right) \tag{5.10}$$

where n is the number of filled traps, and b is the order of kinetics. The order of kinetics describes the relationship between the probability of recombination of the liberated carrier from the trap (A_m) and the probability of its re-trapping (A_n). We distinguish between first and second-order kinetics as well as intermediate kinetics. First-order kinetics (b = 1) refer to a situation where the probabilities satisfy the condition $A_m >> A_n$ (recombination dominates), and the evolution of the system is described by the Randall-Wilkins equation [4]:

$$\mathrm{I(T)} = \mathrm{n_0 s/\beta} \cdot \exp\left(-\frac{\mathrm{E}}{\mathrm{K_B T}}\right) \exp\left[-\frac{\mathrm{s}}{\beta} \cdot \int_{\mathrm{T_0}}^{\mathrm{T}} \exp\left(-\frac{\mathrm{E}}{\mathrm{K_B T'}}\right)\mathrm{dT'}\right] \tag{5.11}$$

where the factor β represents the heating rate. In the reverse case, when $A_n >> A_m$ (re-trapping dominates), we refer to second-order kinetics (b = 2), which is described by the Garlick-Gibson equation [5]:

$$\mathrm{I(T)} = \mathrm{n_0}^2 \mathrm{s} \cdot \exp\left(-\frac{\mathrm{E}}{\mathrm{K_B T}}\right) \cdot \left[1 + \frac{\mathrm{n_0 s}}{\beta} \cdot \int_{\mathrm{T_0}}^{\mathrm{T}} \exp\left(-\frac{\mathrm{E}}{\mathrm{K_B T'}}\right) \mathrm{dT'}\right]^{-2} \tag{5.12}$$

The Randall-Wilkins and Garlick-Gibson equations are valid when we introduce the theoretical assumption of the existence of only one type of trap. In practice, there are many types of traps, so we must apply the following relationship (the one below concerns the first-order kinetics):

$$\mathrm{I(T)} = \sum_{i=1}^{N} \mathrm{n_{0,i}} s_i \cdot \exp\left(-\frac{\mathrm{E}_i}{\mathrm{k_B T}}\right) \cdot \exp\left[-\frac{s_i}{\beta} \cdot \int_{\mathrm{T_0}}^{\mathrm{T}} \exp\left(-\frac{\mathrm{E}_i}{\mathrm{k_B T'}}\right)\mathrm{dT'}\right] \tag{5.13}$$

An simplification of this model involves assuming a constant parameter s for each trap in the investigated material and replacing integration over energy with summation (due to various computational difficulties). By applying these approximations, we obtain the following model function:

$$\mathrm{M(T, E, s, A)} = \sum_{\mathrm{j=1}}^{\mathrm{N}} \mathrm{A_J s} \cdot \exp\left(-\frac{\mathrm{E_j}}{\mathrm{k_B T}}\right) \cdot \exp\left[-\frac{\mathrm{s}}{\beta} \cdot \int_{\mathrm{T_0}}^{\mathrm{T}} \exp\left(-\frac{\mathrm{E_j}}{\mathrm{k_B T'}}\right)\mathrm{dT'}\right] \tag{5.14}$$

where the energy values E_j belong to a certain range (E_0, E_n) created from n intervals of width ΔE, and A_j is a set of amplitudes characterizing the distributions of traps. Simulations have shown that any continuous distribution can be assumed for the unknown continuous distribution. Therefore, based on the work of Medlin [8], we can use Gaussian distributions G. In this case, our model takes the form:

$$I(T) = \sum_{j=1}^{n} \sum_{l=1}^{m} G(n_{0,l}, E_{0,l}, \sigma_l, E_j)\, s \cdot \exp\left(-\frac{E_j}{k_B T}\right) \cdot \exp\left[-\frac{s}{\beta} \cdot \int_{T_0}^{T} \exp\left(-\frac{E_j}{k_B T'}\right) dT'\right] \Delta E \tag{5.15}$$

The method of fitting distributions is very effective for ceramic materials because we can treat them as assemblies of small crystals. A single peak in the thermoluminescence spectrum will not have a single defined energy in this method, but rather several different energy values depending on how many Gaussian functions were applied in a given distribution along with their contributions to the total glow curve.

In order to assess the quality of the fits we employ the FOM (figure of merit) parameter proposed by Bos et al. [9] and Chen [10], which can be expressed as:

$$\mathrm{FOM} = \sum_{i=1}^{N} \frac{|I_i - M(T_i)|}{A} \cdot 100\% \tag{5.16}$$

in which i numbers the successive datapoints, I_i are the experimental values of TL intensity at temperatures T_i, $M(T_i)$ – the values of the fitted function at T_i, and A – the integral of the fitted glow curve. The values of FOM not exceeding a few percent usually indicate good fits (the lower the value, the better the fit) [9]. As an alternative parameter for the fit quality evaluation we utilize the adjusted coefficient of determination R^2 defined as:

$$\bar{R}^2 = 1 - \frac{\sum_{i=1}^{N}(I_i - M(T_i))^2}{\sum_{i=1}^{n} I_i^2} \frac{N}{N-P} \tag{5.17}$$

(N – the total number of datapoints, P – the number of model parameters). The closer to unity the value of R^2, the better the fit.

Some of the examined glow curves of β-Ga_2O_3 (pure, not doped) exhibit a prominent peak around 80 K. The bottom part of **Fig. 5.34** and **Fig. 5.36** depicts the comprehensive thermoluminescence measurement, encompassing experimental data, the heating profile, a tri-exponential fit employed to diminish background noise, and a linear fit to the heating profile essential for determining the heating rate β. Subsequent figures, the left parts of **Fig. 5.34** and **Fig. 5.36** show the heating profile, while the right parts depict the glow peaks observed in the samples. Subsequently, in **Fig. 5.35** and **Fig. 5.37**, a histogram is presented, describing the distribution of peaks utilized for fitting the glow curve. Alongside the overall histogram, smaller windows are depicted, offering a magnified view of less prominent sections of the entire histogram. The solid black line denotes the envelope, while the colored dashed lines represent individual distributions.

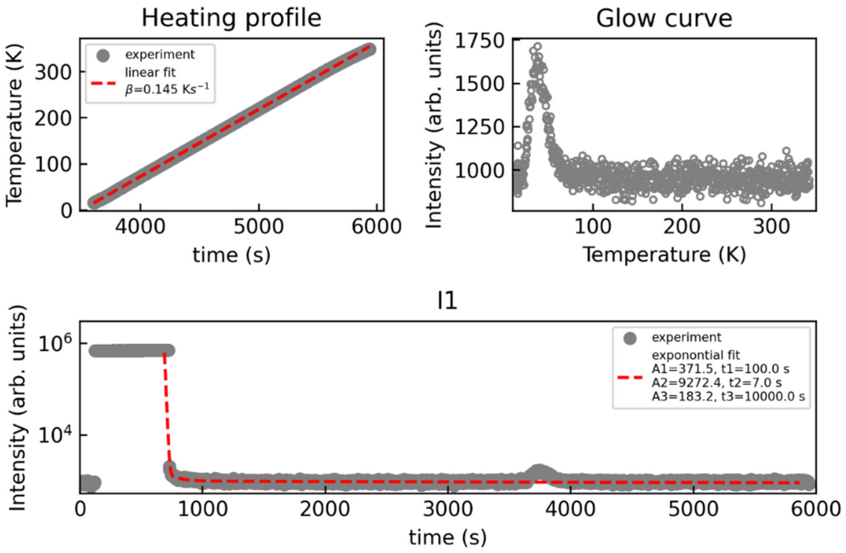

Fig. 5.34. The chart depicting the overall thermoluminescence measurement of β-Ga_2O_3 sample I1.

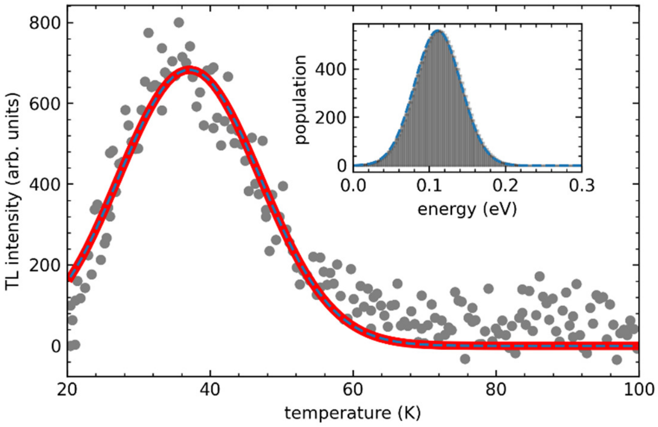

Fig. 5.35. The distribution of Gaussian distributions used for fitting traps for β-Ga_2O_3 sample I1.

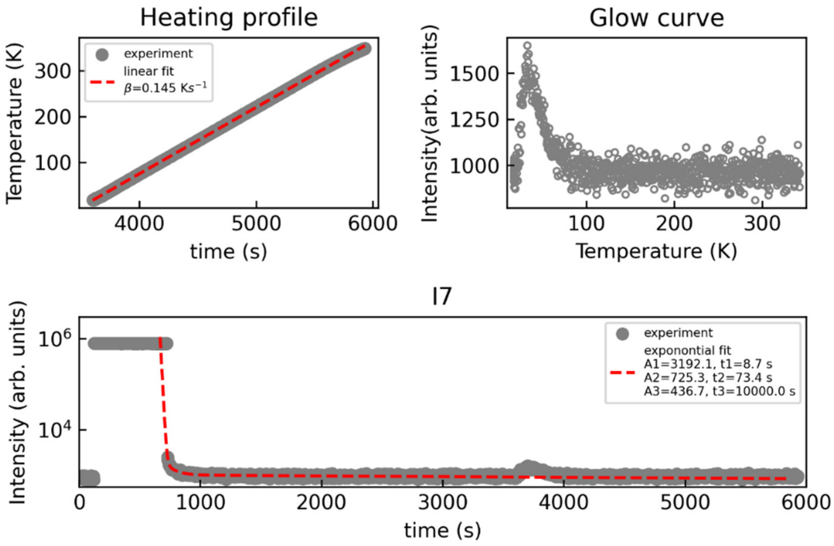

Fig. 5.36. The chart depicting the overall thermoluminescence measurement of sample β-Ga_2O_3 I7.

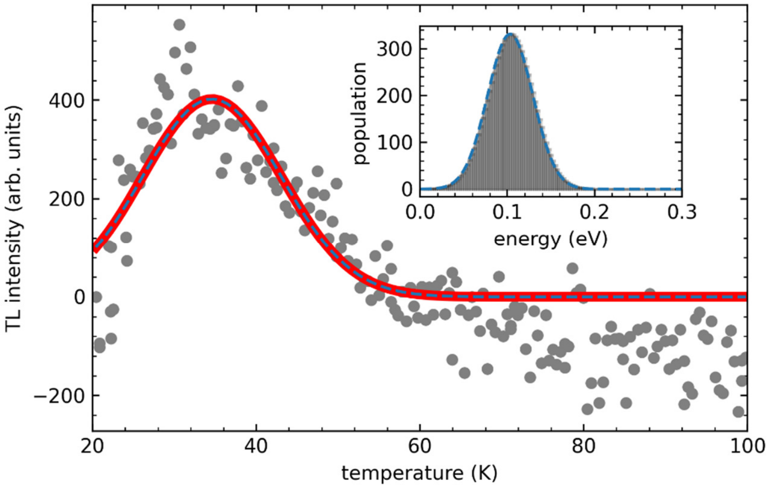

Fig. 5.37. The distribution of Gaussian distributions used for fitting traps for β-Ga_2O_3 sample I7.

We are particularly interested in the detailed fitting of the glow curve (see **Fig. 5.37** and **Fig. 5.35**), as it provides valuable insights into trap parameters. During our investigation, many of the samples examined (including all Si-doped) showed no signs of traps (no glow peaks), with the exception of two outliers, specifically I1 and I7, which displayed noticeable thermoluminescence characteristics. Fitting the glow curve allows us to extract essential parameters of individual distributions, such as their activation energy (E), amplitude (n_e), and the σ factor. The σ factor plays a critical role in determining the width of the Gaussian function at its midpoint. Additionally, smaller windows adjacent to the main peak offer detailed views of regions where smaller peaks are present. In the case of samples I1 and I7, we employed a model featuring single distributions to accurately capture the entire glow curve. Detailed information regarding these distributions can be found in the accompanying **Tab 5.7.**

Tab. 5.7. Parameters of the distribution used for fitting the glow curve of β-Ga_2O_3 samples I1 and I7.

ID	Sample	n_e (cm^{-3})	Distribution	E (meV)	σ (meV)	s (s^{-1})	FOM (%)	$\overline{R}^2$
I1	β-Ga_2O_3	$2.5 \cdot 10^{16}$	1	111	30	10^{14}	25	0.94
I7	β-Ga_2O_3	$8.9 \cdot 10^{16}$	1	103	26		34	0.88

Upon analyzing the parameters derived from the distribution data and their associated traps, it becomes evident that the sole trap present in each sample holds paramount importance. This single trap, situated at an energy level of 111 MeV for sample I1 and 103 MeV for sample I7, exhibits the highest significance. Conversely, there are no other traps present in these samples, emphasizing the dominance of this singular trap in determining the luminescence characteristics.

5.1.5 Temperature dependence of β-Ga_2O_3 and β-Ga_2O_3:Si

This section delves deeper into the setup used for temperature dependency measurements of relative light yield, already introduced in section **4.3.2**. Specifically, a cryostat tailored for experimentation with CsI:Tl scintillators [11] was utilized. This cryostat, comprising an aluminum cylinder with an 88 mm diameter, featured a beryllium window positioned at the top to enable investigation of the scintillator's response to low-energy γ-rays and X-rays. To cool the scintillator to a temperature close to the boiling point of LN_2, a copper frame attached to a copper rod was employed. Additionally, the MPPC (Multi-Pixel Photon Counter) was mounted on a separate copper frame, which was then connected to the outer aluminum walls of the cryostat, maintaining a distance of approximately 2 to 3 mm between the crystal's bottom surface and the MPPC to minimize temperature fluctuations of the photodetector resulting from crystal cooling and heating. A schematic of the experimental setup is depicted in **Fig. 5.38.**

Moreover, two 3-terminal fixed voltage regulators were mounted on the crystal holder and utilized as heaters to raise the scintillator's temperature to the desired level. This allowed for the adjustment of the sample's temperature between 90 K and room temperature (RT) when the copper rod was submerged in LN_2 or between RT and 451 K when the copper rod was exposed to ambient air. Two DT-600 silicon diode temperature sensors from Lake Shore Cryotronics were employed to monitor the temperatures of the sample and the MPPC. **Fig. 5.39,** displays photographs of the inner portion of the cryostat assembled prior to a measurement session. Despite the thermal coupling of the MPPC with the cryostat housing and the cryostat being maintained in a vacuum, heat dissipation occurred during cooling with LN_2 and heating using the voltage regulators, resulting in temperature fluctuations of the MPPC ranging between 287 and 316 K. Considering the sensitivity of MPPC gain to temperature variations [12], a procedure was implemented to ensure consistent gain throughout the experiment. Initially, after reaching a stable temperature, the breakdown voltage of the MPPC at the specified temperature was measured using a high-precision Keysight B2901A source/measure unit. Subsequently, the MPPC was biased using the same device with a 2.000 V overvoltage of negative polarity. Following this, the γ-ray response of the scintillator with MPPC readout was recorded. Throughout this process, temperature fluctuations were maintained below 1 °C. The temperature of the setup was then adjusted, and the measurement procedure was repeated.

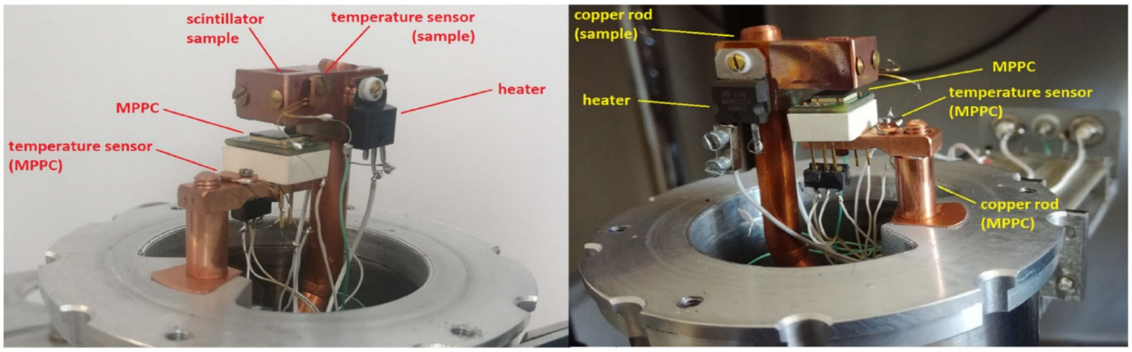

Fig. 5.38. The inside of the LN_2 cooled cryostat with a tested scintillator and the MPPC photodetector mounted on separate copper frames.

The temperature dependence of the relative light output was assessed using 662 keV γ-rays emitted from a ^{137}Cs source. Two distinct shaping time constants, namely 1 µs and 10 µs, were applied independently, with the latter aimed at incorporating contributions from slower components. Furthermore, supplementary measurements of photoelectron yield were conducted at 1 µs and 10 µs shaping time intervals using a Hamamatsu R6231 photomultiplier tube (PMT) at room temperature, serving as a reference for model calculations.

Our approach to studying the temperature dependence of light yield necessitated the separation of the photodetector from the tested sample undergoing either cooling or heating. Consequently, changes in relative light yield were measured, and the energy resolution of spectra recorded at various temperatures was not optimal, owing to inherent light losses associated with the transfer of scintillation light to the MPPC. **Fig 5.39** displays pulse height spectra captured at various temperatures for the brightest β-Ga_2O_3 crystal ($n_e = 2.5 \cdot 10^{16}$ cm^{-3}). As temperature increases, the Full Energy Peak (FEP) visibly shifts towards lower channels, indicating a decrease in scintillation yield. **Fig. 5.40** illustrates the dependence of yield on temperature, based on the positions of FEPs. Due to the unsuitability of 0.5 mm thick samples for temperature-dependent investigations using the setup, a 2.5 mm thick sample was obtained from the same bulk crystal. Consequently, its observed scintillation yield at room temperature (RT) is slightly lower than the previously determined 9,090 ph/MeV for the 0.5 mm thick sample, attributed to significant internal light losses in β-Ga_2O_3. Nonetheless, for clarity in **Fig. 5.40**, we maintain the value of 9,090 ph/MeV as the reference level at RT. Notably, only 40% of the yield is retained at RT compared to 90 K. This significant difference can be attributed to the decrease in free electron concentration towards lower temperatures, a typical behavior in semiconductors, as previously observed in Czochralski-grown β-Ga_2O_3 crystals. By approximating the scintillation yield at 60 K, where the free electron concentration substantially diminishes, a value of about 23,000 ph/MeV is obtained, suggesting a "semi-empirical limit" for β-Ga_2O_3. It is important to note that apart from the temperature-dependent free electron concentration, thermal quenching mechanisms, possibly linked to the thermal activation of non-radiative recombination processes at Fe impurities, along with contributions from Auger quenching, may also contribute to the decline in yield with temperature.

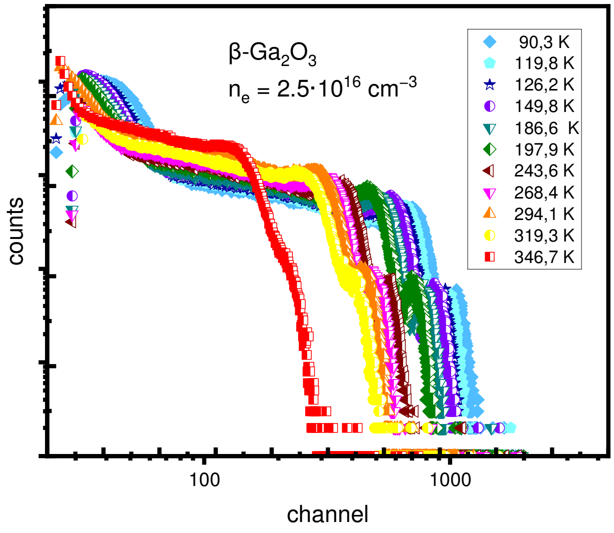

Fig. 5.39.Pulse height spectra of β-Ga_2O_3 measured at various temperatures between 90.3 and 346.7 K.

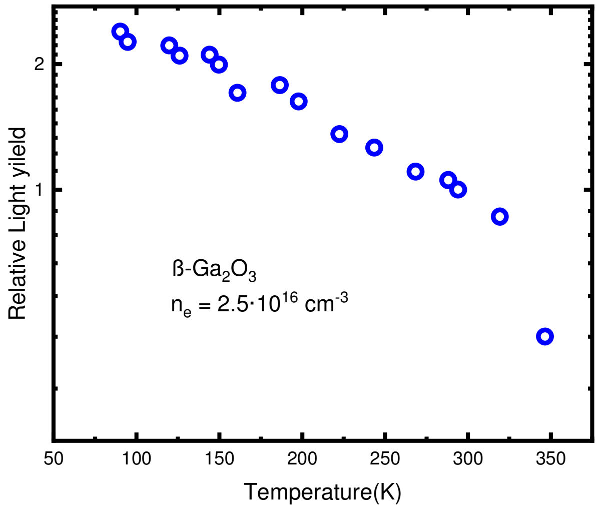

Fig. 5.40. Scintillation yield as a function of temperature of β-Ga_2O_3.

5.2 $MgGa_2O_4$ and $ZnGa_2O_4$ single crystals

In this section an analysis of the fundamental scintillation characteristics observed for $MgGa_2O_4$ and $ZnGa_2O_4$ crystals, produced at Leibniz-Institut für Kristallzüchtung in Berlin using the Czochralski and Vertical Gradient Freeze methods, respectively, will be presented. Our findings highlight that both Ga-based spinels exhibit scintillation behavior upon exposure to gamma radiation, with current scintillation yields reaching levels of approximately 2,500 ph/MeV. Moreover, we delve into the examination of scintillation time profiles, uncovering an inverse correlation between scintillation yields and decay rates; specifically, lower yields are associated with faster decays. Additionally, our observations suggest that the radioluminescence of both $MgGa_2O_4$ and $ZnGa_2O_4$ is notably more pronounced at lower temperatures, indicating the presence of robust thermal quenching mechanisms that diminish their yields as they approach room temperature.

Tab. 5.8. Growth Details and Scintillation Properties of the Studied $MgGa_2O_4$ and $ZnGa_2O_4$ Samples (Cz – Czochralski, VGF – Vertical Gradient Freeze, O_2 - Oxygen Concentration in the Growth Atmosphere, n_e - Free Electron Concentration, Y - Scintillation Yield, R - Energy Resolution at 662 keV, τ_i - Scintillation Decay Time Constants with Their Contributions, τ_{mean} - Scintillation Mean Decay Time).

Material	**ID**	**Growth method**	**O_2 (vol%)**	**n_e (cm^{-3})**	**Y (ph/MeV)**	**R (%)**	**τ_i (ns)**	**τ_{mean} (ns)**
$MgGa_2O_4$	Mg1	Cz	0.6	insulator	very low	n/a	17.4 (18%) 137 (31%) 823 (51%)	466
	Mg2	Cz	2	insulator	920	30.9	14 (10%) 85.8 (31%) 676 (59%)	427
	Mg3	VGF	10^{-4}	$1.5\cdot10^{18}$	2490	29.9	36.3 (7%) 208 (20%) 1495 (73%)	1130
$ZnGa_2O_4$	Zn1	VGF	2	$5\cdot10^{18}$	2120	19.5	36.3 (4%) 202 (17%) 1449 (79%)	1180
	Zn2	VGF	20	$3\cdot10^{19}$	very low	n/a	12.8 (9%) 73.1 (36%) 435 (55%)	267
	Zn3	VGF	2	$3\cdot10^{19}$	very low	n/a	11.7 (12%) 56.9 (39%) 309 (49%)	175

5.2.1 Pulse height spectra of $MgGa_2O_4$ and $ZnGa_2O_4$

The pulse height spectra of $MgGa_2O_4$ and $ZnGa_2O_4$ spinel samples were recorded using a gain of 0.3×10 and a shaping time of 2 μs, i.e. with the same experimental settings as for β-Ga_2O_3.

Fitting of the full energy peak was carried out using a single Gaussian function. This analysis provided a scintillation efficiency, derived from the photomultiplier's quantum efficiency determined through radioluminescence.

Fig. 5.41 and **Fig. 5.42** display the pulse height spectra of the three $MgGa_2O_4$ and three $ZnGa_2O_4$ samples, respectively. **Tab 5.8** summarizes the values of scintillation yield and energy resolution. The sample IDs were provided, where possible, in ascending order of the free electron concentration level, starting from electrical insulators or semi-insulators (where the Hall effect was not measurable and resistivity was > 10^8 Ω cm) and ending with the highest values of the free electron concentration.

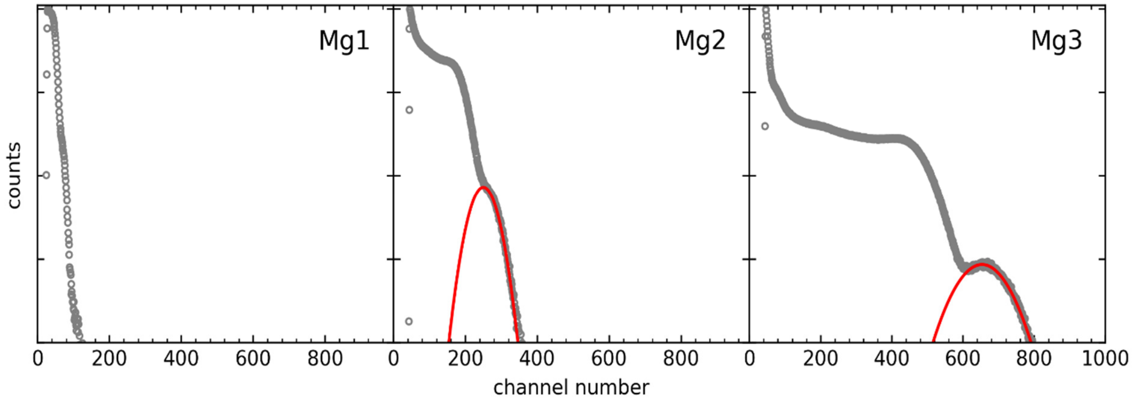

Fig. 5.41. Pulse height spectra of the $MgGa_2O_4$ samples.

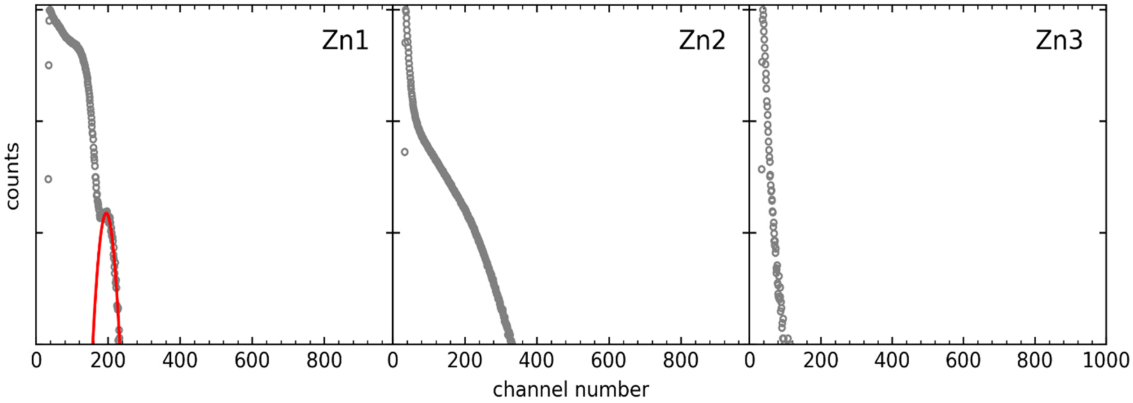

Fig. 5.42. Pulse height spectra of the $ZnGa_2O_4$ samples.

The initial pair of $MgGa_2O_4$ samples (Mg1 and Mg2), synthesized via the Czochralski technique, demonstrate electrical insulating properties. However, their pulse height spectra exhibit noticeable differences. Mg1 shows no distinct full energy peak, making it difficult to accurately estimate its scintillation yield, even with the Compton edge as a reference. Therefore, to avoid potential misinformation, we categorize its yield as "very low". Additionally, the absence of a full energy peak complicates the determination of its energy resolution. Conversely, the insulating Mg2 sample displays a pulse height spectrum with a well-resolved full energy peak, enabling the calculation of its scintillation yield (920 ph/MeV) and energy resolution (30.9%). This variance suggests that the Mg2 sample may have a higher residual free electron concentration. Notably, despite the unmeasurable Hall effect, the residual free electron concentration in oxide semiconductors like Mg2 could potentially reach levels of 10^{15} cm^{-3} or lower, leading to their classification as semi-insulators. In contrast, the semiconducting Mg3 sample, produced via the VGF method, emerges as the most promising specimen in this comparison. It exhibits a scintillation yield approaching 2,500 ph/MeV with an energy resolution of 29.9%.

For $ZnGa_2O_4$, three semiconductor samples with varying levels of free electron concentration are studied. The initial sample, Zn1, features a pulse height spectrum with a well-defined full energy peak, resulting in a scintillation yield of 2,120 ph/MeV and an energy resolution of 19.5%. However, the remaining two samples, Zn2 and Zn3, with significantly higher free electron concentrations, lack discernible full energy peaks in their pulse height spectra. Similar to the Mg1 sample, their scintillation yields must be considered as very low. It is worth noting the observed patterns in β-Ga_2O_3 crystals: insulating crystals demonstrate poor scintillation properties, while semiconducting ones exhibit robust scintillation, with scintillation yield decreasing as free electron concentration rises.

Essentially, the most promising scintillating samples exhibit relatively low levels of electrical conductivity, around mid-10^{16} cm^{-3}. This trend appears consistent in both $MgGa_2O_4$ and $ZnGa_2O_4$. Neither the insulating crystals of $MgGa_2O_4$ nor the highly conducting crystals of $ZnGa_2O_4$ present ideal candidates for scintillation. Only crystals with free electron concentrations on the order of 10^{18} cm^{-3}, in both $MgGa_2O_4$ and $ZnGa_2O_4$, display promising scintillation properties, especially regarding scintillation yield. It is plausible that a further reduction in free electron concentration while maintaining the semiconductor state could yield even higher scintillation yields, similar to β-Ga_2O_3. However, it is important to note that the source of electrical conductivity in Ga-based spinels (antisite defects) differs from that in β-Ga_2O_3 (dopants or impurities).

5.2.2 Scintillation time profiles of $MgGa_2O_4$ and $ZnGa_2O_4$

The scintillation time profiles, depicted in **Fig. 5.43** and **Fig. 5.44**, offer valuable insights into the behavior of $MgGa_2O_4$ and $ZnGa_2O_4$, respectively. These profiles, remain unaffected by afterpulses, ensuring their suitability for accurate decay time constant calculations. By employing a three-exponential decay fitting approach, we achieve satisfactory alignment between the experimental and fitted time profiles, yielding precise results. **Tab 5.8** present the decay constants and their contributions for all investigated samples. Additionally, to enhance comparability, further insights are gained through the scintillation mean decay time (τ_{mean}), as discussed previously.

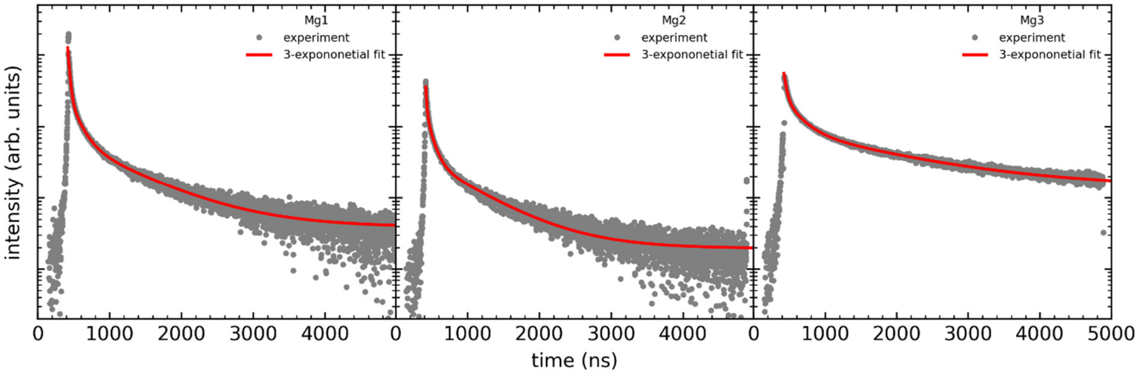

Fig. 5.43. Scintillation time profiles of the $MgGa_2O_4$ samples.

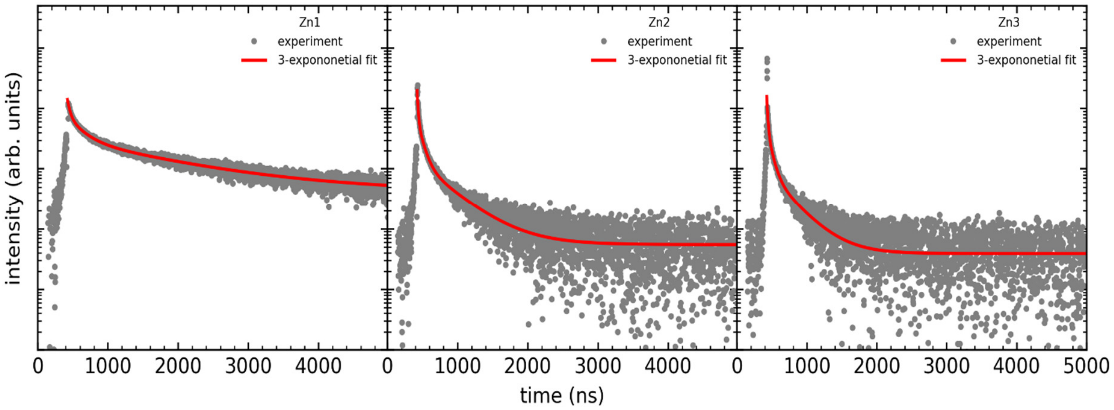

Fig. 5.44. Scintillation time profiles of the $ZnGa_2O_4$ samples.

Among the three $MgGa_2O_4$ samples, the comparison between the insulating (Mg1 and Mg2) and semiconducting (Mg3) variants reveals a significant disparity in scintillation characteristics. Specifically, the insulating samples exhibit notably faster scintillation compared to the semiconducting counterpart. This distinction is evident in the decay times, with the former (Mg1-2) displaying decay times approximately 2.5 times shorter (427-466 ns) than the latter (Mg3) with a decay time of 1130 ns. Additionally, the contribution of decay time components further underscores this contrast. In the "fast" profiles of Mg1 and Mg2, the combined contribution of the two prompt components (τ_1: 14-17 ns, and τ_2: 86-137 ns) exceeds 40%, whereas in the "slow" profile, it diminishes below 30%, accompanied by longer decay times (36 and 208 ns for τ_1 and τ_2, respectively).

In the case of $ZnGa_2O_4$, all samples exhibit semiconductor properties. Notably, an increase in free electron concentration correlates with a shift in the contribution of specific decay components towards shorter durations, resulting in significantly shorter decay times. For the sample with the lowest free electron concentration, the scintillation mean decay time measures 1180 ns. However, an order of magnitude increase in free electron concentration leads to a substantial reduction in the mean decay time to 175-267 ns.

Comparing the results of PHS and STP experiments, we observe a significant influence of free electron concentration on the scintillation performance of both $MgGa_2O_4$ and $ZnGa_2O_4$. Semiconducting crystals with high free electron concentrations on the order of 10^{18} cm^{-3} demonstrate efficient scintillation, contrasting with electrically insulating crystals and those with the highest free electron concentrations (more than 10^{19} cm^{-3}). However, when considering scintillation time profiles, the situation is the other way round. Samples that demonstrate the highest scintillation yield often exhibit slower scintillation, whereas achieving faster scintillation typically results in reduced yield. As a result, similar to β-Ga_2O_3, finding a free electron concentration that achieves a balance between fast and efficient scintillation poses a challenge.

5.2.3 Radioluminescence of $MgGa_2O_4$ and $ZnGa_2O_4$

The radioluminescence properties of $MgGa_2O_4$ and $ZnGa_2O_4$ samples were investigated over a temperature range spanning from 10 to 350 K. This comprehensive examination involved analyzing representative radioluminescence spectra acquired at temperatures of 10, 100, 200, and 300 K, as well as evaluating the dependence of RL yield (divided into two components) on temperature, as demonstrated in the right section of the figures using Shibata's model as previously described. **Figs. 5.45, 5.47, 5.49, 5.51, 5.53** and **5.55** showcase these findings. To aid in comparison, the spectra were normalized to the same maximum intensity at either 10 K or 100 K. The spectral patterns, predominantly characterized by a peak around 350 nm, closely resemble cathodoluminescence spectra documented in the literature for $MgGa_2O_4$ [13] and $ZnGa_2O_4$ [14]. Additionally, they exhibit similarities with radioluminescence spectra observed in β-Ga_2O_3 crystals, where the dominant band is attributed to self-trapped excitons [15]. Furthermore, the second figure illustrates all radioluminescence spectra plotted as a function of temperature, presented in the form of a spectral map, as depicted in **Figs. 5.46, 5.48, 5.50, 5.52, 5.54** and **5.56.**

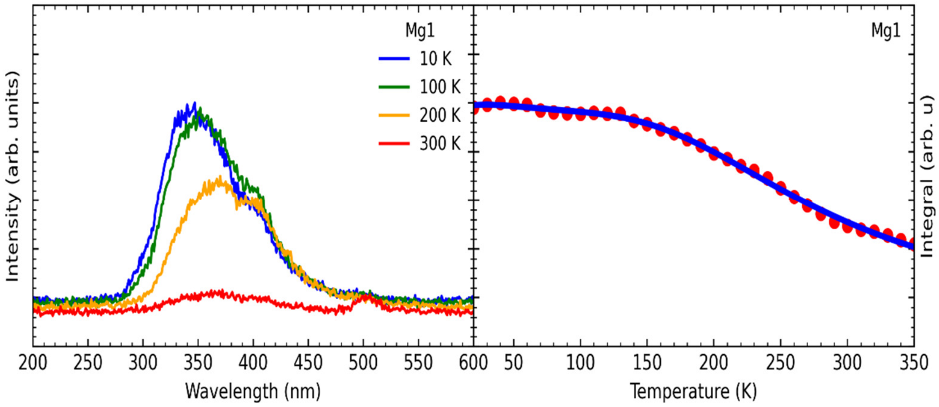

Fig. 5.45. Radioluminescence spectra for four specific temperatures (left side) and the NTQ chart with its fitting (right side) for sample Mg1.

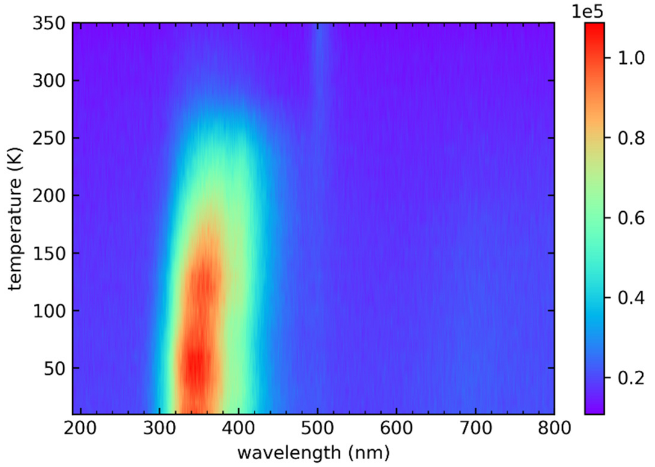

Fig. 5.46. Spectral map for sample Mg1.

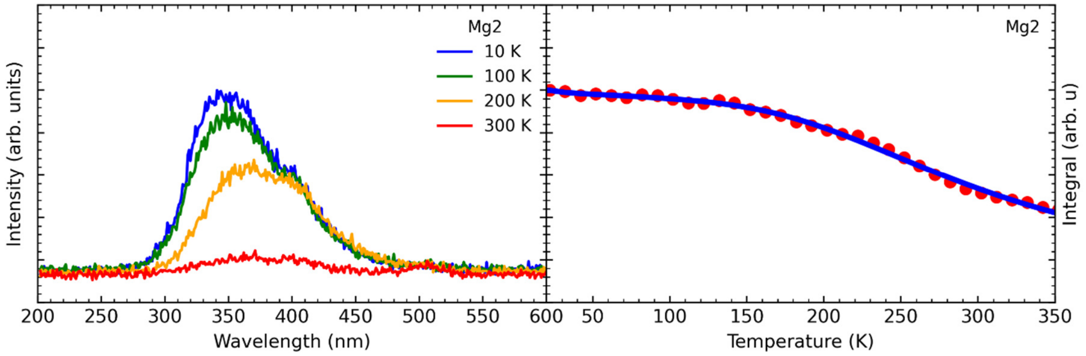

Fig. 5.47. Radioluminescence spectra for four specific temperatures (left side) and the NTQ chart with its fitting (right side) for sample Mg2.

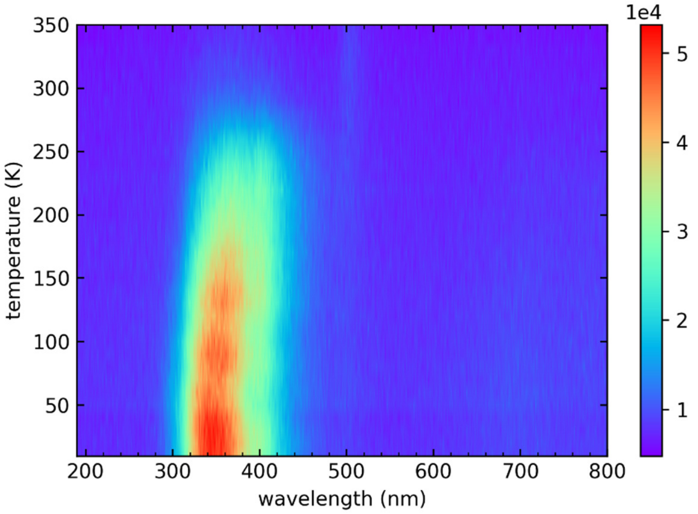

Fig. 5.48. Spectral map for sample Mg2.

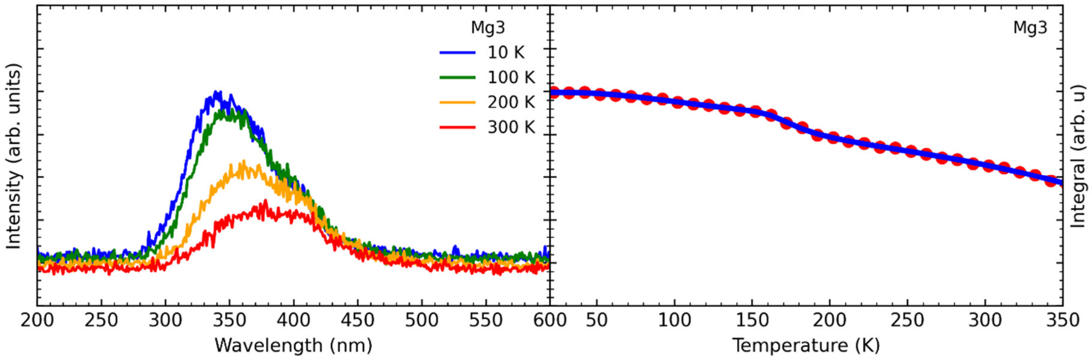

Fig. 5.49. Radioluminescence spectra for four specific temperatures (left side) and the NTQ chart with its fitting (right side) for sample Mg3.

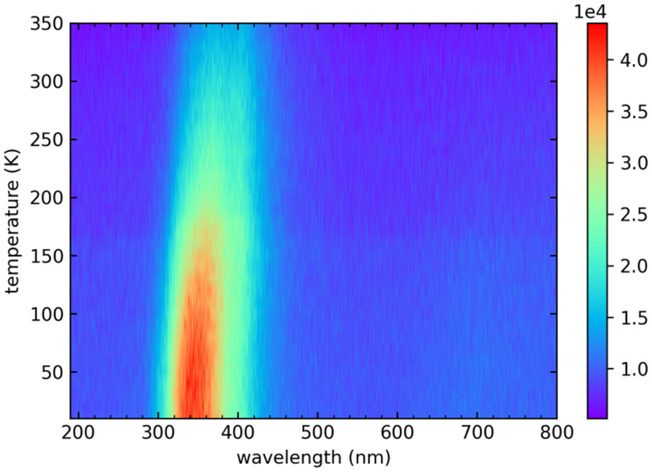

Fig. 5.50. Spectral map for sample Mg3.

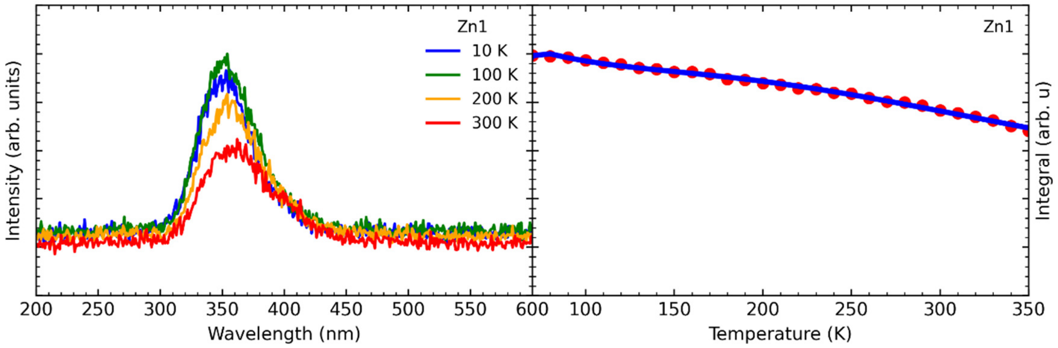

Fig. 5.51. Radioluminescence spectra for four specific temperatures (left side) and the NTQ chart with its fitting (right side) for sample Zn1.

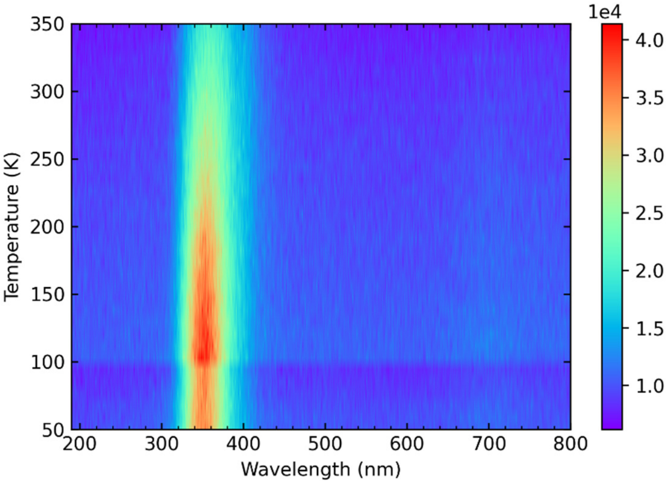

Fig. 5.52. Spectral map for sample Zn1.

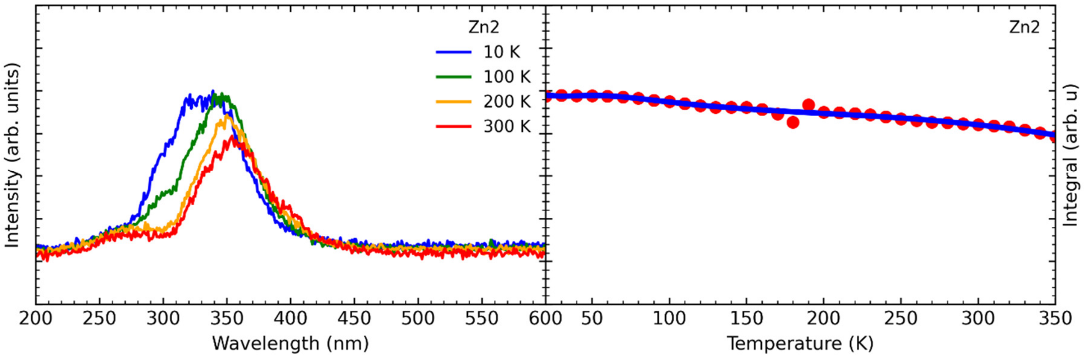

Fig. 5.53. Radioluminescence spectra for four specific temperatures (left side) and the NTQ chart with its fitting (right side) for sample Zn2.

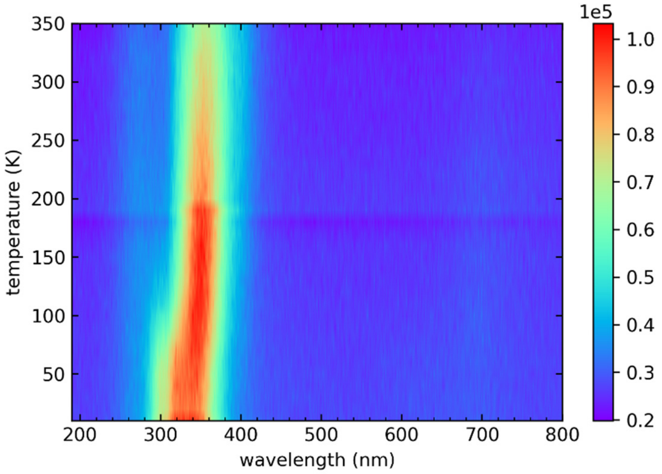

Fig. 5.54. Spectral map for sample Zn2.

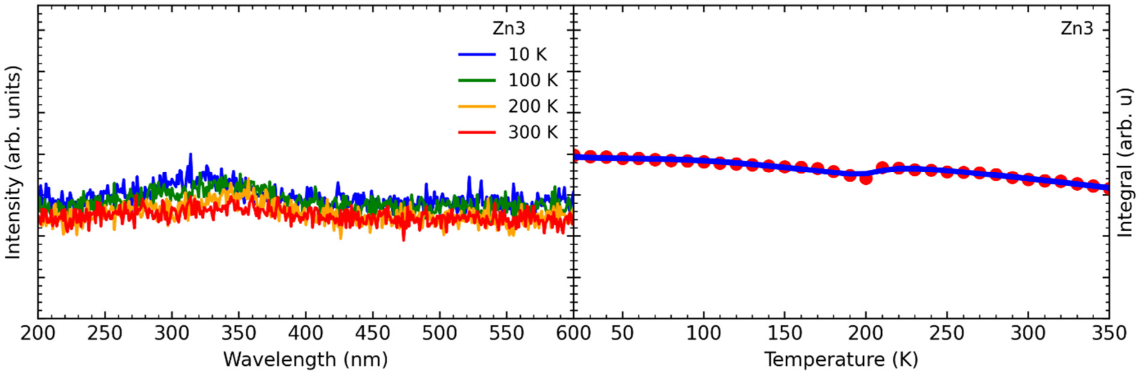

Fig. 5.55. Radioluminescence spectra for four specific temperatures (left side) and the NTQ chart with its fitting (right side) for sample Zn3.

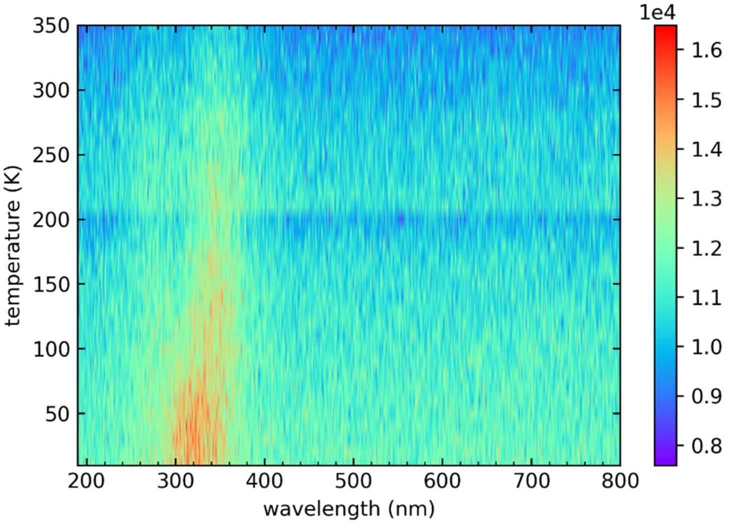

Fig. 5.56. Spectral map for sample Zn3.

For $MgGa_2O_4$, the radioluminescence (RL) spectra at lower temperatures (10, 100, 200 K) exhibit a similar appearance. At room temperature (RT), there is little variation among the spectra, although a minor additional band at approximately 500 nm of unidentified origin appears in the insulating samples. The key observation pertains to the relative intensities of the bands corresponding to specific temperatures. X-ray emission is notably suppressed at RT for all samples, yet the extent of suppression is notably lower for the semiconducting sample (Mg3), which actually demonstrates the highest scintillation yield. It appears that the suppression mechanism, necessitating further investigation, is more pronounced for insulating crystals (Mg1-2), hindering their effectiveness as scintillators.

In the case of $ZnGa_2O_4$, the behavior of the semiconducting sample with the lowest free electron concentration (Zn1) closely resembles that of the semiconducting $MgGa_2O_4$ sample (Mg3).

Although the degree of suppression is even smaller in Zn1 compared to Mg3, its scintillation yield is inferior. This could be attributed to the presence of metallic nanoparticles in $ZnGa_2O_4$ crystals resulting from significant thermal decomposition during growth. Interestingly, the two remaining $ZnGa_2O_4$ samples (Zn2-3) with considerably higher free electron concentrations, although they have similar scintillation properties (low yield, relatively fast decay), they display variation in radioluminescence. Zn1 and Zn2 samples showcase distinct spectra at all examined temperatures, suggesting minimal thermal quenching. However, it is noteworthy that despite this, the scintillation yield is relatively modest in these samples, potentially due to the aforementioned nanoparticles. Conversely, the spectra of the Zn3 sample are barely discernible above noise.

Tab. 5.9. Fitting parameters of the NTQ curves for samples from $MgGa_2O_4$ and $ZnGa_2O_4$.

ID	**Sample**	**A(0)**	**D1**	**E_1^N(meV)**	**C1**	**E_1^D(meV)**	**C2**	**E_2^D(meV)**	**C3**	**E_3^D(meV)**
Mg1	$MgGa_2O_4$	$8.99\cdot10^6$	$2.74\cdot10^2$	10	$10\cdot10^3$	10	$2.89\cdot10^3$	10.6	$2.09\cdot10^5$	85
Mg2	$MgGa_2O_4$	$8.85\cdot10^6$	$2.15\cdot10^3$	9.06	$5.73\cdot10^2$	34	$2.20\cdot10^3$	9.12	$5.67\cdot10^4$	101
Mg3	$MgGa_2O_4$	$8.65\cdot10^6$	$6.84\cdot10^9$	3.31	$4.17\cdot10^{-1}$	19.2	$1.23\cdot10^{10}$	337	$1.41\cdot10^{12}$	532
Zn1	$ZnGa_2O_4$	$7.63\cdot10^6$	$7.75\cdot10^{13}$	180	$1.81\cdot10^{-1}$	7.9	$6.16\cdot10^{-1}$	181	$2.2\cdot10^{14}$	272
Zn2	$ZnGa_2O_4$	$1.7\cdot10^8$	$1.62\cdot10^1$	54	4.28	0.03	60.9	46	$2.29\cdot10^2$	112
Zn3	$ZnGa_2O_4$	$7.01\cdot10^6$	$1.21\cdot10^5$	61	1.48	57	1.52	61	4.33	92

Based on **Tab. 5.9,** the insulating $MgGa_2O_4$ samples (Mg1 and Mg2), characterized by relatively low free carrier concentrations, the luminescence intensity is notably low, indicating weak scintillation properties. The presence of deep traps, indicated by the high activation energies (E_1^N), suggests that radiative transitions from these states contribute minimally to the overall luminescence. Conversely, for the semiconductor $MgGa_2O_4$ sample (Mg3), the higher free carrier concentration results in enhanced luminescence intensity. Moderate activation energies and contribution factors for radiative transitions indicate the presence of trap states that influence luminescence, albeit to a lesser extent compared to insulating samples.

In the case of $ZnGa_2O_4$ samples, the luminescence characteristics vary with the concentration of free carriers. Zn1, with a moderate free carrier concentration, exhibits moderate luminescence intensity and relatively low activation energies for radiative transitions, suggesting the presence of shallow traps. As the free carrier concentration increases in Zn2 and Zn3 samples, the luminescence intensity also increases, but with a shift towards higher activation energies for radiative transitions, indicating a more complex trap distribution. Zn3, in particular, demonstrates significant thermal excitation, suggesting the presence of shallow traps contributing to luminescence at higher temperatures.

Overall, the Shibata model elucidates the intricate interplay between trap parameters and free carrier concentration, providing valuable insights into the radioluminescence properties of $MgGa_2O_4$ and $ZnGa_2O_4$ crystals across varying temperature ranges. These insights are crucial for optimizing the scintillation performance of these materials for potential applications in radiation detection and imaging.

5.2.4 Thermoluminescence of $MgGa_2O_4$ and $ZnGa_2O_4$

The glow curve analysis reveals that certain samples exhibit a notable peak at around 80 K in **Fig. 5.57** (sample Mg1) and 92 K in **Fig. 5.59** (sample Zn2), respectively. The detailed thermoluminescence assessment, depicted in **Figs. 5.57** and **5.59**, illustrates experimental findings alongside the heating protocol, a tri-exponential fit employed to minimize background interference, and a linear fit utilized to determine the heating rate (β). Subsequent to this, **Fig.5.58** and **5.60** present the distributions used for fitting traps.

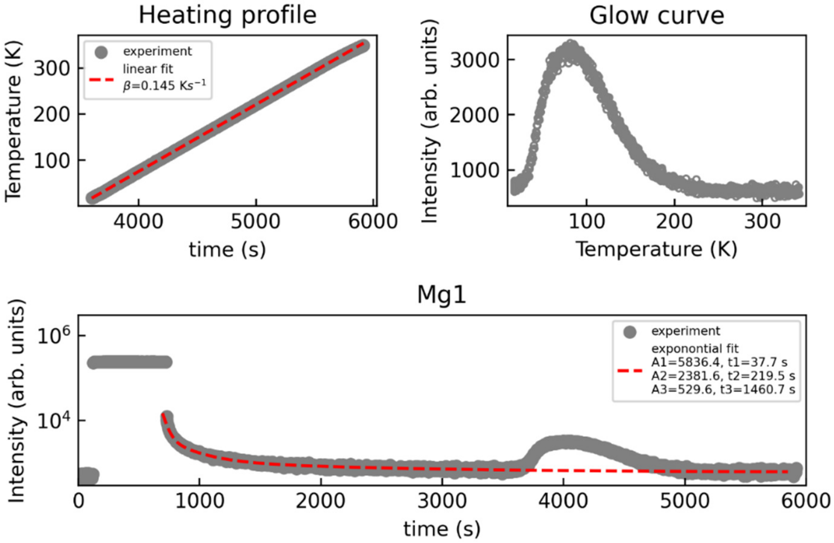

Fig. 5.57. The chart depicting the overall thermoluminescence measurement of sample Mg1.

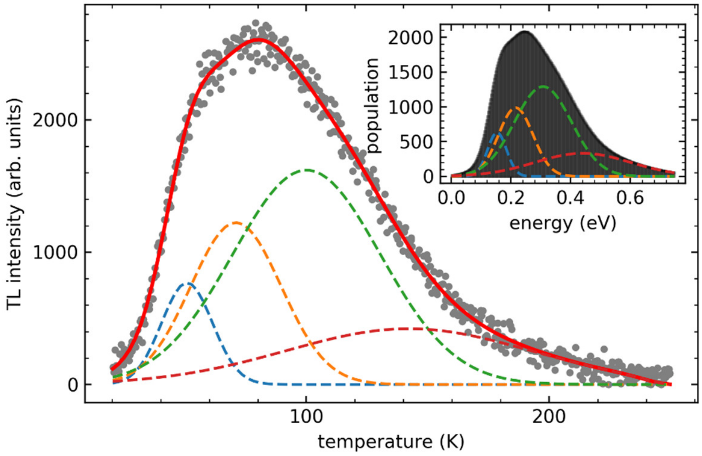

Fig. 5.58. The distribution of Gaussian distributions used for fitting traps for sample Mg1.

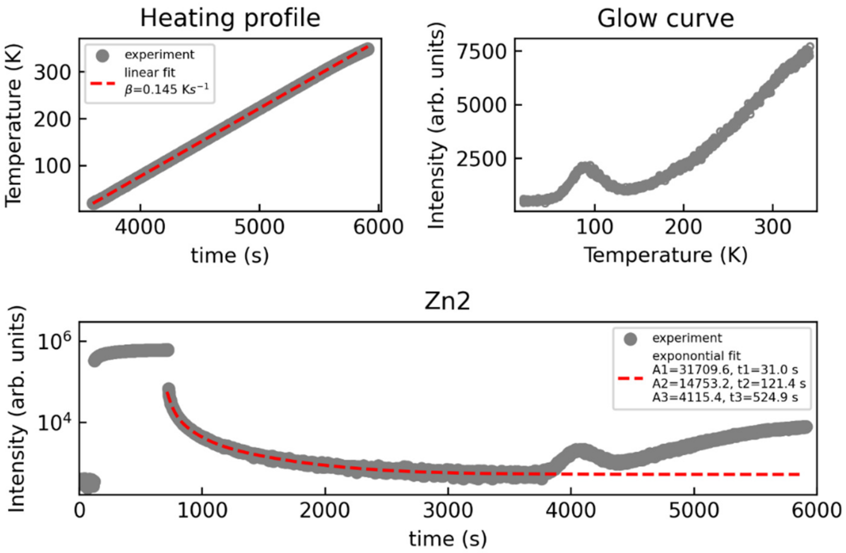

Fig. 5.59. The chart depicting the overall thermoluminescence measurement of sample Zn2.

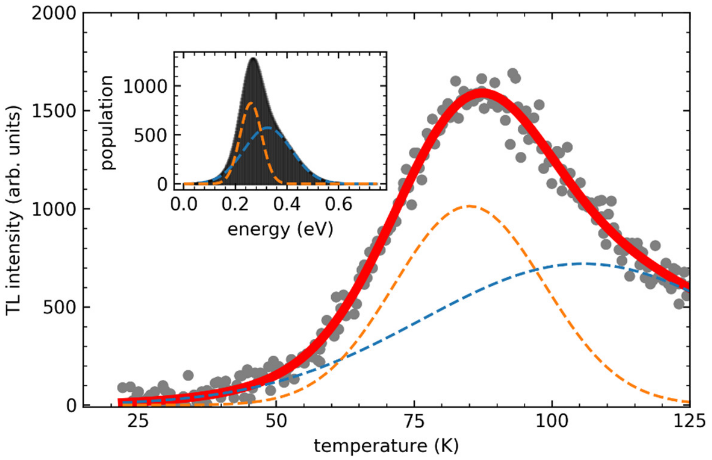

Fig. 5.60. The distribution of Gaussian distributions used for fitting traps for sample Mg1.

We are particularly focused on the comprehensive fitting of the glow curve (refer to **Fig. 5.58** and **5.60**), as it yields crucial insights into trap parameters. Throughout our investigation, most of the examined samples exhibited no resolvable glow peaks, except for Mg1 and Zn2. By fitting the glow curve we extracted essential parameters of individual distributions, including their activation energy (E), free electrons concentarion (n_e), and the σ factor. Likewise for β-Ga$_2$O$_3$, we employed a model featuring a distinct distribution to accurately capture the entire luminescence curve. Detailed information regarding these distributions are collected in **Tab 5.10.**

Tab. 5.10. Parameters of the distribution used for fitting the glow curve of sample Mg1 and Zn2.

ID	Sample	n_e (cm^{-3})	Distribution	E (meV)	σ (meV)	s (s^{-1})	FOM (%)	R (%)
Mg1	$MgGa_2O_4$	insulator	1	154	32	$1 \cdot 10^{14}$	5.29	0.997
			2	216	58			
			3	308	96			
			4	441	160			
Zn2	$ZnGa_2O_4$	$3 \cdot 10^{19}$	1	326	92		6.65	0.995
			2	260	42			

Upon analyzing the parameters derived from the distribution data and their associated traps, it becomes evident that the sole trap present in each sample holds paramount importance. This single trap, situated at an energy level of 111 MeV for sample I1 and 103 MeV for sample I7, exhibits the highest significance. Conversely, there are no other traps present in these samples, emphasizing the dominance of this singular trap in determining the luminescence characteristics

5.2.5 Temperature dependence of $MgGa_2O_4$ and $ZnGa_2O_4$

In this part, we present the temperature dependence of the scintillation properties for $MgGa_2O_4$ and $ZnGa_2O_4$ crystals, focusing on their respective light yields across different temperatures. For $MgGa_2O_4$, we observe a clear nonlinear relationship between temperature and relative light yield. The maximum light yield for this series of crystals is approximately 2.5k ph/MeV, occurring at a temperature of 145 K. As the temperature increases beyond this point, the relative light yield decreases noticeably. Particularly, for temperatures above 178 K, the light yield is consistently lower than the yield observed at room temperature (299 K). This indicates a significant reduction in scintillation efficiency as the temperature rises above the optimal point, suggesting the presence of a temperature-dependent quenching mechanism that diminishes the material's ability to scintillate effectively at higher temperatures.

On the other hand, the temperature dependence of $ZnGa_2O_4$ does not exhibit any significant change in relative light yield across the temperature range studied. The scintillation yield remains relatively stable, indicating that $ZnGa_2O_4$'s scintillation efficiency is less affected by temperature variations compared to $MgGa_2O_4$. This stability can be advantageous in applications where the operating temperature may vary, ensuring consistent performance of $ZnGa_2O_4$ under different thermal conditions.

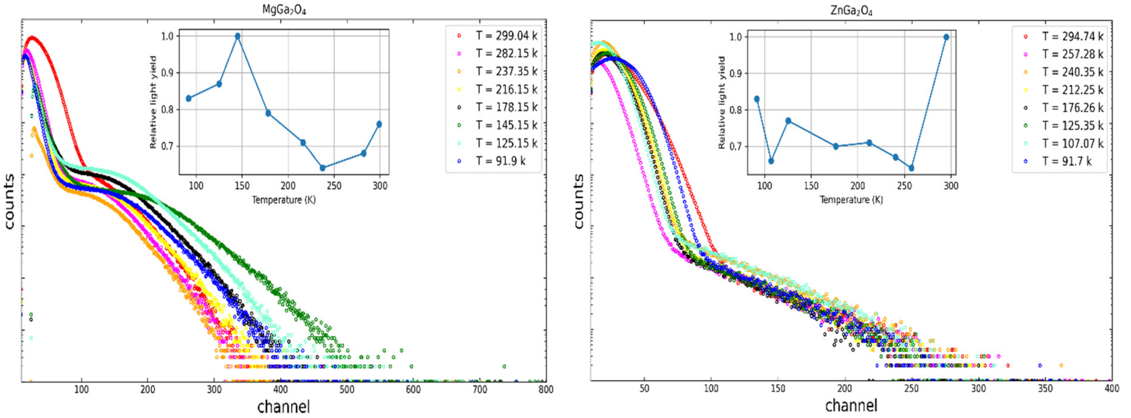

Fig. 5.61. Temperature dependence of pulse height spectra for $MgGa_2O_4$ and $ZnGa_2O_4$ crystals under 662 keV excitation from a ^{137}Cs source

$MgGa_2O_4$ shows a pronounced temperature dependence with a peak light yield at 145 K, followed by a decrease at higher temperatures, suggesting a strong quenching effect. In contrast, $ZnGa_2O_4$ demonstrates a stable scintillation yield across the temperature range, highlighting its potential for applications requiring temperature-insensitive performance.

5.3 ZnSe and (Zn,Be)Se crystals

The development and characterization of II-VI semiconductors have opened new frontiers in various technological applications, spanning visible radiation sources, green laser diodes, spintronics, solar cells, ionizing radiation detection, infrared detectors, and substrates. This chapter explores the scintillation properties of ZnSe and (Zn,Be)Se crystals, emphasizing significant advancements achieved through annealing processes. Initially, our investigations focused on the scintillation properties of pure ZnSe and mixed (Zn,Be)Se crystals. ZnSe, a semiconductor with a bandgap of approximately 2.7 eV at room temperature and a density of 5.27 g/cm^3, showed limited scintillation efficiency in its as-grown state, yielding only a few thousand ph/MeV. However, annealing in zinc vapor led to a remarkable improvement, increasing the scintillation yield to 26,200 ph/MeV for ZnSe and 15,100 ph/MeV for (Zn,Be)Se. Encouraged by these results, we expanded our research to include (Zn,Be)Se samples with varying beryllium concentrations from 2% to 20% at our institute. This phase explores the scintillation and thermal properties of these new samples and investigates how annealing affects their performance. Additionally, we conducted measurements to understand the energy gaps of these samples and their implications for electronic properties influenced by beryllium concentration.

Our study aims to comprehensively understand how different beryllium concentrations impact the scintillation and thermal properties of (Zn,Be)Se crystals. By systematically analyzing these properties and energy gaps, we seek to elucidate the mechanisms behind the enhanced scintillation observed post-annealing. This knowledge not only advances our understanding of II-VI semiconductors, but also lays the foundation for developing more efficient scintillation materials for diverse applications.

5.3.1 Pulse height spectra of ZnSe and (Zn,Be)Se

In our initial series of samples, we have studied two primary compositions:

- ZS-A: Annealed ZnSe samples,

- ZS-N: Non-annealed ZnSe samples,

- ZB1-A: Annealed (Zn,Be)Se samples with 10% beryllium,

- ZB1-N: Non-annealed (Zn,Be)Se samples with 10% beryllium.

For the second series, we have examined:

-ZB2-A to ZB5-A: Annealed (Zn,Be)Se samples with beryllium concentrations ranging from 2% to 25%,

-ZB2-N to ZB5-N: Non-annealed (Zn,Be)Se samples with beryllium concentrations ranging from 2% to 25%.

Tab. 5.11. Growth details and scintillation properties of the first series of (Zn,Be)Se samples (Y - Scintillation Yield, R - Energy Resolution at 662 keV, τ_i - Scintillation Decay Time Constants with Their Contributions, τ_{mean} - Scintillation Mean Decay Time)

Material	ID	Growth method	Y (ph/MeV)	R (%)	τ_i (µs)	τ_{mean} (µs)
ZnSe	ZS-A	Bridgman	26 200	18.3	4.9 (38%) 20.1 (62%)	14.4
	ZS-N		-	-	-	-
$Zn_{0.9}Be_{0.1}Se$	ZB1-A		15 100	21.2	5.9 (9%) 30.5 (91%)	28.3
	ZB1-N		-	-	-	-

Tab. 5.12. Growth details and scintillation properties of the second series of (Zn,Be)Se samples (Y - Scintillation Yield, R - Energy Resolution at 662 keV, τ_i - Scintillation Decay Time Constants with Their Contributions, τ_{mean} - Scintillation Mean Decay Time)

Material	Composition of Be (%)	ID	Growth method	Y (ph/MeV)	R (%)	τ_i (μs)	τ_{mean} (μs)
(Zn,Be)Se	2	ZB2-A	Bridgman	7 720	23.6	17.4 (98%) 0.2 (2%)	17.0
		ZB2-N		2 030	33.6	37.6 (28%) 0.12 (72%)	10.6
	5	ZB3-A		6 060	21.0	17.7 (95%) 0.11 (5%)	17.0
		ZB3-N		2 580	26.5	13.5 (96%) 0.1 (4%)	13.0
	10	ZB4-A		3 780	26.1	16 (98%) 0.14 (2%)	15.6
		ZB4-N		2 060	22.7	14.9 (79%) 0.08 (21%)	11.8
	20	ZB5-A		2 200	19.1	37.0 (59%) 0.11 (41%)	22.1
		ZB5-N		~1 000 - 2 000	-	73.2 (85%) 0.93 (15%)	31.7

The pulse height spectra of ZnSe and (Zn,Be)Se were evaluated using a gain of 0.3×10 and a shaping time of 2 μs. The full energy peak was fitted using a single Gaussian function. This analysis provided the scintillation efficiency, derived from the photomultiplier's quantum efficiency as determined through radioluminescence.

Figs. 5.62-5.63 and **Figs. 5.64-5.67** display the recorded pulse height spectra for the initial and second series of ZnSe and (Zn,Be)Se samples, respectively. **Tables 5.11** and **5.12** summarize the scintillation yield and energy resolution values. The sample IDs are provided, where possible, in ascending order based on whether they were annealed under zinc vapor or not.

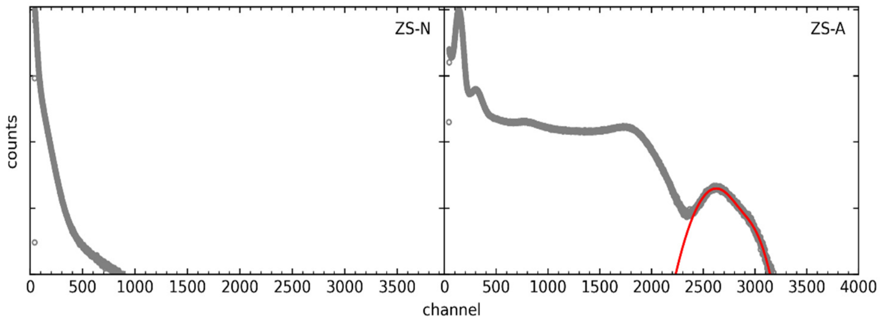

Fig. 5.62. Pulse height spectra of the ZnSe samples.

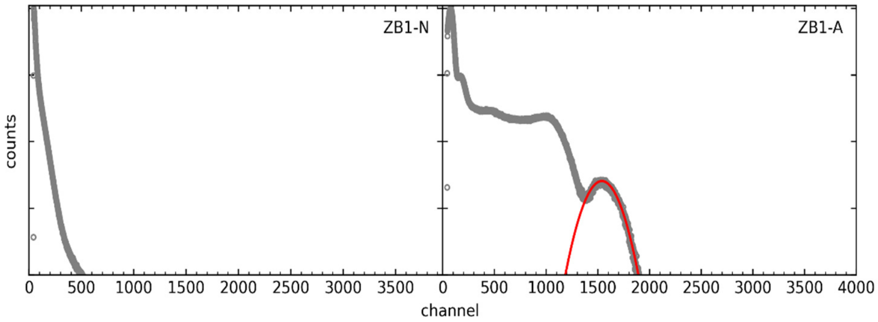

Fig. 5.63. Pulse height spectra of the (Zn,Be)Se samples ZB1.

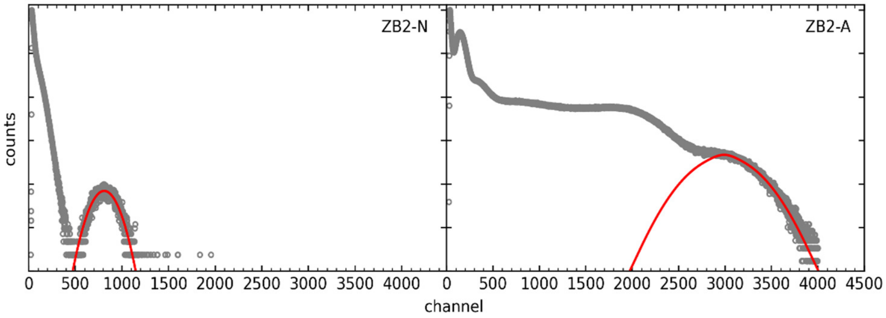

Fig. 5.64. Pulse height spectra of the (Zn,Be)Se samples ZB2.

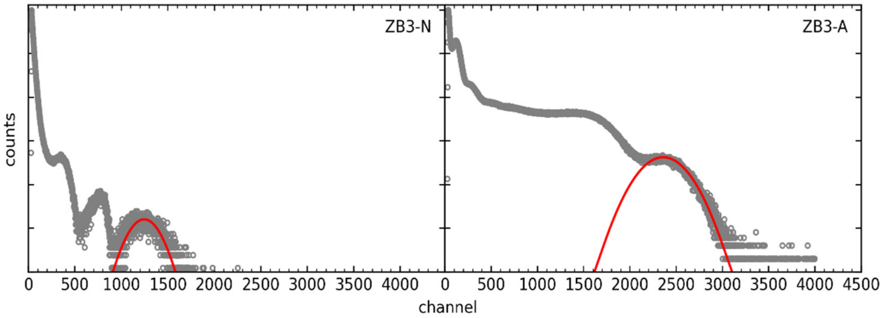

Fig. 5.65. Pulse height spectra of the (Zn,Be)Se samples ZB3.

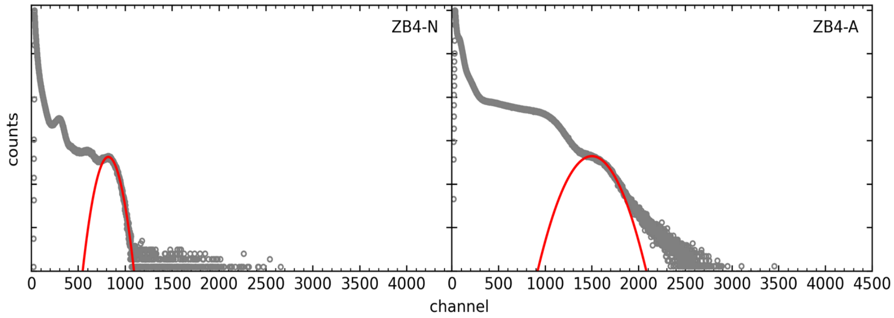

Fig. 5.66. Pulse height spectra of the (Zn,Be)Se samples ZB4.

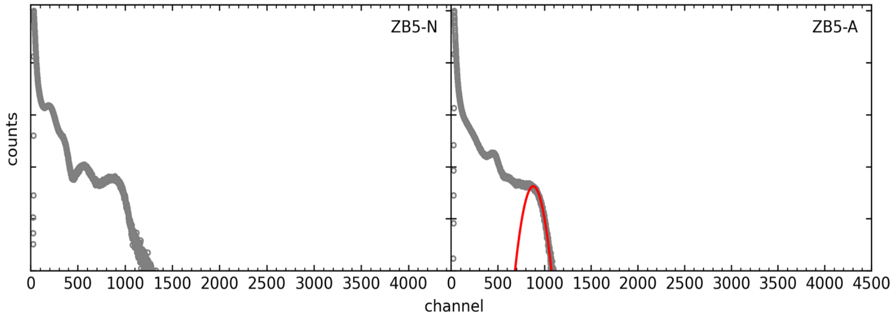

Fig. 5.67. Pulse height spectra of the (Zn,Be)Se samples ZB5.

In the initial series of samples, the pulse height spectra of ZnSe (ZS-A, ZS-N) and (Zn,Be)Se (ZB1-A, ZB1-N) are presented in **Figs. 5.62**, **5.63**, along with light yield and energy resolution estimates in **Tab. 5.11**. The uncertainties for each parameter are below 5%. The annealed ZnSe sample showed a yield of 26,000 ph/MeV, while the (Zn,Be)Se sample yielded 15,400 ph/MeV. Non-annealed samples exhibited yields lower by an order of magnitude, highlighting the significant enhancement in scintillation light output due to annealing in a zinc atmosphere. Despite this improvement, the yields for both ZnSe and (Zn,Be)Se, the energy resolution for ZnSe (around 18%) and (Zn,Be)Se (around 19%) is less satisfactory compared to other scintillating materials, such as e.g. LuAG:Pr crystals having an energy resolution of 4.6%. This indicates considerable room for improvement in these materials' scintillation properties.

The pulse height spectra of second series of samples (Zn,Be)Se are presented in **Figs. 5.64-5.67,** revealing significant variations in light yield and energy resolution based on the Be composition and annealing treatment. The annealed samples, particularly such as ZB2-A and ZB3-A, exhibit higher light yields of 7,720 ph/MeV and 6,060 ph/MeV, respectively, compared to their non-annealed counterparts ZB2-N and ZB3-N, which yield 2,030 ph/MeV and 2,580 ph/MeV respectively. This underscores the importance of annealing in enhancing scintillation light output. Furthermore, in case of the ZB3-N and ZB5-N samples, the pulse height spectra reveal a strange double structure, which disappears upon annealing. Despite this improvement, the yields for (Zn,Be)Se samples remain lower than the reported 26,000 ph/MeV for annealed ZnSe samples and other values from literature, indicating a need for further optimization. Energy resolution varies significantly, with ZB2-N showing the highest at 33.6% and ZB4-N the lowest at 14.6%, suggesting that while annealing improves the light yield, energy resolution still requires substantial enhancement. These findings highlight the potential for (Zn,Be)Se as scintillating materials, but also the considerable room for improvement to match the performance of leading scintillators like LuAG:Pr crystals.

5.3.2 Scintillation time profiles of ZnSe and (Zn,Be)Se

The scintillation time profiles for the first and second series of samples are shown in **Figs. 5.68, 5.69** and **Figs. 5.70-5.73**, respectively, highlighting the behavior of annealed and non-annealed (Zn,Be)Se. These profiles, also known as scintillation decays, are unaffected by afterpulses, ensuring their accuracy for calculating decay time constants. Using a two-exponential decay fitting approach, we achieve a strong correlation between the experimental and fitted time profiles, yielding precise results. **Tabs 5.11**, **11.12** provide the decay constants and their contributions for all investigated samples. To enhance comparability, additional insights are offered through the parameter known as the "scintillation mean decay time" (τ_{mean}), as previously discussed.

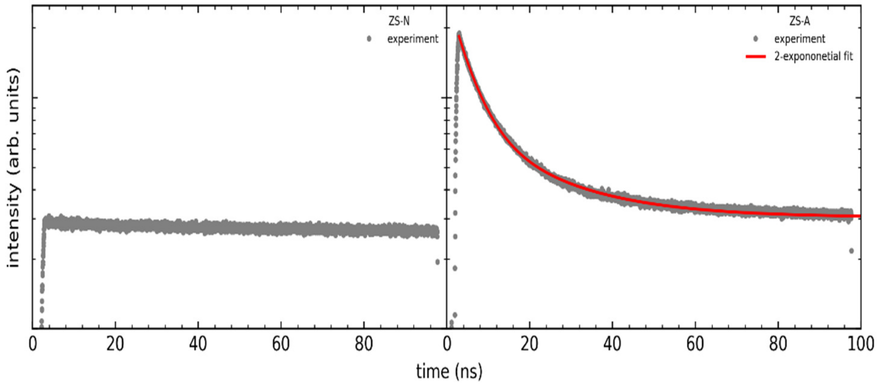

Fig. 5.68. Scintillation time profile of the ZnSe samples.

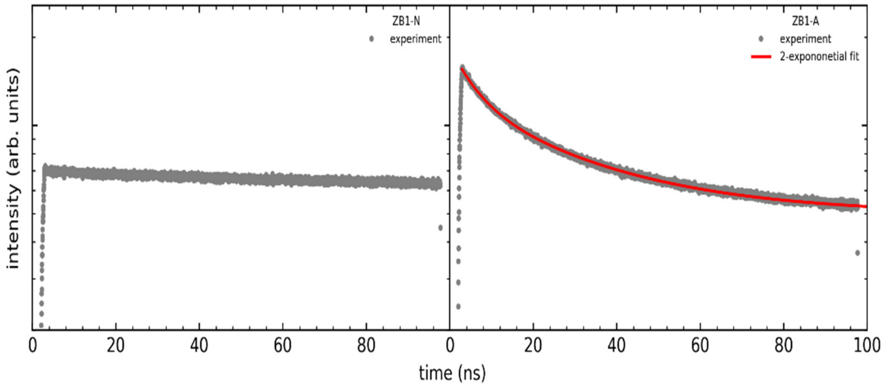

Fig. 5.69. Scintillation time profile of the (Zn,Be)Se samples.

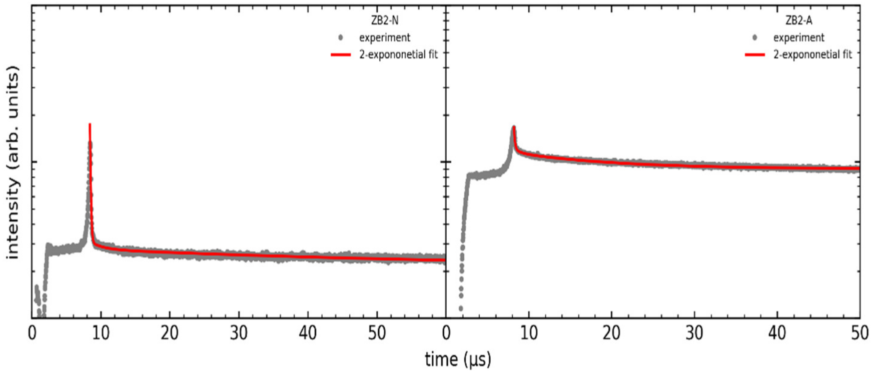

Fig. 5.70. Scintillation time profile of the (Zn,Be)Se samples

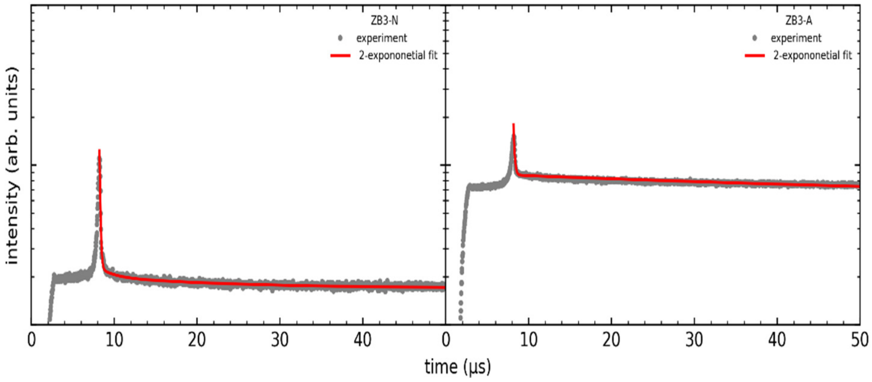

Fig. 5.71. Scintillation time profile of the (Zn,Be)Se samples

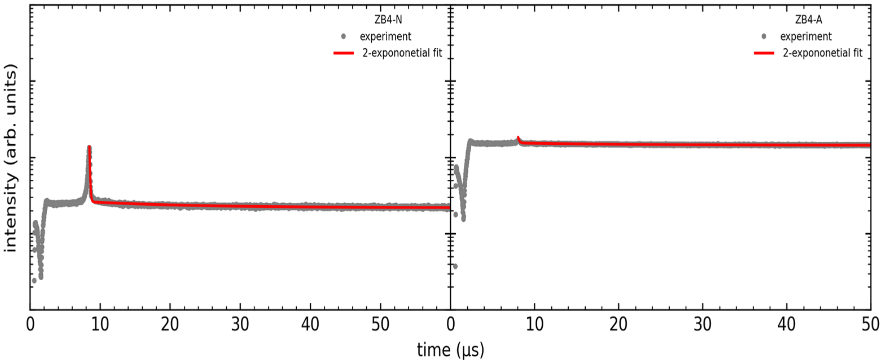

Fig. 5.72. Scintillation time profile of the (Zn,Be)Se samples

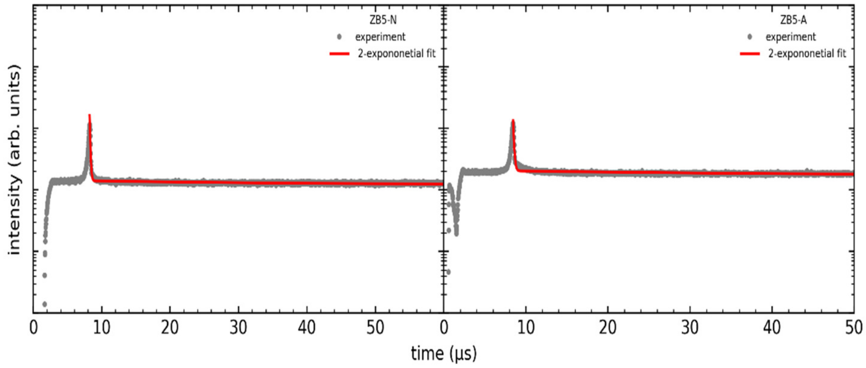

Fig. 5.73. Scintillation time profile of the (Zn,Be)Se samples

The mean decay time (τ_{mean}) for the first series of crystals significant differs in scintillation behavior between ZnSe and $Zn_{0.90}Be_{0.1}Se$, influenced by both annealing in zinc vapor and the incorporation of beryllium (Be). The ZnSe sample (ZS-A), grown using the Bridgman method and annealed in zinc vapor, exhibits a mean decay time of 14.4 µs. This relatively moderate decay rate results from a combination of two decay constants: 4.9 µs (38%) and 20.1 µs (62%), indicating a dominant slower component. In contrast, the $Zn_{0.9}Be_{0.1}Se$ sample (ZB1-A), also grown by the Bridgman method and annealed in zinc vapor, shows a significantly longer mean decay time of 28.3 µs. This prolonged decay is primarily due to the longer decay constant of 30.5 µs, which contributes 91% to the overall decay process. The extended τ_{mean} for $Zn_{0.9}Be_{0.1}Se$ suggests a more sustained scintillation response compared to ZnSe, which may influence its suitability for applications requiring rapid timing. The incorporation of Be into the ZnSe matrix appears to slow down the scintillation decay process, as evidenced by the longer decay constants in the $Zn_{0.9}Be_{0.1}Se$ sample. This indicates that Be plays a critical role in modifying the decay characteristics of the material. The annealing process in zinc vapor enhances the light yield and adjusts the decay profiles, while the addition of Be significantly influences the decay time, underscoring the importance of both factors in optimizing scintillation properties.

For the second series of (Zn,Be)Se samples reveal the significant influence of both beryllium content and annealing in zinc vapor on scintillation behavior. Annealed samples generally exhibit longer mean decay times, indicating that annealing enhances scintillation properties. For instance, ZB2-A (2% Be) has a τ_{mean} of 17 µs compared to 10.6 µs for the non-annealed ZB2-N, and ZB3-A (5% Be) has a τ_{mean} of 17 µs compared to 13 µs for ZB3-N. Increasing Be content also affects decay times: ZB4-A (10% Be) has a τ_{mean} of 15.6 µs, while ZB5-A (20% Be) has a substantially longer τ_{mean} of 22.1 µs. Non-annealed samples with higher Be content show even more pronounced effects, with ZB5-N (20% Be) having the longest τ_{mean} of 31.7 µs. The proportion of the slower decay constant significantly influences τ_{mean}, with samples exhibiting a higher percentage contribution from the longer decay component showing extended decay times. For example, ZB5-N has 85% contribution from a 73.2 µs decay constant, resulting in a τ_{mean} of 31.7 µs. These results underscore the crucial roles of annealing and Be content in optimizing the scintillation decay profiles of (Zn,Be)Se materials for specific applications.

5.3.3 Radioluminescence of ZnSe and (Zn,Be)Se

The radioluminescence properties of ZnSe and (Zn,Be)Se samples were investigated over a temperature range of 10 to 350 K. This study included representative radioluminescence spectra captured at 10, 100, 200, and 300 K, analyzing the temperature dependence of RL yield, divided into two components as shown in the right part of the figure using Shibata's model, as previously described. In the following figures, we showcase only the samples that exhibit the best RL characteristics. **Figs. 5.74-5.87** present these findings. For comparison, the spectra were normalized to the same maximum intensity at either 10 K or 100 K. We observed two bands peaking at 465 and 640 nm for ZnSe, and at 428 and 580 nm for $Zn_{1-x}Be_xSe$. The first emission, referred to in the literature as edge emission, is strongly quenched above 150 K for both samples and is associated with shallow donor-acceptor pair recombination (DAP emission), likely involving either Ga-Na or LiZn-VSe pairs. The second observed emission consists of two subbands and is related to recombination between deep levels (DL emission). Stacking faults and nonstoichiometric flaws, including intrinsic point defects such as vacancies and interstitials, are responsible for DL emission. Undoped ZnSe exhibits the DL emission band, indicating that intrinsic point defects, including vacancies, interstitials, and antisites, may be involved. Researchers have identified zinc vacancies, zinc interstitials, and Frenkel pairs involving zinc vacancies and zinc interstitials with varied separation in bulk ZnSe through optical detection of magnetic resonance and electron paramagnetic resonance studies.

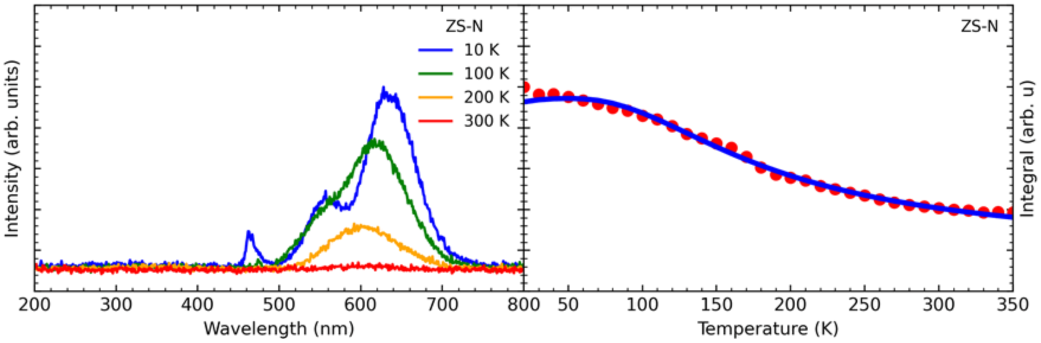

Fig. 5.74. Radioluminescence spectra for four specific temperatures (left side) and the NTQ chart with its fitting (right side) for sample ZS-N.

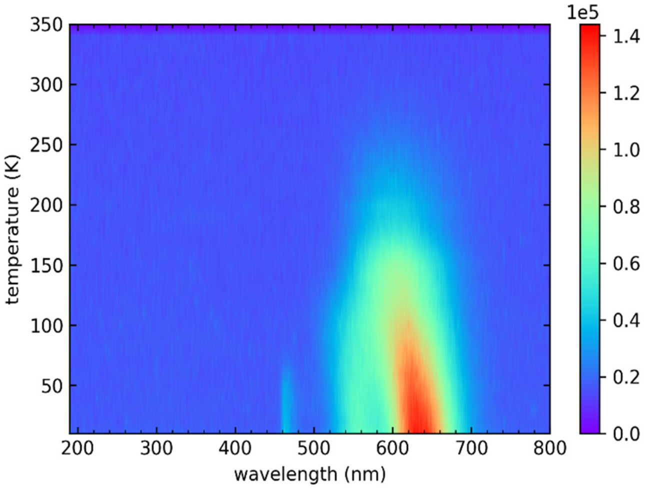

Fig. 5.75. Spectral map for sample ZS-N.

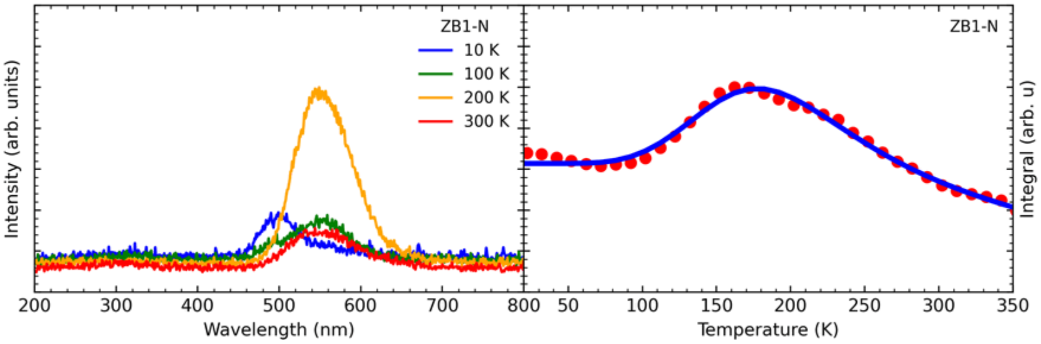

Fig. 5.76. Radioluminescence spectra for four specific temperatures (left side) and the NTQ chart with its fitting (right side) for sample ZB1-N.

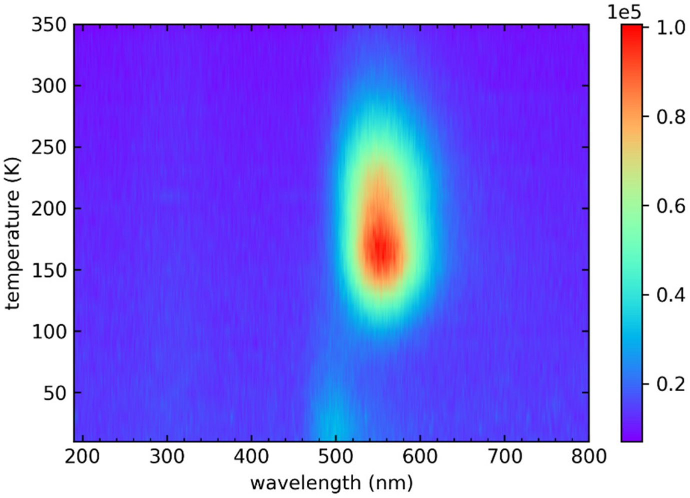

Fig. 5.77. Spectral map for sample ZB1-N.

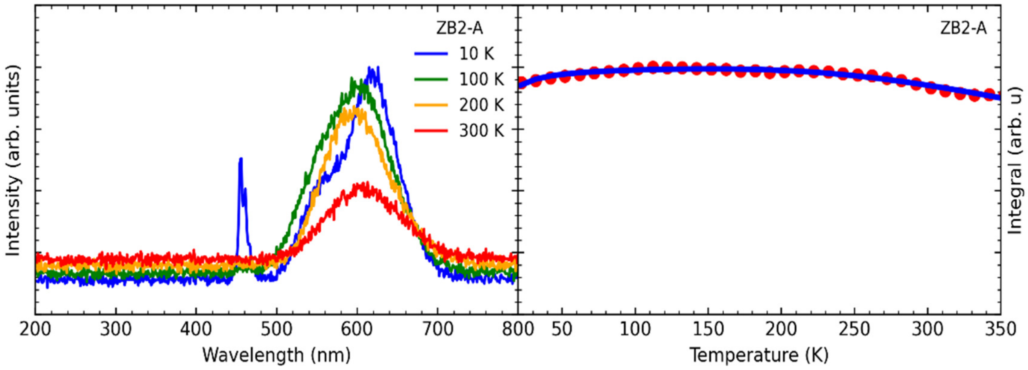

Fig. 5.78. Radioluminescence spectra for four specific temperatures (left side) and the NTQ chart with its fitting (right side) for sample ZB2-A.

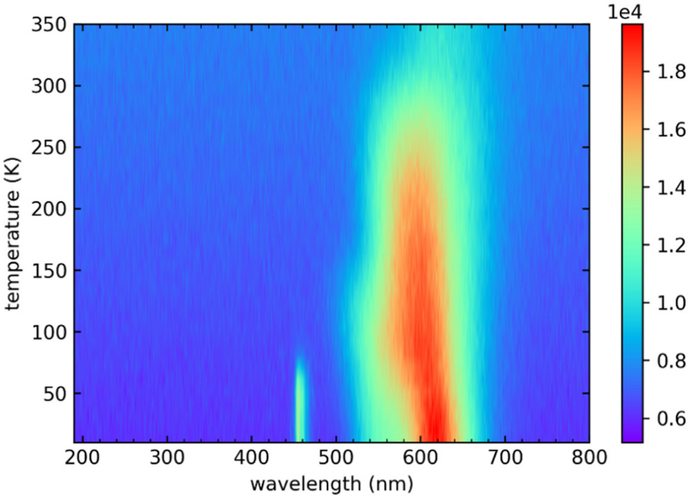

Fig. 5.79. Spectral map for sample ZB2-A.

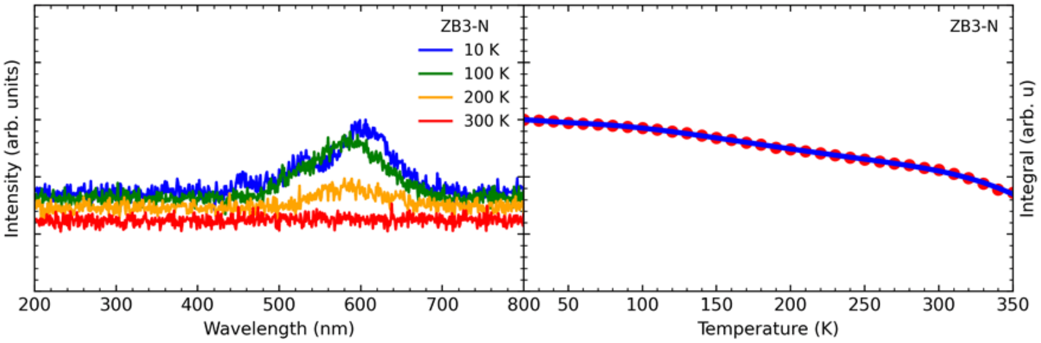

Fig. 5.80. Radioluminescence spectra for four specific temperatures (left side) and the NTQ chart with its fitting (right side) for sample ZB3-N.

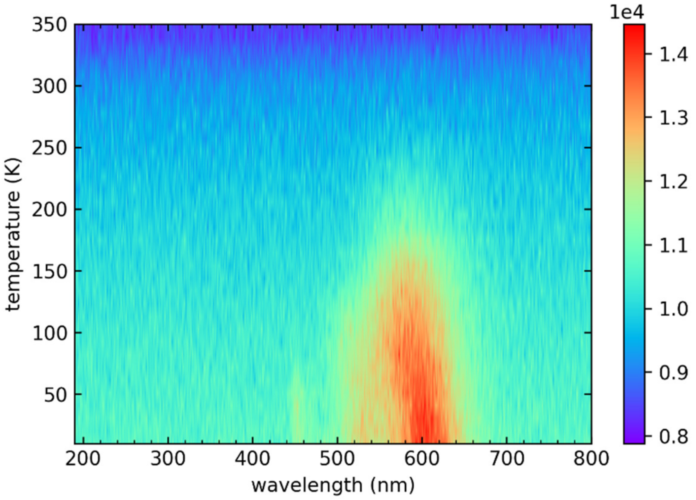

Fig. 5.81. Spectral map for sample ZB3-N.

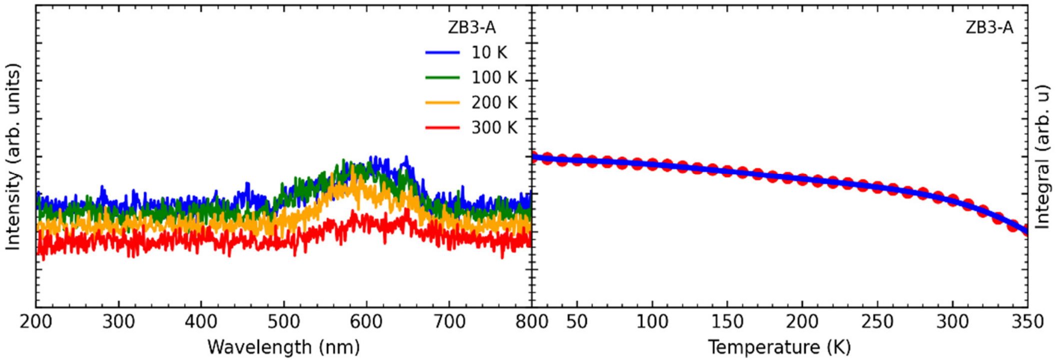

Fig. 5.82. Radioluminescence spectra for four specific temperatures (left side) and the NTQ chart with its fitting (right side) for sample ZB3-A.

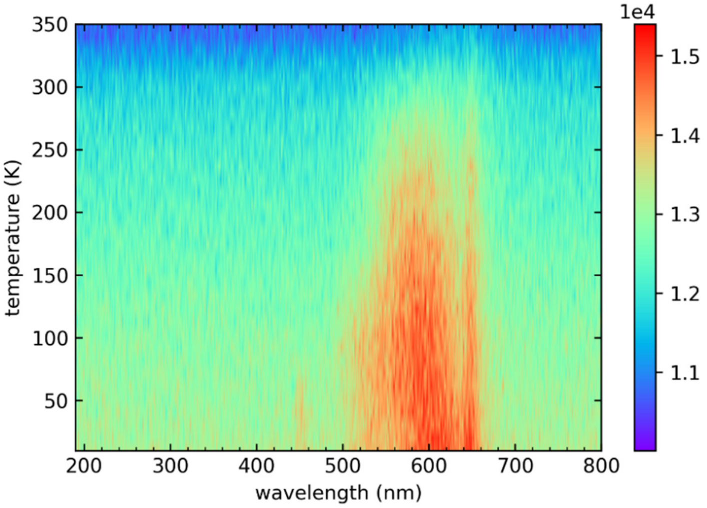

Fig. 5.83. Spectral map for sample ZB3-A.

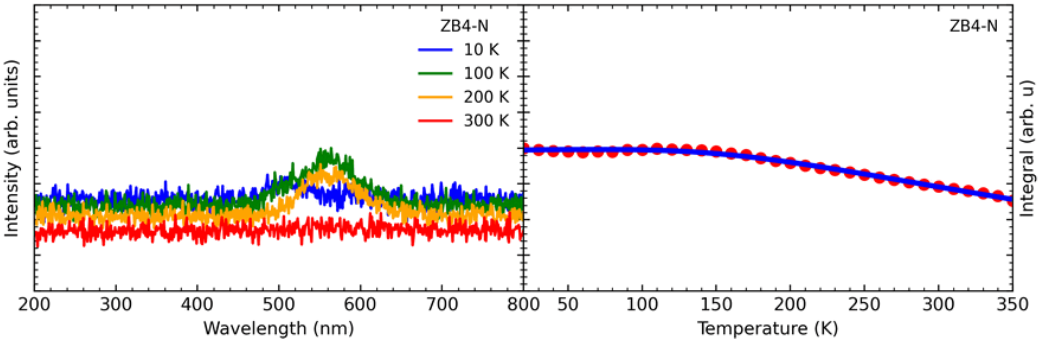

Fig. 5.84. Radioluminescence spectra for four specific temperatures (left side) and the NTQ chart with its fitting (right side) for sample ZB4-N.

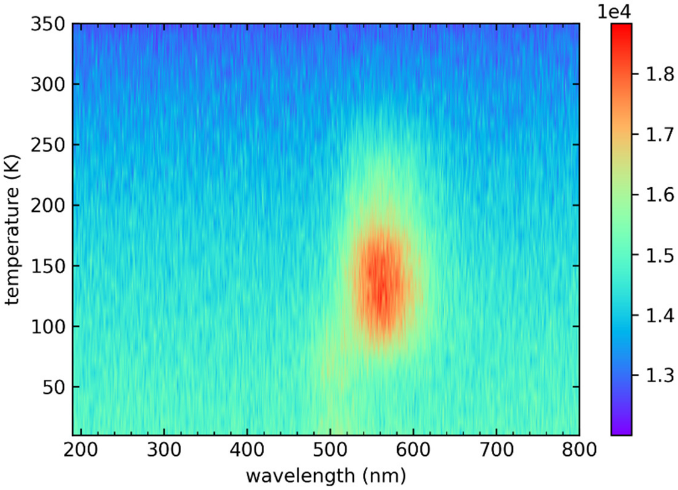

Fig. 5.85. Spectral map for sample ZB4-N.

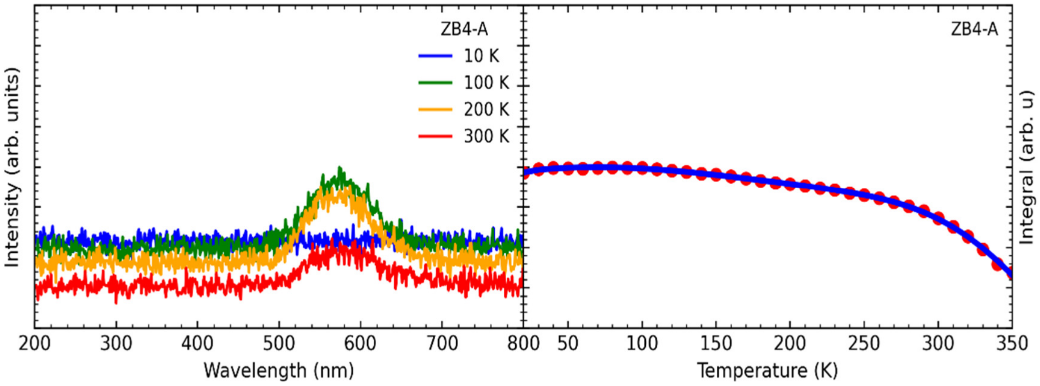

Fig. 5.86. Radioluminescence spectra for four specific temperatures (left side) and the NTQ chart with its fitting (right side) for sample ZB4-A.

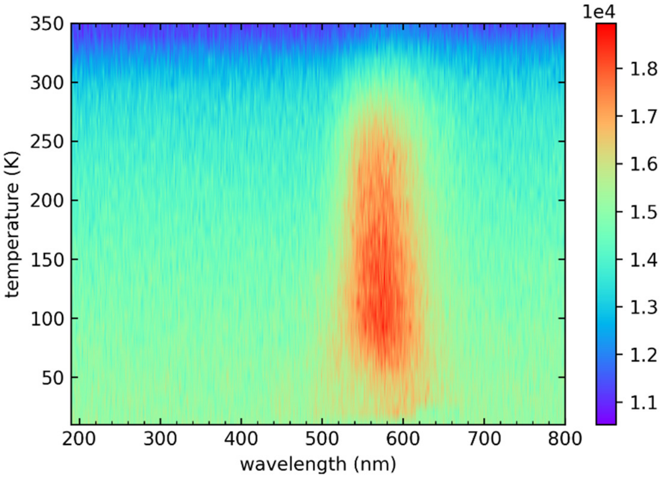

Fig. 5.87. Spectral map for sample ZB4-A.

Tab. 5.13. Fitting parameters of the NTQ curves for samples from ZnSe and (Zn,Be)Se.

ID	Be (%)	A(0)	D1	E_1^N(meV)	C1	E_1^D(meV)	C2	E_2^D(meV)	C3	E_3^D(meV)
ZS-N	0	$2.81 \cdot 10^5$	$7.67 \cdot 10^1$	0.58	5.47	760	5.21	35	$7.90 \cdot 10^5$	971
ZB1-N	10	$9.29 \cdot 10^6$	$3.43 \cdot 10^1$	51	$2.68 \cdot 10^2$	99	$7.71 \cdot 10^5$	451	$8.19 \cdot 10^5$	923
ZB2-A	2	$3.14 \cdot 10^5$	$2.84 \cdot 10^2$	0.12	$1.58 \cdot 10^1$	0.013	$6.11 \cdot 10^1$	105	$8.18 \cdot 10^5$	999
ZB3-A	5	$1.15 \cdot 10^6$	$8.84 \cdot 10^3$	2.69	$3.78 \cdot 10^2$	40	$1.28 \cdot 10^3$	2.72	$1 \cdot 10^6$	265
ZB3-N	5	$3.48 \cdot 10^5$	$9.62 \cdot 10^2$	1.89	$4.99 \cdot 10^1$	2	$3.23 \cdot 10^1$	35	$3.34 \cdot 10^5$	332
ZB4-A	10	$1.64 \cdot 10^5$	$5{,}56 \cdot 10^1$	0.34	$8.55 \cdot 10^2$	99.9	$3.9 \cdot 10^{-1}$	3.6	$2.11 \cdot 10^3$	271
ZB4-N	10	$3.02 \cdot 10^5$	$2.91 \cdot 10^2$	0.123	$1.14 \cdot 10^1$	59	8.83	0.1	$8.71 \cdot 10^5$	601

Based on **Tab. 5.13**, it is clear that the energy levels are significantly influenced by the concentration of beryllium (Be) and the sample treatment, whether annealed (A) in zinc vapor or non-annealed (N). For instance, the E_1^N energy level varies considerably across samples, ranging from 0.12 meV in the ZB2-A sample (2% Be, annealed) to 51 meV in the ZB1-N sample (10% Be, non-annealed). The E_1^D energy level also shows substantial variation, from 0.013 meV in the ZB2-A sample to 760 meV in the ZS-N sample (0% Be, non-annealed).

These variations indicate a strong dependency on both Be concentration and the annealing process. For instance, the ZB3-A and ZB3-N samples (both with 5% Be) show E_1^Nvalues of 2.69 meV and 1.89 meV respectively, while their E_1^Dvalues are 40 meV and 2 meV, highlighting the impact of annealing. Additionally, the highest energy level E_3^Dvaries from 2.11 meV in the ZB4-A sample (10% Be, annealed) to 10^6 meV in the ZB3-A sample (5% Be, annealed), further emphasizing the significant influence of beryllium concentration and sample preparation on these energy levels.

The variations in energy levels suggest that increasing the Be concentration introduces additional energy states within the material, altering the electronic structure and introducing defect levels within the band gap. Annealing in zinc vapor appears to enhance the incorporation of Be into the lattice, reduce defects and stabilize the material, leading to higher and more consistent energy levels. This implies that annealed samples are more thermally stable, with improved thermal activation characteristics, which is crucial for applications requiring consistent performance at varying temperatures. Therefore, by carefully controlling Be concentration and annealing conditions, it is possible to optimize the electronic properties of these materials for targeted applications, such as optoelectronic devices or scintillators.

5.3.4 Thermoluminescence of ZnSe and (Zn,Be)Se

The glow curve analysis reveals that certain samples exhibit a notable peak at around 100 K in **Figs. 5.88**, **5.90**, and **5.94** (samples ZB1-A, ZB1-N, and ZB4-N) and around 90 K in **Fig. 5.92** (sample ZB2-N). The detailed thermoluminescence assessment, the same figures we have experimental findings alongside the heating protocol, a tri-exponential fit to minimize background interference, and a linear fit to determine the heating rate (β). **Figs. 5.89**, **5.91**, **5.93**, and **5.95** present the distributions used for fitting traps.

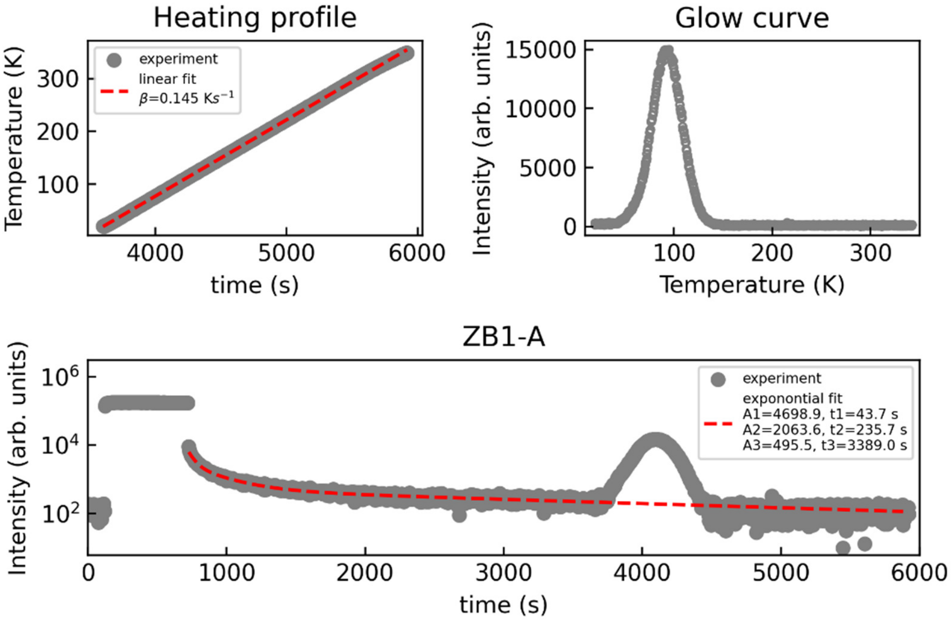

Fig. 5.88. The chart depicting the overall thermoluminescence measurement of sample ZB1-A.

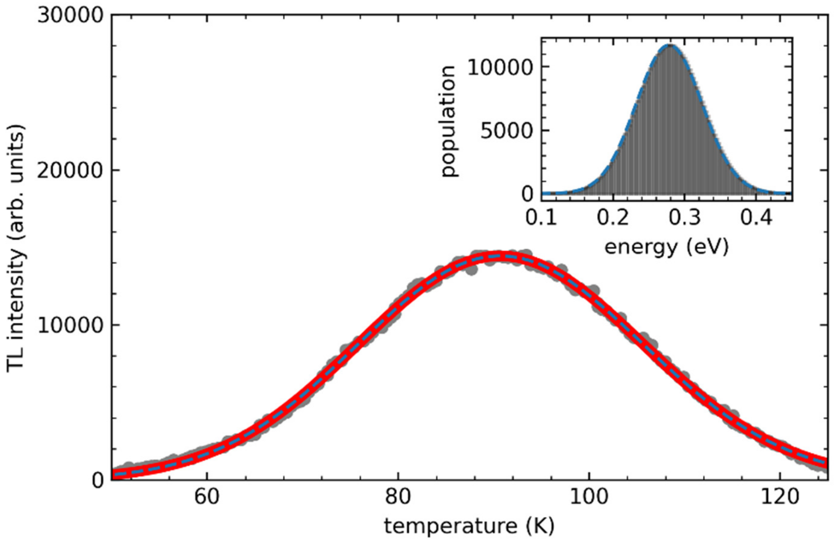

Fig. 5.89. The distribution of Gaussian distributions used for fitting traps for sample ZB1-A.

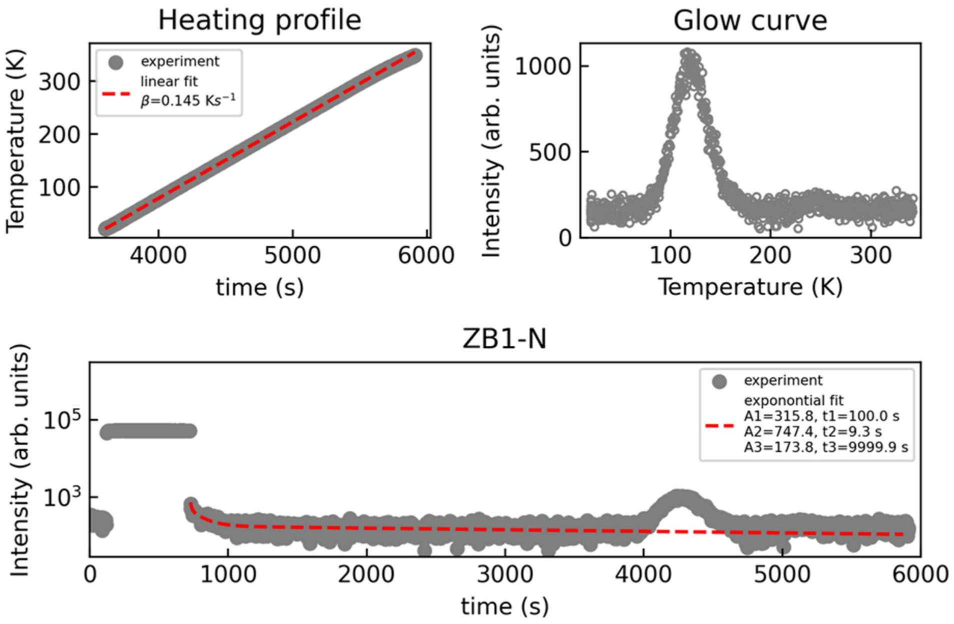

Fig. 5.90. The chart depicting the overall thermoluminescence measurement of sample ZB1-N.

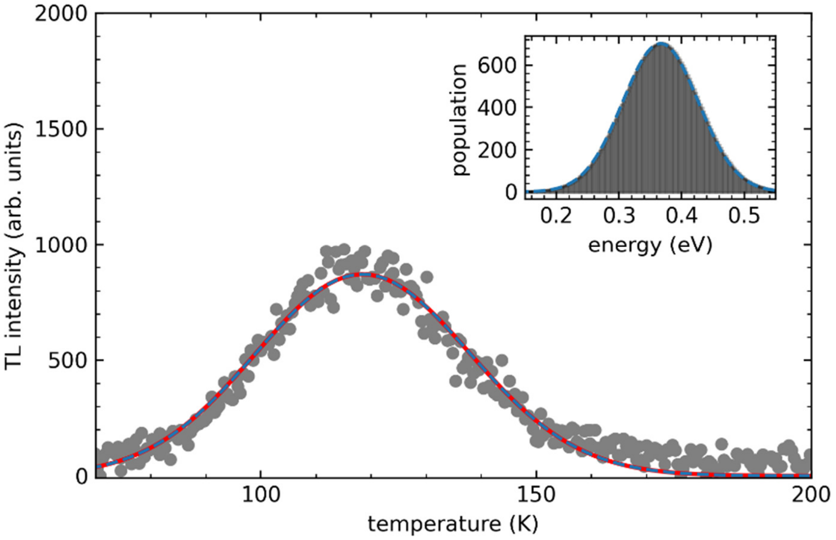

Fig. 5.91. The distribution of Gaussian distributions used for fitting traps for sample ZB1-N.

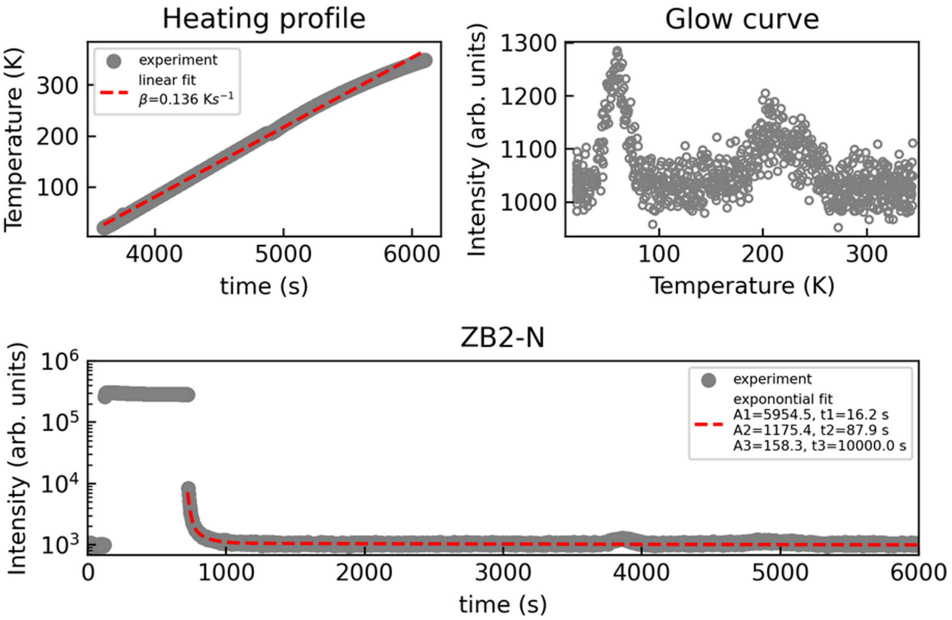

Fig. 5.92. The chart depicting the overall thermoluminescence measurement of sample ZB2-N.

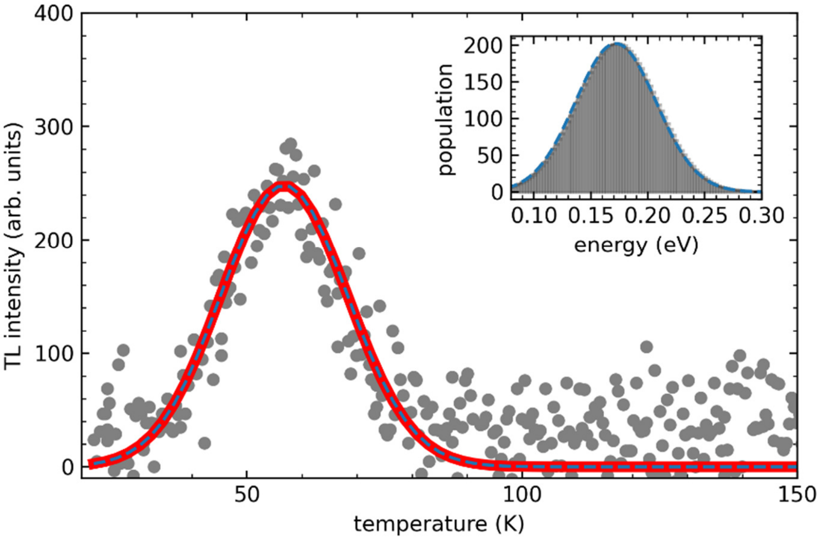

Fig. 5.93. The distribution of Gaussian distributions used for fitting traps for sample ZB2-NA.

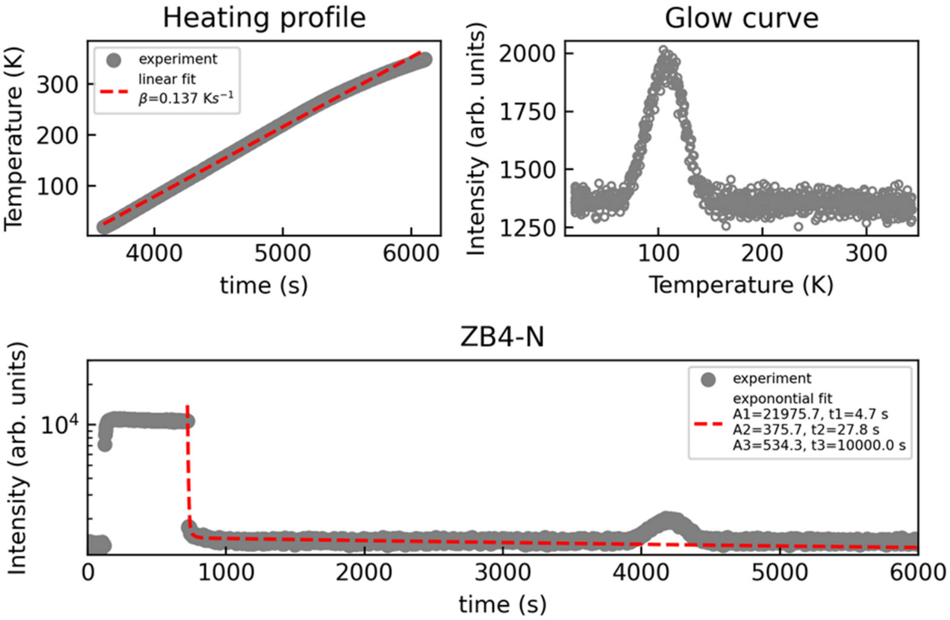

Fig. 5.94. The chart depicting the overall thermoluminescence measurement of sample ZB4-N.

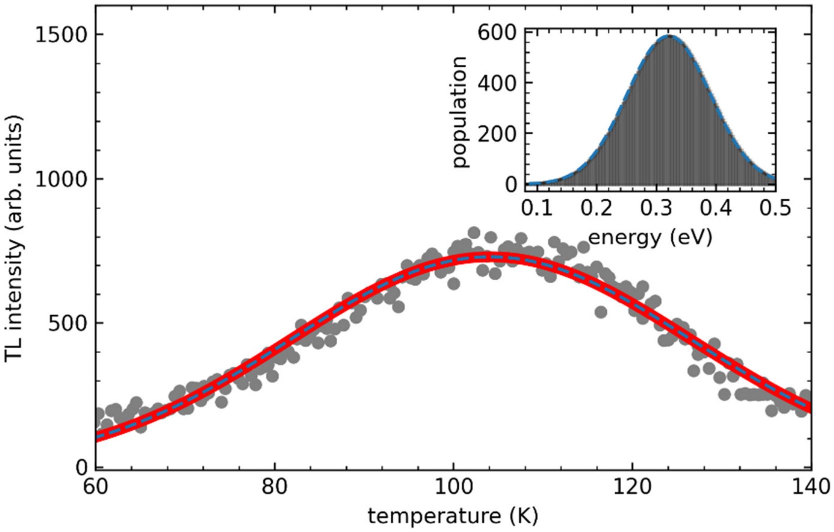

Fig. 5.95. The distribution of Gaussian distributions used for fitting traps for sample ZB4-N.

We are particularly focused on the comprehensive fitting of the glow curve (refer to **Figs. 5.89**, **5.91**, **5.93**, and **5.95**), as it yields crucial insights into trap parameters. Throughout our investigation, most of the examined samples exhibited no resolvable glow peaks, except for the first series of samples ZB1-A and ZB1-N, and from the second series, samples ZB2-N and ZB4-N. By fitting the glow curve, we extracted essential parameters of individual distributions, including their activation energy (E) and the σ factor. We employed a model featuring a distinct distribution to accurately capture the entire luminescence curve. Detailed information regarding these distributions is provided in **Tab 5.14.**

Tab. 5.13. Parameters of the distribution used for fitting the glow curve of sample ZnSe and (Zn,Be)Se.

ID	Sample	Be (%)	Number of distributions	E (meV)	σ (meV)	s (s^{-1})	FOM (%)	R (%)
ZB1-A	(Zn,Be)Se	10	1	278	46	10^{14}	34	99
ZB1-N		10	1	366	61		16.4	97
ZB2-N		2	1	172	35		66	60
ZB4-N		10	1	321	70		9.11	98

Upon analyzing the parameters derived from the distribution data and their associated traps, it becomes evident that the primary trap present in each sample holds paramount importance. For the first series of samples, ZB1-A and ZB1-N, the traps are situated at energy levels of 278 meV (σ = 46 meV, s = 10^{14} s^{-1}) and 366 meV (σ = 61 meV), respectively. In the second series of samples, ZB2-N and ZB4-N, the traps are located at energy levels of 172 meV (σ = 35 meV) and 321 meV (σ = 70 meV), respectively. The figures of merit (FOM) and R-values for these distributions are also notable, indicating the reliability of these fits. No other significant traps are present in these samples, underscoring the dominance of these singular traps in determining the luminescence characteristics (**Tab 5.14**).

5.3.5 Temperature dependence of (Zn,Be)Se

In this part, we present the pulse height spectra of non-annealed $Zn_{0.98}Be_{0.02}Se$ from the second series of crystals, recorded at various temperatures. The room temperature light yield of this sample falls within the range observed for this series of crystals. Given that the experiment spans several days and the sample contains only 2% Be, this sample was selected as a representative compromise for both (Zn,Be)Se. Although the full energy peak is not clearly resolved, we observe that as the temperature increases, the Compton edge shifts towards lower channels. This shift indicates a decrease in scintillation yield as the temperature rises. To quantify this effect, we analyzed the inflection points of the Compton edge and plotted the temperature dependence of the yield in the inset of **Fig. 5.96**. It is evident that only about 20% of the scintillation yield is retained at room temperature compared to 90 K. This significant reduction in light yield suggests the presence of a strong quenching mechanism that becomes more pronounced at higher temperatures, preventing the material from maintaining a higher light output. Further analysis indicates that annealing the samples in a zinc atmosphere might mitigate this quenching effect. This hypothesis is supported by the observation that annealed samples exhibit significantly better scintillation performance at room temperature. The annealing process likely alters the defect structure or impurity levels within the crystal, thereby enhancing its ability to scintillate efficiently even at elevated temperatures.

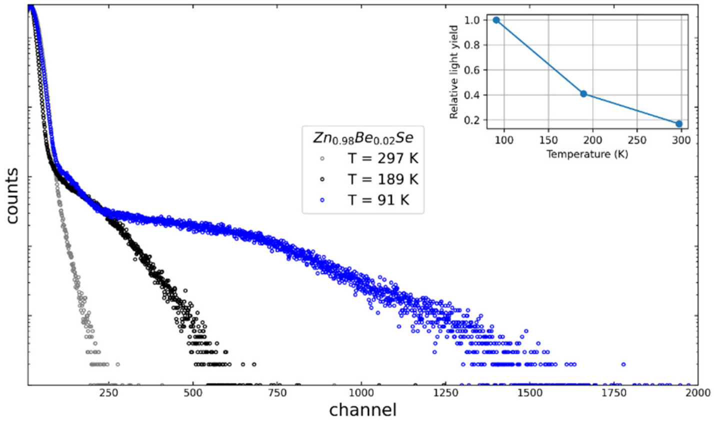

Fig. 5.96. Temperature dependence of pulse height spectra for $Zn_{0.98}Be_{0.02}Se$ under 662 keV excitation from a ^{137}Cs source

In conclusion, the pulse height spectra analysis of non-annealed $Zn_{0.98}Be_{0.02}Se$ demonstrates a clear temperature-dependent decrease in scintillation yield, attributed to a strong quenching mechanism. The potential for annealing in a zinc atmosphere to reduce this quenching effect underscores the importance of post-growth treatment in optimizing the scintillation properties of (Zn,Be)Se crystals. This study highlights the delicate balance between material composition, processing conditions, and operational temperature in determining the overall performance of scintillation materials.

5.4 Thermal properties of ZnSe and (Zn,Be)Se

This study explores thermal properties plus energies gap of the second series of $Zn_{1-x}Be_xSe$ crystals. The mass ratio (x) of Be in the initial material ranged from x = 0.02 to x = 0.2. The mixed crystals were synthesized using a modified Bridgman method under high pressure and high temperature. Band gap energy for each sample was measured through absorption spectroscopy. Thermal properties were assessed using photopyroelectric (PPE) calorimetry in both back and front detection modes. Thermal diffusivity and thermal effusivity values were extracted from experimental data, and thermal conductivity was calculated using theoretical relationships between thermal parameters. The effect of Be concentration on the optical and thermal properties of $Zn_{1-x}Be_xSe$ crystals is analyzed and discussed.

5.4.1 Energy gap results

The absorption spectra of $Zn_{1-x}Be_xSe$ mixed crystals with varying zinc concentrations of x, both annealed in zinc vapor and non-annealed, are shown in **Fig. 5.97**. It is evident that the absorption spectra gradually shift to the high energy side with increasing beryllium content, and also decrease due to annealing in the same composition. The Tauc diagram method [16] was used to estimate the band gap of the semiconductors based on their absorption spectra. The band gap energies for $Zn_{1-x}Be_xSe$ mixed crystals with different zinc contents were calculated by extrapolating the slope of the absorption coefficient squared versus photon energy to the baseline. **Fig. 5.97** depicts room temperature absorption spectra for $Zn_{1-x}Be_xSe$ mixed crystals with various Be contents (x = 0.02-0.2). **Tab 5.15** summarizes the calculated band gap energies of $Zn_{1-x}Be_xSe$ mixed crystals at room temperature.

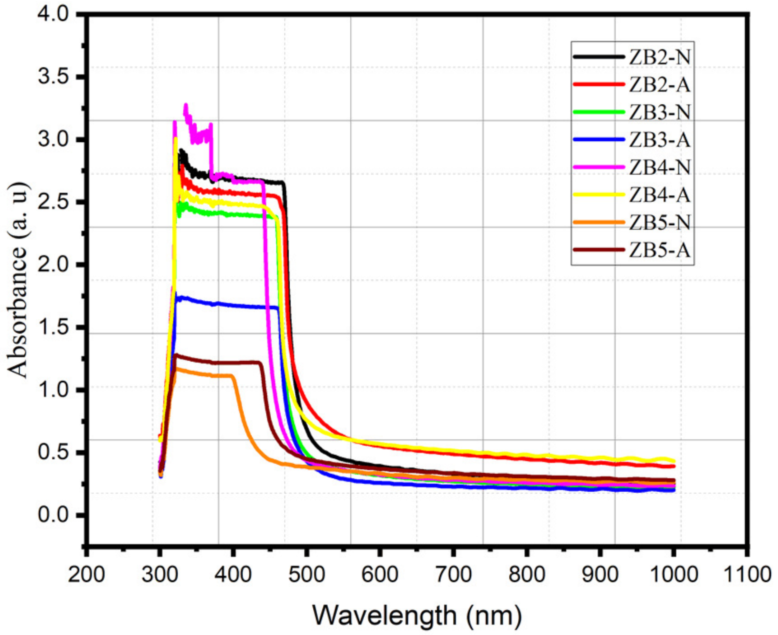

Fig. 5.97. Room temperature absorption spectra for $Zn_{1-x}Be_xSe$ mixed crystals with varying Be content.

Tab. 5.14. Band gap energy values for $Zn_{1-x}Be_xSe$ mixed crystals as a function of Be composition and annealing in zinc vapor.

ID	Sample	Be (%)	Energy gap (eV)
ZB2-N	(Zn,Be)Se	2	2.60
ZB2-A		2	2.58
ZB3-N		5	2.65
ZB3-A		5	2.63
ZB4-N		10	2.76
ZB4-A		10	2.64
ZB5-N		20	3.00
ZB5-A		20	2.74

5.4.2 PPE thermal results

All samples investigated in this work were measured using both back and front configurations of the PPE method (see chapter 4). Phase characteristics of the $Zn_{1-x}Be_xSe$ samples, measured as a function of the square root of the modulation frequency, are presented in **Fig. 5.98**. Nonlinear behavior of the phase can be observed in the low-frequency regime, caused by a thermally thin sample and/or the sensor. Therefore, linear fits started at 8 Hz, where the sample and the detector are both thermally thick. The least squares method was used for the fitting procedure. Differences in the slopes between the curves presented in **Fig. 5.98** can be found. The thermal diffusivity of the $Zn_{1-x}Be_xSe$ sample was calculated according to **Eq. 4.10** (check chapter 4). The obtained thermal diffusivity values are the averages of five separate measurements, with the standard deviation as an uncertainty. $Zn_{0.98}Be_{0.02}Se$ (ZB2-A, ZB2-N) and $Zn_{0.8}Be_{0.2}Se$ (ZB5-A, ZB5-N) exhibit the highest and lowest thermal diffusivity, respectively.

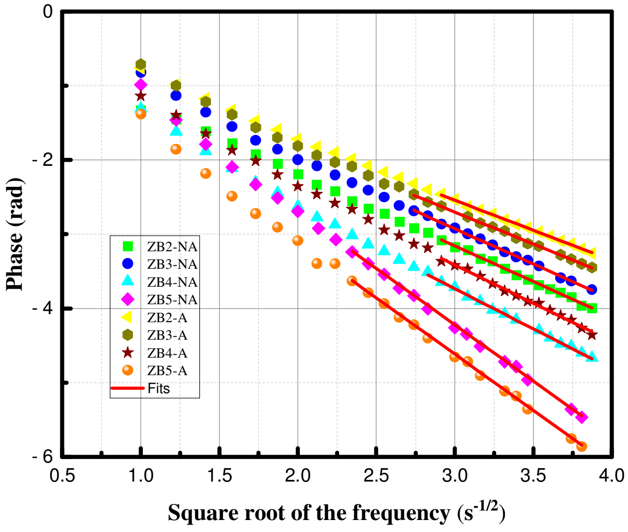

Fig. 5.98. The phase responses of all samples investigated using the BPPE method, plotted against the square root of the modulation frequency (experimental data are indicated by points, and the corresponding linear fits are shown as lines).

The thermal effusivity of the studied materials was determined using the PPE technique in a front measurement configuration combined with a frequency scanning procedure (as been described in chapter 4). For this analysis, the following parameters of the $LiTaO_3$ detector were used: $\alpha_p = 1.36 \times 10^{-6}$ m² s^{-1} and $e_p = 3660$ W s$^{1/2}$ m^{-2} K^{-1} [17]. **Fig. 5.99** displays the experimental phase behavior of the $Zn_{1-x}Be_xSe$ samples as a function of frequency, with data points representing the measured values and lines showing the best fits obtained via the least-squares method using **Eq. 4.11** (see chapter 4). The thermal effusivity values for $Zn_{1-x}Be_xSe$ samples are presented in descending order. These values were calculated as averages from five separate measurements, with the standard deviation indicating the uncertainty.

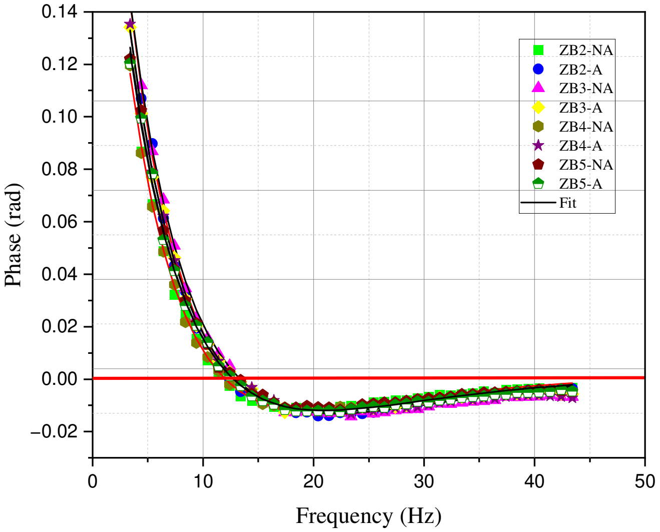

Fig. 5.99. The FPPE phase responses of all investigated samples plotted against the modulation frequency.

It can be observed that all curves intersect the zero phase point at the same modulation frequency. This indicates that the measurement and normalization procedures were executed correctly. According to **Eq. 4.11**, this intersection point can be utilized to determine the thermal properties of the sensor if needed. The error associated with the fitting procedure is illustrated in **Fig. 5.100**.

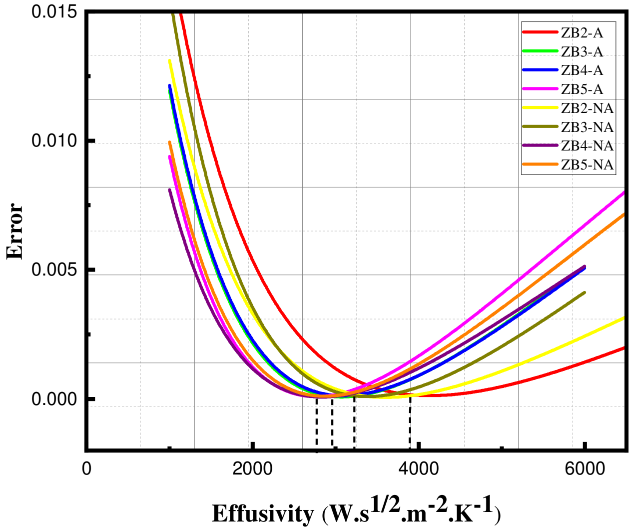

Fig. 5.100. The fitting procedure error as a function of the effusivity values.

The minimum point observed in the fitting error graph corresponds to the thermal effusivity value of the investigated sample. Simple relationships connect the thermal parameters. The thermal conductivity of the investigated crystals was determined using the following formula:

$$k = e\alpha^{1/2} \tag{5.1}$$

All thermal parameters and sample thicknesses as a function of composition are provided in the reference table. High experimental repeatability demonstrated that the uncertainties are within 1% or even less of the measured values. The micrometer used to measure thickness has an accuracy of 0.01 mm, resulting in an uncertainty of 1.0 to 1.5%. The primary source of error is fluid interaction between the sample and the sensor. Previous studies have shown that it is possible to reduce this uncertainty to around 2-3%. Taking all contributions into account, the total uncertainty of the values obtained is approximately 4.0 to 5.5%.

Tab. 5.15. The thermal parameters of $Zn_{1-x}Be_xSe$ mixed crystals of different compositions of Be element.

Be (%)	Thermal Diffusivity $(m^2 \cdot s^{-1}) \cdot 10^{-6}$		Thermal Effusivity $(W \cdot m^{-2} \cdot K^{-1/2})$		Thermal Conductivity $(W \cdot m^{-1} \cdot K^{-1})$	
	Annealed	Non-Annealed	Annealed	Non-Annealed	Annealed	Non-Annealed
2	5.7	6	3617	3483	7	8.5
5	4.1	3.7	3228	3525	6.8	6.5
10	3.2	3.3	3033	2853	5.2	5.4
20	2.4	2.7	2753	2818	4.6	4.2

Based on the data in **Tab 5.16**, both beryllium incorporation and annealing in zinc vapor have a significant impact on the thermal properties of the crystals. Generally, these processes lead to a reduction in thermal diffusivity, thermal effusivity, and thermal conductivity. Specifically, annealed samples consistently show lower thermal diffusivity across all beryllium levels compared to their non-annealed counterparts. At lower beryllium concentrations, annealed samples also exhibit higher thermal effusivity, although this trend reverses with increasing beryllium content. Additionally, thermal conductivity is consistently reduced in annealed samples, highlighting that annealing generally decreases the material's thermal conductivity.

In relation to scintillation performance, despite the lower thermal parameters, annealed samples demonstrate improved scintillation efficiency. For example, at 2% beryllium, the annealed sample achieves a significantly higher light yield of 7,720 ph/MeV compared to 2,030 ph/MeV for the non-annealed sample (as previously mentioned). This improvement is notable considering the lower thermal diffusivity and conductivity of the annealed samples. Annealing helps reduce thermal quenching effects, where excess heat diminishes scintillation efficiency by enhancing crystal quality and minimizing defect density. This leads to more efficient light emission and better overall scintillation performance. Consequently, although annealed samples have reduced thermal parameters, their enhanced scintillation efficiency makes them more suitable for applications requiring high light yield and reduced quenching.

5.4.3 Thermal resistivity of the lattice

Recognizing that every imperfection in the crystal structure acts as a scattering center for phonons is crucial, as this impairs the material's ability to conduct heat efficiently. Therefore, the thermal conductivity of a material is influenced by the presence, purity, and concentration of defects within the crystal, as well as its overall quality. In semiconductor alloys, the random distribution of atoms within the sublattice sites has a significant impact on lattice thermal conductivity. To better understand this, Abeles [18] proposed a phenomenological model to explain the thermal conductivity mechanisms. Later, Adachi [19] provided a more straightforward approach, showing that for $A_xB_{1-x}C$ compounds the thermal resistivity can be expressed with the formula:

$$W(x) = xW_{AC} + (1 - x)W_{BC} + x(1 - x)C_{A\text{-}B} \qquad (5.2)$$

where W_{AC} and W_{BC} are the thermal resistivities of the binary components, and $C_{A\text{-}B}$ accounts for the effect of lattice disorder.

Adachi's formula greatly simplified the analysis of thermal resistivity in semiconductor alloys by offering a clear relationship between compositional parameters, such as x, and thermal resistivity. This advancement has paved the way for more effective study and design of semiconductor materials with targeted thermal properties. From the provided equation, we can also derive the lattice thermal conductivity K(x):

$$K(x) = \frac{1}{W(x)} = \frac{1}{xWAC + (1 - x)WBC + x(1 - x)CA - B} \qquad (5.3)$$

Fig. 5.101 illustrates the thermal conductivity of the ternary $Zn_{1-x}Be_xSe$ semiconductor as a function of composition at room temperature. The fitting shown in **Fig. 5.100** enabled us to determine the additional thermal resistivity $C_{Zn\text{-}Be}$ due to chemical disorder, which was found to be 38 $W^{-1}\cdot cm\cdot K$. The coefficient of determination R^2, which reflects the accuracy of the fitting procedure, was 0.99. As observed, thermal conductivity decreases rapidly at x values close to 0 and increases significantly near x = 1, with a plateau appearing in the middle of the graph. The $C_{Zn\text{-}Be}$ value is notably lower compared to previously studied crystals such as CdZnTe, CdBeTe, or ZnMgSe, where it exceeded 100. Instead, it aligns more closely with the values reported for III-V mixed crystals studied by Adachi [20]. This indicates that a substantial amount of Mg can be incorporated without causing significant disruption to the lattice, which is promising for potential applications of this material.

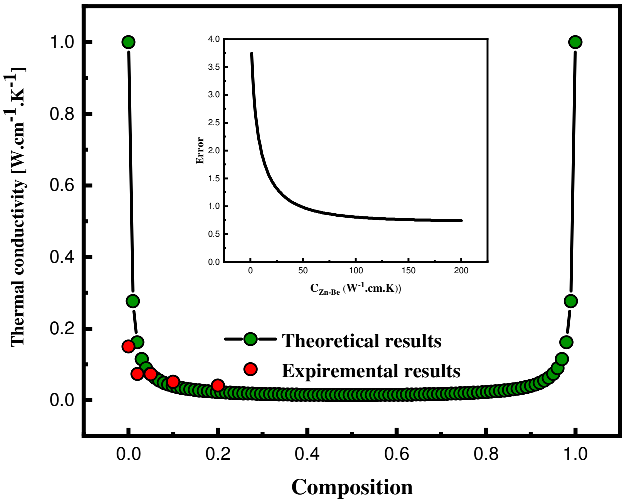

Fig. 5.101. Thermal conductivity curve versus composition (the error graph arising from the least square approach is presented in the inset)

References (chapter 5)

[1] Y. R. Wu, C.-Y. Huang, Y. Zhao, and J. S. Speck, “Nitride Semiconductor Light Emitting Diodes (LEDs),” Mater. Technol. Appl., no. 1, p. 250, 2014

[2] G. Zatryb and M. M. Klak, “On the choice of proper average lifetime formula for an ensemble of emitters showing non-single exponential photoluminescence decay”, Journal of Physics: Condensed Matter., vol. 32, no. 41, p. 415902, 2020

[3] H. Shibata, “Negative thermal quenching curves in photoluminescence of solids,” Japanese Journal of Applied Physics., vol. 37, no. 2, p. 550, 1998.

[4] J.T. Randall, M.H.F. Wilkins, “Phosphorescence and electron traps II. The interpretation of long-period phosphorescence” Proceedings of the Royal Society of London., vol. A184 p. 366, 1945

[5] G.F.J. Garlick, A.F. Gibson, “The Electron Trap Mechanism of Luminescence in Sulphide and Silicate Phosphors” Proceedings of the Physical Society., vol. 60, p. 574, 1948

[6] S.W.S. McKeever, “On the analysis of complex thermoluminescence. Glow-curves: Resolution into individual peaks ” physica status solidi A ., vol. 62, p. 331, 1980

[7] R. Chen, “Theory of Thermoluminescence and Related Phenomena”, World Scientific, Singapore / River Edge, N.J. p. 576 1997

[8] W.L. Medlin, “Decay of Phosphorescence from a Distribution of Trapping Levels” Physical Review., vol. 123, p. 502, 1961

[9] A.J.J. Bos, T.M. Piters, J.M.G. Ros, A. Delgado, “ An Intercomparison of Glow Curve Analysis Computer Programs: II. Measured Glow Curves, Radiation Protection Dosimetry.,vol. 51, 150, p. 257, 1994

[10] R. Chen, “Theory of thermoluminescence and related phenomena” World Scientific, Singapore; River Edge, N.J. 1997.

[11] L. Swiderski, et al., “Scintillation response to gamma-rays measured at wide temperature range for Tl doped CsI with SiPM readout” Nuclear Instruments and Methods in Physics Research., vol. 916, p. 32, 2019

[12] M. Grodzicka, et al, “Performance of FBK high-density SiPMs in scintillation spectrometry”, Journal of Instrumentation., vol. 9, P. P08004, 2014

[13] Z. Galazka, D. Klimm, K. Irmscher, R. Uecker, M. Pietsch, R. Bertram, M. Naumann, M. Albrecht, A. Kwasniewski, R. Schewski, and M. Bickermann, “$MgGa_2O_4$ as a new wide bandgap transparent semiconducting oxide: growth and properties of bulk single crystals” Physical Status Solidi A., vol. 212, no. 7, p. 1455, 2015

[14] Z. Galazka, “Transparent Semiconducting Oxides - Bulk Crystal Growth and Fundamental Properties”., p. 750, 2020

[15] Z. Galazka, R. Schewski, K. Irmscher, W. Drozdowski, M. E. Witkowski, M. Makowski, A. J. Wojtowicz, I. M. Hanke, M. Pietsch, T. Schulz, D. Klimm, S. Ganschow, A. Dittmar, A. Fiedler, T. Schroeder, and M. Bickermann, “Bulk β-Ga_2O_3 single crystals doped with Ce, Ce+Si, Ce+Al, and Ce+Al+Si for detection of nuclear radiation,” Journal of Alloys and Compounds., vol. 818, p. 152842, 2020

[16] P. Makuła, M. Pacia, W. Macyk, “How To Correctly Determine the Band Gap Energy of Modified Semiconductor Photocatalysts Based on UV–VIS Spectra,” Journal of Physical Chemistry Letters., vol. 9, p.6814, 2018

[17] D. Dadarlat, M. Streza, M.N. Pop, V. Tosa, S. Delenclos, S. Longuemart, A.H. Sahraoui, “Photopyroelectric calorimetry of solids,” Journal of Thermal Analysis and Calorimetry., vol. 101, p. 397, 2010

[18] B. Abeles, “Lattice Thermal Conductivity of Disordered Semiconductor Alloys at High Temperatures,” Physical Review., vol. 131, p. 1906, 1963

[19] S. Adachi, “Lattice thermal conductivity of group-IV and III–V semiconductor alloys,” Journal of Applied Physics., vol. 102, p. 063502, 2007

[20] D. Barbier, B. Montegu, A. Laugier, “Temperature dependence of the energy gap of $Mg_xZn_{1-x}Te$ semiconductors alloys,” Solid State Communication. vol. 28, p. 525, 1978

Chapter 6

6 Summary and conclusions

The primary objective of this doctoral dissertation was to present and analyze the measurement results of semiconductor scintillators from two distinct categories of crystals. The first category includes β-Ga_2O_3 crystals, both pure and silicon-doped, as well as two Ga-based spinels, $MgGa_2O_4$ and $ZnGa_2O_4$, grown at IKZ in Berlin and studied under the Polish-German project (no. 2016/23/G/ST5/04048 (NCN) / GA 2057/2-1 (DFG)). The second category involves pure ZnSe and (Zn,Be)Se crystals grown at Nicolaus Copernicus University in Toruń with an active participation of the author of the thesis. The results from these studies are categorized into three groups. The first category involves the measurement of scintillation and luminescent properties, focusing on gallium oxide crystals, Ga-based spinels, ZnSe, and (Zn,Be)Se. The second category includes temperature-dependent relative light yield measurements for all crystals, conducted during the author's internship at NCBJ in Świerk. The third category explores the thermal properties of (Zn,Be)Se crystals.

The initial phase of the research involved measuring pulse height spectra to assess the scintillation efficiency of each crystal, with detailed results presented in subsection **5.1.1**. Analysis of data in **Tabs 5.3** and **5.4** reveals that pure β-Ga_2O_3 crystals with free carrier concentrations ranging from 10^{16} to 10^{17} cm^{-3} exhibited the highest scintillation efficiency. The reduction in light yield (LY) with increasing free carrier concentration is attributed to the parasitic Auger effect (n^3) relative to scintillation. The undoped sample I1 demonstrated the highest scintillation efficiency of 9090 ph/MeV and the best energy resolution among the studied crystals ($R = 10.6\%$). Silicon doping did not positively affect the scintillation efficiency. Pulse height spectra for $MgGa_2O_4$ and $ZnGa_2O_4$ single crystals, discussed in section **5.2.1**, confirmed that Ga spinel crystals scintillate under gamma excitation, achieving 2,500 ph/MeV with an energy resolution of 29.9%. Finally, section **5.3.1** presents the pulse height spectra for ZnSe and (Zn,Be)Se crystals, exploring the impact of annealing in zinc vapor. This process significantly enhanced scintillation efficiency, reaching 26,000 ph/MeV for ZnSe and 15,000 ph/MeV for (Zn,Be)Se.

The subsequent phase focused on measuring scintillation decay profiles (subsections **5.1.2**, **5.2.2**, **5.3.2**). To ensure accurate analysis, the deconvolution method was used to isolate the decay profile attributable solely to the studied sample. For the semi-conductive samples, including both undoped and Si-doped β-Ga_2O_3 and Ga-spinels, a triple-exponential scintillation decay was observed. In contrast, a double-exponential decay was sufficient to fit the deconvoluted data for ZnSe and (Zn,Be)Se crystals. Fitting parameters for both crystal series are provided in **Tabs 5.5**, **5.8**, and **5.12**. The average decay time (τ_{mean}) was calculated for each sample, allowing for comparisons between multi-exponential decays. The lowest τ_{mean} values were found in samples with free carrier concentrations higher than 10^{18} cm^{-3} or those with insulating properties; however, these samples (mostly β-Ga_2O_3:Si) showed low scintillation efficiency. A balance between efficiency and scintillation speed is necessary, with an optimal focus on crystals with free carrier concentrations in the range of 10^{16}–10^{18} cm^{-3}, offering a good compromise between relatively high efficiency and fast scintillation decay.

The radioluminescence spectra results for both crystal series are detailed in subsections **5.1.3**, **5.2.3**, and **5.3.3**. Most samples exhibited a dominant peak around 350 nm, except for ZnSe and (Zn,Be)Se, which displayed two bands peaking at 460 nm and 600 nm, with the first emission known as edge emission in the literature. Each sample showed negative thermal quenching of luminescence, in line with Shibata's theory, providing further insight into the energy levels. A summary of the data is presented in **Tabs 5.6**, **5.9**, and **5.13**. This research also involved the low-temperature thermoluminescence measurements in the range of 10 to 350 K, as detailed in subsections **5.1.4**, **5.2.4**, and **5.3.4**. The presence of characteristic peaks in glow curves was demonstrated, and curve fittings were obtained using the model proposed by Randall and Wilkins. The fitting results are presented in **Tabs 5.7**, **5.10**, and **5.14**. However, doubts were raised about the accuracy of using equation **4.15**, particularly due to the very low s-parameter values. Standard values for the frequency factor should be around 10^{14} s^{-1}. Fitting parameters for glow curves, considering trap distributions for both crystal series, are presented in Tables **5.7**, **5.10**, and **5.14**.

The second phase conducted at the Nuclear Equipment and Technology Department, under the expert guidance of Prof. Łukasz Świderski, involved selecting four samples from each class of materials to explore their temperature dependence. Detailed information on these experiments can be found in chapter 5, in the last section of each sample category. The results demonstrated a clear temperature-dependent decrease in scintillation yield, attributed to a strong quenching mechanism, with most samples showing less than 50% of the light yield at room temperature.

The third and final phase of research examined the thermal properties and energy gaps of the second series of crystals, specifically ZnSe mixed with beryllium ($Zn_{1-x}Be_xSe$). The mass ratio (x) of Be in the initial material ranged from x = 0.02 to 0.2. The mixed crystals were synthesized using a modified Bridgman method under high pressure and high temperature. Band gap energy for each sample was measured through absorption spectroscopy, aiming to understand the reason behind the scintillation improvement after annealing in zinc vapor, as well as the effect of annealing on the energy gap for each composition of the Be element.

List of Figures

List of tables

Dissemination of results

Peer-reviewed publications

[1] **A. Bachiri**, M. Makowski, M.E. Witkowski, W. Drozdowski, Z. Galazka, "Assessment of the Scintillation Properties of $MgGa_2O_4$ and $ZnGa_2O_4$ Single Crystals", *Optical Materials Express* **13** (2023), 1345-1352 (doi:10.1364/OME.489134)

[2] W. Drozdowski, M. Makowski, **A. Bachiri**, M.E. Witkowski, A.J. Wojtowicz, L. Swiderski, K. Irmscher, R. Schewski, Z. Galazka, "Heading for Brighter and Faster β-Ga_2O_3 Scintillator Crystals", *Optical Materials X* **15** (2022), 100157/1-5 (doi:10.1016/j.omx.2022.100157)

[3] P.Y.D. Maulida, S. Hartati, D. Kowal, L.J. Diguna, M.A. Kuddus Sheikh, M.H. Mahyuddin, I. Mulyani, D. Onggo, F. Maddalena, **A. Bachiri**, M.E. Witkowski, M. Makowski, W. Drozdowski, Arramel, M.D. Birowosuto, "Organic Chain Length Effect on Trap States of Lead Halide Perovskite Scintillators", *ACS Applied Energy Materials* **6** (2023), 5912-5922 (doi:10.1021/acsaem.3c00340)

[4] L.J. Diguna, L. Jonathan, M.H. Mahyuddin, Arramel, F. Maddalena, I. Mulyani, D. Onggo, **A. Bachiri**, M.E. Witkowski, M. Makowski, D. Kowal, W. Drozdowski, M.D. Birowosuto, "BA_2XBr_4 (X = Pb, Cu, Sn): from Lead to Lead-Free Halide Perovskite Scintillators", *Materials Advances* **3** (2022), 5087-5095 (doi:10.1039/D2MA00258B)

[5] F. Maddalena, M.E. Witkowski, M. Makowski, **A. Bachiri**, Arramel, T. Yang, M. Mahyuddin, M. Baravaglio, M. Boutchich, W. Drozdowski, C. Dujardin, M. Birowosuto, C. Dang, "Photodetection and scintillation characterizations of novel lead-bismuth double perovskite halides", *Journal of Materials Chemistry* **C10** (2022), 11266-11275 (doi.org/10.1039/D2TC01646J)

[6] F. Maddalena, M.E. Witkowski, M. Makowski, **A. Bachiri**, B. Mahler, Y.C. Wong, C.Y.E. Chua, J.X. Lee, W. Drozdowski, S.V. Springham, C. Dujardin, M.D. Birowosuto, C. Dang, "Stable and Bright Commercial $CsPbBr_3$ Quantum Dot-Resin Layers for Apparent X-ray Imaging Screen", *ACS Applied Materials & Interfaces* **13** (2021), 59450-59459 (doi:10.1021/acsami.1c16171)

[7] J. Zakrzewski, M. Maliński, **A. Bachiri**, K. Strzałkowski, "Photothermal determination of the optical and thermal parameters of $Cd_xZn_{1-x}Se$ mixed crystals", *Materials Science and Engineering* **B271** (2021), 115305/1-8 (doi:10.1016/j.mseb.2021.115305)

Oral scientific communications

1. The 15th Copernican Doctoral Seminar

   - Location: Toruń, Poland
   - Date: 20-22.06.2022

- Contribution: Oral presentation
- Title: “Scintillation and Luminescence Properties of $MgGa_2O_4$ and $ZnGa_2O_4$ Single Crystals”
- Authors: **A. Bachiri**, M. Makowski, W. Drozdowski, M.E. Witkowski, A.J. Wojtowicz, K. Irmscher, R. Schewski, Z. Galazka

2. 16th Copernican Doctoral Seminar

- Location: Toruń, Poland
- Date: 28-29.06.2023
- Contribution: Oral presentation
- Title: “Scintillation Properties of ZnSe and ZnBeSe Crystals”
- Authors: **A. Bachiri**, K. Strzałkowski, M.E. Witkowski, M. Makowski, W. Drozdowski

Scientific posters

1. 11th International Conference on Luminescent Detectors and Transformers of Ionizing Radiation (LumDeTr)

- Location: Bydgoszcz, Poland
- Date: 13-17.09.2021
- Contribution: Poster presentation
- Title: “Scintillation yield of Czochralski-grown β-Ga_2O_3 and β- Ga_2O_3:Si crystals”
- Authors: **A. Bachiri**, M. Makowski, W. Drozdowski, M.E. Witkowski, A.J. Wojtowicz, K. Irmscher, R. Schewski, Z. Galazka

2. The 14th Copernican Doctoral Seminar

- Location: Toruń, Poland
- Date: 20-22.09.2021
- Contribution: Poster presentation
- Title: “Scintillation yield of β-Ga_2O_3 and β-Ga_2O_3:Si studied by pulse height technique”
- Authors: **A. Bachiri**, M. Makowski, W. Drozdowski, M.E. Witkowski, A.J. Wojtowicz, K. Irmscher, R. Schewski, Z. Galazka

3. The Seventh International Workshop on Advanced Spectroscopy and Optical Materials (IWASOM)

- Location: Gdansk, Poland
- Date: 10-15.07.2022
- Contribution: Poster presentation

- Title: “Gamma Spectroscopy of $MgGa_2O_4$ and $ZnGa_2O_4$ Semiconductor Scintillators”
- Authors: **A. Bachiri**, M. Makowski, M.E. Witkowski, W. Drozdowski, Z. Galazka

4. International Conference on Excited States of Transition Elements (ESTE)
   - Location: Świeradów-Zdrój, Poland
   - Date: 3-8.09.2023
   - Contribution: Poster presentation
   - Title: “Scintillation properties of ZnSe and (Zn,Be)Se crystals”
   - Authors: **A. Bachiri**, K. Strzałkowski, M.E. Witkowski, M. Makowski, K.J. Drozdowski, W. Drozdowski, L. Swiderski
5. The 17th International Conference on Scintillating Materials and their Applications (SCINT)
   - Location: University of Milano-Bicocca, Milan, Italy
   - Date: 8-12.07.2024
   - Contribution: Poster presentation
   - Title: “Bridgman Growth and Scintillation Properties of $Zn_xBe_{1-x}Se$ Crystals”
   - Authors: **A. Bachiri**, K. Strzałkowski, M. Boumhamdi, K.J. Drozdowski, A. Guerchi, M.E. Witkowski, W. Drozdowski